Sorbonne University
Nanyang Technological University

Doctoral school 388 – Sorbonne University

Interdisciplinary Graduate School (IGS) – Nanyang Technological University

UNDERSTANDING THE INTERFACE CONSTITUTION OF A SUBSTRATE/COATING SYSTEM DEPOSITED BY CATHODIC MAGNETRON SPUTTERING HiPIMS

ANGELIQUE ANNIE CHABANON

A thesis submitted the Nanyang Technological University in partial fulfilment of the requirement for the degree of Doctor of Philosophy

Supervised by Dr Fanny Balbaud-Célérier and Associate Professor Zhili Dong

Oral defense on the 28th January, 2022

Jury members:

PEBERE Nadine, Research Director

SANCHETTE Frédéric, Professor

VIVIER Vincent, Research Director

BOISSIERE Cédric, Research Director

CHEN Zhong, Professor

LIU Erjia, Associate Professor

BALBAUD-CELERIER Fanny, Research Director, PhD director

DONG Zhili, Associate Professor, Co-PhD director

JOUAN Pierre-Yves, Professor, Guest

Statement of Originality

I hereby certify that the work embodied in this thesis is the result of original research, is free of plagiarised materials, and has not been submitted for a higher degree to any other University or Institution.

10 April, 2022
Date

Angelique Annie CHABANON

Supervisor Declaration Statement

I have reviewed the content and presentation style of this thesis and declare it is free of plagiarism and of sufficient grammatical clarity to be examined. To the best of my knowledge, the research and writing are those of the candidate except as acknowledged in the Author Attribution Statement. I confirm that the investigations were conducted in accord with the ethics policies and integrity standards of Nanyang Technological University and that the research data are presented honestly and without prejudice.

10 April, 2022
Date

Assoc Prof Dong Zhili

Authorship Attribution Statement

This thesis **does not** contain any materials from papers published in peer-reviewed journals or from papers accepted at conferences in which I am listed as an author.

10 April, 2022
Date

Angelique Annie CHABANON

Acknowledgements

Je tiens tout d'abord à remercier Nadine Pébère et Frédéric Sanchette, qui ont accepté d'être rapporteurs de mon travail de doctorat. Je remercie également le président du jury, Vincent Vivier, et les membres du jury, Cédric Boissière, Zhong Chen et Erjia Liu, pour avoir accepté d'évaluer ma thèse et pour nos discussions enrichissantes lors de la soutenance.

J'ai eu la chance de réaliser mes travaux de doctorat au SEARS et plus particulièrement, dans le laboratoire d'ingénierie des surfaces et des lasers (LISL). Je remercie donc Lionel Gosmain et Hicham Maskrot de m'avoir accueillie dans leur service et laboratoire, respectivement. Merci de m'avoir donné les moyens de faire cette thèse.

Je remercie bien évidemment ma directrice de thèse, Fanny Balbaud-Célérier, et mon co-directeur de thèse, Zhili Dong, sans qui ce travail n'aurait pas été possible. Merci pour leur confiance et leur investissement dans cette thèse. Un grand merci aux personnes qui m'ont encadrée et accompagnée pendant ces trois ans et trois mois : Alexandre Michau, Michel Schlegel, Frédéric Schuster, Beatriz Puga (CEA/LECNA), Srikanth Narasimalu (NTU/ERIAN) et Pierre-Yves Jouan (IMN). Merci Alexandre pour ta disponibilité et ton aide au quotidien, que ce soit pour l'utilisation/réparation des machines de dépôt ou pour m'avoir remontée le moral dans les moments de doute. Merci Michel pour avoir cru en moi dès mon stage de fin d'étude et pour ta pédagogie tout au long de ma thèse. Merci Frédéric pour tes conseils et ton expertise scientifique/industrielle durant ce travail de doctorat. Merci également à Beatriz pour ta bonne humeur, ta disponiblité et ton aide pour les essais d'électrochimie. Enfin, je remercie Pierre-Yves et Srikanth pour leur investissement, même à distance, dans cette thèse, leur aide et leurs conseils.

Je souhaite également remercier Michel Tabarant (CEA/LANIE), Frédéric Miserque (CEA/LECA), Georges Beainy (CEA/DMN) et Cristelle Pareige (GPM Rouen) pour leur expertise et leurs conseils. Merci aux personnes de l'institut CORRODYS et l'entreprise DEPHIS avec lesquelles j'ai été amenée à travailler.

Je remercie l'ensemble des personnes des bâtiments 391, 458 et 467 du CEA Saclay pour leur accueil et les moments partagés tous ensemble. Un grand merci à Géraldine, Barbara et Céline pour leur énergie positive et nos discussions qui rendaient tout le reste plus léger.

Je tiens également à remercier l'ensemble des personnes que j'ai cotoyé et qui m'ont aidé à NTU comme Claude Guet, Binqing Yao, Sekar Manoj, Lek Jun Yan ou encore Lifei Xi.

Merci à tous les jeunes docteurs, doctorants et stagiaires présents pendant ma thèse. Vous avez permis à ces trois années et trois mois d'être inoubliables. Merci aux derniers représentants des pigeons et jeunes docteurs : Axel, Luisa, Edouard, Kévin, Gautier et Erwan pour leurs précieux conseils en début de thèse. Merci à Anne-Sophie pour ces repas « popote » qui nous ont permis de râler et de relativiser pendant cette 3ème année de thèse. Merci à mes camarades du quotidien stagiaires/doctorants/docteurs/apprentis : Timothée, Quentin, Thomas, Vincent, Ulysse, Christina, Théo, Daniel, Marion, Ayoub, Sylvain, Clément, Ayse, Kenza, Florent et Julie. Un grand merci à Edouard, Timothée et enfin Quentin avec qui j'ai partagé mon bureau pendant cette thèse. Merci à vous pour m'avoir supportée, entendue râler à maintes reprises, réconfortée, faite rigoler, etc. Cette période au LISL n'aurait pas été la même sans vous ! Un merci particulier à toi, Timothée, pour avoir toujours été là dans les bons et les mauvais moments, à Thomas pour son incroyable savoir sur la ligne Maginot et Vincent pour sa connaissance inépuisable en modélisation. Je remercie tous ceux que j'ai pu oublier dans les paragraphes précédents et qui ont participé à ces travaux.

Enfin, je souhaite exprimer ma reconnaissance à toute ma famille qui m'a toujours encouragée et soutenue dans mes choix. Un merci particulier à mes parents qui ont toujours fait leur maximum pour me permettre de faire les études que je voulais et sans qui rien n'aurait été possible. Pour finir, je tiens à remercier l'amour de ma vie et mon futur mari, Michaël, qui a été présent pendant toute cette période et a su être d'un soutien indéfectible. Merci pour tout ce que tu m'apportes au quotidien, sache que sans toi je n'en serais pas là aujourd'hui.

Table of contents

Introduction 5

References 10

Literature review 13

1. Substrate/coating system interfaces 14

1.1 Interfaces formed by PVD 14
1.1.1 Sputtering processes 14
1.1.2 Types of interfaces 16
1.1.3 Parameters influencing the substrate/coating interface 17
1.1.4 Thin film nucleation and growth through sputtering technique 18
1.2 PVD for the optimization of substrate/coating system interfaces 22
1.2.1 Pre-treatment prior to deposition 22
1.2.2 Deposition of a bond coat 24
1.3 Conclusions 25

2. Relationship between interfaces and corrosion resistance 26

2.1 Nitric acid environment 26
2.1.1 Corrosion processes 27
2.1.2 Choice of massive materials for corrosion resistance 29
2.1.3 Methods for corrosion protection 31
2.2 Marine environment 33
2.2.1 Corrosion processes 33
2.2.2 Methods for corrosion protection 34
2.3 Complex substrate/coating system 36
2.4 Conclusion 38

3. Titanium dioxide (TiO_2) and zirconia (ZrO_2) protective coatings 40

3.1 Introduction 40
3.2 Global properties 40
3.2.1 Crystal structure 40
3.2.2 Stability 41
3.2.3 Thermodynamic properties 42
3.3 Deposition by reactive HiPIMS 44
3.3.1 Principle of reactive sputtering 44
3.3.2 Parameters influencing the deposition of oxide coatings by R-HiPIMS 46
3.4 Corrosion resistance properties 47
3.4.1 TiO_2 coatings 47
3.4.2 ZrO_2 coatings 49
3.5 Conclusions 51

4. Conclusions 52

References 54

Materials and Methods 67

1. Materials and Deposition chambers 68

1.1 304L austenitic stainless steel substrate (ASS) 68
1.2 Substrate surface preparation 70
1.3 PVD coating equipments 70
1.3.1 TriPros 70
1.3.2 DEPHIS deposition machine 72

2. Materials characterization methods 73

2.1 Structural and physico-chemical characterizations 73

2.1.1 Scanning Electron Microscopy (SEM) with Energy Dispersive X-ray analysis (EDX) 73
2.1.2 Focused Ion Beam (FIB) and Transmission Electron Microscopy (TEM) with Energy Dispersive X-ray analysis (EDX) ... 73
2.1.3 X-Ray Diffraction (XRD) ... 74
2.1.4 X-Ray Photoelectron Spectrometry (XPS) ... 75
2.1.5 Raman Spectroscopy ... 76
2.1.6 Atom Probe Tomography (APT) ... 76
2.2 Corrosion resistance ... 77
2.2.1 Electrochemical measurements in saline and nitric acid environments ... 77
2.2.2 Immersion tests ... 81
2.3 Roughness and mechanical properties characterization ... 86
2.3.1 Interferometric Microscopy ... 86
2.3.2 Scratch-test ... 87
3. Calculation of ion implantation (SRIM) ... 88
4. Conclusions ... 88
References ... 90
Surface modification and interface engineering by HiPIMS pre-treatment ... 92
1. Etching pre-treatment and metal coating deposition ... 94
1.1 Process parameters ... 94
1.1.1 Etching step ... 94
1.1.2 Metal coating deposition ... 95
2. Surface modification and interface engineering ... 96
2.1 Modeling of implantation profiles ... 96
2.2 Structural and chemical analyses of etched samples ... 97
2.3 Interface characterization ... 104
2.3.1 Chemical analyzes ... 104
2.3.2 Adhesion properties of the substrate/metallic bond coat system ... 111
2.3.3 Modeling of the substrate/bond coat interface ... 115
2.4 Conclusion ... 116
3. Corrosion resistance investigations of the etched samples ... 118
3.1 Electrochemical measurements ... 118
3.1.1 In nitric acid ... 118
3.1.2 In sodium chloride (NaCl) solution ... 126
3.2 Immersion tests ... 128
3.2.1 In nitric acid ... 128
3.2.2 In NaCl solution ... 131
3.2.3 In Cherbourg natural seawater ... 133
3.3 Conclusions ... 136
4. Corrosion resistance investigations of the etched and bond coat deposited samples ... 137
4.1 Electrochemical measurements ... 137
4.1.1 In nitric acid ... 138
4.1.2 In sodium chloride (NaCl) environment ... 148
4.2 Immersion tests ... 152
4.2.1 In NaCl solution ... 152
4.2.2 In Cherbourg natural seawater ... 155
4.3 Conclusions ... 158
Conclusions ... 160
References ... 164

Preliminary assessment of anticorrosion performance of an architectured substrate/coating system 171
Introduction 172
1. Deposition of oxide and multilayer thin films 174
1.1 Process parameters 174
1.2 Structural and chemical properties 176
1.2.1 Ti-based thin films 176
1.2.2 Zr-based coatings 179
1.3 Mechanical properties 183
2. Performance of the architectural substrate/coating system in aggressive environments 186
2.1 Corrosion in nitric acid solution 187
2.1.1 Electrochemical measurements 187
2.1.2 Immersion tests 197
2.2 Corrosion in sodium chloride (NaCl) environment 200
2.2.1 Electrochemical measurements 200
2.2.2 Immersion tests 205
2.3 Conclusion 212
Conclusions 214
References 216
Conclusion and outlook 221
Appendix 1: Optimization of in situ substrate surface pre-treatment 227
1. Preliminary study of the influence of etching parameters on substrate/coating interface 227
1.1 Parameters 227
1.1.1 XPS analysis 228
1.1.2 Interface characterizations 232
1.1.3 Electrochemical measurements 234
2. Optimization of etching parameters to reduce contaminations 235
2.1 Aluminum plate technique 235
2.2 New technique 240
Appendix 2: Corrosion resistance of the metal bond coat with interface contamination 244
1. Electrochemical measurements 244
1.1 In saline environment 244
1.2 In nuclear fuel reprocessing environment 245
2. Immersion tests 247
2.1 Singapore seawater 247
2.2 In a 3.56 wt.% NaCl solution 247
2.3 Nitric acid solution 249
Appendix 3: Bode diagrams of Ti- and Zr-based oxide coatings showing the presence of porosity 254

Summary

Résumé :

Dans le cadre des recherches menées sur l'amélioration de la durabilité des composants en milieux corrosifs, le développement de traitements de surface respectueux de l'environnement, industriellement et économiquement viables est effectué. Dans ce but, des systèmes substrat/revêtement développés par procédé HiPIMS sont étudiés. L'objectif est de comprendre et de caractériser en détail le rôle des différentes interfaces rencontrées dans ces systèmes afin d'optimiser leur résistance à la corrosion dans l'acide nitrique et l'eau de mer. Dans un premier temps, le pré-traitement du substrat par décapage ionique HiPIMS et son influence sur un système substrat/sous-couche métallique sont étudiés. Différents décapages ioniques (Ar^+, Ti^+ et Zr^+) sont effectués et mènent à une modification de la surface du substrat par implantation des éléments pulvérisés sur les premiers nanomètres. Cela entraîne la modification de la composition chimique de la couche passive et améliore la résistance à la corrosion des substrats décapés aux ions métalliques dans les deux milieux d'étude. Suite à l'ajout d'une sous-couche métallique d'environ 200 nm (Ti/Zr), cet effet bénéfique du décapage aux ions métalliques est toujours observé, ce qui suggère que ces espèces métalliques peuvent agir comme sites de nucléation préférentiels pour la croissance de la couche métallique et promouvoir un film probablement plus dense. Dans un second temps, un système substrat/couche de liaison métallique/revêtement oxyde (TiO_2/ZrO_2) non-optimisé d'environ 5 µm est étudié. Les résultats indiquent que les systèmes à base de Zr sont prometteurs pour la protection contre la corrosion dans nos deux milieux d'étude.

Mots clés : Acier inoxydable, revêtement PVD, HiPIMS, décapage, interface, corrosion

Abstract:

Sustainability issues are essential for component performance in many corrosive environments. For this purpose, the development of environmentally friendly, industrially and economically viable surface treatments is performed. In this work, substrate/coating systems developed by HiPIMS process are studied. The objective is to understand and characterize in detail the role of the different interfaces encountered in these systems in order to optimize their resistance to corrosion in nitric acid and seawater. Firstly, the pre-treatment of the substrate by HiPIMS ion etching and its influence on a substrate/metallic bond coat system are studied. Three types of ion etching (Ar^+, Ti^+ and Zr^+) are performed and lead to a modification of the substrate surface by implantation of the sputtered elements on the first nanometers. This leads to the modification of the chemical composition of the passive layer and improves the corrosion resistance of the metal ion-etched substrates in both studied environments. Then, a 200 nm-thick metallic bond coat (Ti/Zr) is deposited on the etched substrates to study the substrate/metallic bond coat interface. The beneficial effect of metal ion etching is still observed after deposition of the bond coat, suggesting that the metal species can act as a preferential nucleation site for metallic layer growth and probably promote a denser film. Secondly, a 5 µm-thick non-optimized substrate/metallic bond coat/oxide coating (TiO_2/ZrO_2) system is studied. The results indicate that Zr-based systems are promising for corrosion protection in our two study media.

Keywords: stainless steel, coating, HiPIMS, interface, corrosion resistance

Introduction

Sustainability issues are essential for components performance in many corrosive environments. For this purpose, the development of environmentally friendly, industrially and economically viable surface treatments is performed. The objective is to minimize the use of critical or strategical resources, and develop durable components with improved lifespans.

In this PhD work, performed in the frame of a cotutelle agreement between Sorbonne University/CEA, France and Nanyang Technological University (NTU), Singapore, the objective is to work on coating systems developed by physical vapor deposition (PVD), to understand and characterize in detail the role of the various interfaces encountered in this coating systems in order to optimize their performances regarding corrosion resistance. For this purpose, two aggressive environments were selected: nitric acid and seawater.

First, the focus is on the nitric acid environment studied *i.e.* spent nuclear fuel reprocessing. The nuclear fuel cycle (Figure 1) includes successive industrial operations: uranium mining, concentration and conversion, enrichment, fuel fabrication, use in the reactor, reprocessing, waste treatment and disposal [1-3]. Most countries do direct storage of the nuclear waste as in the United States, while others countries such as France prefer reprocessing.

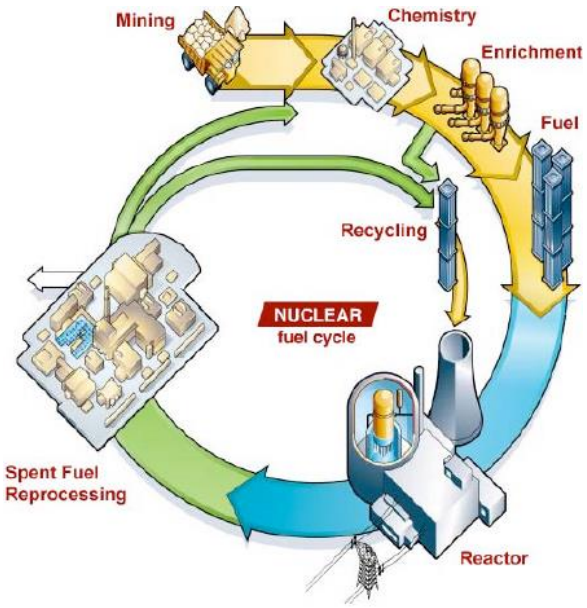

Figure 1: Nuclear fuel cycle processes in France, from [3].

To this end, spent nuclear fuel is reprocessed to recover the reusable materials (uranium and plutonium) and to condition the ultimate waste (fission products and minor actinides). In fact, reprocessing started in the 1940s in the United States for military purposes and was commercialized from the 1960s using the PUREX (Plutonium and Uranium Redox Extraction) process. France has chosen to build its own nuclear fuel reprocessing plants (at Marcoule and near La Hague) as the UK and Russia. In France, the reprocessing of spent fuel relies on the PUREX process performed in the processing plant located near La Hague. When the spent nuclear

fuel is received at the reprocessing plant, it is first stored in a spent fuel pool for further cooling. Actual reprocessing starts by cutting the fuel rods into small pieces. These fuel fragments are dissolved in hot concentrated (up to 14.4 mol/L) nitric acid. Then, this solution of dissolved fuel undergoes liquid-liquid extraction steps to separate uranium and plutonium. Fission products and minor actinides remain in the nitric acid solution and are concentrated, calcined and vitrified in a glass matrix inside a metallic canister and stored as nuclear waste, while recovered uranium and plutonium are stored or recycled to be reused in mixed oxide fuel (MOX) [1, 2, 4].

Throughout the reprocessing, nitric acid solutions at different temperatures (up to 110-120°C) and concentrations (up to 14.4 mol/L) are used. In addition, some dissolved species (oxidizing ions such as Pu(IV) or Np(VI), fission products such as iodine and cations such as Fe(III) or Cr(III)) are present in these nitric media [4]. Therefore, the equipment of reprocessing plants must be built with corrosion resistant materials. For the lowest acidic condition, 304L austenitic stainless steel (ASS) is the materials of choice, whereas Si-doped ASS and zirconium (Zr) are used at high concentrations. Generally, 304L ASS is used for the major part of the equipment whereas Zr alloys are preferred for the most critical corrosion equipment such as fuel dissolver and nitric acid recovery concentrators [2, 4, 5]. For all of these materials, a stable passive layer of oxides forms in nitric acid medium and protects these materials against corrosion. However, deterioration of this layer may lead to extensive corrosion and therefore to premature failure of the reprocessing equipment [4]. Consequently, improvement in corrosion resistance properties is necessary to extend the lifespan of non-critical tools and infrastructure in a nitric acid environment.

Component sustainability issues are also observed in another corrosion-driving environment: seawater [6]. Oceans and seas cover more than 70% of the earth's surface, and seawater contains inorganic, organic and biological components such as salt, silt, dissolved gases and microorganisms that can corrode most of metals [6]. However, many metal-using industries and metal-made infrastructures such as ships, coastal industrial plants (ports and shipyards), offshore facilities for oil and gas production, and power plants [7] are located in marine environment. 304L ASS is commonly used in this environment thanks to the formation of a corrosion-protecting passive layer. However, in some conditions such as stagnant seawater, local attack (pitting corrosion) can occur and cause failure of this protective layer. In addition, other phenomena such as erosion due to solid particles present as observed in turbid coastal waters can compound this degradation issue. To withstand this degradation, corrosion protection can rely on surface treatments.

For these two cases of applications, spent nuclear fuel reprocessing and marine industry, the substrate selected is a material largely used in both environments: 304L ASS. For the coatings, ceramic coatings are considered. More specifically, ZrO_2 [8, 9] and TiO_2 [10-12] coatings are being investigated due to their unique chemical, thermal and mechanical properties [13]. Indeed, ZrO_2 thin films are used as corrosion protective barriers for metals, as a result of a thermal expansion coefficient close to that of metals [14, 15] and chemical inertness [14-17]. TiO_2 coatings are also applied owing to high durability [18] and insulating properties [11].

In the past few years, ceramic coatings have been elaborated by PVD techniques, most notably by reactive magnetron sputtering [10, 11, 19]. They have shown

improved corrosion resistance properties compared to uncoated material in nitric acid for example [10, 11]. The structural properties of ceramic protective coatings may be further optimized by using high power impulse magnetron sputtering (HiPIMS) [20]. Compared to other PVD techniques, HiPIMS allows obtaining layers with denser microstructure and reduced surface roughness without the need of secondary plasma source. This is because the HiPIMS plasma provides a high energy flux of ionic metallic species, which can enhance surface mobility of the species on the growing films. As a result, the control of composition, microstructure and mechanical properties of the coating is improved [21, 22]. Moreover, the substrate surface pre-treatment and the coating architecture (*i.e.* presence of a bond coat and/or multilayer architecture) also play a key role in the overall performances of the coating system.

It has been recognized that corrosion of coated samples is mainly initiated from coating defects (pores, pinholes or scratches) and species trapped at the substrate/coating system interfaces [8, 23, 24]. Thus, defect-free interfaces should improve coating resistance against corrosion. To this end, HiPIMS can be used to remove contaminants and impurities from the surface prior to coating deposition (named hereafter etching step) to improve coating adhesion. Furthermore, a bond coat is often required to improve adhesion between a ceramic coating and a substrate of distinct thermal expansion coefficients and crystal lattices [25-29]. Another solution is the development of multilayer coatings, which can decrease the electrolyte infiltration into the substrate/coating space [30-33]. Hence, optimization of all substrate/coating interfaces is a processing route to improve the performances of the coated component under service conditions. The coating process must be optimized step by step to offer the best anticorrosive and mechanical properties.

The aim of this study is to understand in detail the role played by the interfaces of a substrate/coating system on the properties of the final substrate/coating system. The main objective is to master interfaces properties during deposition process to optimize the corrosion resistance of the substrate/coating system under service conditions. HiPIMS has been chosen as substrate etching pre-treatment and deposition technique for this study. The 304L ASS substrate is used and pre-treated (*i.e.* etched) prior to deposition of a metallic bond coat (around 200 nm-thick). Then, an oxide coating is added to the substrate/metallic bond coat system to obtain the final component (required thickness: 5 µm) (Figure 2a). The influence of the coating system architecture is studied by synthesizing metal/oxide multilayer coatings (Figure 2b).

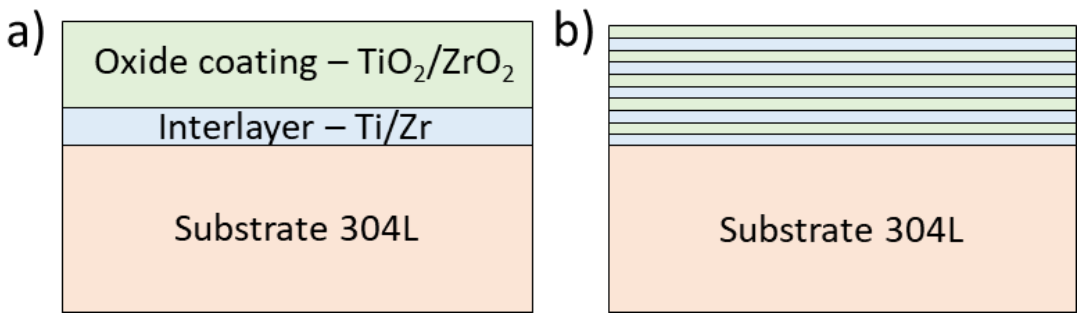

Figure 2: a) Starting substrate/coating system and b) architectural substrate/coating system studied.

The investigation will thus be presented in four chapters.

The first chapter is dedicated to a state of art on the interfaces of a substrate/coating system obtained by PVD. A review of the interfaces formed by PVD and the methods of interface optimization is presented, then the relationship between the interfaces and corrosion resistance properties by explaining the corrosion processes known and the solutions proposed for corrosion protection in the two studied environments are described. Finally, the oxide coatings to be deposited are presented to introduce the deposition process in reactive atmosphere and to discuss the architecture of the system to reach better corrosion resistance

The second chapter details the experimental strategy and the analytical techniques implemented for the elaboration and the characterization of the coatings. First, the materials studied *i.e.* 304L ASS and the deposition chambers used are presented. The structural, physicochemical and mechanical characterization tools (interferometric microscopy and scratch-test) are presented. The different types of corrosion resistance tests (electrochemical measurements and immersion tests) are discussed. Finally, the methodology used to calculate ion implantation is mentioned.

The third chapter is dedicated to the study of the influence of the etching step on the substrate/metallic bond coat system. For this purpose, different types of etchings are performed and their effects on the surface are analyzed using experimental techniques. In addition, the ion implantation on the surface is calculated using SRIM software to know the order of magnitude of the implantation depth. This allows comparing the theoretical calculations with the experimental results. Finally, substrate/metallic bond coat adhesion and its corrosion resistance using electrochemical measurements and immersion tests are evaluated in nitric acid and 3.56 wt.% NaCl solutions.

The fourth chapter deals with the anticorrosion performance of a non-optimized architectured system *i.e.* substrate/metallic bond coat/oxide coating. For this purpose, four architectured systems are studied. The deposition process are presented and the properties (structural, chemical and adhesion) of the architectured substrate/coating systems are studied using experimental techniques. Finally, electrochemical measurements and immersion tests are performed in nitric acid and natural seawaters, both in Singapore and Cherbourg, to assess the improvement in corrosion resistance compared to initial 304L ASS and Ta.

This cotutelle agreement between Sorbonne University/CEA should have implied spending one year out of the three years of the PhD in the partner institution (NTU). Unfortunately, only six months could be spent in 2019 in Singapore because of the health crisis. In Singapore, focused ion beam (FIB) microscope sample preparation for transmission electron microscopy (TEM) analyzes as well as immersion tests in natural environment were performed during these six months at NTU. Then, monthly meetings were planned in order to ensure the supervision of the PhD work, moreover common research work actively continued through exchanges of samples to perform additional analyses on the coating systems, essentially TEM and complementary immersion tests.

REFERENCES

[1] Rodriguez-Penalonga L. & Yolanda Moratilla Soria B. (2017) “A Review of the Nuclear Fuel Cycle Strategies and the Spent Nuclear Fuel Management Technologies.” Energies 10, 1235.

[2] Tcharkhtchi-Gillard E. (2014) “Passivité et rupture de passivité de l’acier 304L en milieu acide nitrique concentré et chaud.” Chimie analytique, Université Pierre et Marie Curie – Paris VI. tel-01020901

[3] Schneider M. & Marignac Y. (2008) “Spent Nuclear Fuel Reprocessing in France.” Research Report No. 4, International Panel on Fissile Materials.

[4] Fauvet P. (2012) “Chapter 19: Corrosion issues in nuclear fuel reprocessing plants.” Nuclear corrosion science and engineering (pp. 679-728), Woodhead Publishing, ISBN: 978- 1845697655

[5] Feron D. (2012) “Chapter 2: Overview of nuclear materials and nuclear corrosion science and engineering.” Nuclear corrosion science and engineering (pp. 31-56), Woodhead Publishing, ISBN: 978- 1845697655

[6] Boyd W.K. & Fink F.W. (1978) “Corrosion of Metals in Marine Environments.” Metals and Ceramics Information Center, Technical Report MCIC-78-37.

[7] Valdez B., Ramirez J., Eliezer A., Schorr M., Ramos R. & Salinas R. (2016) “Corrosion assessment of infrastructure assets in coastal seas.” Journal of Marine Engineering & Technology 15: 124-134.

[8] Kazazi M., Haghighi M., Yarali D. & Zaynolabedini M.H. (2018) “Improving Corrosion Resistance of 316L Austenitic Stainless Steel Using ZrO_2 Sol-Gel Coating in Nitric Acid Solution.” Journal of Materials Engineering and Performance 27: 1093-1102.

[9] Ningshen S., Kamachi Mudali U., Krishnan R. & Raj B. (2011) “Corrosion behavior of Zr-based metallic glass coating on type 304L stainless steel by pulsed laser deposition method.” Surface and Coatings Technology 205: 3961-3966.

[10] Padhy N., Kamal S., Chandra R., Mudali K. & Raj B. (2010) “Corrosion performance of TiO_2 coated type 304L stainless steel in nitric acid medium.” Surface and Coatings Technology 204: 2782-2788.

[11] Padhy N., Mudali K., Chawla V., Chandra R. & Raj B. (2011) “Corrosion behaviour of single (Ti) and duplex (Ti–TiO_2) coating on 304L stainless steel in nitric acid medium.” Materials Chemistry and Physics 130: 962-972.

[12] Li C., Chen W., Jiang Q., Wang L.& Luo D. (2014) “Corrosion resistance of Ti-based metallic glass coating in concentrated nitric acid.” Materials Chemistry and Physics 143: 900–903.

[13] Bensaha R. & Bensouyad H. (2012) “Synthesis, Characterization and Properties of Zirconium Oxide (ZrO_2)-Doped Titanium Oxide (TiO_2) Thin Films Obtained via Sol-

Gel Process." F. Czerwinski (Ed.) Heat Treatment - Conventional and Novel Applications, IntechOpen.

[14] Nouri E., Shahmiri M., Rezaie H. & Talayian F. (2011) "Investigation of structural evolution and electrochemical behaviour of zirconia thin films on the 316L stainless steel substrate formed via sol–gel process." Surface and Coatings Technology 205: 5109-5115.

[15] Holgado J.P., Pérez-Sánchez M., Yubero F., Espinós J.P. & González-Elipe A.R. (2002) "Corrosion resistant ZrO_2 thin films prepared at room temperature by ion beam induced chemical vapour deposition." Surface and Coatings Technology 151-152: 449-453.

[16] Cubillos G., Olaya J., Bethencourt M., Cifredo G.& Blanco G. (2013) "Resistance to Corrosion of Zirconia Coatings Deposited by Spray Pyrolysis in Nitrided Steel." Journal of Thermal Spray Technology 22: 1242-1252.

[17] Kaliaraj G.S., Vishwakarma V., Kirubaharan K., Dharini T., Ramachandran D. & Muthaiah B. (2018) "Corrosion and biocompatibility behaviour of zirconia coating by EBPVD for biomedical applications." Surface and Coatings Technology 334: 336-343.

[18] Shajudheen V.P.M., Rani K.A., Kumar V.S., Maheswari A.U., Sivakumar M. & Kumar S.S. (2018) "Comparison of Anticorrosion Studies of Titanium Dioxide andNickel Oxide Thin Films Fabricated by Spray Coating Technique." Materials Today: Proceedings 5: 8889-8898.

[19] Portinha A., Teixeira V., Carneiro J.O., Costa M., Barradas N. & Sequeira D. (2004) "Stabilization of ZrO_2 PVD coatings with Gd_2O_3." Surface and Coatings Technology 188–189: 107–115.

[20] Kouznetsov V., Macák K., Schneider J.M., Helmersson U. & Petrov I. (1999) "A novel pulsed magnetron sputter technique utilizing very high target power densities." Surface and Coatings Technology 122: 290-293.

[21] Sarakinos K., Alami J.& Konstantinidis S. (2010) "High power pulsed magnetron sputtering: A review on scientific and engineering state of the art." Surface and Coatings Technology 204: 1661-1684.

[22] Ougier M., Michau A., Schuster F., Maskrot H. & Schlegel M.L. (2020) "Effects of HiPIMS discharges and annealing on Cr-Al-C thin films." Surface and Coatings Technology 399: 126141.

[23] Reinhard C., Ehiasarian A.P. & Hovsepian P.E. (2007) "CrN/NbN superlattice structured coatings with enhanced corrosion resistance achieved by high power impulse magnetron sputtering interface pre-treatment." Thin Solid Films 515: 3685-3692.

[24] Wang Q.-Y., Xi Y.-C., Liu X.-Y., Liu S., Bai S.-I. & Liu Z.-D. (2017) "Microstructure and mechanical properties of interface between laser cladded Hastelloy coating and steel substrate." Transactions of Nonferrous Metals Society of China 27: 733-740.

[25] Santiago J.A., Fernandez-Martinez I., Wennberg A., Molina-Aldareguia J., Castillo-Rodríguez M., Rojas T., Sanchez Lopez J., Gonzalez M., Garcia-Martin J.-M., Li H., Bellido V., Monclus M.& González-Arrabal R. (2018) “Adhesion enhancement of DLC hard coatings by HiPIMS metal ion etching pretreatment.” Surface and Coatings Technology 349: 787-796.

[26] Bakoglidis K., Schmidt S., Greczynski G.& Hultman L. (2016) “Improved adhesion of carbon nitride coatings on steel substrates using metal HiPIMS pretreatments.” Surface and Coatings Technology 302: 454-462.

[27] Bull S.J. (1992) “Techniques for improving thin film adhesion.” Vacuum 43: 517-520.

[28] Vassallo E., Caniello R., Cremona A., Dellasega D.& Miorin E. (2013) “Titanium interlayer to improve the adhesion of multilayer amorphous boron carbide coating on silicon substrate.” Applied Surface Science 266: 170-175.

[29] Pischow K.A., Eriksson L., Harju E., Korhonen A.S.& Ristolainen E.O. (1993) “The influence of titanium interlayers on the adhesion of PVD TiN coatings on oxidized stainless steel substrates.” Surface and Coatings Technology 58: 163-172.

[30] Shanaghi A., Ghasemi S., Chu P. K., Ahangarani S. & Zhao Y. (2019) “Effect of Ti interlayer on corrosion behavior of nanostructured Ti/TiN multilayer coating deposited on TiAl6V4.” Materials and Corrosion 70: 2113-2127.

[31] Perez-Martino J., Lau K.H., Alvarez E., Malhotra R., Hornbostel M., Krishnan G. & Sanjurjo A. (2008) “Multilayer coatings for corrosion protection of coal gasifier components.” Materials Chemistry and Physics 112: 180-185.

[32] Lei Z., Zhang Q., Zhu X., Ma D., Ma F., Song Z. & Fu Y. Q. (2018) “Corrosion performance of ZrN/ZrO_2 multilayer coatings deposited on 304 stainless steel using multi-arc ion plating.” Applied Surface Science 431: 170-176.

[33] Wiklund U., Hedenqvist P., Hogmark S., Stridh B. & Arbell M. (1996) “Multilayer coatings as corrosion protection of Zircaloy.” Surface and Coatings Technology 86-87: 530-534.

Literature review

The aim of this chapter is to review the state of knowledge on the interfaces of a substrate/coating system obtained by physical vapor deposition (PVD). Their understanding is essential to optimize the performance of our system in terms of corrosion resistance in nitric acid and marine environments. A review of the interfaces formed by PVD and the methods of interface optimization will be presented. Then, a second section will describe the relationship between the interfaces and corrosion resistance properties by explaining the corrosion processes known and the solutions proposed for corrosion protection in our study environments. Finally, a section dealing with the oxide coatings to be deposited will be presented to introduce the deposition process in reactive atmosphere and to discuss the architecture of the system to reach better corrosion resistance.

1. SUBSTRATE/COATING SYSTEM INTERFACES

1.1 INTERFACES FORMED BY PVD

The substrate/coating system interfaces can be defined between the substrate and coatings and between several coating layers. In this work, all these interfaces are formed by a PVD process, which is described below. Moreover, the different types of interfaces are presented as well as the main growth modes of the coatings, which depend on the interfaces formation.

1.1.1 Sputtering processes

The sputtering process consists of bombarding a target (cathode) of the material to be deposited with energetic ions from a plasma. This plasma is created by introducing an inert gas such as argon in a vacuum chamber and applying a high negative voltage between the target and the substrate. The target atoms are then sputtered and ejected, forming an atomic vapor. These species condense on the surface of the substrate and form a coating [1-6]. In fact, the condensation of atomic species on the substrate surface results in a reciprocal interaction, mostly chemical reaction or pseudodiffusion phenomenon, and formation of bonds between the substrate and the coating [7]. In addition, secondary electrons are emitted from the target during sputtering and play a role in maintaining the plasma discharge [2, 6]. Nonetheless, the use of this technique without plasma confinement results in low deposition rates, low ionization efficiency of the plasma and high substrate heating effects [5]. That is why magnetron sputtering (MS) technique (Figure 3), based on the use of an external magnetic field applied to the target (permanent magnets), is developed [2, 5]. This allows electrons to be trapped close to the target, which in turn attracts ions from the plasmagenic gas in the vicinity of the target because of the requirement of local electroneutrality [1, 5, 6]. This results in a higher probability of collision with the gas atoms present in the plasma and a denser plasma due to the presence of ionizing energetic species in the target region [5, 6]. The ionization efficiency and ion bombardment of the target are thereby improved, locally at the racetrack. Moreover, higher sputtering rates and higher deposition rates at the substrate are observed [1, 2, 5, 6]. MS is one of the most commonly used PVD technique in industry [1, 3, 8, 9] due to these advantages allowing high purity coatings [1], high reproducibility [8] and good control of coating properties [8]. In this technique, the plasma can be generated by direct-current (DCMS) or high power impulse (HiPIMS).

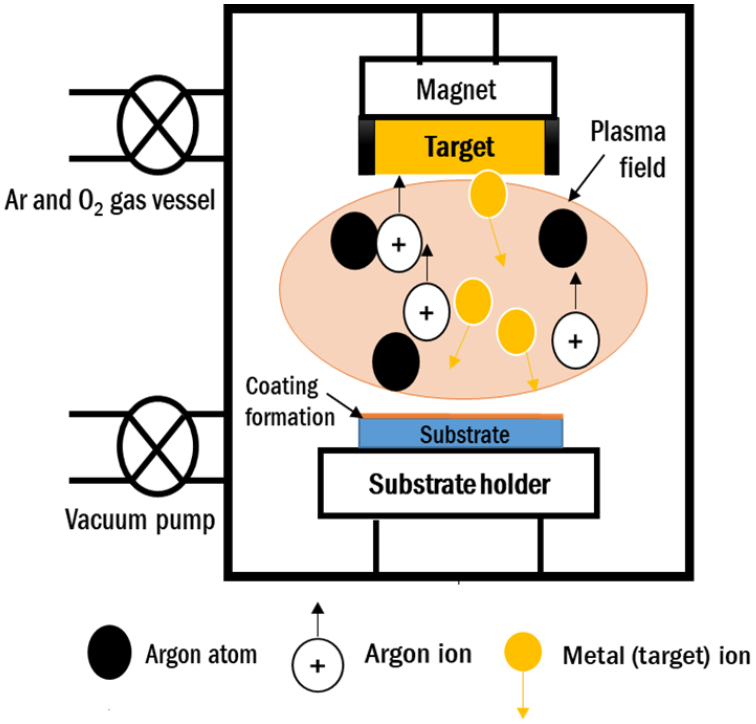

Figure 3: Schematic drawing of magnetron sputtering process.

The DCMS technique is the simplest and cheapest method of MS [1, 3], and consists of applying a continuous negative potential (hundreds to thousands of volts) directly to the target [1, 4, 6]. As this technique requires the target to conduct electricity, it is necessary to use metallic or conductive compound targets [4, 5]. Then, a coating of approximatively the same composition as the target is obtained. It should be noted that compositional variations can be observed in the case of compound targets due to differences in ionization potentials, sputtering direction or mean free path in the plasma. High deposition rates (µm/h) are observed on the substrate, which makes the use of the DCMS relevant for the deposition of metallic thin films or microelectronics components [1, 4]. However, sometimes DCMS technique does not provide sufficient energy input to obtain a dense structure of thick coatings (> 1µm), hence the interest in creating ions to bombard the film during its growth, as in HiPIMS technique. The interfaces formed by DCMS differ from those obtained by HiPIMS because the energy of the vapor particles condensing on the substrate surface influences their formation [7]. In fact, higher particles energy is preferred to form defect-free interface. Nonetheless, no study detailing the interfaces formation by DCMS was found in the literature, limiting the understanding of the phenomena taking place.

The HiPIMS power supply is characterized by high peak power pulses applied to the cathode [10, 11]. A high-density plasma with a high ionization fraction of the sputtered species is then obtained in the cathode vicinity [10-14]. As the vapor particles are highly energized, this results in a strong reciprocal interaction between the substrate and the coating and formation of strong bonds [7]. For example, metal ions have a high bonding affinity and can be incorporated at lattice sites of the substrate as

replacements and thus promote the formation of strong bonds (metallic or ionic) between the substrate and the subsequently deposited coating. This may lead to higher adhesion of HiPIMS deposited coatings to the substrate than those obtained by DCMS. HiPIMS is mainly used to deposit dense and smooth coatings [11, 14] and to modify thin films properties such as resistivity and refractive index [11]. In addition, this technique can be used for the deposition process but also for *in situ* surface preparation because of the presence of ionized metal in the plasma [14]. Actually, using HiPIMS for ion etching can improve the coating/substrate adhesion [11] and the high degree of ionization of the sputtered metal also improves some coating properties such as density [10, 14]. Moreover, by applying a bias voltage on the substrate, the energy and direction of the ion sputtered material can be controlled that allows a better coverage of complex surfaces by coatings [10]. However, HiPIMS is hampered by low deposition rates and the possible occurrence of arc discharges [10-13]. Arcs sometimes occur on the target surface and can produce microdroplets [10]. This problem can be mitigated by using a power supply with an efficient arc management, reducing the pulse length [12, 13] and the power level [10]. Otherwise, deposition rate of HiPIMS is generally 20-80% lower than for DCMS for pure metallic systems [10, 11] because ionized metals species are attracted back to the cathode [10]. The low deposition rate also results from gas rarefaction near the target cathode during the discharge, which further limits sputtering by Ar^+ ions [11]. Hybridization of the sputtering processes can overcome this obstacle. Hybridization corresponds to the sequential or simultaneous use of two distinct coating techniques for a synergistic improvement of the coatings. For example, the hybrid HiPIMS-DCMS method combines the advantages of both methods to deposit better quality coatings i.e. denser, harder and with lower compressive residual stress due to the formation of re-nucleation islands as a result of the increased adatom mobility thanks to metal ion bombardment [15-18]. This bombardment can reduce the number of point defects in the highly distorted lattice, and filling-up atomic-scale voids. The HiPIMS technique generally produces coatings with better properties (denser, harder and lower residual stresses) and higher adhesion compared to DCMS. As a result, the DCMS known for high deposition rates is chosen to improve the deposition rate of HiPIMS [15, 16, 18]. Nonetheless, recent studies show that HiPIMS deposition rate could become equal or higher than those of conventional sputtering by modifying the target peak current [11].

1.1.2 Types of interfaces

Several types of interfaces have been identified but two types are more frequently observed during PVD deposition: mechanical and pseudodiffusion interfaces.

1.1.2.1 Mechanical interface (abrupt with interlocking)

The mechanical interface (Figure 4a) is characterized by penetration of the depositing atoms into the roughness of the substrate (pores, grain boundaries, *etc*.), providing mechanical interlocking and atom-to-atom bonding [7, 19-21]. This type of interface takes place if the mobility of the depositing atoms is high enough [7, 21]. Adhesion of the coating to the substrate occurs via mechanical anchoring [21]. Consequently, adhesion strength can be high because a fracture spreads with difficulty in the interface [20]. However, in some particular cases, adhesion can become poor. For example, interfacial voids may appear and decrease the adhesion if the pores are not

filled properly [20]. As a result, the adhesion of a mechanical interface is dependent on the physical characteristics of all materials involved [7] and on the surface characteristics (roughness, wettability, interpenetration, *etc.*). Mechanical interface can be observed in the HiPIMS technique as a large number of ions are generated in the vaporization process [19].

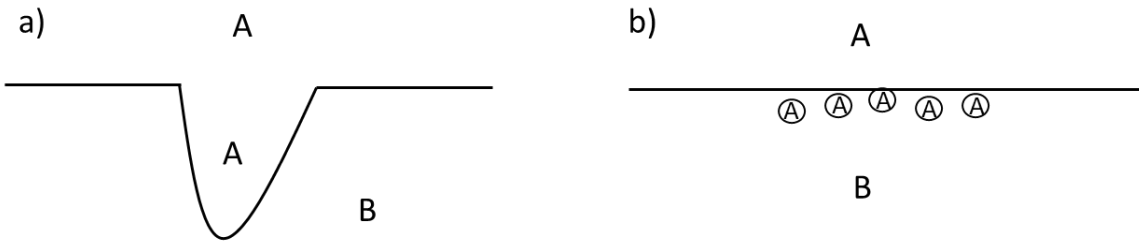

Figure 4: Schematic drawing of a) mechanical interface and b) pseudodiffusion interface between two materials A and B.

1.1.2.2 Pseudodiffusion interfacial region

The pseudodiffusion interface (Figure 4b) is characterized by a gradient of composition from one deposited material to the other without the need for diffusion between materials. This interface can be formed between two insoluble materials [20], which do not diffuse mutually [7]. Actually, this type of interface takes place when a gradual change of the interface chemical composition is introduced, for example during the deposition of a coating [7, 19-21]. The pseudodiffusion interfacial region is formed under high energy conditions [21] such as implantation of energetic ions [7, 19, 20], recoil implantation [19, 20] and sputtering [7, 19]. In addition, a pseudodiffusion type interface leads to good adhesion if oxidation of the substrate does not take place before the deposition of the coating [20].

In practice, a single type of interface is rarely observed, a combination of various interface types generally occur, making their study more complicated. It can be assumed that a mechanical type interface could be formed during etching step prior to coating deposition if there are surface defects and in parallel, the pseudodiffusion interface could be formed due to the ion bombardment leading to the implantation of these ions into the substrate.

1.1.3 Parameters influencing the substrate/coating interface

1.1.3.1 Properties of the substrate surface

The literature shows that the substrate surface must display homogeneous properties and have a high fracture toughness [22] to form a defect-free interface. Moreover, the adhesive strength of a coating on a substrate is related to the surface roughness [23]. The presence of defects or inhomogeneities on the surface is then problematic, as surface flaws can weaken the interface [22] and decrease the adhesion [23] by acting as stress concentration areas [24]. This can be observed at mechanical interfaces if the pores are not filled properly and lead to the formation of interfacial voids. The inhomogeneities of the substrate surface such as random distribution of dopants can

lead to inhomogeneous distribution of dislocations [25]. Preliminary surface treatments such as polishing and etching can modify the mechanical and chemical structures of the substrate surface [7] to improve the nucleation and the interface formation [22, 24]. Indeed, thermal activation of the surface and formation of active nucleation centers can be achieved by performing preliminary preparation of the surface. An example is substrate etching prior to coating deposition to remove all kinds of contaminants such as the native oxide layer and can implant ions into the substrate, which acts as preferential nucleation sites [27]. When metal ions are used during etching step, they can be implanted as replacements in the substrate and lead sometimes to new phases formation [27].

1.1.3.2 Substrate temperature

Increasing the substrate temperature can favor interfacial chemical reactions and diffusion both parallel to the surface and into the substrate material [7]. Consequently, the adhesion of a coating on the substrate can be enhanced. In addition, substrate heating generates a better contact between the coating particles and the substrate and can eliminate moisture and some chemical contaminants [23]. Heating can relax the growth stresses of the coating, guaranteeing a good adhesion and limiting cracks or delamination. Substrate preheating and heating can be done during the deposition process, as frequently observed in PVD techniques [22, 23].

1.1.4 Thin film nucleation and growth through sputtering technique

1.1.4.1 Growth modes

The microstructure and morphology of thin films growth through sputtering techniques are determined by surface diffusion of condensing particles (so-called adatoms) and by the subsequent film formation phenomena, such as nucleation and crystal growth [28]. So far, there are three stable growth modes, which depend on the substrate surface interaction between the adatoms and the substrate material, as illustrated in Figure 5.

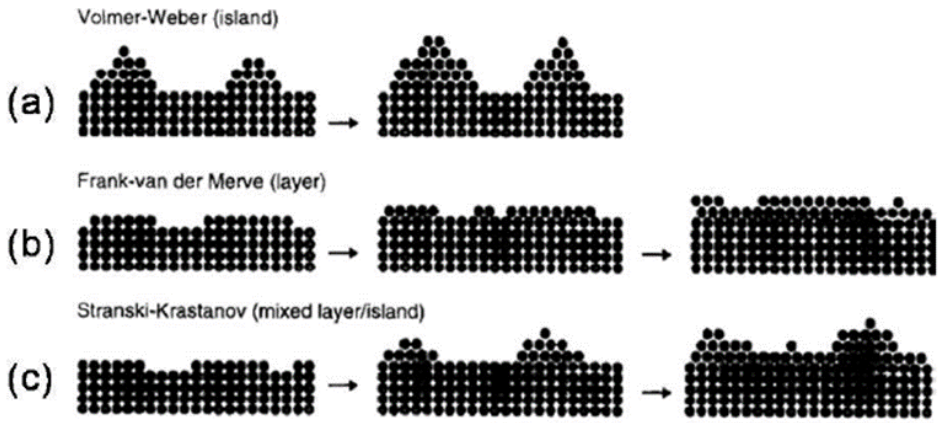

Figure 5: The three main growth modes of coatings a) Volmer-Weber mode, b) Frank-Van-der-Merwe mode and c) Stranski-Krastanov mode, from [28].

The three basic modes are:

- 3D island (Volmer-Weber) growth

  This type of growth can occur when the surface tension of film material is larger than the surface tension of the substrate or when a metal film is grown on dielectric substrate such as deposition on Al_2O_3 or SiO_2. In this mode, nucleation occurs in the form of clusters (or islands) on the substrate surface. Then, both the number and the size of clusters increase until they stew with each other to form a continuous film.

- 2D layer (Frank-van der Merwe) growth

  This type of growth is mostly observed where there is no lattice mismatch between film and substrate, such as epitaxial film. Nucleation occurs in the form of a monolayer of the deposited atoms, *i.e.* in a layer-by-layer manner.

- Stranski-Krastanov growth (mixed layer/island)

  This growth mode is the most commonly observed. After formation of a few monolayers, a crossover from 2D to 3D can take place due to the increase in surface roughness. This is mainly caused by the formation of defects such as edge, screw dislocation or impurity. For example, the first monolayers can be amorphous, mainly due to the lattice mismatch between sputtered atoms and substrate, and can start to form crystallized islands after few nanometers.

1.1.4.2 Influence of the deposition parameters on the structure and microstructure

Films grown by PVD techniques exhibit a variety of microstructures that are correlated to the individual deposition parameters and categorized in the so-called structure zone model (SZM). SZM describes the structure and morphology of sputter film, knowing only the parameters of the deposition.

In 1969, Movchan and Demchishin have developed the first version of SZM [29]. In their model, the microstructure is controlled by surface and bulk diffusion processes, *i.e.* the deposition temperature (T_s). In particular, the effect of the temperature is quantified using the so-called homologous temperature T, which represents the T_s/T_m ratio, where T_m is the melting temperature of the deposited material. The obtained microstructural features can be classified in Zones I, T and II (Figure 6).

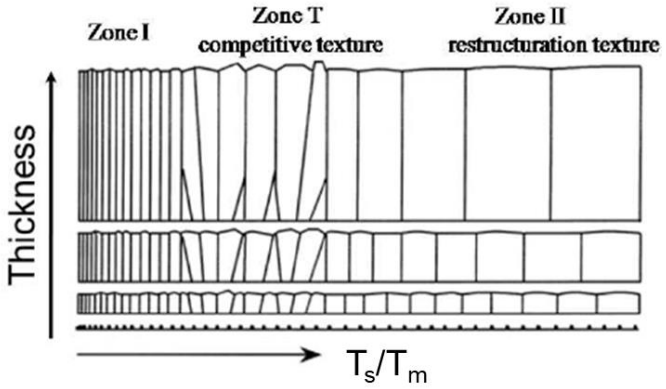

Figure 6: Structure zone model as a function of the coating thickness and T_s/T_m, from [30].

In Zone I (typically for $T_s/T_m < 0.3$), the film exhibits porous and rough morphologies. A random texture is observed due to the limited surface diffusion, low mobility of the adatoms and the atomic shadow effects, which are produced by the various incidence angles at which the atoms arrive at the substrate surface.

In zone T ($0.3 < T_s/T_m < 0.4$), film growth is controlled by surface diffusion due to the increasing of substrate temperature. A columnar morphology, smoother surfaces and strong film texture are obtained. At higher temperatures ($T_s/T_m > 0.4$; Zone II), the diffusion into the grains becomes significant and leads to a dense columnar microstructure, which is retained from the interface to the film surface.

The SZM model has been further expanded to better describe the influence of deposition parameters on the sputter-films by Thornton [30], where the film microstructure was depicted as a function of T and working gas pressure P. However, this model is not suitable for energetic plasma-based deposition process such as HiPIMS, where ion energy (controlled by the bias voltage) and ion fluxes can be used to tune the microstructure of the film. In particular, ion bombardment of the substrate can have the same effect on the mobility and adsorption of the atoms as an increase in the temperature.

Recently, A. Anders introduced the latest modification to SZM (Figure 7), where the microstructure of the film is now described in a three-dimensional space [31]. The two horizontal axes represents the normalized energy flux delivered by the bombarding particles (i.e. ions), E*, and the generalized substrate temperature, T*. The third vertical axis gives an idea of the thickness of the film, which can be correlated to the density of the film.

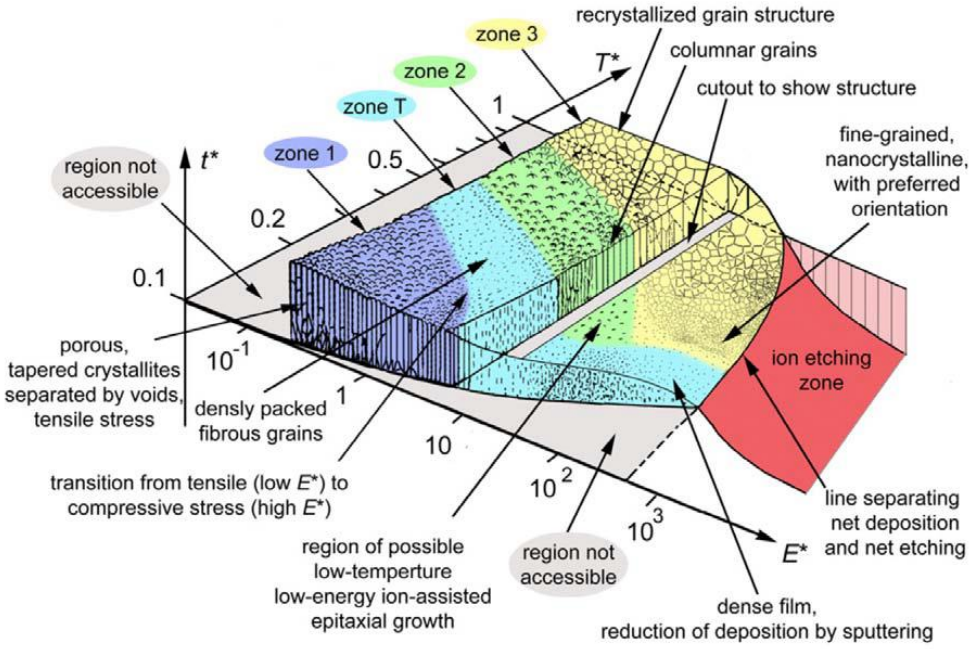

Figure 7: Structure zone model for plasma-based deposition from Anders, from [31].

A brief description of each zone is presented in the following paragraph.

- Zone 1 (porous structure): The film is composed of fine crystallites or textured fibers of a small diameter. A high density of defects and imperfections is observed due to the very limited adatom mobility.

- Zone T (Thornton): The surface diffusion has considerable influence on the film growth. The film microstructure is typically formed by V-shaped columns due to the competitive grains growth at the interface. Grains with different crystallographic orientations provide different diffusion coefficients and therefore may limited surface diffusion for the adatoms. Intercolumnar porosity may still be observed.

- Zone 2 (columnar structure): At higher temperature, the film microstructure is dense and composed of columnar grains, which is retained from the interface to the film surface.

- Zone 3 (recrystallization): The bulk atoms can participate in diffusion processes within the film volume thanks to the high energy supply by ion bombardment, resulting in gradual coalescence and grain coarsening. The size of the grains also increases with T*.

- Ion etching zone: Above 400 eV, the thickness of the deposited film decreases due to the increasing sputtering yield of the bombarding ions. In such conditions, the ion sputtering rate equals the film deposition (or formation) rate. This means that for even higher energies, the substrates are not coated but etched. It can be mentioned that the ion etching zone is commonly used as

surface pre-treatment prior to film deposition in order to remove the surface oxides and other impurities.

1.2 PVD FOR THE OPTIMIZATION OF SUBSTRATE/COATING SYSTEM INTERFACES

The structure of the interfacial region is essential to obtain a good adhesion of the coating on the substrate [21, 22, 27]. For this purpose, intimate contact and strong bonding between the materials are necessary [22]. One way to reach this state is to start with a clean and dense interface, which will allow a direct contact between the coating and the substrate and permit the formation of the metallic, covalent, or ionic bonds as opposed to the significantly weaker van der Waals bonds between these two entities [12, 27, 32]. In contrast, the presence of surface defects and chemical impurities likely will hinder good adhesion [21, 22, 27]. Different types of imperfections exist at the interface such as voids [21, 22], microcracks [21], lattice defects [22] and misfit dislocations [27]. Solutions have been proposed to reduce the number of flaws and to enhance coating adhesion on the substrate such as surface pre-treatment prior to deposition, ion implantation and deposition of a bond coat between the substrate and the coating.

1.2.1 Pre-treatment prior to deposition

1.2.1.1 Ion etching

Ion etching pre-treatment by PVD techniques takes place before the film deposition to clean and sometimes modify the substrate surface, which facilitates the formation of a defect-free and dense interface and improves the adhesion of the coating on the substrate. It is usually performed by the plasma gas ions present in the deposition chamber (usually Ar ions), or metal ions from the targets. The most common type of *in situ* surface pre-treatment is made by removing the contaminants from the substrate surface by etching with voltage-accelerated Ar ions [10-12, 33, 34]. However, this ion etching pre-treatment has several drawbacks. First, in addition to the substrate, the etching of the entire deposition chamber is performed, which can lead to arcing and substrate contamination. Moreover, the incorporation of Ar ions into the substrate surface can be detrimental to the interface formation [11, 14, 27, 33]. Ar is incorporated as interstitials in the crystal lattice, which induces stresses in the lattice and weakens the interface. Consequently, substrate etching by Ar sometimes does not improve the adhesion [14].

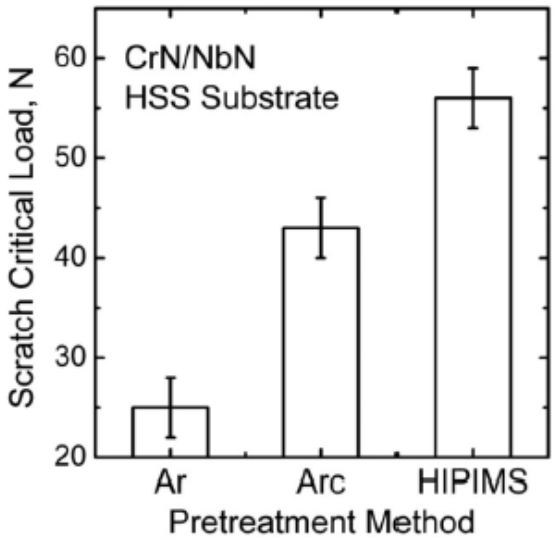

Figure 8: Critical loads measured during the scratch-test of CrN/NbN coatings on high speed steel substrate pretreated by Ar glow discharge, cathodic arc and HiPIMS discharges, from [14].

Cathodic arc evaporation (CAE) [27, 33, 35] and HiPIMS [10-12, 14, 27, 33, 34, 36] ion metal etching pre-treatment are developed to avoid these potential problems. For instance, etchings by HiPIMS discharge seem to provide dense interfaces and favor the implantation of metal ions [27] (Figure 8). The metal ions are incorporated (ions with energies of 600-1000 eV in 5-8 nm penetration depth) into the substrate lattice by substitution of structural atoms (replacements), thus preserving the crystal structure and strengthening the interface [27]. In addition, a gradual change in composition and properties can be observed upon metal ions incorporation [10, 14]. This leads to a higher substrate/coating adhesion strength [27, 33, 35] due to the formation of strong chemical bonds between the depositing and surface atoms [7, 19]. Consequently, the choice of metal for pre-treatment is dictated by its chemical affinity with coating materials [33].

1.2.1.2 Ion implantation

PVD ion etching can be compared to ion implantation in terms of implantation depth (< 1 µm) and mechanisms (atom replacements or incorporation in interstitial sites) but much lower energy is used for ion etching (around 0.9 keV in our case). Ion implantation is a technique used to modify the extreme surface of materials without altering their bulk properties [37-53]. This method uses very high ion energies (between 10 and 200 keV) that causes physical and chemical modifications on the surface, usually limited to a shallow depth (< 1 µm) [39, 40, 51, 52]. These physical changes are due to radiation damage produced during ion bombardment [42, 46] and lead to the deformation of the crystalline structure by creating dislocations, vacancies and atom displacements [37, 45]. The ion mass plays an important role in these physical modifications: a heavier ion promotes a higher number of collisions leading to higher surface damage [45]. The chemical changes are associated with the nature of the implanted elements [42]. For instance, the implantation of inert gas ions such as Ar is known to physically weaken and modify the material surface by increasing the local compressive stress by moving into interstitial sites, and breaking the crystalline structure through the formation of Ar bubbles [42, 45, 46]. This can also be observed

during Ar^+ etching of the substrate by PVD [27]. This implantation in stainless steel can also alter the chemical properties of the surface by increasing the Cr/Fe ratio of the passive film which enhances its protective properties compared to other implantations (N, Si, N + Si) studied here [45]. This fact was probably related to the breakdown of the crystalline structure of the stainless steel near the surface. In contrast, bombardment of metal ions allows alloying elements to be introduced into the material, which leads to the removal of the initial surface oxide layer and the formation of a new one including the implanted elements [41, 42, 46, 47]. For example, N_2^+ ion has been implanted into Ti coated on 316 SS to form nitride layer, which improved substantially the corrosion and oxidation resistance compared to the untreated substrates [42]. Titanium ion implantation are also investigated to improve the corrosion resistance of AZ91 magnesium alloy due to the more compact surface oxide film formed on the implanted surface [47]. Therefore, this method is mainly used to improve the adhesion of the coating to the substrate [42, 47, 51]. Furthermore, ion implantation can lead to the enhancement of hardness, wear and corrosion resistance [43, 44, 53]. Recently, it has been shown that the co-implantation of two elements can be used to further improve the corrosion resistance properties of materials [53]. A similar effect could be observed in the case of Ti (Zr) metal ion etching in an Ar plasmagenic gas, which would result in the bombardment and implantation of both elements *i.e.* Ti (Zr) and Ar ions.

1.2.2 Deposition of a bond coat

In some cases such as lack of adhesion due to distinct thermal expansion coefficients and crystal lattices, a bonding interlayer (bond coat) is required to improve coating adhesion, especially for ceramic coatings [33, 34, 54-56]. This bond coat reduces internal stresses at the interface by smoothing the difference in lattice parameters between the substrate and the coating, acting as a compliant film [33, 54-56]. In addition, it can absorb residual contaminants from the substrate surface [54], thereby forming stronger chemical bondings between the substrate and the coating [56]. For optimized thickness it improves overall adhesion of the coating by modifying the type of failure associated to scaling (a ductile failure is desirable) [56]. The bond coat optimal thickness depends on the whole system, *i.e.* substrate, bond coat materials and deposition process. For example, for a Si substrate, Ti bond coat and RF magnetron sputtering, the minimum thickness allowing an improved adhesion is 300 nm [55], whereas for a steel substrate, Al, Cr or W bond coat and HiPIMS technique, a 20 nm interlayer is sufficient to enhance thin film adhesion [34]. It should be noted that bond coat between 100 and 200 nm-thick are used in most studies in the literature [33, 54, 57-60]. Moreover, the formation of a bond coat can compensate the limitations of Ar^+ etching in cleaning the substrate surface [33, 34, 54] (Figure 9).

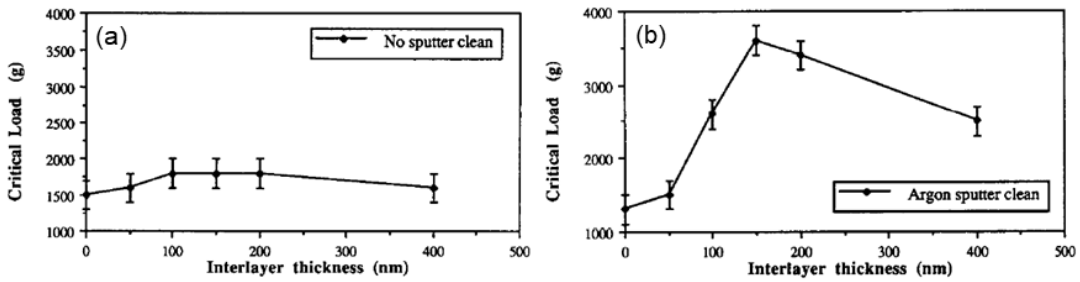

Figure 9: Variation of critical load for coating spallation with Ti interlayer thickness for 2 µm TiN coatings on stainless steel: (a) no sputter clean and (b) sputter clean in argon, from [54].

Furthermore, the combination of HiPIMS etching and deposition of a metallic interlayer (Cr, Ti, Nb, *etc.*) results in a significant increase of the adhesive strength compared with only deposition of an interlayer. Clearly, the best adhesion is obtained when a HiPIMS metal ion etching pretreatment is combined with a metallic bond coat [33].

1.3 CONCLUSIONS

The interfaces formed by PVD depend on the deposition process used, which provides a different energy of the vapor particles. The higher the energy of the vapor particles, the stronger the interaction between the substrate and the coating, resulting in the formation of strong bonds at the interface. Two types of interfaces, *i.e.* mechanical and pseudodiffusion, occur particularly during PVD coating deposition but a combination of them is most often observed. Moreover, certain properties of the substrate such as surface roughness and substrate temperature influence the formation of these interfaces, which can play a role in the nucleation and growth of coatings. Defects and inhomogeneities on the surface can act as stress concentration areas leading to a decrease of the substrate/coating interface adhesion strength. These interfaces can be optimized to enhance the performance of the substrate/coating system, especially the adhesion of the coating on the substrate that affects the corrosion resistance and mechanical properties of the system. A clean and defect-free interface leads to direct contact between the substrate and the coating, which induces the formation of strong bonds between them. The presence of impurities and defects at this interface can be reduced or eliminated by using several techniques. First, pre-treatment prior to coating deposition (ion etching) can be performed to remove all kinds of contaminants and implant ions into the substrate. The structural modifications of the substrate vary according to the type of ions used: Ar is incorporated as interstitials in the crystal lattice, whereas metal ions are incorporated as replacements (substitution of structural atom). Another solution is the deposition of a bond coat, which can reduce internal stresses at the interface by smoothing the difference in lattice parameters between the substrate and the coating and absorb residual contaminants from the substrate surface leading to the formation of stronger chemical bondings between the substrate and the coating. Finally, a combination of these two techniques can result in a significant enhancement of the substrate/coating adhesion.

2. RELATIONSHIP BETWEEN INTERFACES AND CORROSION RESISTANCE

The constantly evolving demands of new industries and technologies require development of advanced materials in terms of mechanical, tribological, optical, electrical or anticorrosion properties. Therefore, corrosion is a global phenomenon leading to significant expenses and even safety issues [61].

In the nuclear field, materials are selected or specifically tailored to withstand aggressive environments, such as concentrated acids, high temperatures, irradiation, molten media, *etc*. For some specific media, corrosion can remain an important concern to take into account to increase the components' lifespan. In the case of the treatment and recycling of spent nuclear fuel performed in France, concentrated and hot nitric acid is used as dissolution medium of the fuel. Therefore, highly resistant materials have been selected to be used in this oxidizing environment. Looking for sustainable solutions to maximize the lifespan of the component remains a challenge for a durable development of industrial systems. Marine environment is also a corrosive environment due to the presence of chemical and biological species (anions, cations, molecules, bacteria, *etc.*) that can cause material degradation [62]. The huge necessity of having long lasting installations for a large broad of marine applications like the development of renewable marine energies is essential in a sustainable vision of industrial development.

To limit the impact of corrosion on materials such as stainless steel in aggressive environments, protective coatings appear to be a very promising solution. Over the past few years, large variety of coatings and materials have been used to prevent corrosion, namely organic, inorganic, metallic and non-metallic coatings. Nowadays, one of the most important aspects of the design of coatings for corrosion protection is the use of environmental friendly compounds. The coatings produced via PVD routes are considered to be solvent free, with reduced waste while creating a thin, but dense films with minor defects and good anti-corrosion properties. In the presence of a protective coating, among other parameters, the performance of the corrosion protection system (substrate/coating) depends on the substrate/coating interfaces [63]. Some interfacial properties such as degradation, adhesion strength, interphase composition and chemistry must be controlled to promote the best resistance to corrosion [63-65]. Actually, since corrosion is mainly initiated from coating defects (pores, pinholes or scratches) and species trapped at the substrate/coating system interfaces, defect-free interfaces should improve adhesion and anticorrosive properties [20, 22, 64-67]. The methods used to obtain this type of interface can be the mechanical burnishing or shot peening [22] for coating-environment interface, and pre-treatments [68, 69] to clean substrate/coating interfaces. In addition, the adhesion strength of the coatings can be improved by the use of bond coat as shown in the section 1.2.2. Another solution is the development of multilayer coatings, which can decrease the electrolyte infiltration into the substrate/coating space [58, 70-76].

2.1 NITRIC ACID ENVIRONMENT

In France, the reprocessing of spent fuel relies on the PUREX process performed in the processing plant located near La Hague. Actual reprocessing starts by cutting the

fuel rods into small pieces. These fuel fragments are dissolved in hot concentrated (up to 14.4 mol/L) nitric acid. Then, this solution of dissolved fuel undergoes liquid-liquid extraction steps to separate uranium and plutonium. Fission products and minor actinides remain in the nitric acid solution and are concentrated, calcined and vitrified in a glass matrix inside a metallic canister and stored as nuclear waste, while recovered uranium and plutonium are stored or recycled to be reused in mixed oxide fuel (MOX) [77-79]. Throughout the reprocessing, nitric acid solutions at different temperatures (up to 110-120°C) and concentrations (up to 14.4 mol/L) are used. In addition, some dissolved species (oxidizing ions such as Pu(IV) or Np(VI), fission products such as iodine and cations such as Fe(III) or Cr(III)) are present in these nitric media [79]. Therefore, the equipment of reprocessing plants must be built with corrosion resistant materials. For the lowest acidic condition, 304L austenitic stainless steel (ASS) is the materials of choice, whereas Si-doped ASS and zirconium (Zr) are used at high concentrations to prevent intergranular corrosion occurring for these highly oxidizing conditions. Generally, 304L ASS is used for the major part of the equipment whereas Zr alloys are preferred for the most critical corrosion equipment such as fuel dissolver and nitric acid recovery concentrators [78-80]. Moreover, another material under investigation for enhanced corrosion resistance in nitric acid environment is tantalum (Ta). It exhibits good corrosion resistance over a wide concentration and temperature range [81]. For example, Ta in 70 wt.% nitric acid at boiling temperature exhibits negligible corrosion rate values [82]. However, Ta is considered for use as a thin film rather than a massive material due to its high density, high cost and as it is also a critical material that should be limited in use.

2.1.1 Corrosion processes

The electrochemical corrosion of 304L ASS in nitric acid environment can be described by the schematic current-potential curve shown in Figure 10 [83]. Three distinct ranges of surface potentials can be identified: active, passive and transpassive regions. The first region is the active state of the 304L ASS, where anodic dissolution takes place. This is the case for low oxidizing media, where proton reduction usually occurs. In this domain, generalized uniform corrosion occurs but can reach high rates. For moderate oxidizing conditions (in the presence of nitric acid only), 304L ASS is in its passive state. This domain can be extended over a large range of potentials (a few hundreds of mV). The formation of an oxide film (mixture of Fe(III) and Cr(III) oxides) on the surface that acts as a barrier against the nitric acid is observed. However, in highly oxidizing conditions, for example in the presence of oxidizing cations such as Ce(IV), V(V), Cr(VI), passive films may be locally broken down and localized corrosion can occur. The transition from passive to transpassive domain means that Cr(III) in the passive layer is oxidized to Cr(VI), which readily dissolves. In this domain, intergranular corrosion of the steel occurs, characterized by intergranular indentations for the less severe conditions and loss of grains for the most severe ones.

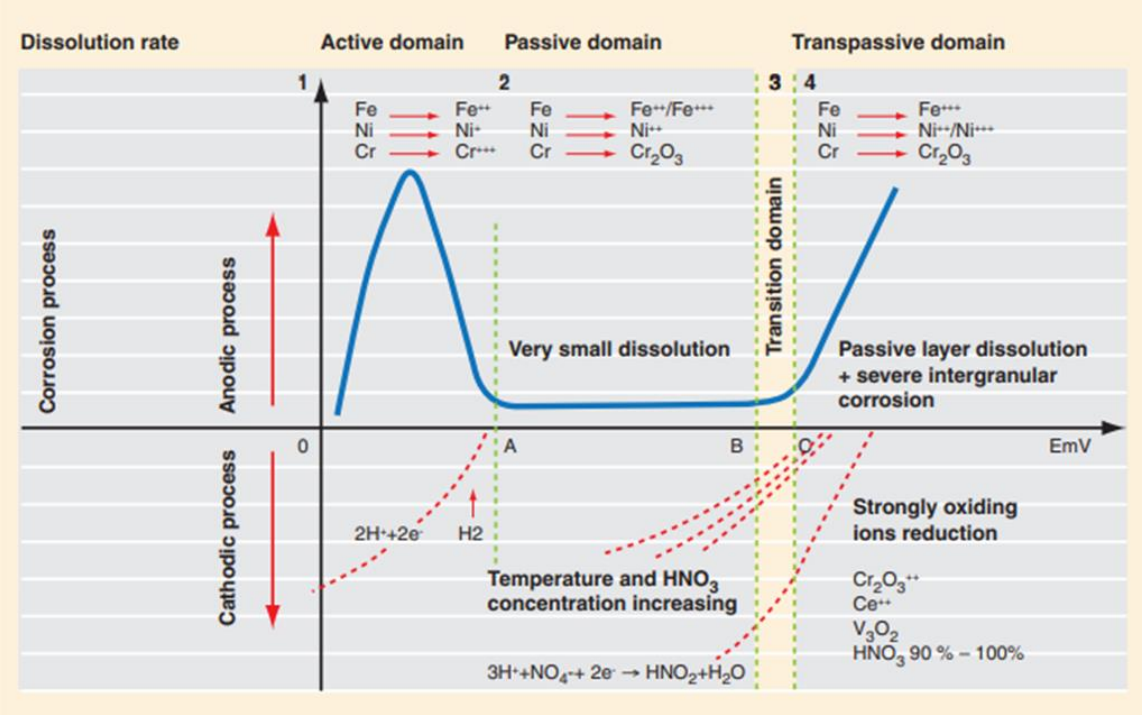

Figure 10: Current-potential curve for 304L ASS in HNO_3 environment at room temperature, from [83].

Several pieces of equipment used for reprocessing of nuclear fuel are made of 304L ASS in contact with concentrated nitric acid. As it was said before, two kinds of corrosion, summarized in Table 1 can occur for 304L in nitric acid environment [83]: generalized (uniform) corrosion, and localized corrosion, mostly at the boundaries of metal grains, *i.e.* intergranular corrosion.

Table 1: Corrosion processes observed in nitric acid environments.

Corrosion processes	Illustration	Principle	References
Generalized uniform corrosion	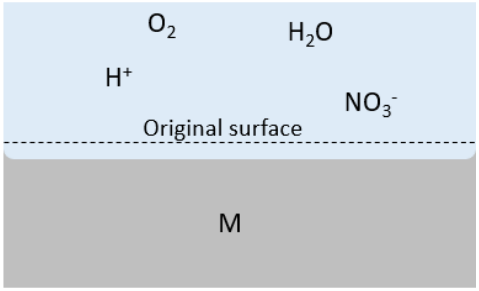	Anodic and cathodic reactions occurring in a homogeneous manner over the entire metal surface	[84]

Intergranular corrosion	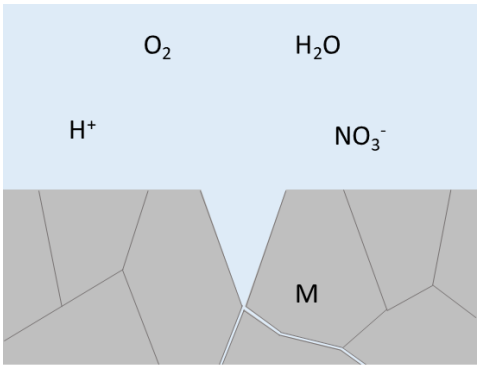	Localized phenomenon occurring at the boundary or in the immediate vicinity of metal grains	[62, 85-88]

2.1.2 Choice of massive materials for corrosion resistance

2.1.2.1 Zirconium and zirconium alloys

For the reprocessing of nuclear fuel, the most important selection criteria for materials are good mechanical properties and excellent resistance to corrosion in nitric acid environment. Zirconium and its alloys perfectly meet the nuclear industry criteria. The high resistance to corrosion of zirconium results from its affinity with oxygen, which results in the formation of a surface protective film of oxide (ZrO_2) that limits the overall corrosion reactions. This results in low corrosion current densities (J_{corr}) (< 1 µA/cm²) regardless of the nitric acid concentrations (0.5 up to 14.4 mol/L). Increasing the nitric acid concentration leads to an increase of the corrosion potential (E_{corr}) but the depassivation potential tends to decrease, reducing the margin to depassivation that remains however sufficient up to the azeotropic concentration at boiling temperature [79]. For concentrations close to the one used in our work (2 and 3.1 mol/L), E_{corr} value is between 500 and 700 mV/SHE and J_{corr} around 0.05 µA/cm² (Figure 11). Note that, contrary to 304L ASS, the transition from passive to transpassive domain is sharp without a transition domain (Figure 10).

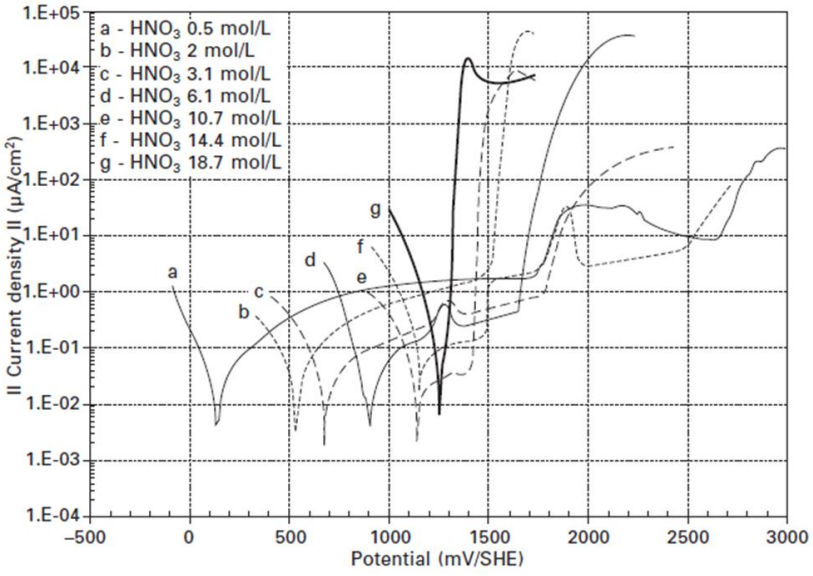

Figure 11: Current-potential curves of zirconium for different concentrations of nitric acid at boiling temperature after 24 h of immersion, from [79].

Therefore, for hot and concentrated nitric acid environments, zirconium alloys are preferred to stainless steels [79, 80]. For example, in 14.4 mol/L HNO_3 at boiling temperature, the corrosion rate of zirconium is much lower than that of ASS. Moreover, zirconium corrodes uniformly while stainless steels are affected by intergranular corrosion. However, some phenomena, such as the presence of fluoride ions, can damage the passivation film and decrease the protecting properties of zirconium alloys [79]. These fluoride ions usually come from spent fuel or reagent impurities [79, 80].

2.1.2.2 ASS

As for zirconium alloys, the high corrosion resistance of ASS in nitric acid environments can be explained by the formation of a very thin (typically 1-10 nm thick) passive oxide layer on the surface [79, 89-91]. This film is described as a bilayer oxy-hydroxide structure: the outer layer composed of hydroxide species, which exchanges with the electrolyte, and an inner film composed of Fe and Cr oxides acting as a barrier to charge transfer [91, 92]. The corrosion protection of ASS is mainly due to the presence of chromium in the passive film [90-92]. Therefore, an increase in chromium content in ASS promotes faster formation and greater lifetime of the passive film, thus reducing the corrosion rates. However, the most common types of stainless steel (304L and 316L) can be sensitive to intergranular corrosion. This intergranular corrosion occurs in highly oxidizing conditions for example in the presence of oxidizing ions (Cr(VI), Ce(IV) or V(V)) or in non-renewed media allowing the accumulation of both oxidation products (Fe(III), Cr(III), Ni(II)) and reduction products, which leads to the increase of the nitric acid reduction rate due to its autocatalytic characteristic. Therefore, a shift of the corrosion potential in the transpassive domain is observed. This phenomenon is illustrated in the presence of Fe(III) ions: by increasing the Fe(III) concentration the corrosion potential of 304L ASS shifts in its transpassive domain leading to a higher J_{corr} (Figure 12). In 8 mol/L HNO_3, J_{corr} is about 0.5 µA/cm² while for a solution of 5 mol/L HNO_3 and 1 mol/L $Fe(NO_3)_3$ it increases to about 50 µA/cm². Note that in our case, the solution used for corrosion tests will also contain Fe(III).

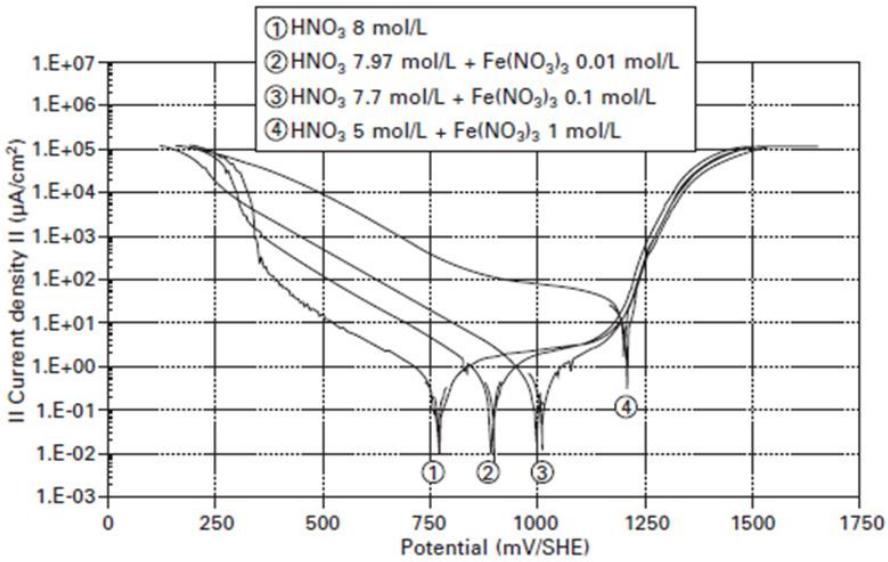

Figure 12: Influence of $Fe(NO_3)_3$ on the cathodic reduction of nitric acid on 304L ASS in a nitric acid solution at 100 °C, from [79].

The intergranular corrosion observed for 304L ASS in nitric acid is illustrated using SEM micrographs (Figure 13). After 21 days of immersion in a 6 mol/L HNO_3 solution at 108 °C, 304L just begins to etch while after 57 days, a severe intergranular corrosion is observed with a loss of grain rows [93]. This effect can be countered by the addition of silicon in the steel, which inhibits intergranular corrosion at concentrations between 3 and 4 wt% [79]. This has led to the development of nitric acid grade (NAG) ASS for applications in spent nuclear fuel reprocessing plants.

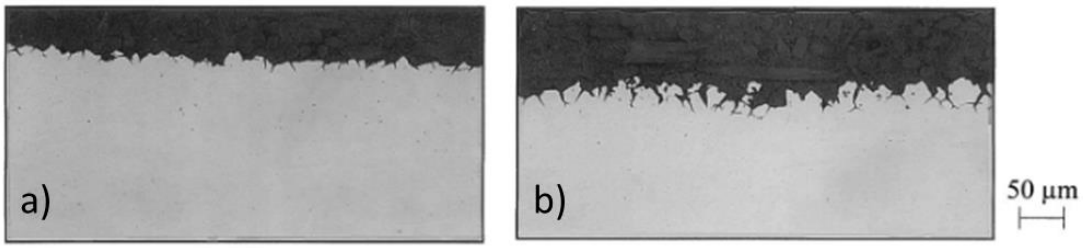

Figure 13: SEM micrographs of the cross-section of a 304L sample after a)21 days and b) 57 days in 6 mol/L HNO_3 solution at 108 °C, from [93].

As previously explained, zirconium alloys perform better than ASS in highly oxidizing environments. However, they can be up to five times more expensive than ASS and are harder to machine and shape. Moreover, they are susceptible to fluoride and stress corrosion [79, 80]. Consequently, they are only used for specific applications such as fuel dissolvers and concentrators for nitric acid recovery.

2.1.3 Methods for corrosion protection

2.1.3.1 Ion implantation for corrosion resistance improvement

The effect of ion implantation on corrosion resistance in nitric acid is partially studied in the literature. Nitrogen (N) ion implantation is mainly reported as a method to increase the corrosion resistance properties of 316 and 304L steels [43, 94]. For instance, an implantation depth estimated to 76 ± 33 nm is observed for nitrogen ions implanted at 70 keV in the dose of 2.5×10^{17} N^+/cm^2. The N-implanted sample shows nobler E_{corr} (375 mV *vs.* Ag/AgCl) and lower J_{corr} (5×10^{-2} µA/cm²) compared to initial 304L (120 mV vs. Ag/AgCl and 1×10^0 µA/cm²) in a 1 mol/L HNO_3 solution [94]. This enhancement in corrosion resistance is attributed to the formation of a stable passive film. N enrichment on the surface results in the formation of ammonium ions, which in turn can form nitrite and nitrate ions, thus improving passivation properties [94]. Moreover, nitrides can form in interstitial sites during polarization that decreases surface dissolution process.

2.1.3.2 Coatings for corrosion protection

Various metal-based coatings can be deposited on ASS to prevent corrosion in nuclear fuel reprocessing plants such as zirconium-based [63, 95], titanium-based [57, 94, 96] and tantalum-based [97] coatings. Zr-based coatings regroup several types of materials such as metallic alloys or ceramic compounds [63, 95]. As far as ceramic films are concerned, various deposition processes were studied such as spray pyrolysis (coating thickness: 200-400 nm [98]), sol-gel methods (coating thickness

<100 nm [99]) or PVD techniques (coating thickness of a few µm [68]). On the other hand, Ti-based oxide [57, 94], metal [57] or metallic glass [96] coatings were investigated. The potentiodynamic polarization curves of 1 µm-thick Ti coating deposited by reactive magnetron sputtering on 304L ASS show improved corrosion resistance (E_{corr} = 330 mV vs. Ag/AgCl and J_{corr} = 4.5 × 10^0 µA/cm²) compared to initial 304L substrate (E_{corr} = 250 mV vs. Ag/AgCl and J_{corr} = 10 × 10^0 µA/cm²) in 1 mol/L HNO_3 solution (Figure 12) [57].

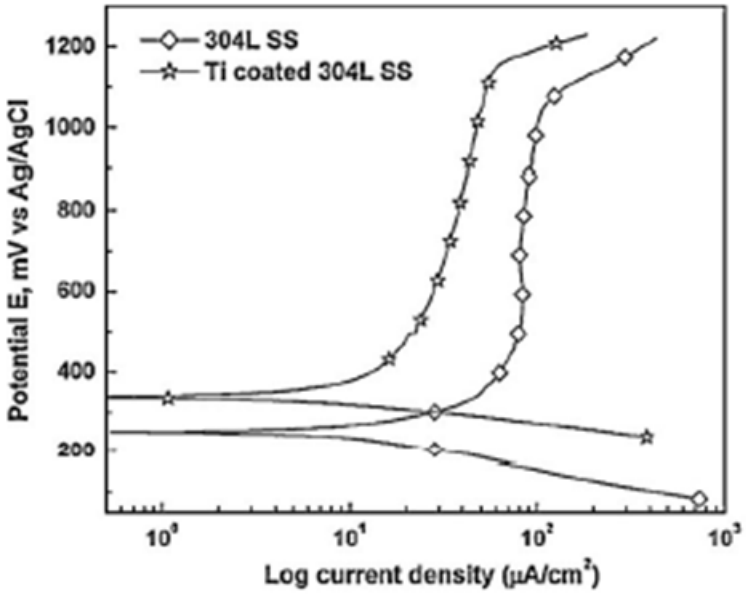

Figure 14: Potentiodynamic polarization curves of initial and Ti coated 304L ASS in 1 mol/L HNO_3 solution at room temperature (Ag/AgCl electrode), from [57].

The characterization of the electrochemically investigated surfaces by AFM shows grain boundary dissolution for the initial 304L (Figure 15a) compared to the Ti-coated one (Figure 15b). This indicates that the Ti coating offers a good resistance to surface dissolution in this environment.

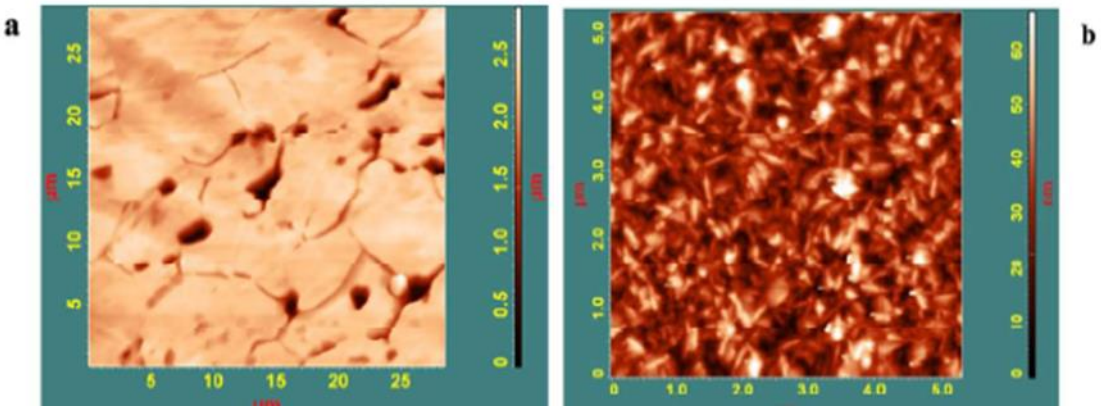

Figure 15: AFM surface morphology of a) initial and b) Ti coated 304L ASS after electrochemical measurements in 1 mol/L HNO_3 solution, from [57].

Ti-based metallic glass coatings are developed to further improve corrosion resistance in aggressive environments. Again, these coatings exhibit better corrosion resistance than 304L ASS in concentrated nitric acid. Moreover, Ta-based metal coating deposited by thermo-chemical decomposition technique on commercially pure titanium (Cp-Ti) shows four times better corrosion resistance (down to a corrosion rate of 0.08 ± 0.01 mm/year) than initial Cp-Ti in boiling 65% nitric acid solution [97].

2.2 MARINE ENVIRONMENT

2.2.1 Corrosion processes

Metals in contact with seawater are exposed to an extremely complex environment, containing inorganic dissolved salts, organic and biological molecules, microorganisms and dissolved gases in water. Other possible processes besides uniform corrosion include pitting corrosion, crevice corrosion, galvanic corrosion and biocorrosion [62]. These various corrosion processes are summarized in Table 2. Moreover, corrosion can be compounded by additional aggressive mechanisms [86, 87]. For example, in turbid waters such as Singapore bay, solid particles mechanically erode marine components, even more reducing their lifespan.

Table 2: Corrosion processes observed in marine environments.

Corrosion processes	Illustration	Principle	References
Pitting corrosion	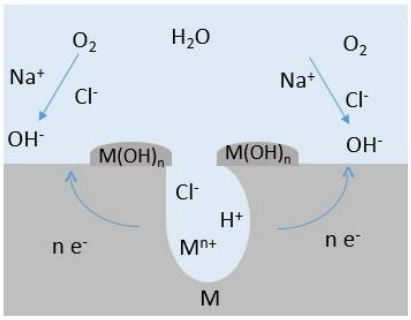	Formation of holes or pits at the surface of a material that can extend deeply in the bulk material	[62, 85, 100]
Crevice corrosion	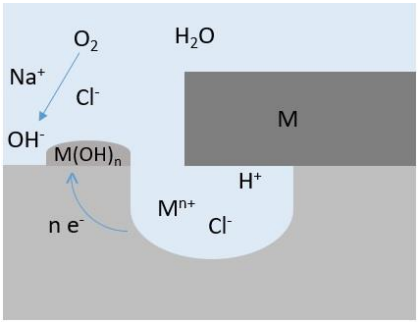	Presence of a stagnant solution in a narrow crack or crevice leading to the deoxygenation of the crack environment and local acidification of the electrolyte	[62, 85, 101]

Galvanic corrosion	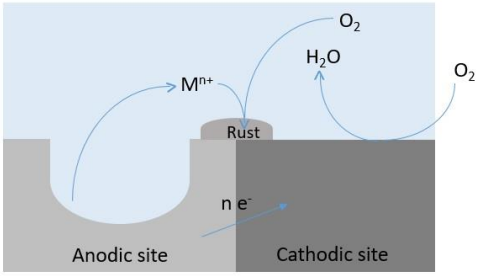	The onset of a galvanic cell between two dissimilar metals in electrical contact with each other and immersed in a continuous electrolyte	[62, 84, 85]

In addition, microbiologically influenced corrosion, also known as biocorrosion, which describes the specific impact of the presence and bioactivity of microorganisms on corrosion processes can be observed in the marine environment. This process relates to the formation of a biofilm on the surface of a metal immersed in contaminated environments such as marine ecosystems. The biofilm contains microorganisms that promote specific corrosion types and modify the global corrosion rate [62, 102, 103]. Corrosion acceleration can then occur due to local acidification in the biofilm [104], reduction of Fe(III) to Fe(II) preventing the formation of a passive layer, or even direct oxidation of metal as an electron donor for metabolic reactions [105, 106]. An example of corrosion acceleration is given by sulfate-reducing bacteria that reduce structural Fe(III) from passivating oxide layers [107]. The most common countermeasures against biocorrosion is the incorporation of biocide agents to limit bacteria proliferation in the surrounding environment and on the material as well as the modification of the surface properties to prevent biofilm adhesion and growth [108].

2.2.2 Methods for corrosion protection

2.2.2.1 Ion implantation for corrosion resistance improvement

Ion implantation is a commonly used technique for modifying corrosion resistance of 304 ASS in saline environment [45, 46, 109]. For instance, the implantation of N, Ar and Si ions up to an ion dose of 1×10^{15} ions/cm² at an accelerating potential of 150 keV shows an implantation depth from 90 (Ar) to 170 nm (N) and better corrosion resistance. An increase in E_{corr} and a decrease in J_{corr} (Figure 16) is observed for all implanted samples compared to initial 304L ASS [46]. However, these elements act differently: N stabilizes the passive layer by forming ions, Si creates a protective oxide (SiO_2) layer on the surface and Ar increases the Cr/Fe ratio of the passive film making it more resistant [45, 46].

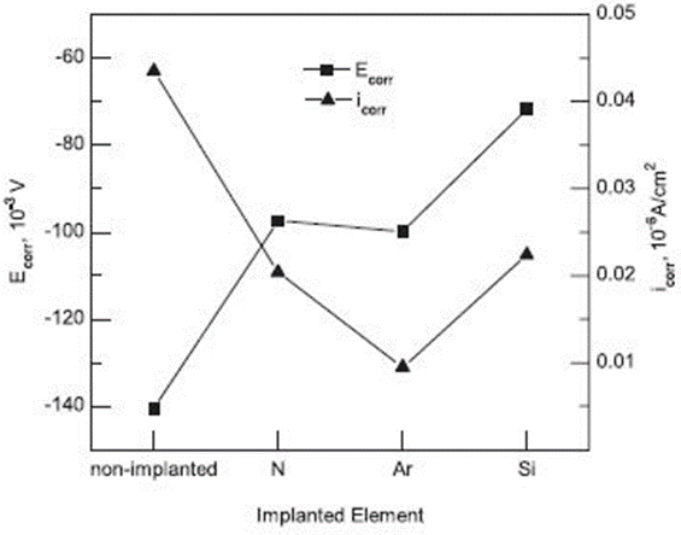

Figure 16: E_{corr} and i_{corr} for non-implanted and implanted (N, Ar and Si) 304 ASS samples in 0.5 mol/L NaCl at room temperature (Ag/AgCl electrode), from [46].

2.2.2.2 Coatings for corrosion protection

Among the coatings investigated for seawater or saline environments, Zr-based [67, 110, 111] and Ti-based [112-114] compounds dominate the literature of corrosion protection of various types of steels and alloys. Zr-based coatings typically correspond to ceramics such as Zr oxide [67], nitride [110] or oxynitride [111], all of them showing good wear properties and corrosion resistance. For example, in a 3.5% NaCl solution, ZrN and ZrO_xN_y efficiently protect 316L SS from corrosion [110, 111]. ZrO_xN_y coating shows E_{corr} of 2.26 x 10^{-1} V *vs.* Ag/AgCl and J_{corr} of 2.54 ×10^{-9} A/cm² compared to -9.88 × 10^{-2} V *vs.* Ag/AgCl and 1.98 × 10^{-8} A/cm² for 316L SS [111]. These coatings can be synthesized by various methods such as plasma spraying, CAE, HiPIMS, UBMS (unbalanced magnetron sputtering) or ultrasonic spray pyrolysis-nitriding (SPY). On the other hand, the most used Ti-based coatings in marine environment are oxides [112, 113] and nitrides, sometimes alloyed with additional elements [102, 114]. These coatings are deposited by various techniques, such as CVD (chemical vapor deposition), DCMS and HiPIMS. TiN-based coatings are developed to successfully improve corrosion resistance of steels [114]. For example, Figure 17 shows that TiN and especially TiCN coatings deposited by magnetron sputtering (J_{corr} = 4.15 × 10^{-2} mA/cm² and 2.05 × 10^{-4} mA/cm², respectively) have superior anticorrosion properties compared to XC48 steel in a 3.5% NaCl solution (J_{corr} = 0.11 mA/cm²). The TiCN coating has the best corrosion protection probably because of its denser microstructure [114].

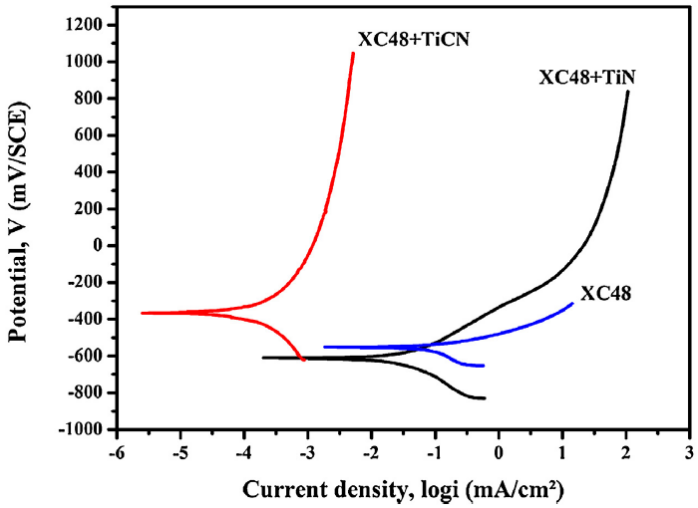

Figure 17: Potentiodynamic polarization curves of TiN and TiCN coatings in 3.5% NaCl solution at 25 °C (SCE electrode), from [114].

In this environment, severe pitting corrosion is observed on the initial XC48 sample (Figure 18a), while the TiCN coating does not show any obvious surface change, *i.e.* surface remains smooth (Figure 18b).

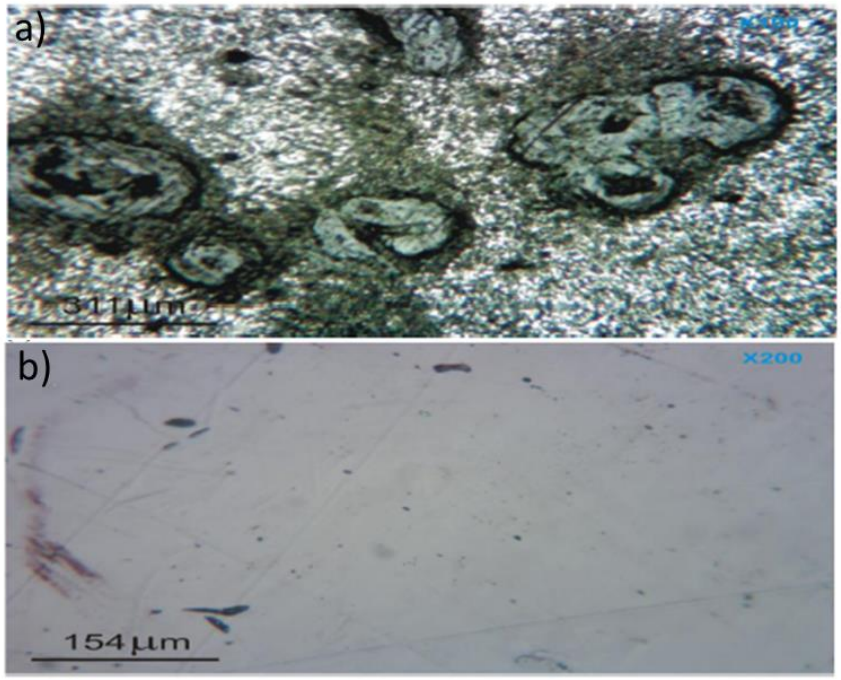

Figure 18: Optical micrographs of a) initial and b) TiCN coated XC48 after electrochemical measurements in 3.5 % NaCl solution at 25 °C, modified from [114].

2.3 COMPLEX SUBSTRATE/COATING SYSTEM

Ion implantation and coatings have been shown to be effective in improving corrosion resistance in our two study media. More complex systems can be used to enhance

lifespan of the steels regardless the environment such as substrate/bond coat/ceramic coating or multilayer (*i.e.* number of layers > 2) coatings.

2.3.1.1 Bond coat

Zr and Ti bonding layers are frequently used prior to deposition of ceramic coatings to improve the substrate/coating adhesion (see section 1.2.2), which can affect the final properties of the coating system. The effect of these bond coats on corrosion resistance is studied in acid [57, 115] and saline [58, 60, 116] environments. Zr/ZrN coatings of similar thickness (1.2-1.5 µm) deposited by reactive DCMS [116] and ion plating [115] on steels show higher corrosion resistance than the ZrN thin film in 3.5 % NaCl and 0.5 mol/L H_2SO_4 + 0.05 mol/L KSCN. The Zr/ZrN coating shows a higher E_{corr} (- 437 mV/SCE) and lower J_{corr} (1.3 µA/cm²) compared to ZrN coating (E_{corr} = - 442 mV/SCE and J_{corr} = 6.5 µA/cm²) [109]. This is due to the decrease in interfacial stresses that prevent the ZrN coating from delaminating and the reduction of pinholes in the thin film, which minimizes the exposure area and limits localized corrosion.

Similar results are obtained in NaCl solution for Ti/TiN coatings of different thicknesses (200-300 nm and 1.4 µm) deposited by reactive MS on a steel [60] and a $TiAl_6V_4$ alloy [58]. The enhancement in corrosion resistance is attributed to the reduction of residual and shear stresses at the interface and to the interruption of pinholes in the coating by Ti interlayer, as already observed for the Zr/ZrN coating. Figure 19 shows that the presence of a 100 nm-thick Ti bond coat is also effective to increase the corrosion resistance of a 1.1 µm-thick TiO_2 coating deposited using reactive MS on a 304L substrate in a 8 mol/L nitric acid solution at room temperature. The coating shows a higher E_{corr} of 582 mV *vs.* Ag/AgCl and lower J_{corr} of 11 × 10^0 µA/cm² compared to initial 304L ASS (E_{corr} = 340 mV *vs.* Ag/AgCl and J_{corr} = 7 × 10^1 µA/cm²). Ti interlayer reduces structural heterogeneities and can form itself a protective oxide film in case of TiO_2 coating failure in nitric acid medium [57].

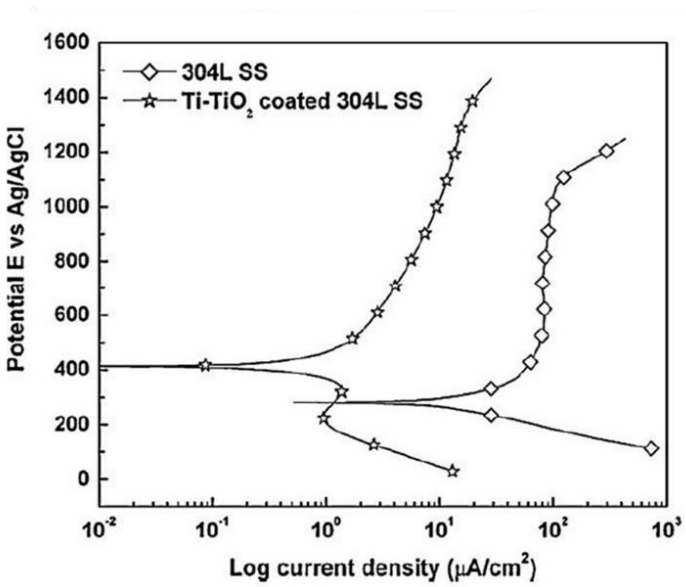

Figure 19: Potentiodynamic polarization curves of initial 304L and Ti/TiO_2 coating in 8 mol/L HNO_3 at room temperature (Ag/AgCl electrode), from [57].

2.3.1.2 Multilayers

For a better corrosion resistance, multilayer coatings can be synthesized to increase the number of interfaces between the substrate and the surrounding environment [58, 70-76]. In general, the corrosion resistance of multilayer coatings is higher for a larger number of interfaces [74, 76]. This is due to the barrier effect of interfaces against electrolyte penetration that reduces pathways to the substrate [71, 74, 76]. Moreover, the multiplication of interfaces can decrease the number and size of defects such as pores, pinholes or cracks by alternating the deposition of different types of layers, which modifies their nucleation and growth [71, 74]. Another explanation for the improved corrosion resistance of multilayer coating is the reduction of internal stresses in the coating due to the metallic sublayers [73, 75].

The architecture of multilayer coatings varies according to the literature but mostly metal/ceramic (Zr/Zr_xN [72], Ti/TiN [58, 74, 75] and Zr/CrN [76]) and ceramic/ceramic (ZrN/CrN [71], ZrN/ZrO_2 [73]) coating systems are developed for corrosion resistance. The thickness of the sublayers also varies and the results about their effect on the corrosion resistance differ. Similar sublayer thicknesses improve the high temperature corrosion resistance of Ti/TiN multilayer coatings [74], whereas for Zr/CrN coatings the thicker the CrN layer, the more resistant the multilayer coating is in artificial seawater [76].

However, in some cases, multilayer coatings do not improve corrosion resistance and delamination of the coating is observed. This is the case when porosities or particles are present on the surface of a layer that has a different electrode potential than the next layer, which can induce local galvanic corrosion. For instance, in the case of multilayer Zr/CrN coatings, metal-rich micro-particles can induce local galvanic coupling between coating matrix and micro-particles [76]. In addition, a rough and dirty surface is detrimental to the growth of multilayer coatings and lead to their delamination due to lack of adhesion to the substrate. In fact, an insufficient cleaning of the surface can affect coating growth and lead to less dense coatings [74].

2.4 CONCLUSION

The main corrosion processes taking place in the nuclear fuel reprocessing are uniform and intergranular corrosion. 304L ASS is used for the major part of the equipment of reprocessing plants while Zr alloys are preferred for the most critical corrosion equipment. For all of these materials, a stable passive layer of oxides forms in nitric acid medium and protects these materials against corrosion. However, deterioration of this layer may lead to extensive corrosion and therefore to premature failure of the reprocessing equipment. Consequently, improvement in corrosion resistance properties is necessary to extend the lifespan of non-critical tools and infrastructure in a nitric acid environment. First, ion implantation that shows the surface modification of a steel on a thin depth (< 1 µm) can improve its corrosion resistance, especially by modifying the passive layer. For example, nitrogen ion implanted sample shows nobler E_{corr} (375 mV *vs.* Ag/AgCl) and lower J_{corr} (5×10^{-2} µA/cm²) compared to initial 304L (120 mV vs. Ag/AgCl and 1×10^{0} µA/cm²) in a 1 mol/L HNO_3 solution. Moreover, Zr-, Ti- and Ta-based coatings are being studied to improve corrosion resistance in nitric acid environment due to the formation of a

passive layer on their surface as 304L ASS. For instance, 1 µm-thick Ti coating deposited by reactive magnetron sputtering on 304L ASS show improved corrosion resistance (E_{corr} = 330 mV vs. Ag/AgCl and $J_{corr} = 4.5 \times 10^0$ µA/cm²) compared to initial 304L substrate (E_{corr} = 250 mV vs. Ag/AgCl and $J_{corr} = 10 \times 10^0$ µA/cm²) in 1 mol/L HNO_3 solution.

In marine environment, the corrosion processes observed are pitting, crevice, galvanic and biocorrosion in addition to uniform corrosion. 304L ASS is commonly used for many metal-using industries and metal-made infrastructures such as ships, coastal industrial plants (ports and shipyards), offshore facilities for oil and gas production, and power plants due to the formation of a corrosion-protecting passive layer. However, in some conditions such as stagnant seawater, local attack (pitting corrosion) can occur and cause failure of this protective layer. To withstand this degradation, corrosion protection can rely on surface treatments such as ion implantation and coating deposition. For instance, the implantation of N, Ar and Si ions at 150 keV in the dose of 1 x 10^{15} ions/cm² shows a better corrosion resistance. Moreover, Ti- and Zr-based coatings such as TICN and ZrO_xN_y improve corrosion resistance of XC48 and 316L steel, respectively. They lead to an increase of E_{corr} (up to 2.26×10^{-1} V *vs.* Ag/AgCl for ZrO_xN_y coating compared to -9.88×10^{-2} V *vs.* Ag/AgCl for 316L SS) and a decrease of J_{corr} (down to 2.05×10^{-4} mA/cm² for TiCN compared to 0.114 mA/cm² for XC48 steel).

Understanding and optimizing the substrate/coating system interfaces is essential to ensure good corrosion protection. Corrosion is mainly initiated by defects in coatings or contamination on the substrate surface, therefore clean and defect-free interfaces lead to better corrosion resistance. The first step to obtain this type of interface is the pre-treatment of the substrate (etching) to remove the contaminants on the substrate surface. Etching is close to ion implantation (the major difference is the ions energy: 0.9 keV in our case and generally 10 to 200 keV for ion implantation), which suggests that it may have a beneficial effect on the corrosion resistance of the substrate. However, no study has shown this phenomenon so far. The next step consists on the deposition of a bond coat to enhance substrate/coating adhesion. This bonding layer has been shown to improve the corrosion resistance of the substrate/coating system by decreasing residual and shear stresses at the interface and reducing defects such as pinholes in the coating. For instance, Zr/ZrN coating shows a higher E_{corr} (- 437 mV/SCE) and lower J_{corr} (1.3 µA/cm²) compared to ZrN coating (E_{corr} = - 442 mV/SCE and J_{corr} = 6.5 µA/cm²) due to the decrease in interfacial stresses that prevent the ZrN coating from delaminating. A similar effect is observed where a Ti bond coat is deposited prior to TiO_2 coating by reactive MS on a 304L substrate. Ti interlayer reduces structural heterogeneities and can form itself a protective oxide film in case of TiO_2 coating failure, which leads to a higher E_{corr} of 582 mV *vs.* Ag/AgCl and lower J_{corr} of 11×10^0 µA/cm² compared to initial 304L ASS (E_{corr} = 340 mV *vs.* Ag/AgCl and $J_{corr} = 7 \times 10^1$ µA/cm²). Finally, deposition of multilayer coatings is discussed to further enhance the corrosion protection by multiplying the interface between the substrate and the surrounding environment. This increase in the number of interfaces limits the penetration of the electrolyte and is supposed to prevent it from reaching the substrate due to a barrier effect of the interfaces. These interfaces also lead to the reduction of the internal stresses and decrease of the defects by alternating sublayers deposition.

It should be noted that a pre-requisite for the deposition of multilayer coatings is a clean and smooth substrate surface, which is related to a defect-free and clean interface.

The interfaces formed by PVD and methods to optimize them to improve the properties of the final system were discussed. In addition, the relationship between these interfaces and the corrosion resistance in our two study environments (nitric acid and NaCl) were highlighted in this section. Now, the focus is placed on the substrate/coating systems that will be synthesized and studied in this work *i.e.* with Ti- and Zr-based oxide coatings.

3. TITANIUM DIOXIDE (TiO_2) AND ZIRCONIA (ZrO_2) PROTECTIVE COATINGS

3.1 INTRODUCTION

Titanium (TiO_2) and zirconium (ZrO_2) dioxides have widespread applications resulting from their unique chemical, thermal and mechanical properties [117]. These two metallic oxides share some interesting structural similarities. In addition, the sputtering behavior of Ti and Zr are similar *i.e.* their sputtering threshold energy for an incident ion Ar^+ is around 20 eV and their sputter yields at different incident ion Ar^+ energies (from 100 eV to 600 eV) follow similar trends. For instance for an incident Ar^+ energy of 200 eV, the sputter yield of Ti is 0.22 atoms/ion and for Zr it is 0.28 atoms/ion [118]. Their 1st and 2nd ionization energies are also similar. Both information indicate that a similar effect in terms of ion bombardment and etching can be expected. However, they notably differ by the weight and size of their primary cations. The standard atomic weight of zirconium equals 91.224 u, significantly larger than the values for titanium (47.867 u) and argon (39.948 u) [119]. The different atomic weight between Ar, Ti and Zr may also have an effect on ion etching, their implantation and their diffusion into the substrate. Therefore, interfaces prepared with either Ti or Zr species are expected to differ, which could influence the properties of the final component *i.e.* substrate/metal interlayer/oxide coating. However, the study of etching pre-treatment on substrate/oxide coating system is not reported in the literature.

3.2 GLOBAL PROPERTIES

3.2.1 Crystal structure

The most common crystal structures of titanium dioxide (TiO_2) at (near-) ambient conditions are rutile and anatase and the main stable polymorph of zirconium dioxide (ZrO_2) has monoclinic unit cells (Table 3). At room temperature, the rutile structure is the most stable and exhibits a lower free energy of formation than anatase. Moreover, zirconia is monoclinic and known as baddeleyite at room temperature and ambient pressure [120].

Rutile is mainly used for interference applications (high refractive index), for its effective absorption of ultraviolet rays in sunscreen or for biomedical applications (good blood compatibility). On the other hand, anatase shows higher photoactivity performances than rutile and is therefore preferable for photocatalytic applications

[121, 122]. Photocatalytic properties are essential to protect against biocorrosion as they allow degrading the biofilm formed on the surface of materials immersed in seawater.

Table 3: Main crystal structures of TiO_2 and ZrO_2

	TiO_2		**ZrO_2**
	Rutile	**Anatase**	**Monoclinic**
Temperature of formation	From 500-600 °C	From 25 °C to 400-500 °C	Below 1100-1200 °C
Crystal system	Tetragonal ($P4_2/mnm$ space group)	Tetragonal ($I4_1/amd$ space group)	Face-centered (space group $P2_1/c$)
Cell parameters	a = b = 4.584 Å c = 2.953 Å c/a = 0.644	a = b = 3.782 Å c = 9.502 Å c/a = 2.512	a = 5.313 Å b = 5.212 Å c = 5.147 Å c/a = 0.968 β = 99.218
Illustration of the crystal structure	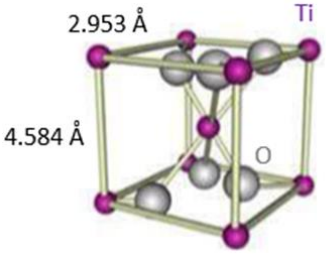	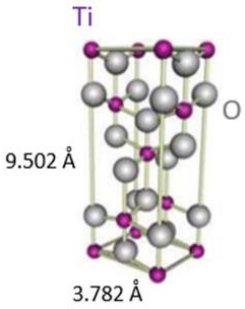	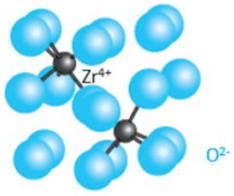
Phase transition	X	From anatase to rutile for temperature ranging from 400 to 1200 °C	X
References	[123-125]	[122, 123, 126, 127]	[120, 128, 129]

3.2.2 Stability

Figure 20 shows the Ellingham diagram, reporting the temperature dependence of the Gibbs free energy of formation of metal oxides. The oxygen partial pressure is taken as 1 atmosphere, and all the reactions are normalized to consume one mole of O_2. As shown on the diagram, Zr is the most reducing metal compared to Ti and then, Cr and Fe. Therefore, Zr and Ti should reduce the Fe and Cr metallic oxides to form respectively ZrO_2 and TiO_2 [130]. This indicates that a Ti- or Zr-based coating

deposited on 304L ASS should form a more stable oxide layer than the passive oxide layer of the initial 304L if there are no kinetic limitations.

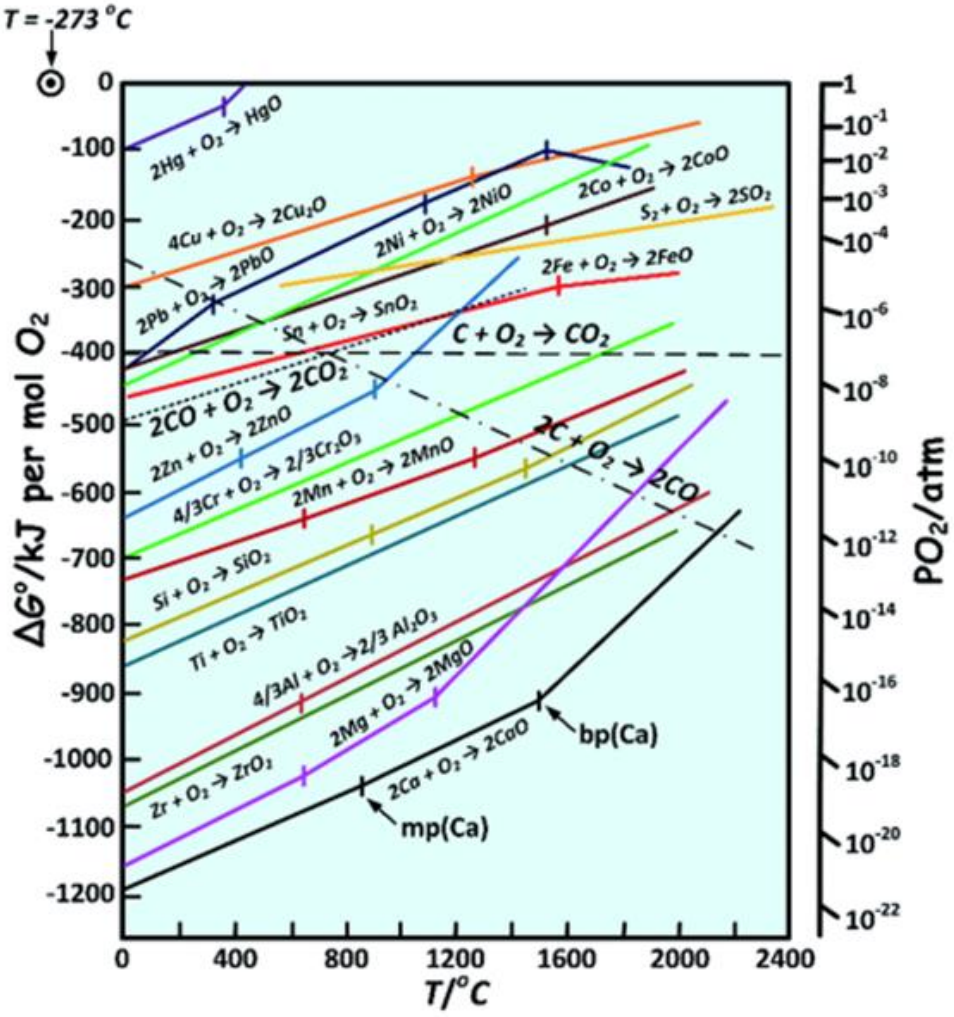

Figure 20: Ellingham diagram for oxides, from [130].

3.2.3 Thermodynamic properties

In electrochemistry, a Pourbaix diagram, also known as a potential/pH diagram, allows to determine for a given element, stable/predominant phases as a function of potential and pH. These diagrams are commonly used to predict corrosion of pure metals in an aqueous environment by superposing metal elements' diagrams with water diagram. Other diagrams can be used for other electrolytes e.g nitrogen for nitric acid medium. However, these diagrams are purely based on thermodynamic data and do not provide any information on the reaction kinetics. As illustrated in Figure 21, neither Ti nor Zr are thermodynamically stable in water [131], as their domain of stability lie well below that of water. However, both elements exhibit passivation behavior at ambient temperature and usual pH conditions, due to the formation of passive oxide layer. This stable covering oxide protects the metal from further deterioration. Zr covers itself with a passive film of ZrO_2 while TiO_2 is formed on Ti.

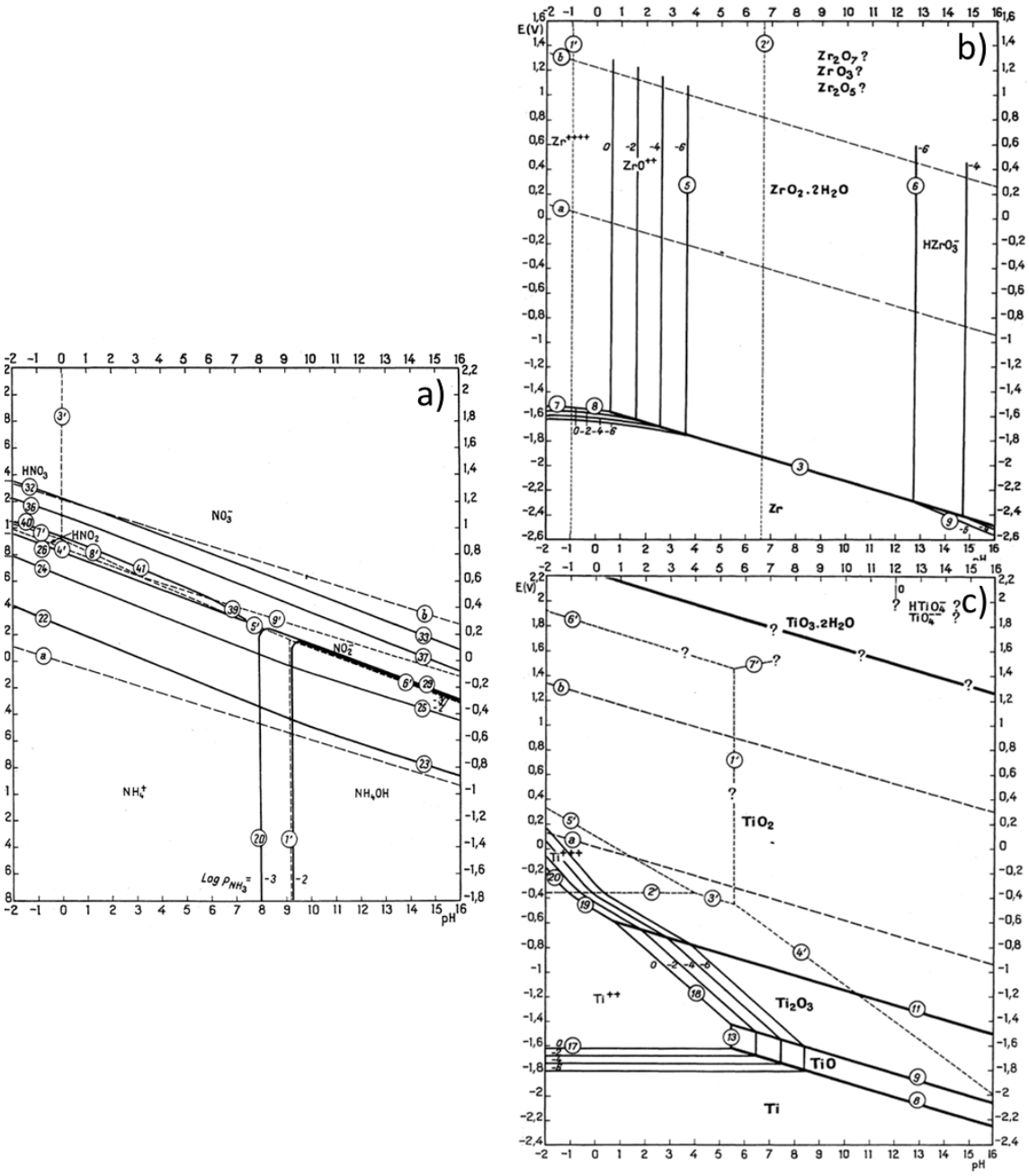

Figure 21: Pourbaix diagrams of a) N, b) Zr and c) Ti in H_2O at 25 °C, from [131].

The Pourbaix diagram of nitrogen (N) is presented to show the predominance domain of nitric acid: E > 0.9 V and pH < 0 (Figure 21a). Under these conditions, Zr^{4+} should be observed as Zr shows domain of corrosion (Figure 21b). However, the experimental data contradict this due to the significant stability of ZrO_2, which has low dissolution kinetics. It is well known that Zr is particularly resistant to many acids, in particular sulphuric acid, hydrochloric acid, phosphoric acid and nitric acid at various concentrations (up to 14.5 N), even in presence of Cr^{6+} [132]. In comparison, Zr should be corrosion resistant in seawater (pH ≈ 8) due to the formation of ZrO_2 layer. Ti is resistant to corrosion in the presence of any non-complexing solutions due to passivation of the metal for all pH (Figure 21c), with the exception of very oxidizing

solutions such as hydrogen peroxide solutions. Note that hydrofluoric acid attacks the metal even for low concentration.

Another material of interest to increase corrosion resistance in nuclear spent fuel reprocessing environment is tantalum (Ta). Ta tends to cover itself with a layer of oxide for all pH [133] (Figure 22). Notably, the position of the domain of stability of tantalum pentoxide shows that it is thermodynamically stable in the presence of acid, neutral and alkaline non-complexing solutions.

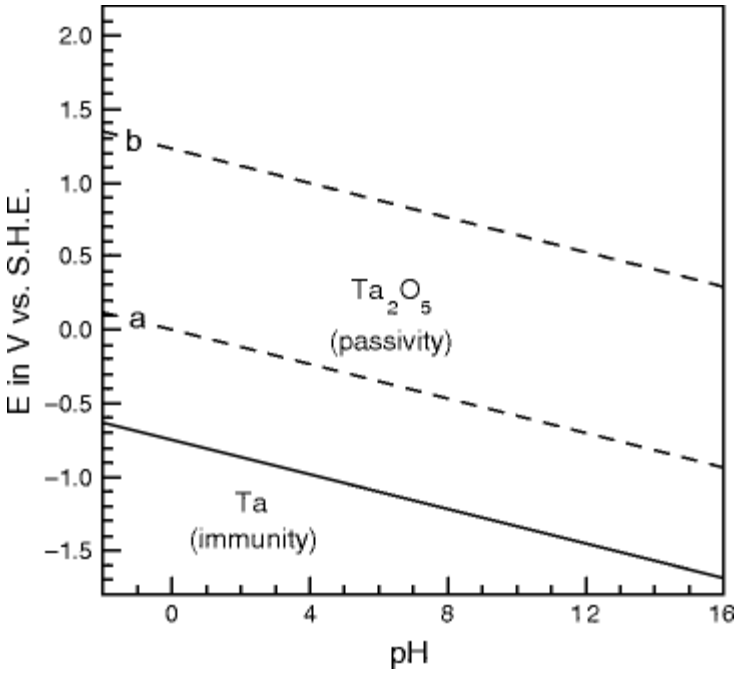

Figure 22: Pourbaix diagram for the system tantalum-water, at 25°C, from [133].

3.3 DEPOSITION BY REACTIVE HIPIMS

3.3.1 Principle of reactive sputtering

Reactive sputtering processes consist of adding a reactive gas (O_2, N_2, *etc*.) in the vacuum chamber to synthesize compound coatings [134-137]. This technique allows the deposition of protective coatings of metal oxides or nitrides for example [134]. In reactive sputtering, the target surface is partially poisoned [137], leading to the formation of a compound layer on the target which is then effectively removed by the bombarding Ar ions. [134-137]. The compound layer is sputtered and condenses on the substrate surface to form the compound coating [135, 136]. However, if the compound layer formation rate exceeds the sputtering rate, the target is referred to as poisoned. In this case, formation of a compound on target surface may result in positive charge accumulation due to the impact of ions, especially when the formed compounds are dielectric, which implies that the deposition process becomes unstable. This may give rise to arcing and the subsequent formation of droplets. In general, systematic study of the influence of the partial pressure of reactive gas shows that a hysteresis loop appears for several parameters (total pressure, target voltage and optical emission) as a function of increase/decrease in gas flow (Figure 23).

This curve displays three distinct zones: metallic mode, transition mode or hysteresis zone and compound mode. The metallic mode is associated to an insufficient quantity of reactive gas to form a compound material whereas the compound mode corresponds to the complete poisoning of the target. The hysteresis is due to a complex relationship between process parameters and reactive gas flow rate. It can be defined as an unstable transition zone where increase and decrease in the pressure does not occur at the same value of the reactive gas flow as shown in Figure 23 [134, 136]. The hysteresis effect is a real issue in reactive processes [137] because it complicates the formation of stoichiometric compound thin films (oxides, nitrides or carbides) [138].

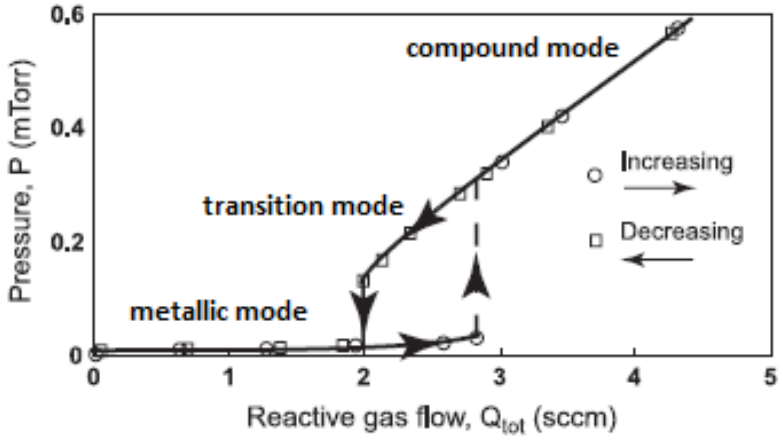

Figure 23: Typical hysteresis curve for a reactive sputtering process, modified from [139]

The pulsed magnetron sputtering (PMS) process, in particular pulsed DCMS, has been first introduced to improve reactive sputtering process [2, 4, 8, 140]. By pulsing the magnetron discharge at medium frequency range (20-350 kHz), arcing phenomena are eliminated and the reactive process is stabilized [2, 4, 9, 140]. It has been found that applying pulses at frequencies below 20 kHz does not suppress the arcing phenomenon [2]. During the pulsed DCMS process, the target voltage is switched on during a fixed “pulse-on time”. This results in ignition of the plasma discharge leading to the target sputtering. Then, the target voltage is switched off (“pulse-off time”) to decay the plasma discharge. This phenomenon is repeated in a cyclical manner throughout the deposition duration to limit target poisoning that occurs usually during the reactive sputtering process. [2, 140]. This new process leads to the deposition of insulating materials such as oxides on the substrate. The formation of high quality coatings with fewer defects due to hotter and more energetic plasmas compared to conventional DCMS are observed [1, 4, 9]. In addition, deposition rates are improved and approach those obtained for the synthesis of metallic coatings (µm/h) [2, 4, 9].

In some applications, sometimes DCMS and PMS techniques do not provide sufficient energy input to obtain a compact structure of thick oxide coatings (> 1µm), hence the interest in creating metallic ions to bombard the film during its growth, as in HiPIMS technique. Regarding reactive HiPIMS (R-HiPIMS), some authors claim that the use of HiPIMS discharges reduces, shifts, or even suppresses the hysteresis phenomenon while others explain that hysteresis actually becomes more important [93, 136-137,

139]. The main parameters influencing the hysteresis effect are related to the HiPIMS parameters (peak current, frequency, *etc*.) [134, 137, 139] and the pumping system [138, 139]. In the industrial process, a feedback-controlled technique of the reactive gas is commonly used to reduce target poisoning and limit hysteresis phenomenon. For instance, plasma emission monitoring (PEM) method allows regulating the reactive gas flow using the optical emission of the plasma [141, 142].

3.3.2 Parameters influencing the deposition of oxide coatings by R-HiPIMS

The final properties of oxide coatings deposited by R-HiPIMS depend on the process parameters, which can modify the crystal phases obtained, the microstructure, *etc*. The studies performed on ZrO_2 and TiO_2 coatings show essentially the influence of oxygen flow rate [143, 144], pulsed-off time [145], peak current [146] and deposition angle [147]. The focus is first placed on the effect of pulse-off time on ZrO_2 coatings deposited on glass and ITO (indium-thin-oxide)/glass substrates. Figure 24 shows the differences in surface roughness observed by atomic force microscopy (AFM) for various pulse-off times. The smoothest film is obtained for the longest off time *i.e.* 2500 µs, likely due to an increase of the target power density from 1.1 to 1.8 kW/cm² [145]. As the surface roughness is related to the coating microstructure, this tends to indicate that for long pulse-off times the columnar structure is decreased due to the ion bombardment. This has an effect on the global properties of coatings as the lowest leakage current density (electrical property) is obtained for ZrO_2 coating synthesized with the longest pulse-off time.

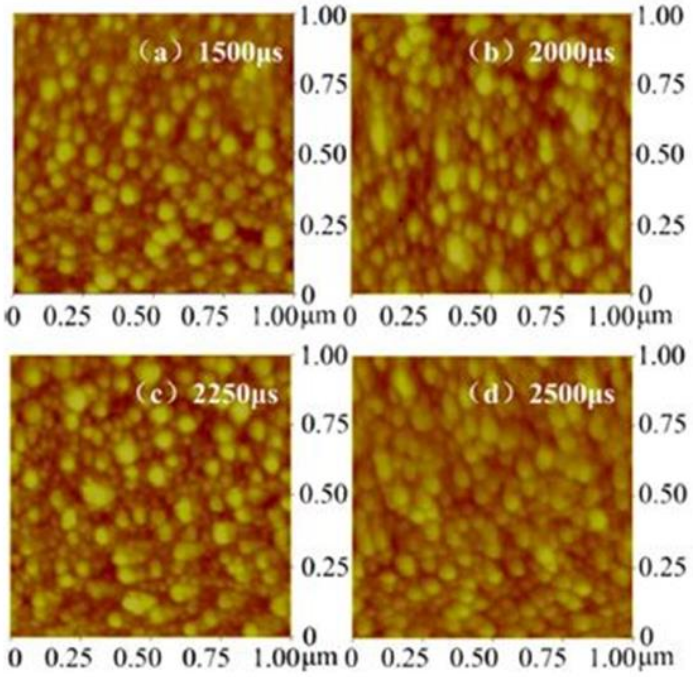

Figure 24: AFM images of ZrO_2 films prepared with various pulse-off time of a) 1500 µs, b) 2000 µs, c) 2250 µs and 2500 µs from [145].

The effect of the peak current is studied on TiO_2 coatings deposited on silicon wafers. For this purpose, two peak currents are used: 26 A and 70 A. The results indicate that

the surface roughness is lower when the peak current is higher, showing that more intense and energetic ion bombardment lead to a decrease of surface roughness [146]. This may be correlated to the reduction of the columnar structure and the achievement of more compact coatings due to higher adatom mobility. This leads to improved TiO_2 coating properties such a refractive index and density.

3.4 CORROSION RESISTANCE PROPERTIES

3.4.1 TiO_2 coatings

The anticorrosion properties of TiO_2 results mainly from the formation of a protective (passive) barrier against the diffusion of reactants and species [148-152]. The TiO_2 thin film has a high electrochemical stability, a high durability [150] and insulating properties [151]. The improved corrosion resistance achieved by TiO_2 thin films synthesized by atomic layer deposition (ALD) is illustrated by comparing electrochemical measurements of initial and Ti-coated coupons of stainless steel in 3% NaCl aqueous solution (Figure 25). The presence of a TiO_2 thin film of 50 nm thickness shifts the corrosion potential to positive values (from – 0.96 V/SCE to – 0.63 V/SCE) and decreases the corrosion current density from 7.0×10^{-7} A/cm² to 6.3×10^{-8} A/cm² [149].

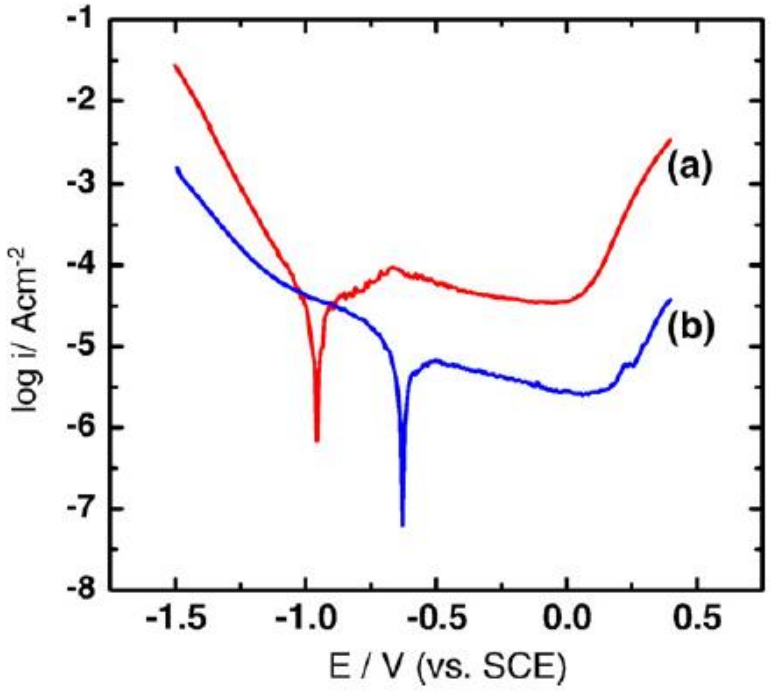

Figure 25: Polarization curves of (a) stainless steel and (b) 50 nm TiO_2 coated stainless steel in 3% NaCl aqueous solution at room temperature (SCE electrode), from [149].

Similar behaviors are observed for thicker films (620 nm in [99]), in other electrolytes such as 3.5% NaCl [150], concentrated HNO_3 [151], 25% HCl [152] and 50% H_2SO_4 [152] and for other substrates [153]. For instance, TiO_2 coating deposited on 304L ASS by reactive MS shows higher E_{corr} (550 mV *vs.* Ag/AgCl) and lower J_{corr} (4×10^1 µA/cm²) values than initial 304L ASS (E_{corr} = 340 mV *vs.* Ag/AgCl and $J_{corr} = 7 \times 10^1$

µA/cm²) in 8 mol/L nitric acid solution at room temperature (Figure 26a) [151]. The surface characterization using AFM shows the grain boundary structure of 304L ASS after electrochemical measurements due to intergranular corrosion in this environment (Figure 26b), whereas the surface of TiO_2 coated sample remains intact, indicating a higher resistance to surface dissolution (Figure 26c).

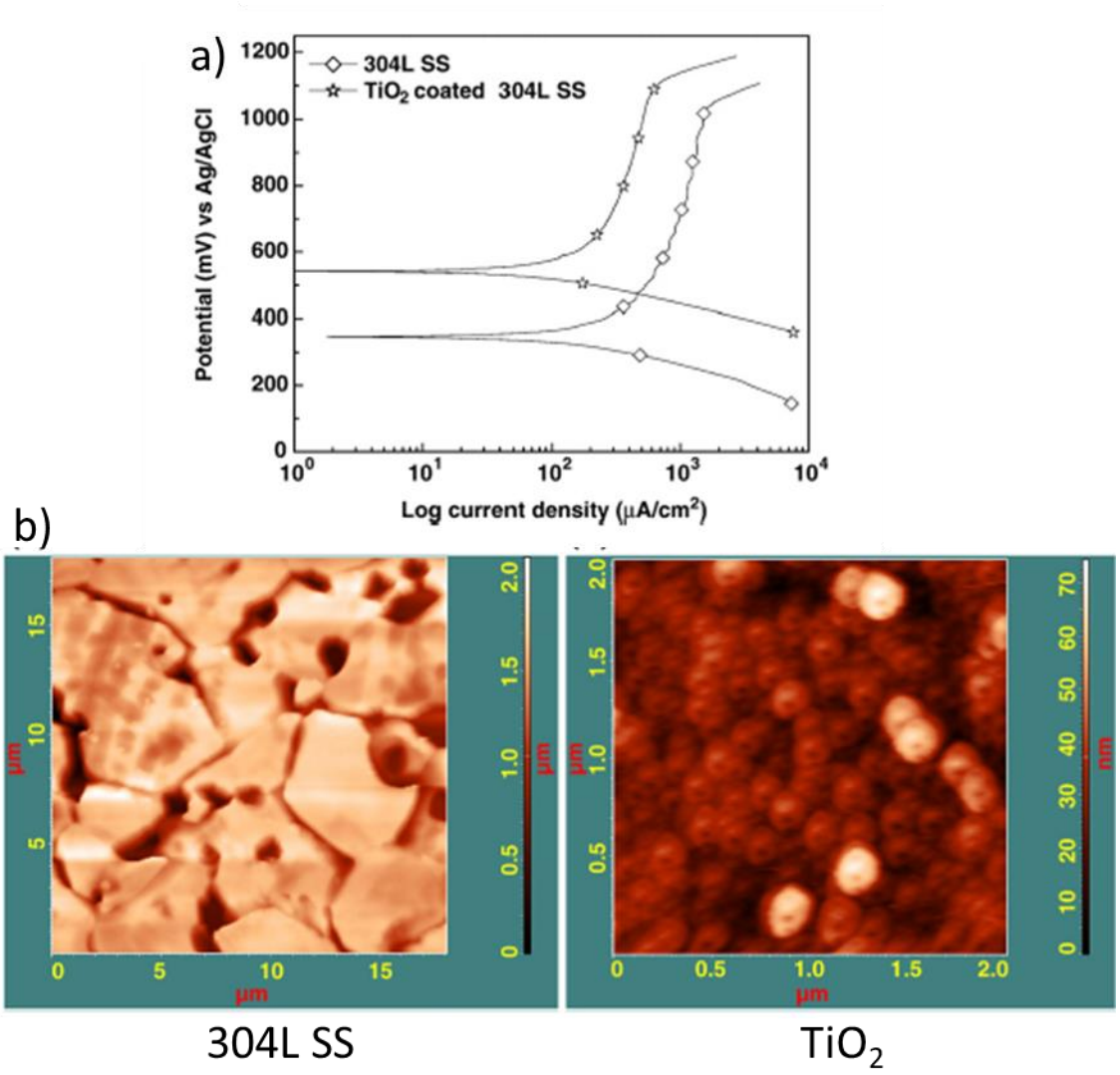

Figure 26: a) Potentiodynamic polarization curves for initial and TiO_2 coated 304L SS in 8 mol/L HNO_3 at room temperature (Ag/AgCl electrode) and b) AFM surface morphology after potentiodynamic polarization, from [151].

Moreover, TiO_2-based multilayer coatings can be synthetized for enhancing corrosion protection properties. For instance, Al_2O_3/TiO_2 multilayer coating deposited by ALD [153] and sol-gel dip-coated ZnO/TiO_2 multilayer thin films [154] improve the corrosion resistance of SS in NaCl solution. The 100 nm-thick Al_2O_3/TiO_2 multilayer coatings are more effective for corrosion protection in 9 g/L NaCl solution than TiO_2 monolayer (10^{-7} A/cm²) by decreasing the corrosion current density down to 10^{-10} A/cm², as the multilayer configuration increases the resistance to delamination by multiplying the interfaces [153].

In addition, photocatalysis and photo-induced superhydrophilicity can take place simultaneously on the TiO_2 surface and their effects combine for some applications such as self-cleaning properties of a surface [155]. TiO_2 show photocatalytic properties that can be used to protect marine structures against the formation of biofilms by applying a TiO_2 thin film [156, 157]. For instance, for a 500 nm coating of TiO_2, after six months immersed in marine natural ambient, biofouling is not observed on the surface while corrosion is present. In contrast, a thick crust develop on the face coated only with plastic paint (Figure 27) [158]. However, these photocatalytic properties cannot remove a preexisting biofilm [157], explaining why antifouling properties based on the combination of photocatalytic and superhydrophilicity are hardly studied [158, 159].

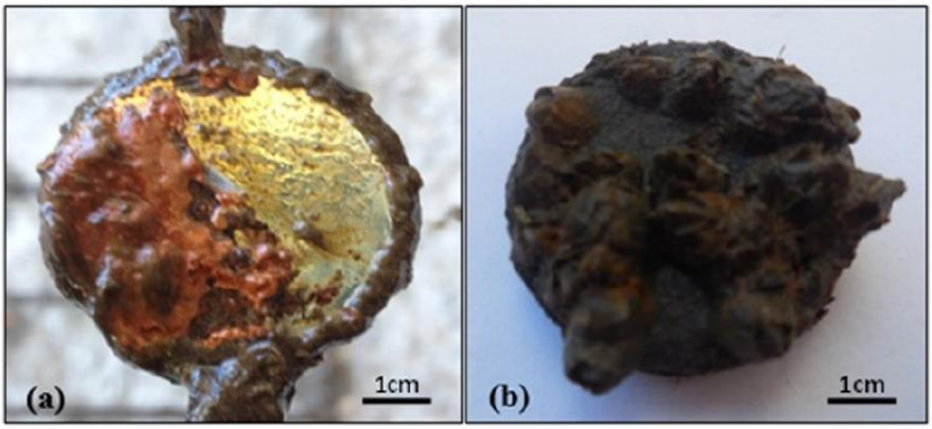

Figure 27: a) Face coated with TiO_2 and b) face coated with plastic paint after 6 months of immersion in marine natural ambient, from [158].

3.4.2 ZrO_2 coatings

ZrO_2 thin films are used as corrosion protective barriers for various metals such as ASS, brass and magnesium [160-165]. This is mainly because of its thermal expansion coefficient, which is close to that of metals [160, 162], its chemical inertness [160, 162, 163, 165] and its high corrosion resistance [160-165]. The improved corrosion resistance of stainless steel coated by ZrO_2 [161] prepared by sol-gel method has been investigated in a highly concentrated nitric acid solution (Figure 28a). The presence of the coating decreases the corrosion current density by one order of magnitude (9.9×10^0 µA/cm² compared to 2.1×10^2 µA/cm² for 316L SS) and shifts the corrosion potential to positive values (63 mV *vs.* Ag/AgCl compared to – 81 mV *vs.* Ag/AgCl for 316L SS). After electrochemical measurements, the SEM micrographs of the 316L SS surface shows severe intergranular corrosion (Figure 28) due to high oxidizing power of HNO_3, while the ZrO_2 coating indicates a good corrosion resistance (no intergranular corrosion observed).

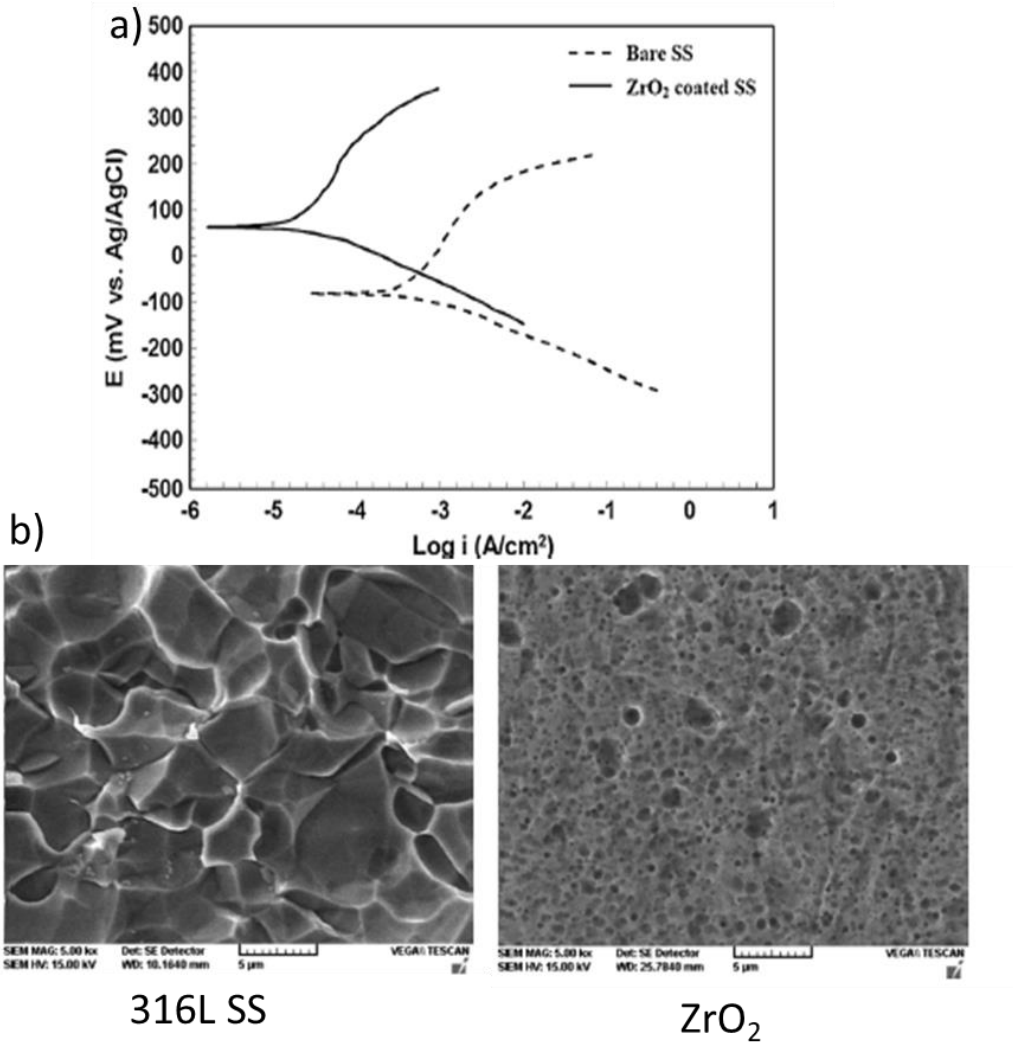

Figure 28: a) Potentiodynamic polarization curves of initial and ZrO_2-coated 316L SS in 10 mol/L HNO_3 at room temperature (Ag/AgCl electrode) and b) SEM micrographs of the surface after electrochemical measurements, from [161]

The efficiency of ZrO_2 coatings for protection against corrosion is also observed in different environments such as sulfuric acid [160], borate buffer [161], NaCl [163, 164] and artificial saliva [165] solutions. For instance, a 150 nm-thick ZrO_2 coating deposited on pure magnesium (Mg) disk using reactive pulsed-DCMS shows a higher E_{corr} (- 1.32 V *vs.* Ag/AgCl) and lower J_{corr} (27.79 µA/cm²) than bulk Mg (- 1.41 V *vs.* Ag/AgCl and 51.93 µA/cm²) after 30 min of immersion in 0.9 wt.% NaCl solution. However, this protection is not perfect as some corrosion pits appeared on the ZrO_2 coating after immersion in a saline solution [164]. On the other hand, a 10 nm ZrO_2 thin film seems to be thick enough to improve significantly the corrosion resistance of a brass substrate in a solution of borate buffer and NaCl [162]. This coating is very thin compared to the thicknesses usually used for corrosion protection by standard PVD techniques. In addition, ZrO_2-based multilayer coatings show good corrosion resistance in 3.5 wt.% NaCl solution [73, 166]. For instance, ZrN/ZrO_2 multilayer coating (9 layers) deposited by multi-arc ion plating on 304 ASS enhances corrosion protection (J_{corr} = 1.7 × 10^{-8} A/cm² for multilayer and 3.2 × 10^{-7} A/cm² for 304L SS) by

combining the properties of ZrN and ZrO_2. The multilayer architecture with similar thicknesses for each sublayer reduces the coating stresses. Moreover, the interfaces formed can stop crack propagation paths and prevent electrolyte from reaching the substrate [73].

3.5 CONCLUSIONS

TiO_2 and ZrO_2 are polymorphs and both crystallize in different crystal structures. The crystalline phases of interest in this work are rutile and anatase for TiO_2 and monoclinic for ZrO_2. In addition, the ability of Ti and Zr to form stable TiO_2 and ZrO_2 is illustrated using Ellingham and Pourbaix diagrams as well as the behavior of Ta to passivate. The reactive deposition techniques for these coatings are discussed. Reactive sputtering processes consist of adding a reactive gas in the vacuum chamber to synthesize compound coatings such as oxide or nitride coatings. Reactive HiPIMS can be used to obtain dense oxide coatings structure. Moreover, a feedback-controlled technique of the reactive gas is generally used to control the deposition process and optimize the deposition rate and coating properties. The influence of some process parameters such as oxygen flow rate, pulsed-off time and peak current on the properties of the synthesized coatings are presented to show that optimization of substrate/coating system is possible. For instance, the surface roughness is lower when the peak current is higher, which can lead to a decrease of the columnar structure and the achievement of more compact oxide coatings.

Then, the interest is focused on the corrosion resistance properties of samples coated by TiO_2. A 50 nm-thick TiO_2 coating deposited by ALD shows a shift of E_{corr} towards positive values (from – 0.96 V/SCE to – 0.63 V/SCE) and a decrease of J_{corr} from 7.0×10^{-7} A/cm² to 6.3×10^{-8} A/cm² in a 3% NaCl solution at room temperature. A protecting effect is also observed in 8 mol/L nitric acid solution at room temperature for TiO_2 coating deposited by reactive MS (E_{corr} = 550 mV *vs.* Ag/AgCl and $J_{corr} = 4 \times 10^{1}$ µA/cm²) leading to no intergranular corrosion compared to initial 304L ASS. Moreover, an enhancement of corrosion resistance in 9 g/L NaCl solution at room temperature is achieved using a 100 nm-thick Al_2O_3/TiO_2 multilayer coatings by decreasing the corrosion current density by three orders of magnitude (down to 10^{-10} A/cm²).

ZrO_2 coatings show good protection against corrosion in nitric acid and NaCl solutions. For instance, a sol-gel ZrO_2 coating improves corrosion resistance in 10 mol/L HNO_3 at room temperature by preventing intergranular corrosion. The coating decreases the corrosion current density by one order of magnitude (9.9×10^{0} µA/cm² compared to 2.1×10^{2} µA/cm² for 316L SS) and shifts the corrosion potential to positive values (63 mV vs. Ag/AgCl compared to – 81 mV vs. Ag/AgCl for 316L SS). A similar effect is observed in 0.9 wt.% NaCl solution for a ZrO_2 coating deposited by reactive pulsed-DCMS technique (E_{corr} = - 1.32 V *vs.* Ag/AgCl and J_{corr} = 27.79 µA/cm²). In addition, ZrN/ZrO_2 multilayer coating deposited by multi-arc ion plating show good corrosion resistance in 3.5 wt.% NaCl solution by reducing J_{corr} from 3.2×10^{-7} A/cm² for 304L SS to 1.7×10^{-8} A/cm² for multilayer coating.

The ability of TiO_2 and ZrO_2 to protect components in several environments has been proven as both monolayer and multilayer (ceramic/ceramic) coatings. However, no

studies on the use of these coatings as metal/oxide multilayers for corrosion protection have been reported in the literature. In addition, the antifouling properties of TiO_2 coatings have been investigated but not yet for ZrO_2 although they may be useful for the study of these coatings in marine environment.

4. CONCLUSIONS

The scientific approach of this work aims to understand the phenomena taking place at the substrate/coating system interfaces in order to optimize the corrosion resistance properties of this system. To this end, the knowledge on the interfaces formed by PVD has been presented. The interfaces depend on the deposition process that provides a different energy of the vapor particles. The higher the energy of the vapor particles, the stronger the interaction between the substrate and the coating, resulting in the formation of strong bonds at the interface. Therefore, the formation of strong bonds (metallic, ionic or covalent) is expected in HiPIMS. Usually, a combination of two types of interfaces *i.e.* mechanical and pseudodiffusion is observed, making their study more difficult. Moreover, their formation can influence the nucleation and the growth of coatings. Therefore, these interfaces must be clean and free of defects to ensure the formation of strong bonds between the substrate and the coating, leading to a good adhesion. A solution is proposed to eliminate contaminations and defects present on the substrate surface prior to the coating deposition: a substrate pre-treatment with ion (etching). It should be noted that in addition to cleaning the substrate surface, this etching should also lead to ion implantation to very low depths (1-5 nm) that modifies the crystal structure of the substrate. These modifications vary according to the type of ions used: Ar is incorporated as interstitials in the crystal lattice, whereas metal ions are incorporated as replacements (substitution of structural atom).

In order to improve the lifespan of infrastructures and tools in marine environment or in nuclear fuel reprocessing plants involving hot concentrated nitric acid, the relationship between corrosion resistance and substrate/coating system interfaces has been studied. Literature shows that the corrosion protection properties of the substrate/coating system depend on the interfaces, especially the substrate/coating interface. Corrosion can be initiated by species trapped or defects presents at this interface, which can lead to premature failure and thus complete delamination of the coating. This is consistent with previous findings indicating the need for cleaning of the substrate surface prior to coating deposition. However, the effect of etching on corrosion resistance of the substrate has not been studied yet. Moreover, the behavior of this interface can be improved by depositing a bond coat to enhance the adhesion strength of the coatings, which affects the final properties of the coated component. This layer reduces the stresses usually observed at the interface between a metal substrate and a coating made of a different material. Finally, a last approach is the use of multilayer coatings to increase the number of interfaces separating the substrate from the surrounding environment. This decreases the electrolyte infiltration and is supposed to prevent it from reaching the substrate due to a barrier effect of the interfaces.

In this work, two aggressive environments are chosen to study the behavior of our systems before and after exposure to them: nitric acid solution (2.5 mol/L HNO_3, 2.5

mol/L $NaNO_3$ and 2 g/L $Fe(NO_3)_3$) at boiling temperature (110 °C) and 3.56 wt.% NaCl solution at ambient temperature. The aim is to understand how the interfaces are formed and how they can be improved. First, the effects of the HiPIMS ion etching pre-treatment step on the properties of the modified substrate surface are studied. Note that the scales considered are very fine (a few nanometers), which can make the characterizations difficult. Then, a metallic interlayer (Ti or Zr) is first deposited in order to form a substrate/bond coat system and to understand the substrate/bond coat interface in detail. After the detailed study of this interface, the substrate/coating system is modified to become more complex by depositing a thick oxide coating (TiO_2 and ZrO_2) and/or synthesizing multilayer metal/oxide coating. In this final step, the behavior of a complete system is studied but due to lack of time its optimization has not been performed. For instance, the influence of the type of etching *i.e.* inert gas or metal ion on this system could not be studied.

It should be noted that during the first year of this PhD work, aiming at studying the influence of ion etching pre-treatment on the substrate/coating interface, the presence of substrate elements (Cr and Fe mainly) contamination was observed at the interface due to resputtering of the substrate-holder and deposition chamber walls. Therefore, all the characterizations performed during this first year (microstructural observations, electrochemical measurements, immersion tests in CEA and NTU) were performed on these contaminated samples. These results are presented in Appendix 1 and mentioned at the beginning of the chapter “Surface modification and interface engineering by HiPIMS pre-treatment”.

REFERENCES

[1] Swann S. (1988) “Magnetron sputtering.” Physics in Technology 19: 67-75.

[2] Kelly P. J. & Arnell R. D. (2000) “Magnetron sputtering: a review of recent developments and applications.” Vacuum 56: 159-172.

[3] Baptista A., Silva F., Porteiro J., Miguez J. & Pinto G. (2018) “Sputtering physical vapour deposition (PVD) coatings: a critical review on process improvement and market trend demands.” Coatings 8: 402.

[4] Constantin D. G., Apreutesei M., Arvinte R., Marin A., Andrei O. C. & Munteanu D. (2011) “Magnetron sputtering technique used for coatings deposition; technologies and applications.” RECENT 12: 29-33.

[5] Böhlmark J. (2016) “Fundamentals of high power impulse magnetron sputtering.” Linköping studies in science and technology dissertation no. 1014, ISBN: 91-85523-96-8, ISSN: 0345-7524.

[6] Helmersson U., Lattemann M., Böhlmark J., Ehiasarian A. P. & Gudmundsson J. T. (2006) “Ionized physical vapor deposition (IPVD): a review of technology and applications.” Thin Solid Films 513: 1-24.

[7] Pulker H.K. & Perry A.J. (1981) “Adhesion.” Surface Technology 14: 25-39.

[8] Ratova M., Klaysri R., Praserthdam P. & Kelly P. J. (2017) “Pulsed DC magnetron sputtering deposition of crystalline photocatalytic titania coatings at elevated process pressures.” Materials science in semiconductor processing 71: 188-196.

[9] Vlcek J., Pajdarova A. D. & Musil J. (2004) “Pulsed dc magnetron discharges and their utilization in plasma surface engineering.” Contributions to Plasma Physics 44: 426-436.

[10] Böhlmark J. (2006) “Chapter 7: HiPIMS. Fundamentals of High Power Impulse Magnetron Sputtering”, PhD thesis, Linköping University, ISBN: 91-85523-96-8.

[11] Alami J., Bolz S. & Sarakinos K. (2009) “High power pulsed magnetron sputtering: Fundamentals and applications.” Journal of Alloys and Compounds 483: 530-534.

[12] Sarakinos K., Alami J. & Konstantinidis S. (2010) “High power pulsed magnetron sputtering: A review on scientific and engineering state of the art.” Surface and Coatings Technology 204: 1661-1684.

[13] Moll E. (1992) “Physical Vapor Deposition Techniques II: Ion plating, Arc deposition and Ion beam deposition.” Advanced Techniques for Surface Engineering, Edited by Gissler W. & Jehn H.A., Kluwer Academic Publishers, ISBN: 978-94-017-0631-5.

[14] Ehiasarian A.P. (2010) “High-power impulse magnetron sputtering and its applications.” Pure and Applied Chemistry 82: 1247-1258.

[15] Wang T.-G., Dong Y., Gebrekidan B. A., Liu Y.-M., Fan Q.-X. & Kim K. H. (2017) “Microstructure and properties of the Cr-Si-N coatings deposited by combining high-power impulse magnetron sputtering (HiPIMS) and pulsed DC magnetron sputtering.” Acta Metallurgica Sinica 30: 688-696.

[16] Luo Q., Yang S. & Cooke K. E. (2013) “Hybrid HiPIMS and DC magnetron sputtering deposition of TiN coatings: deposition rate, structure and tribological properties.” Surface and Coatings Technology 235: 13-21.

[17] Fager H., Tengstand O., Lu J., Bolz S., Mesic B., Kölker W., Schiffers Ch., Lemmer O., Greene J. E., Hultman L., PEtrov I. & Greczynski G. (2017) “Low-temperature growth of dense and hard $Ti_{0.41}Al_{0.51}Ta_{0.08}N$ films via hybrid HiPIMS/DC magnetron co-sputtering with synchronized metal-ion irradiation.” Journal of Applied Physics 121: 171902.

[18] Arab Pour Yazdi M, Lomello F., Wang J., Sanchette F., Dong Z., White T., Wouters Y., Schuster F. & Billard A. (2014) “Properties of TiSiN coatings deposited by hybrid HiPIMS and pulsed-DC magnetron co-sputtering.” Vacuum 109: 43-51.

[19] Mattox D.M. (2016) “A Short History: Adhesion, Interface Formation, and Stress in PVD Coatings.” Society of Vacuum Coaters, Bulletin, 32-37.

[20] Mattox D.M. (2010) “Chapter 10: Atomistic growth and some growth-related film properties.” Handbook of Physical Vapor Deposition (PVD) Processing, second edition (pp 333-398), William Andrew Publishing, ISBN: 978-0-8155-2037-5.

[21] Mattox D.M. (1965) “Interface Formation and the Adhesion of Deposited Thin Films.” Sandia Corporation monograph, Sandia Laboratories Report SC-R-65-852.

[22] Mattox D.M. (2010) “Chapter 12: Adhesion and Deadhesion.” Handbook of Physical Vapor Deposition (PVD) Processing, second edition (pp 439-474), William Andrew Publishing, ISBN: 978-0-8155-2037-5.

[23] Lufitha M. (2001) “Effect of Substrate Temperature on Coating Adhesion.” Master thesis, Department of mechanical and industrial engineering of the University of Toronto.

[24] Pang X., Gao K, Yang H., Qiao L. Wang Y. & Volinsky A.A. (2007) “Interfacial Microstructure of Chromium Oxide Coatings.” Advanced Engineering Materials 9: 594-599.

[25] Kosza G., Rausch H. & Kormany T. (1972) “The influence of the substrate on interface properties of homoepitaxial silicon layers.” Thin Solid Films 12: 99-103.

[26] Komolov S.A. & Aliaev Y.G. (2007) “Influence of the Substrate Properties on the Electronic Structure of Organic Film-Inorganic Substrate Interfaces.” Technical Physics 52: 1163-1168.

[27] Ehiasarian A.P., Wen J.G. & Petrov I. (2007) “Interface microstructure engineering by high power impulse magnetron sputtering for the enhancement of adhesion.” Journal of Applied Physics 101, 054301.

[28] Ensinger W. (1997) “Low energy ion assist during deposition – an effective tool for controlling thin film microstructure.” Nuclear Instruments and Methods in Physics Research B 127/127: 796-808.

[29] Movchan B. A. & Demchishin A. V. (1969) “Study of structure and properties of thick vacuum condensates of nickel, titanium, tungsten, aluminium oxide and zirconium dioxide.” Physics of Metals and Metallography-Ussr 28, 83.

[30] Thornton J. A. (1974) “Influence of apparatus geometry and deposition conditions on the structure and topography of thick sputtered coatings.” Journal of Vacuum Science and Technology 11: 666-670.

[31] Anders A. (2010) “Deposition rates of high power impulse magnetron sputtering: Physics and economics.” Journal of Vacuum Science & Technology A: Vacuum, Surfaces, and Films 28: 783-790.

[32] Mattox D.M. (2000) “Ion plating – past, present and future.” Surface and Coatings Technology 133-134: 517-521.

[33] Santiago J.A., Fernandez-Martinez I., Wennberg A., Molina-Aldareguia J.M., Castillo-Rodriguez M., Rojas T.C., Sanchez-Lopez J.C., Gonzalez M.U., Garcia-Martin J.M., Li H., Bellido-Gonzalez V., Monclus M.A. & Gonzalez-Arrabal R. (2018) “Adhesion enhancement of DLC hard coatings by HiPIMS metal ion etching.” Surface and Coatings Technology 349: 787-796.

[34] Bakoglidis K.D., Schmidt S., Greczynski G. & Hultman L. (2016) “Improved adhesion of carbon nitride coatings on steel substrates using metal HiPIMS pretreatments.” Surface and Coatings Technology 302: 454-462.

[35] Ehiasarian A.P., Anders A. & Petrov I. (2007) “Combined filtered cathodic arc etching pretreatment-magnetron sputter deposition of highly adherent CrN films.” Journal of Vacuum Science and Technology A 25: 543-550.

[36] Lattemann M., Ehiasarian A.P., Bohlmark J., Persson P.A.O. & Helmersson U. (2006) “Investigation of high power impulse magnetron sputtering pretreated interfaces for adhesion enhancement of hard coatings on steel.” Surface and Coatings Technology 200: 6495-6499.

[37] Peng D. Q., Bai X. D., Pan F., Sun H. & Chen B. S. (2006) “Influence of titanium ions implantation on corrosion behavior of zirconium in 1 M H_2SO_4.” Applied Surface Science 252: 2196-2203.

[38] Smidt F. A. (1985) “Recent advances in the application of ion implantation to corrosion and wear protection.” Nuclear Instruments and Methods in Physics Research B10/11: 532-538.

[39] Granata R. D., De Crosta M. A., McIntyre J. F. & Leidheiser H. Jr. (1987) “Corrosion-resistant surfaces on ion-implanted iron and steel.” Industrial & Engineering Chemistry Research 26: 427-433.

[40] Ensinger W. & Wolf G. K. (1994) “Electrochemical and corrosion protection properties of ion implanted thin films.” Electrochimica Acta 39: 1159-1164.

[41] He J., Bai X., Ma C. & Chen H. (1995) “The effect of ion implantation of Ar on the aqueous corrosion resistance of Zr-4 alloy.” Nuclear Instruments and Methods in Physics Research B 100: 59-64.

[42] Leroy L., Girault P., Grosseau-Poussard J. L. & Dinhut J. F. (2002) “Ion implantation reinforcement of the protective efficiency of nickel in artificial sea-water.” Nuclear Instruments and Methods in Physics Research B 198: 49-56.

[43] Vigen Karimi M., Sinha S. K., Kothari D. C., Khanna A. K. & Tyagi A. K. (2002) “Effect of ion implantation on corrosion resistance and high temperature oxidation resistance of Ti deposited 316 stainless steel.” Surface and Coatings Technology 158-159: 609-614.

[44] Chang Y.-Y. & Wang D.-Y. (2005) “Corrosion behavior of electroless nickel-coated AISI 304 stainless steel enhanced by titanium ion implantation.” Surface and Coatings Technology 200: 2187-2191.

[45] Martinez L., Gomez C. & Perez F. J. (2005) “Sinergistic effect of ion implantation as a surface modification technique to improve localized corrosion of AISI 304 austenitic stainless steel.” Surface and Coatings Technology 195: 70-80.

[46] Cano E., Martinez L., Simancas J., Perez-Trujillo F. J., Gomez C. & Bastidas J. M. (2006) “Influence of N, Ar and Si ion implantation on the passive layer and corrosion behaviour of AISI 304 and 403 stainless steels." Surface and Coatings Technology 200: 5123-5131.

[47] Liu C., Xin Y., Tian X., Zhao J. & Chu P. K. (2007) “Corrosion resistance of titanium ion implanted AZ91 magnesium alloy.” Journal of Vacuum Science & Technology A 25: 334-339.

[48] Jamesh M., Wu G., Zhao Y. & Chu P. K. (2013) “Effects of silicon plasma ion implantation on electrochemical corrosion behavior of biodegradable Mg-Y-RE alloy.” Corrosion Science 69: 158-163.

[49] Hartwig A., Decker M., Klein O. & Karl H. (2015) “Stoichiometric titanium dioxide ion implantation in AISI 304 stainless steel for corrosion protection.” Nuclear Instruments and Methods in Physics Research B 365: 94-99.

[50] Cheng M., Qiao Y., Wang Q., Qin H., Zhang X. & Liu X. (2016) “Dual ions implantation of zirconium and nitrogen into magnesium alloys for enhanced corrosion resistance, antimicrobial activity and biocompatibility.” Colloids and Surfaces B: Biointerfaces 148: 200-210.

[51] Ryabchikov A. I., Kashkarov E. B., Pushilina N. S., Syrtanov M. S., Shevelev A. E., Korneva O. S., Sutygina A. N. & Lider A. M. (2018) “High-intensity low energy titanium ion implantation into zirconium alloy.” Applied Surface Science 439: 106-112.

[52] Wu H., Xi K., Xiao S., Qasim A. M., Fu R. K. Y., Shi K., Ding K., Chen G., Wu G. & Chu P. K. (2020) “Formation of self-layered hydrothermal coating on magnesium aided by titanium ion implantation: Synergistic control of corrosion resistance and cytocompatibility.” Surface and Coatings Technology 401: 126251.

[53] Qiu Z., Wang F., Li Q., Zheng L., Zhang F. & Zhang H. (2020) “Corrosion and mechanical properties for Cr-coated CSS-42L bearing steel after Ti and C ions co-implantation.” Applied Surface Science 509: 145293.

[54] Bull S.J. (1992) “Techniques for improving thin film adhesion.” Vacuum 43: 517-520.

[55] Vassallo E., Caniello R., Cremona A., Dellasega D. & Miorin E. (2013) “Titanium interlayer to improve the adhesion of multilayer amorphous boron carbide coating on silicon substrate.” Applied Surface Science 266: 170-175.

[56] Pischow K.A., Eriksson L., Harju E., Korhonen A.S. & Ristolainen E.O. (1993) “The influence of titanium interlayers on the adhesion of PVD TiN coatings on oxidized stainless steel substrates.” Surface and Coatings Technology 58: 163-172.

[57] Padhy N., Kamachi Mudali U., Chawla V., Chandra R. & Raj B. (2011) “Corrosion behavior of single (Ti) and duplex (Ti-TiO_2) coating on 304L stainless steel in nitric acid medium.“ Materials Chemistry and Physics 130: 962-972.

[58] Shanaghi A., Ghasemi S., Chu P. K., Ahangarani S. & Zhao Y. (2019) “Effect of Ti interlayer on corrosion behavior of nanostructured Ti/TiN multilayer coating deposited on TiAl6V4.” Materials and Corrosion 70: 2113-2127.

[59] Cheng Y. & Zheng Y. F. (2006) “A study of ZrN/Zr coatings deposited on NiTi alloy by PIIID technique.” IEEE Transactions on Plasma Science 34: 1105-1108.

[60] Huang. J.-H., Ouyang F.-Y. & Yu G.-P. (2007) « Effect of film thickness and Ti interlayer on the structure and properties of nanocrystalline TiN thin films on AISI D2 steel.” Surface and Coatings Technology 201: 7043-7053.

[61] Hays G.F. (2010) “Now is the Time.” Advanced Materials Research 95: 1-2.

[62] Boyd W.K. & Fink F.W. (1978) “Corrosion of Metals in Marine Environments.” Metals and Ceramics Information Center, Technical Report MCIC-78-37.

[63] Kazazi M., Haghighi M., Yarali D. & Zaynolabedini M.H. (2018) “Improving corrosion resistance of 316L austenitic stainless steel using ZrO_2 sol-gel coating in nitric acid solution.” Journal of Materials Engineering and Performance 27: 1093-1102.

[64] Reinhard C., Ehiasarian A.P. & Hovsepian P.Eh. (2007) “CrN/NbN superlattice structured coatings with enhanced corrosion resistance achieved by high power impulse magnetron sputtering interface pre-treatment.” Thin Solid Films 515: 3685-3692.

[65] Wang Q.-Y., Xi Y.-C., Liu X.-Y., Liu S., Bai S.-L. & Liu Z.D. (2017) “Microstructure and mechanical properties of interface between laser cladded Hastelloy coating and steel substrate.” Transactions of Nonferrous Metals Society of China 27: 733-740.

[66] Ehiasarian A.P., Munz W.-D., Hultman L., Helmersson U. & Petrov I. (2003) “High power pulsed magnetron sputtered CrN_x films.” Surface and Coatings Technology 163-164: 267-272.

[67] Liu Z., Dong Y., Chu Z., Yang Y., Li Y. & Yan D. (2013) “Corrosion behavior of plasma sprayed ceramic and metallic coatings on carbon steel in simulated seawater.” Materials and Design 52: 630-637.

[68] Protinha A., Teixeira V., Carneiro J., Costa M.F., Barradas N.P. & Sequeira A.D. (2004) “Stabilization of ZrO_2 PVD coatings with Gd_2O_3.” Surface and Coatings Technology 188-189: 107-115.

[69] Sun S.Q., Ye Y.W., Wang Y.X., Liu M.Q., Liu X., Li J.L. & Wang L.P. (2017) “Structure and tribological performances of CrAlSiN coatings with different Si percentages in seawater.” Tribology International 115: 591-599.

[70] Perez-Martino J., Lau K.H., Alvarez E., Malhotra R., Hornbostel M., Krishnan G. & Sanjurjo A. (2008) “Multilayer coatings for corrosion protection of coal gasifier components.” Materials Chemistry and Physics 112: 180-185.

[71] Samim P. M., Fattah-alhosseini A., Elmkhah H. & Imantalab O. (2020) “Structure and corrosion behavior of ZrN/CrN nano-multilayer coating deposited on AISI 304 stainless steel by CAE-PVD technique.” Journal of Asian Ceramic Societies 8: 460-469.

[72] Major L., Krawiec H., Lackner J. M., Dyner M., Grysakowski B. & Major B. (2020) “Nanoscale characterization of corrosion mechanisms in advanced Zr/Zr_xN and Zr/Zr_xN + A-C/H nano-multilayer coatings for medical tools.” Materials Characterization 168: 110565.

[73] Lei Z., Zhang Q., Zhu X., Ma D., Ma F., Song Z. & Fu Y. Q. (2018) “Corrosion performance of ZrN/ZrO_2 multilayer coatings deposited on 304 stainless steel using multi-arc ion plating.” Applied Surface Science 431: 170-176.

[74] Wiklund U., Hedenqvist P., Hogmark S., Stridh B. & Arbell M. (1996) “Multilayer coatings as corrosion protection of Zircaloy.” Surface and Coatings Technology 86-87: 530-534.

[75] Bahi R., Nouveau C., Beliardouh N. E., Ramoul C. E., Meddah S. & Ghelloudj O. (2020) “Surface performances of Ti-6Al-4V substrates coated PVD multilayered films in biological environments.” Surface and Coatings Technology 385: 125412.

[76] Guan X., Wang Y., Zhang G., Jiang X., Wang L. & Xue Q. (2017) “Microstructures and properties of Zr/CrN multilayer coatings fabricated by multi-arc ion plating.” Tribology International 106: 78-87.

[77] Rodriguez-Penalonga L. & Yolanda Moratilla Soria B. (2017) “A Review of the Nuclear Fuel Cycle Strategies and the Spent Nuclear Fuel Management Technologies.” Energies 10, 1235.

[78] Tcharkhtchi-Gillard E. (2014) “Passivité et rupture de passivité de l’acier 304L en milieu acide nitrique concentré et chaud.” Chimie analytique, Université Pierre et Marie Curie – Paris VI. tel-01020901.

[79] Fauvet P. (2012) “Chapter 19: Corrosion issues in nuclear fuel reprocessing plants.” Nuclear corrosion science and engineering (pp. 679-728), Woodhead Publishing, ISBN: 978- 1845697655.

[80] Feron D. (2012) “Chapter 2: Overview of nuclear materials and nuclear corrosion science and engineering.” Nuclear corrosion science and engineering (pp. 31-56), Woodhead Publishing, ISBN: 978- 1845697655.

[81] Mur, P. Fauvet, P. Lauvinerie & J. Sannier, (1990) “Comportement du zirconium en milieu nitrique.” 2eme rapport d’avancement, RT SCECF 170.

[82] Burns R. H. & Schwartz H. D. (1984) “Corrosion resistance and mechanical properties of a tantalum-40 weight percent niobium alloy.” Corrosion 84, New Orleans, April 1984 (Proc. Conf.), Paper n°148 NACE, Houston (Texas)

[83] Feron D., Richet C. & Bonin B. (2010) “Corrosion and Alteration of Nuclear Materials.” CEA Saclay and Groupe Moniteur, ISBN: 978-2-281-11369-3.

[84] Mendizabal Ortiz de Guzman L. (2016) “TaN thin films deposited by modulated pulsed power magnetron sputtering: Coating solutions for harsh environments.” PhD thesis, Universidad del Pais Vasco.

[85] Bardal E. (2004) "Corrosion and Protection.” Springer-Verlag, London. ISBN: 1852337583.

[86] Liu Y., Mol J.M.C. & Janssen G.C.A.M. (2016) “Combined corrosion and wear of aluminium alloy 7075-T6.” Journal of Bio- and Tribo-Corrosion 2: 9.

[87] Carvalho M.L. (2014) “Corrosion of copper alloys in natural seawater: effects of hydrodynamics and pH.” PhD thesis, University of Pierre and Marie Curie – Paris VI. Tel-01207012.

[88] Liu X., Zhao X., Cui X., Xu L., Li X. & Cheng R. (2018) “Corrosion behavior of 304L Stainless Steel in Nitric Acid-Sodium Nitrate Solutions.” Journal of Chinese Society for Corrosion and Protection 38: 543-550.

[89] Raj B. & Kamachi Mudali U. (2006) “Materials development and corrosion problems in nuclear fuel reprocessing plants.” Progress in Nuclear Energy 48: 283-313.

[90] Robin R., Miserque F. & Spagnol V. (2008) “Correlation between composition of passive layer and corrosion behavior of high Si-containing austenitic stainless steels in nitric acid.” Journal of Nuclear Materials 375: 65-71.

[91] Olsson C.-O. A. & Landolt D. (2003) “Passive films on stainless steels – chemistry, structure and growth.” Electrochimica Acta 48: 1093-1104.

[92] Ma L., Pascalidou E.-M., Wiame F., Zanna S., Maurice V. & Marcus P. (2020) “Passivation mechanisms and pre-oxidation effects on model surfaces of FeCrNi austenitic stainless steel.” Corrosion Science 167, 108483.

[93] Balbaud F., Sanchez G., Fauvet P., Santarini G. & Picard G. (2000) “Mechanism of corrosion of AISI 304L stainless steel in the presence of nitric acid condensates.” Corrosion Science 42: 1685-1707.

[94] Padhy N., Kamal S., Chandra R., Kamachi Mudali U. & Raj B. (2010) “Corrosion performance of TiO_2 coated type 304L stainless steel in nitric acid medium.“ Surface and Coatings Technology 204: 2782-2788.

[95] Ningshen S., Kamachi Mudali U., Krishnan R. & Raj B. (2011) “Corrosion behavior of Zr-based metallic glass coating on type 304L stainless steel by pulsed laser deposition method.” Surface and Coatings Technology 205: 3961-3966.

[96] Li C., Chen W., Jiang Q., Wang L. & Luo D. (2014) “Corrosion resistance of Ti-based metallic glass coating in concentrated nitric acid.“ Materials Chemistry and Physics 143: 900-903. doi:10.1016/j.matchemphys.2013.11.061.

[97] Ravi Shankar A. & Kamachi Mudali U. (2013) “Refractory metal coating on titanium to improve corrosion resistance in nitric acid medium.” Surface and Coatings Technology 235: 155-164.

[98] Ruiz H., Vesteghem H., Di Giampaolo A.R. & Lira J. (1997) “Zirconia coatings by spray pyrolysis.” Surface and Coatings Technology 89: 77-81.

[99] Checmanowski J.G. & Szczygiel B. (2013) “Effect of a ZrO_2 coating deposited by the sol-gel method on the resistance of FeCrAl alloy in high-temperature oxidation conditions.” Materials Chemistry and Physics 139: 944-952.

[100] Ma F.-Y. (2012) “Corrosive Effects of Chlorides on Metals.” Pitting Corrosion, Prof. Nasr Bensalah (Ed.), InTech, ISBN: 978-953-51-0275-5.

[101] Wika S.F. (2012) “Pitting and Crevice Corrosion of Stainless Steel under Offshore Conditions.” Master thesis, Norwegian University of Science and Technology.

[102] Zhang T.F., Wang Q.M., Lee J., Ke P., Nowak R. & Kim K.H. (2012) “Nanocrystalline thin films synthesized from a Ti_2AlN compound target by high power impulse magnetron sputtering technique.” Surface and Coatings Technology 212: 199-206.

[103] Liengen T., Basseguy R., Feron D. & Beech I. (2014) “Understanding Biocorrosion – Fundamentals and Applications.” European Federation of Corrosion, Woodhead Publishing, ISBN: 978-1-78242-120-7.

[104] Daumas S., Magot M. & Crolet J.L. (1993) “Measurement of the net production of acidity by a sulfate-reducing bacterium: experimental checking of theoretical models of microbially influenced corrosion.” Research in Microbiology 144: 327-332.

[105] Enning D. & Garrelfs J. (2014) “Corrosion of Iron by Sulfate-Reducing Bacteria: New Views of an Old Problem.” Applied and Environmental Microbiology 80: 1226-1236.

[106] Venzlaff H., Enning D., Srinivasan J., Mayrhofer K.J.J., Hassel A.W., Widdel F. & Stratmann M. (2013) “Accelerated cathodic reaction in microbial corrosion of iron

due to direct electron uptake by sulfate-reducing bacteria." Corrosion Science 66: 88-96.

[107] Kerber Schutz M. (2013) "The role of hydrogenotrophic iron-reducing bacteria on the corrosion process in the context of geological disposal." PhD thesis, Aix-Marseille University.

[108] Dagbert C. (2009) "Biocorrosion." Technique de l'ingénieur COR130 V1.

[109] Perez F. J., Hierro M. P., Gomez C., Martinez L. & Viguri P. G. (2002) "Ion implantation as a surface modification technique to improve localised corrosion of different stainless steels." Surface and coatings Technology 155: 250-259.

[110] Purandare Y., Ehiasarian A., Santana A. & Hovsepian P. (2014) "ZrN coatings deposited by high power impulse magnetron sputtering and cathodic arc techniques." Journal of Vacuum Science & Technology A 32, 031507.

[111] Cubillos G.I., Bethencourt M. & Olaya J.J. (2015) "Corrosion resistance of zirconium oxynitride coatings deposited via DC unbalanced magnetron sputtering and spray pyrolysis-nitriding." Applied Surface Science 327: 288-295.

[112] Xie D., Wang H., Ganesan R., Leng Y., Sun H. & Huang N. (2015) "Fatigue durability and corrosion resistance of TiO_2 films on CoCrMo alloy under cyclic deformation." Surface and Coatings Technology 275: 252-259.

[113] Villardi de Oliveira C., Alhussein A., Creus J., Schuster F., Schlegel M.L., Dong Z., Jimenez C. & Sanchette F. (2019) "Bifunctional TiO_2/AlZr thin films on steel substrate combining corrosion resistance and photocatalytic properties." Coatings 9, 564.

[114] Madaoui N., Saoula N., Zaid B., Saidi D. & Si Ahmed A. (2014) "Structural, mechanical and electrochemical comparison of TiN and TiCN coatings on XC48 steel substrates in NaCl 3.5% water solution." Applied Surface Science 312: 134-138.

[115] Chou W.-J., Yu G.-P. & Huang J.-H. (2003) "Corrosion resistance of ZrN films on AISI 304 stainless steel substrate." Surface and coatings Technology 167: 59-67.

[116] Subramanian B., Swaminathan V. & Jayachandran M. (2012) "Microstructural, tribological and electrochemical corrosion studies on reactive DC magnetron sputtered zirconium nitride films with Zr interlayer on steel." Metals and Materials International 18: 957-964.

[117] Bensaha R. & Bensouyad H. (2012) "Synthesis, Characterization and Properties of Zirconium Oxide (ZrO_2)-Doped Titanium Oxide (TiO_2) Thin Films Obtained via Sol-Gel Process." Heat Treatment – Conventional and Novel Applications, Frank Czerwinski, IntechOpen.

[118] Wasa K. (2012) "Chapter 2: Sputtering Phenomena." Handbook of Sputtering Technology (Second Edition), William Andrew Publishing (pp 41-75), ISBN 9781437734836.

[119] Meija J., Coplen T.B., Bergluund M., Brand W.A., De Bièvre P., Groning M., Holden N.E., Irrgeher J., Loss R.D., Walczyk T. & Prohaska T. (2016) "Atomic weights

of the elements 2013 (IUPAC Technical Report).” Pure and Applied Chemistry 88: 265-291.

[120] Brown P.L., Curti E., Grambow B. & Ekberg C. (2005) “Chemical thermodynamics of zirconium.” OECD Nuclear Energy Agency, Elsevier, ISBN: 978-0-08045-753-6.

[121] Nikkanen J.-P. (2016) “Synthesis of TiO_2 by various methods. Structural Characteristics, Photocatalytic Activity and Usability of Powders and Coatings.” Thesis, Tampere University of Technology.

[122] Hanaor D.A.H. & Sorrell C.C. (2011) “Review of the anatase to rutile phase transformation.” Journal of Materials Science 46: 855-874.

[123] Melouki M. (2012) “Réalisation et caractérisation des couches minces SnO_2, TiO_2 pour cellules solaire de type Gratzel.” Mémoire, Université des Sciences et de la Technologie d’Oran Mohamed Boudiaf.

[124] Dachille F., Simons P.Y. & Roy R. (1968) “Pressure-temperature studies of anatase, brookite, rutile and TiO_2-II.” The American Mineralogist 53: 1929-1939.

[125] Samat M.H., Taib M.F.M., Hassan O.H., Yahya M.Z.A. & Ali A.M.M. (2017) “Structural, electronic and optical properties of brookite phase titanium dioxide.” Materials Research Express 4, 044003.

[126] Ait Braham J. & Yaici S. (2016) “Élaboration des couches minces de TiO_2, TiO_2 dopé Ag, et nanocomposites Ag/TiO_2 par voie sol-gel. Caractérisations structurales et optiques.” Mémoire, Université Abderrahmane Mira de Béjaia.

[127] Diebold U. (2003) “The surface science of titanium dioxide.” Surface Science Reports 48: 53-229.

[128] Moulin G., Fabergeon J. & Beranger G. (2008) “Zircone - Céramique fonctionnelle.” Technique de l’ingénieur N3210 V1.

[129] Chen Z. (2011) “Relation microstructure et propriété mécanique des films de ZrO_2 obtenus par MOCVD.” PhD thesis, Paris Sud University.

[130] Sahin E. O. (2016) “Development of rare earth-free negative electrode materials for NiMH batteries.” PhD thesis, Middle East Technical University, Turkey.

[131] Pourbaix M. (1974) “Atlas of Electrochemical Equilibria in Aqueous Solutions”, National Association of Corrosion Engineers, Houston, TX.

[132] Pinard Legry G. (1990) “Corrosion resistance of zirconium: general mechanisms, behaviour in nitric acid.” Communication aux Journées d’Etudes sur le zirconium, Lyon, 10-11/10.

[133] McCafferty E. (2010) Thermodynamics of Corrosion: Pourbaix Diagrams. In: Introduction to Corrosion Science. Springer, New York, NY.

[134] Hecimovic A. & Gudmundsson J.T. (2017) “Preface to Special Topic: Reactive high power impulse magnetron sputtering.” Journal of Applied Physics 121, 171801.

[135] Lundin D. & Sarakinos K. (2012) “An introduction to thin film processing using high-power impulse magnetron sputtering.” Journal of Materials Research 27: 780-792.

[136] Anders A. (2017) “Tutorial: Reactive high power impulse magnetron sputtering (R-HiPIMS).” Journal of Applied Physics 121, 171101.

[137] Britun N., Minea T., Konstantinidis S. & Snyders R. (2014) “Plasma diagnostics for understanding the plasma-surface interaction in HiPIMS discharges: a review.” Journal of Physics D: Applied Physics 47, 224001.

[138] Musil J., Baroch P., Vlcek J., Nam K.H. & Han J.G. (2005) “Reactive magnetron sputtering of thin films: present status and trends.” Thin Solid Films 475: 208-218.

[139] Berg S. & Nyberg T. (2005) “Fundamental understanding and modeling of reactive sputtering processes.” Thin Solid Films 476: 215-230.

[140] Wiatrowski A. & Posadowski W. M. (2008) “Pulsed dc self-sustained magnetron sputtering.” Journal of Vacuum Science & Technology A 26: 1277-1281.

[141] Shimizu T., Villamayor M., Lundin D. & Helmersson U. (2016) “Process stabilization by peak current regulation in reactive high-power impulse magnetron sputtering of hafnium nitride.” Journal of Physics A: Applied Physics 49, 065202.

[142] Schiller S. Heisig H., Korndörfer CHR., Beiister G., Rescher J., Steinfelder K. & Strümpfel J. (1987) “Reactive D.C. high-rate sputtering as production technology.” Surface and Coatings Technology 33: 405-423.

[143] Zhao X., Jin J., Cheng J.-C., Lee J.-W., Wu K.-H., Lin K.-C., Tsai J.-R. & Liu K.-C. (2014) “Structural and optical properties of zirconia thin films deposited by reactive high-power impulse magnetron sputtering.” Thin Solid Films 570: 404-411.

[144] El-Hamshary A. A. (2011) “Influence of reactive sputtering process parameters on the structure and properties of TiO_2 thin films.” PhD thesis, RWTH Aachen University, Germany.

[145] Zhao X., Jin J., Cheng J.-C., Lee J.-W., Wu K.-H. & Liu K.-C. (2015) “Effect of pulsed off-times on the reactive HiPIMS preparation of zirconia thin films.” Vacuum 118: 38-42.

[146] Michiels M., Hemberg A., Godfroid T., Douheret O., Colaux J. L., Moskovin P., Lucas S., Caillard A., Thomann a.-L., Laha P., Terryn H., Voué M., Panepinto A., Snyders R. & Konstantinidis S. (2021) “On the relationship between the plasma characteristics, the microstructure and the optical properties of reactively sputtered TiO_2 thin films.” Journal of Physics D: Applied Physics 54, 415202.

[147] Hipler R., Hubicka Z., Cada M., Ksirove P., Wulff H., Helm C. A. & Stranak V. (2017) “Angular dependence of plasma parameters and film properties during high power impulse magnetron sputtering for deposition of Ti and TiO_2 layers.” Journal of Applied Physics 121, 171906.

[148] Ohko Y., Saitoh S., Tatsuma T. & Fujishima A. (2001) “Photoelectrochemical anticorrosion and self-cleaning effects of a TiO_2 coating for type 304 stainless steel.” Journal of the Electrochemical Society 148: B24-B28.

[149] Shan C.X, Hou X. & Choy K.-L. (2008) “Corrosion resistance of TiO_2 films grown on stainless steel by atomic layer deposition.” Surface and Coatings Technology 202: 2399-2402.

[150] Muhamed Shajudheen V.P., Anitha Rani K., Senthil Kumar V., Uma Maheswari A., Sivakumar M. & Saravana Kumar S. (2018) “Comparison of anticorrosion studies of titanium dioxide and nickel oxide thin films fabricated by spray coating technique.” Materials Today: Proceedings 5: 8889-8898.

[151] Padhy N., Kamal S., Chandra R., Kamachi Mudali U. & Raj B. (2010) “Corrosion performance of TiO_2 coated type 304L stainless steel in nitric acid medium.” Surface and Coatings Technology 204: 2782-2788.

[152] Hu Y., Huang S., Liu S. & Pan W. (2012) “A corrosion-resistance superhydrophobic TiO_2 film.” Applied Surface Science 258: 7460-7464.

[153] Marin E., Guzman L., Lanzutti A., Ensinger W. & Fedrizzi L. (2012) “Multilayer Al_2O_3/TiO_2 atomic layer deposition coatings for the corrosion protection of stainless steel.” Thin Solid Films 522: 283-288.

[154] Boukerche S., Himour A., Bououdina M., Bensouici F. & OUchenane S. (2019) “Multilayered ZnO/TiO_2 nanostructures as efficient corrosion protection for stainless steel 304.” Materials Research Express 6, 055052.

[155] Mills A., Lepre A., Elliott N., Bhopal S., Parkin I.P. & O’Neill S.A. (2003) “Characterization of the photocatalyst Pilkington Activ^{TM}: a reference film photocatalyst?” Journal of Photochemistry and Photobiology A: Chemistry 160: 213-224.

[156] Raulio M., Pore V., Areva S., Ritala M., Leskela M., Linden M., Rosenholm J.B., Lounatmaa K. & Salkinoja-Salonen M. (2006) “Destruction of Deinococcus geothermalis biofilm by photocatalytic ALD and sol-gel TiO_2 surfaces.” Journal of Industrial Microbiology and Biotechnology 33: 261-268.

[157] Jalvo B., Faraldos M., Bahamonde A. & Rosal R. (2017) “Antimicrobial and antibiofilm efficacy of self-cleaning surfaces functionalized by TiO_2 photocatalytic nanoparticles against Staphylococcus aureaus and Pseudomonas putida.” Journal of Hazardous Materials 340: 160-170.

[158] Soethe V.L., Delatorre R.G., Ramos E.M. & Parucker M.L. (2017) “TiO_2 thin films for biofouling Applications.” Materials Research 20: 426-431.

[159] Kallio T., Alajoki S., Pore V., Ritala M., Laine J., Leskela M. & Stenius P. (2006) “Antifouling properties of TiO_2: Photocatalytic decomposition and adhesion of fatty and rosin acids, sterols and lipophilic wood extractives.” Colloids and Surfaces A: Physicochemical and Engineering Aspects 291: 162-176.

[160] Nouri E., Shahmiri M., Rezaie H.R. & Talayian F. (2011) “Investigation of structural evolution and electrochemical behaviour of zirconia thin films on the 316L

stainless steel substrate formed via sol-gel process." Surface and Coatings Technology 205: 5109-5115.

[161] Kazazi M., Haghighi M., Yarali D. & Zaynolabedini M.H. (2018) "Improving corrosion resistance of 316L austenitic stainless steel using ZrO_2 sol-gel coating in nitric acid solution." Journal of Materials Engineering and Performance 27: 1093-1102.

[162] Holgado J.P., Perez-Sanchez M., Yubero F., Espinos J.P. & Gonzalez-Elipe A.R. (2002) "Corrosion resistant ZrO_2 thin films prepared at room temperature by ion beam induced chemical vapour deposition." Surface and Coatings Technology 151-152: 449-453.

[163] Cubillos G.I., Olaya J.J., Bethencourt M., Cifredo G. & Blanco G. (2013) "Resistance to corrosion of zirconia coatings deposited by spray pyrolysis in nitrided steel." Journal of Thermal Spray Technology 22: 1242-1252.

[164] Kotoka R., Yarmolenko S., Pai D. & Sankar J. (2015) "Corrosion behavior of reactive sputtered Al_2O_3 and ZrO_2 thin films on Mg disk immersed in saline solution." Journal of Materials Science & Technology 31: 873-880.

[165] Kaliaraj G.S., Vishwakarma V., Kirubaharan K., Dharini T., Ramachandran D. & Muthaiah B. (2018) "Corrosion and biocompatibility behavior of zirconia coating by EBPVD for biomedial applications." Surface and Coatings Technology 334: 336-343.

[166] Sun T., Wang L., Yu Y., Wang Y., Wang X. & Tang B. (2007) "TiN/ZrO_2 multilayers synthesized on GCr15 bearing steel using plasma immersion ion implantation and deposition." Surface and Coatings Technology 201: 6615-6618.

Materials and Methods

This chapter presents the materials studied, the experimental devices and the characterization techniques used during this project.

1. MATERIALS AND DEPOSITION CHAMBERS

1.1 304L AUSTENITIC STAINLESS STEEL SUBSTRATE (ASS)

The austenitic stainless steel used as a substrate in this work is a 304L steel supplied by Icaunaise des Metaux, France from a casting of the company Aperam, Belgium. The chemical composition of the 304L steel from the supplier material certificate as well as values obtained during the controls performed at SEARS/LANIE by inductively coupled plasma optical emission spectrometry (ICP-OES) and glow discharge mass spectrometry (GDMS) are presented in Table 1 and compared to the chemical composition specifications imposed for the use of the material in reprocessing plants. The chemical compositions obtained by our different techniques are mostly in accordance with the supplier material certificate and the specifications. Only C and N contents differ slightly from the supplier material certificate, which can be due to the difficulty to measure these elements with our control techniques.

Table 1: Chemical composition of 304L ASS obtained by various methods compared to chemical composition specifications for use in reprocessing plants.

Elements	Specifications for use in reprocessing plants (wt.%) [1]	Supplier material certificate (wt.%)	GDMS measurements (wt.%)	ICP-OES measurements (wt.%)
C	≤ 0.030	0.024	0.014 ± 0.002	-
Mn	0.50-2.00	1.34	1.33 ± 0.05	1.31 ± 0.05
P	≤ 0.045	0.03	0.03 ± 0.01	-
Si	0.20-1.00	0.47	0.42 ± 0.02	0.48 ± 0.02
S	≤ 0.030	0.001	0.001 ± 0.000	-
Cr	17.5-19.0	18.11	17.73 ± 0.41	18.04 ± 0.35
Ni	9.0-12.0	10.08	9.82 ± 0.16	9.89 ± 0.21
Cu	-	0.32	0.32 ± 0.01	0.33 ± 0.02
Co	-	0.136	0.125 ± 0.003	0.131 ± 0.030
N	-	0.033	0.001 ± 0.000	-

The steel was rolled and annealed several times by Aperam between the initial casting and the final coil thickness. The final heat treatment was a hyperquenching at 1050 °C. Then, the 304L coil was rolled again by Icaunaise des Metaux to provide strips of

1 meter long, 5 cm wide and 1.5 mm thick. The supplier claimed a 0.2% offset yield strength ($R_{p0.2\%}$) of 234 MPa, a tensile strength (R_m) of 555 MPa and a hardness of 79 HRBW (≈ 150 HV). This hardness value was checked with two types of hardness measurements: Vickers micro-hardness and Rockwell hardness measurements. A hardness of 154 HV for micro-hardness measurements with a 5 kg applied load (HV5) and a Vickers indenter was obtained according to NF EN ISO 6507-1 (*Matériaux métalliques – Essai de dureté Vickers – Partie 1 : méthode d'essai, 40 p., 2018*). On the other hand, Rockwell hardness measurements using a 60 kg load applied and a diamond indenter showed a value of 43 HRA (≈ 125 HV) according to ASTM E18-20 (*Standard test methods for Rockwell hardness of metallic materials, 39 p., 2020*). The hardness values obtained vary slightly depending on the measurement method used, this may be due to the depth analyzed. In the case of Vickers micro-hardness tests, the hardness values depend mainly on the extreme surface of the material, as the penetration depth is lower than for Rockwell measurements. Nonetheless, all the hardness values obtained are similar to the values reported in the literature for a 304L ASS, which are 160 HV [2] and 79 HRB (≈ 150 HV) [3].

This 304L ASS substrate microstructure (surface and core) was further characterized using an SEM-FEG equipped with an electron backscatter diffraction (EBSD) detector. The EBSD analyses were performed at 15 kV and 8 nA on a surface of 1296×972 µm². Prior to this analysis, an electrolytic polishing with oxalic acid solution (10%) was performed during 30 seconds at 15V, which allowed highlighting the sample microstructure. The phases, grain sizes and distribution are summarized in Table 2. The 304L microstructure consists of an austenitic matrix of face-centered cubic (FCC) type and small amount of body-centered cubic ferrite (BCC). Differences are observed between the surface and the core of the material, indicating a higher amount of ferrite at the 304L surface (2 %). On the other hand, the grain size seems to be comparable between the surface (23 ± 9 µm) and the core (24 ± 10 µm) of 304L ASS, which shows that the faster cooling of the surface compared to the core of the material did not significantly modify the grain size. Results showing residual ferrite phase (1-2 %) and similar grain sizes have already been observed on 304L ASS [4]. It should be noted that ferrite can be preferentially attacked in nitric acid for example, which would make its presence detrimental to corrosion resistance [5].

Table 2: EBSD analysis results on the surface and core of the 304L substrate.

	304L surface	**304L core**
Phases (%)	98 % Austenite (FCC) 2 % Ferrite (BCC)	99 % Austenite (FCC) 1 % Ferrite (BCC)
Grain size (µm)	23 ± 9	24 ± 10

Grain distribution	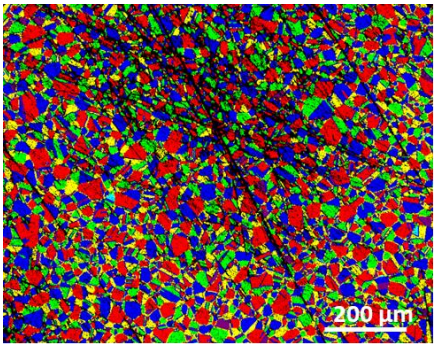	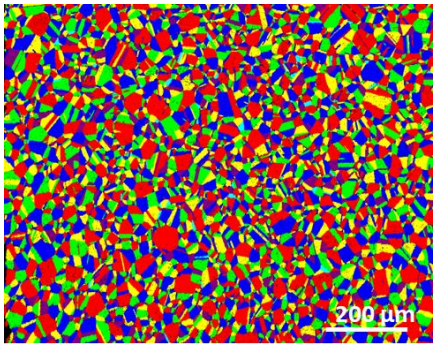

1.2 SUBSTRATE SURFACE PREPARATION

The 304L coupons were cut from strips using a waterjet cutting machine and pierced with a suspension hole by NICOT, France (Figure 1). Two sizes of substrates are required to perform the desired characterizations: 30×10×1.5 mm^3 coupons were used for microscopy analyses (optical microscopy, XRD, SEM, TEM, XPS, APT), 30×20×1.5 mm^3 ones for corrosion resistance study (electrochemical measurements, immersion tests in nitric acid solution and Cherbourg natural seawater) and 50×50×1.5 mm^3 (immersion tests in NaCl solution and Singapore natural seawater). The preparation of the substrates counts several steps: mechanical polishing (using SiC abrasive papers from 120 to 4000 grit), cleaning with distilled water and ethanol, drying with compressed air, ultrasonically cleaning during 10 minutes in acetone and then ethanol, and finally drying with argon. The purpose of this surface preparation procedure is to obtain a homogeneous surface and to eliminate potential contaminations due to the cutting operations for example. Some samples were not polished but only cleaned and dried to be closer to the service conditions of the components.

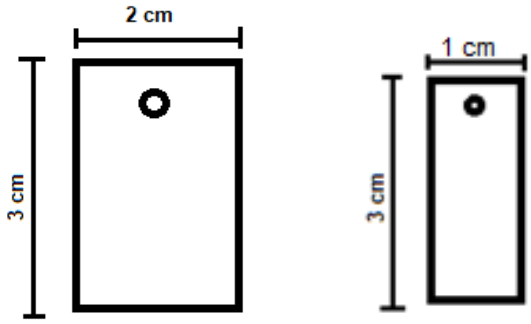

Figure 1: Shape and size of the 304L substrates.

1.3 PVD COATING EQUIPMENTS

1.3.1 TriPros

Three types of etchings and metallic bond coats deposition were performed in a dedicated machine (TriProS from DEPHIS, France) in CEA Saclay (DPC/SEARS). TriPros is a multi-process prototype deposition chamber developed for the coatings

synthesis by HiPIMS, pulsed-DCMS, cathodic arc and PE-CVD techniques. It consists of an electrical bay, a gas panel, a pumping system, a cooling system, a computer control system and a deposition chamber, with full dimensions of 4.15×1.40×2.60 m^3 (Figure 2). The electrical bay houses three DC generators GX100/100 (ADL, Germany) combined with three pulse generators SPIK 3000A (MELEC, Germany) supplying two pairs of rectangular magnetrons and the bias of the substrate-holder. The pumping system consists of a rotary vane pump, a turbomolecular secondary pump and a butterfly valve to regulate the pressure inside the vacuum chamber. Note however that the gas pressure can also be regulated by adjusting the gas flow rates. The gas management is performed with flow meters in the gas panel. The gases are mixed and then injected into the vacuum chamber from below using two inlets. In addition, measuring instruments are present in the vacuum chamber such as an optical emission spectrometer, which can be used to study the composition of the plasma formed during coating deposition. It is generally used in the case of reactive deposition for oxide or nitride coatings to determine the optimal ratio of reactive gas to plasmagenic gas. In our study, it was not used because the oxide coatings deposition was subcontracted to DEPHIS company.

The main vacuum chamber is a 0.75×0.75×0.75 m^3 stainless steel cube equipped with a cooling circuit and two windows to allow visual observation of its interior. The access to the interior of the vacuum chamber is possible through front door (Figure 2). Four cathodes placed on each vertical face of the chamber operate in bipolar modes *i.e.* by pairs. Each pair is connected to the outputs of one pulse generator and one DC generator. The rectangular targets (dimension of 636×127 mm^2) can be protected by removable shutters to prevent their contamination. In this work, Ti and Zr targets (99.5% purity) supplied by Nano&Micro PVD, France were sputtered (Table 3).

Table 3: Chemical composition (wt.%) of targets used for etching and coating deposition.

Target	Fe (wt.%)	C (wt.%)	N (wt.%)	O (wt.%)	H (wt.%)	Hf (wt.%)	Cr (wt.%)	Balance
Ti	0.037	0.009	0.011	0.140	0.001	-	-	Ti
Zr	0.05	0.016	0.007	0.11	0.0007	1.82	< 0.01	Zr

The substrate-holder displays three distinct vertical axes of rotation (central axis, secondary axes and tertiary axes) for full coating of the samples (Figure 2). The workpiece supports are biased, but neither the bottom plate of the substrate-holder nor the various bearings are. This prevents the occurrence of electric arcing, limits temperature increase in the bearings and avoids unnecessary power dissipation. Loading and unloading of the substrate-holder is performed using a trolley equipped with a guiding and securing device.

Figure 2: Photographs of the a) inside, b) outside of TriPros reactor and c) drawing of the substrate-holder.

1.3.2 DEPHIS deposition machine

The synthesis of thick oxide and multilayer coatings (≈ 5-µm-thick) was subcontracted and performed to DEPHIS, France. Depositions took place in an in-house equipment, operated in a hybrid pulsed-DCMS and HiPIMS mode (Figure 3). This machine consists of a deposition chamber, a pumping system (turbomolecular pump), an electrical bay, a gas panel, a cooling system and a computer control system. The electrical bay houses the generators required to supply two magnetrons and the bias of the substrate-holder.

The main vacuum chamber is 0.37×0.75×0.43 m^3 stainless steel vat equipped with a cooling circuit. Two cathodes (400×125 mm^2) are opposite each other inside the chamber (Figure 3). One operates in pulsed-DCMS thanks to a MAGIX 3 kW (SOLVIX, USA) generator (50 kHz, t_{OFF} = 4 µs). The second operates in HiPIMS mode, using a DC generator GX100/100 (ADL, Germany) combined with a pulse generator SPIK 3000A (MELEC, Germany). In addition, the substrate-holder is negatively biased thanks to a HIP3 5 kW (SOLVIX, USA) generator (1 kHz, t_{OFF} = 500 µs).

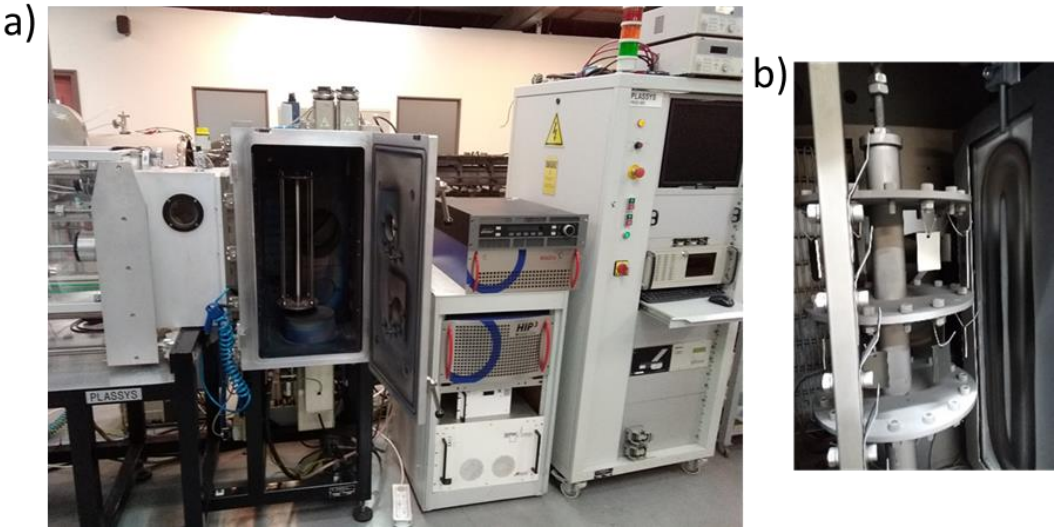

Figure 3: Photographs of a) the DEPHIS deposition chamber and b) the substrate-holder.

The reactor has a rotating substrate-holder (double rotation) that can be biased and is located at the bottom of the deposition chamber (Figure 3). In the case of oxide coatings, the regulation of the oxygen flow rate is performed in a closed loop control system by measuring the intensity of an identified Ti or Zr emission line *i.e.* using plasma emission monitoring (PEM).

2. MATERIALS CHARACTERIZATION METHODS

2.1 STRUCTURAL AND PHYSICO-CHEMICAL CHARACTERIZATIONS

Several techniques were used to characterize the interfaces of the substrate/coating systems as well as the coatings synthesized before and after exposure to aggressive environments. These characterization methods are described briefly in this section.

2.1.1 Scanning Electron Microscopy (SEM) with Energy Dispersive X-ray analysis (EDX)

Scanning electron microscopy (SEM) is a microscopy technique used for micro-characterization of coating surfaces and cross-sections. The surface morphology and topology is analyzed using the secondary electron emission (SE) mode. Back scattering electron (BSE) emission mode is preferred to obtain a composition information, as the backscattering intensity is proportional to the atomic number of the probed volume. The microscope is coupled with an energy dispersive X-ray (EDX) spectrometer for quantitative chemical analysis, operated during point, area, profiles and mapping analyses with a resolution of ≈ 1 µm² *i.e.* laterally and in depth. It can produce very high-resolution images of a specimen surface and reveal details as small as about 1 nm on the surface at 15 kV. The major limitation of this technique is when using insulating samples, which need to be protected by a carbon or gold deposition before analysis. This can result in artifacts during SEM observation.

In this work, coatings were imaged using a SEM JEOL JSM7000F equipped with a field emission gun operated at 15 kV with a beam current of 2 nA and a Bruker XFlash 5010 EDX detector. For cross-sectional observations, the samples were first cut using a micro-cutting machine and then hot-coated in a conductive mounting resin. Samples were then mechanically polished with SiC abrasive papers from 120 to 2000 grit. Finally, a mirror polish was obtained using a colloidal silica suspension solution. The samples observed are generally conductive, so the metallization of the sample surface is not necessary.

2.1.2 Focused Ion Beam (FIB) and Transmission Electron Microscopy (TEM) with Energy Dispersive X-ray analysis (EDX)

Transmission electron microscopy (TEM) is a powerful microscopy technique for analyzing the microstructure and elemental composition of coatings as well as interfaces of a substrate/coating system (nanometer scale). The TEM usual spatial resolution is around 0.1 nm. Images are obtained from electrons transmitted through a sample. This transmission of incident electron flow requires around 100 nm-thick

samples, making them almost electron transparent. Consequently, the sample to observe must be thinned using specific techniques such as ion thinning by Focused Ion Beam (FIB). A protective Pt thin film was deposited on the samples before they were thinned to a thickness of 100 nm. The crystal structure of the material is determined using diffraction mode, which indicates whether the material is monocrystalline (diffraction spots), polycrystalline (diffraction rings) or amorphous. In imaging mode, bright field (BF) and dark field (DF) images can be obtained depending on the type of electrons used. In BF images, the transmitted electrons are selected through an aperture and electron absorption by the sample is visualized on a bright background. In contrast, in DF mode the transmitted electrons are blocked and only the scattered electrons are selected by the aperture, resulting in the observation of the sample on a dark background. In addition, chemical analysis (point, mapping or profiling) can be performed using an EDX detector. The limitations of TEM technique are related to the sample preparation, which can be laborious and create artifacts during observations.

Thin sections were prepared using a ZEISS Crossbeam 540 FIB operated with a probe current up to 40 nA and an accelerating voltage up to 30 kV. TEM imaging and diffraction patterns were performed using a JEOL 2010 UHR operated at 200 kV. In addition, a JEOL JEM 2100F operated at 200 kV and equipped with an EDX analyzer (EDAX EDX detector) was used to perform mapping and profiling. All FIB sample preparations and TEM analyses were performed at FACTS Lab, NTU Singapore.

2.1.3 X-Ray Diffraction (XRD)

X-ray diffraction (XRD) is a non-destructive analytical technique used to identify coating crystal structures. It can also be used to determine lattice parameters of a crystalline material and serve for quantitative phase analyses. This technique is based on the interaction between X-rays and a crystalline sample, which produces constructive interference in a few specific directions determined by Bragg's law: $n\lambda = 2d*sin(\theta)$, where n is an integer, λ is the X-ray wavelength, d is the interplanar spacing and θ the angle between the incident and the diffracted beams. Thus, diffracted X-rays are collected as a function of an angle and a diffraction pattern is obtained. The crystal structure can be determined by indexing the peak positions and comparing them with a database, in our case the Joint Committee on Powder Diffraction Standards (JCPDS). This technique allowed us to identify the presence of crystalline phases after etchings and within coatings after deposition as well as phases formed after exposure to aggressive environments.

Two types of acquisition geometry can be used for XRD analysis on a laboratory powder diffractometer: Bragg-Brentano (θ-2θ) geometry and grazing incidence (Figure 4). In the case of θ-2θ geometry, the X-beam source and detector move simultaneously over a wide range of angles allowing the X-rays to penetrate deeply into the raw material (Figure 4a). This scan is not suitable for measurement of very thin film since the scattering intensity is then very low compared to the substrate contribution. Grazing incidence diffraction (GID) allows analyzing a limited depth (micrometer or nanometer range) by fixing a very low incident angle (a few degrees) while the detector scans a large angular range (Figure 4b). As a result, the intense signal arising from the substrate can be avoided, and the collected information stems

mostly from the thin film itself. For instance, at an incident angle of 0.5°, the penetration depth of X-rays is estimated to about 95 nm in 304L, 220 nm in Ti and 227 nm in Zr according to calculations performed with the AbsorbDX software (Bruker). This method is used to determine the structure of the coatings before and after exposure to aggressive environments and the composition of the products formed at the surface. However, samples must be homogeneous and have large enough crystalline structures because small structures or trace amounts may not be detected by XRD.

In this work, XRD analysis is performed with a D8 Advance (Bruker) diffractometer using Cu-K_α radiation ($\lambda_{K\alpha}$ = 1.540 Å, 40 kV and 40 mA) and a Lynxeye® (Bruker) linear detector. All deposited coatings were analyzed in grazing incidence configuration with an incident angle of 0.5°, whereas all raw materials were analyzed in θ-2θ configuration.

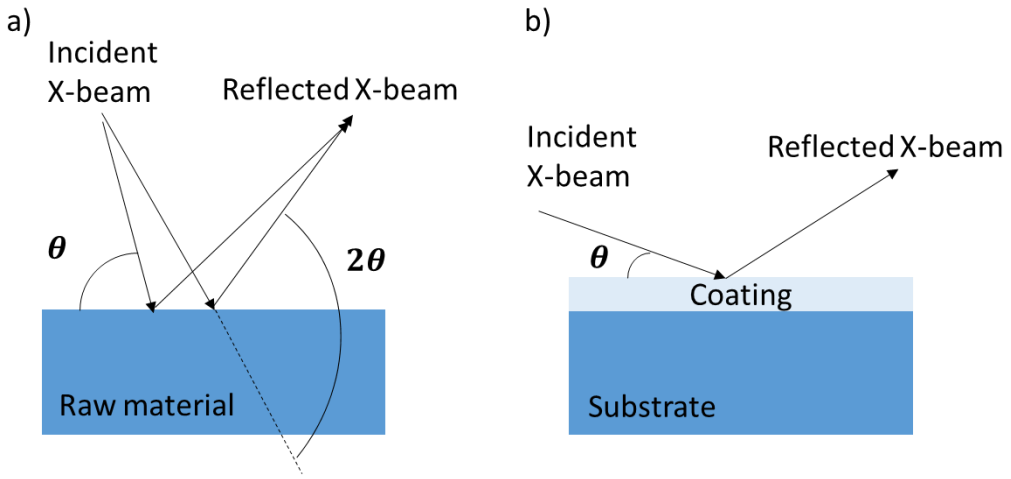

Figure 4: a) Bragg-Brentano (BB) diffraction and b) grazing incidence diffraction.

2.1.4 X-Ray Photoelectron Spectrometry (XPS)

X-ray photoelectron spectroscopy (XPS) is an extreme surface analysis technique (depth of 1 to 10 nanometers) for determining the chemical (atomic) composition and chemical bonding states of an analyzed material. This technique is based on sample irradiation with x-rays in an ultra-high vacuum environment, which results in photoelectrons emission from atom core levels. The kinetic energy of these photoelectrons is measured with an electron analyzer. This energy is characteristic of the elements present in the analyzed volume and its environment. A survey spectrum is usually measured first, representing electron intensity versus binding energy (calculated from the kinetic energy using incident x-rays wavelength). Each peak is referred to a specific element and its chemical environment, which allows identification and quantification of all surface elements, except hydrogen and helium. XPS technique can also be used to perform depth profiles thanks to an ion sputtering system. In this case, a depth profile plotting the element composition versus sputtering time is obtained. The sputtering time can be then correlated to a depth and

thicknesses can be determined. However, this was not done in this work because of the absence of reference material. On the other hand, this technique shows a low resolution and the analysis is performed on a small area (around 10 µm), which can lead to a 10% error relative in repeated analyses.

In this work, XPS measurements were performed using an Escalab 250 XI spectrometer (Thermo Fisher Scientific) equipped with a monochromatic X-ray Al-K_α source (hv = 1486.6 eV). The energy calibration was carried out using the Fermi level (0 eV) and the Ag $3d_{5/2}$ level (368.3 eV) of silver. The spot size diameter for classical analysis was 900 µm and high-resolution spectra were recorded using a constant pass energy of 20 eV. In addition, XPS depth profiles were recorded using Ar^+ ions at 1 keV for surface erosion. Data processing was performed with the commercial software Avantage (Thermo Fisher Scientific) by applying a Shirley-type background to all spectra.

2.1.5 Raman Spectroscopy

Raman spectroscopy is a non-destructive technique for identifying a material by measuring changes in the polarizability of molecular bonds induced by bond vibrations. In addition, Raman spectroscopy coupled with microscopy (micro-Raman spectroscopy) allows high spectral (up to 1.5 cm^{-1}) and spatial resolution (up to 1 µm) of the spectroscopic analysis. This technique is based on the measurement of inelastic scattering of monochromatic light (laser beam) by the sample. Photons are absorbed by the sample and a small number of them are re-emitted with a different energy corresponding to Raman scattering. The characteristic Raman spectral patterns are commonly used to identify component such as oxide and to quantitatively or semi-quantitatively evaluate the proportion of a specific component in a sample. However, this technique can not be used on metals and alloys. Furthermore, care must be taken when samples heating through laser radiation, which can damage them.

A LabRAM HR 800 spectrometer (Horiba Jobin Yvon) was used in this study. It is equipped with a dual-frequency Nd-YAG laser (λ = 532 nm), a focal length of 800 mm and a Peltier-cooled CCD detector. The spectrometer is coupled with an Olympus BX41 microscope with 10×, 50× and 100× objectives. The acquisition time varies from 60 s to several hours, depending on the desired spectral resolution. The acquisition of the spectra is performed using LabSpec 6 software (Horiba Jobin Yvon) and their analysis is carried out by comparing the vibrational bands with reference spectra from the literature [6-10] and databases. Micro Raman spectroscopy is used in this project to identify the different phases of Ti- and Zr-based oxide coatings as well as the different oxides formed on the coating surface after exposure to aggressive environments.

2.1.6 Atom Probe Tomography (APT)

The atom probe tomography (APT) is a high-resolution technique for observing the internal structure and spatial distribution of atoms in a material. This technique consists of evaporating the atoms on the sample surface using an electric field in high vacuum conditions (10^{-8} Pa). The sample is then evaporated atom by atom and atomic layer by atomic layer. The evaporated atoms are collected by a position-sensitive

detector, which allows calculating the initial position of the evaporated atoms in the sample thanks to the time of flight measurements to form a two-dimensional map (Figure 5). Then, a three-dimensional image of the atoms distribution in the sample with atomic resolution is reconstructed [11-13]. The chemical nature of the ions is determined from the mass-to-charge-state ratio given by a time-of-flight mass spectrometry device [11, 12]. The depth resolution is close to an interatomic distance (angstrom scale) and the surface spatial resolution is around one nanometer. However, APT technique has some limitations such as ion trajectory aberrations [11, 12], limited rate of detected ions (detection efficiency from 38% [13] to 60% [12]) and the requirement for high quality sample preparation [12]. This sample is prepared as a fine sharp tip with a curvature radius of 50-150 nm [12, 13] and a shank angle of 16° [13] using a FIB device.

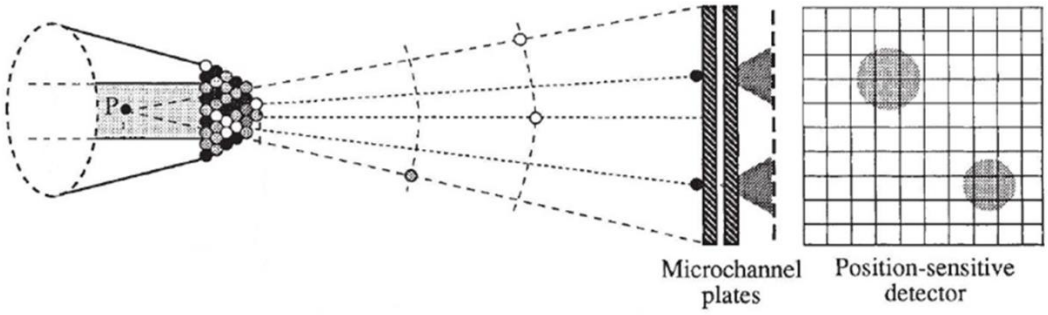

Figure 5: Schematic view of the APT (P: interception point of the ion trajectories) modified from [11].

In this work, atomic scale composition analyzes of the sample (angstrom scale) were performed by Atom Probe Tomography (APT) in two different platforms: CEA/DMN and IRMA-ROUEN. At CEA/DMN, the APT tips were prepared with a Helios 650 NanoLab (FEI) microscope equipped with a gallium ion source operating in the accelerating voltage range from 0.5 to 30 kV. The analyzes were then performed using a LEAP 4000X HR (CAMECA) instrument in laser mode with an energy of 50 pJ and a room temperature of 60 K. Data processing were performed with the IVAS 3.6.12 (CAMECA) software. At IRMA-ROUEN, the APT tips were prepared with a Helios plasma FIB dual beam (Thermo Fisher Scientific). The APT measurements were then conducted in electrical mode with a pulse fraction of 15% at 60 K. Volume reconstruction was performed using IVAS 3.8.0. Data processing were carried out with the 3D APT data software developed by the GPM research group in Rouen, France.

2.2 CORROSION RESISTANCE

2.2.1 Electrochemical measurements in saline and nitric acid environments

Electrochemical measurements were performed using a classical three-electrodes configuration in a 250 mL FlatCell® (BioLogic, France). Using a polymer sample holder and a conductive screw, the reacting surface of the sample to test was pressed against a rubber joint on one side of the cell, so that 1 cm^2 of the surface was exposed to the solution as a working electrode (WE). A platinum grid or wire was used as a counter-electrode (CE), and saturated Hg/Hg_2SO_4 electrode as a reference electrode (RE) in nitric acid medium ($E^0_{Hg2SO4/Hg}$ = 0.650 V/SHE at 25°C). A Luggin-type extension prevented the reference electrode from being in direct contact with the nitric

acid solution using a triple salt bridge filled with a KNO_3 solution. As in immersion tests, a condenser and heating system are used to ensure that the solution remains under boiling conditions as during the evaporation stage of spent fuel reprocessing (Figure 6). For the saline environment study in a 3.56 wt% NaCl solution at room temperature, the condenser and heating systems are not needed and the three-electrodes configuration is simplified. In addition, a saturated Ag/AgCl electrode is used as a reference electrode ($E^0_{AgCl/Ag}$ = 0.197 V/SHE at 25°C). All data were collected using a BioLogic (nitric acid medium) and a PGSTAT 126N (saline environment) potentiostats.

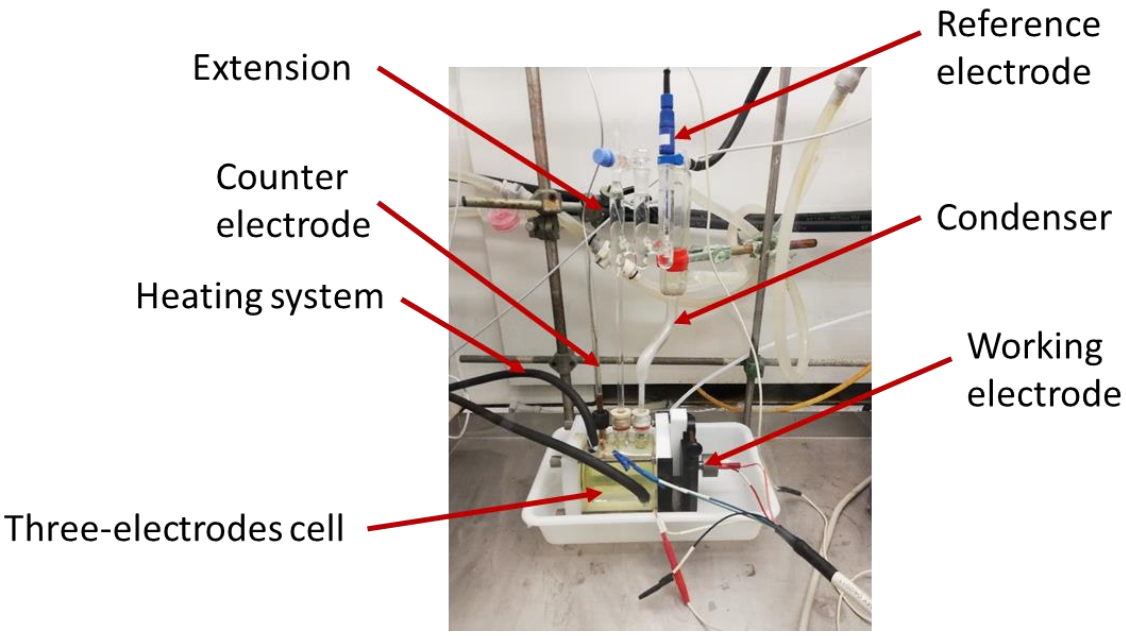

Figure 6: Electrochemical measurement facility for nitric acid environment.

Measurements in nitric acid medium (2.5 mol/L HNO_3, 2.5 mol/L $NaNO_3$, 2 g/L $Fe(NO_3)_3$ at 110°C):

The nitric acid solution used for electrochemical and immersion tests is prepared in a 10 L container by mixing 2922 g of HNO_3 (63.01 g/mol, 52.5 %, 20420.291 VWR), 2125 g of $NaNO_3$ (84.99 g/mol, 99.6 %, 27950.298 VWR) and 144.8 g of $Fe(NO_3)_3$, 9 H_2O (404 g/mol, 100%, 24175.290 VWR). Then, ultra pure water (miliQ) is put in the container to reach 10 L.

First, a 6-hour open circuit potential (E_{OCP}) measurement is performed to assess the potential of the WE until a stable value is reached. This duration was selected thanks to the experience feedback on the 304L ASS. However, it may not be optimized for other materials such as Ti or Zr due to kinetic limitations for example and longer durations should have been performed to reach stationary state. Then, polarization and electrochemical impedance spectroscopy (EIS) techniques are applied to assess electrochemical properties of the WE interface. In this work, when the E_{OCP} is completed, EIS measurement is carried out from 100 kHz to 10 mHz with sinusoidal oscillations of 10 mV amplitudes to remain in a linear regime. Then, an anodic polarization is performed at a rate of 0.2 mV/s from -0.03 V/E_{OCP} to 0.50 V/Eref. This

(OCP, EIS) measurement loop is performed five times to study the corrosion properties of the interface over time. A final anodic polarization at a rate of 0.2 mV/s from -0.03 V/E_{OCP} to 0.50 V/Eref is performed to end the electrochemical study of the coatings. The total analysis duration is about 2 days per sample. This measurement process was chosen to have a compromise between the study of the electrochemical response of the material and its behavior over time.

Measurements in saline environment (3.56 wt.% NaCl solution at room temperature):

A 3.56 wt.% NaCl solution is prepared in a 2 L volumetric flask by putting 71.2 g of NaCl (58.44 g/mol, 99.5%, 1860871 Fisher Chemical) and adding ultra pure water (miliQ) to reach 2 L of solution. This allowed having a salinity similar to natural seawater.

First, a 6-hour measurement of the open circuit potential (E_{OCP}) is performed to assess the potential of the WE until a stable value is reached. Again, this duration may not have been sufficient to reach stationary state for all the materials tested. Then, an anodic polarization at a rate of 0.2 mV/s from -0.09 V/E_{OCP} to 0.30 V/E_{OCP} and a cathodic polarization at a rate of 0.2 mV/s from -0.30 V/E_{OCP} to 0.09 V/E_{OCP} are carried out. The total analysis duration is about 10 hours per sample.

Tafel extrapolation

Assuming a uniform corrosion process and that the stationary state has been reached, the Tafel extrapolation can be used to estimate the corrosion current density (J_{corr}) from potentiodynamic curves. J_{corr} is obtained by extrapolating the linear portion of the anodic and cathodic regions of the polarization curve to E_{corr} (Figure 7). A wrong selection of the Tafel slope lead to uncertainties and erroneous value of the corrosion current density. It is necessary to ensure that the anodic or cathodic regions are observed over at least a decade of current and begin extrapolation at least 50-100 mV away from E_{corr} [14]. In this work, the corrosion potential (E_{corr}) and corrosion current density (J_{corr}) were derived from a Tafel extrapolation of the measured anodic polarization experiment performed to limit sample degradation.

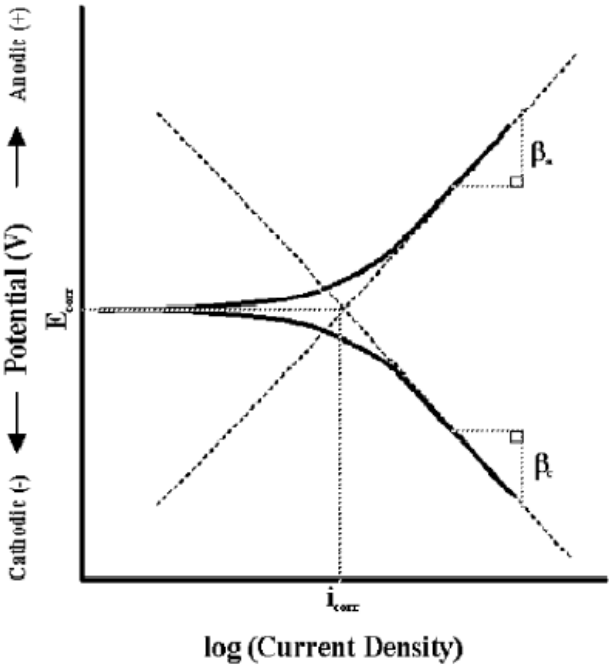

Figure 7: Tafel slopes calculation, from [15].

The corrosion rate can be calculated directly from the corrosion current density determined by Tafel slopes using the Faraday's law [15]:

$$corrosion\ rate\ (mm/year) = \frac{M_w J_{corr}}{ZFA\rho}$$

With M_w: molecular weight of metal (g/mol)
J_{corr}: corrosion current density (µA/cm²)
Z: number of electrons transferred during electrochemical reaction
F: Faraday constant (96 487 C/mol)
A: area of the working electrode (cm²)
ρ: density of the metal (g/cm^3)

The corrosion rate of etched samples is determined using the following values for 304L ASS: M_w is estimated to 25.24 g/mol, Z = 2.9 and the density is 7.93 g/cm^3. Note that Z is not equal to 2 in the case of 304L becase the number of electrons changes according to the corrosion potential to take into account the different redox couples of Fe, Cr and Ni. In our range of corrosion potential *i.e.* between 0.9 and 1.1 V/SHE, Z = 2.9.Then, for the bond coat corrosion rate calculation, the values used for Ti (Zr) are M_w = 47.87 (91.22) g/mol, Z = 2 and ρ = 4.51 (6.52) g/cm^3. Finally, for the determination of the corrosion rate of oxide and multilayer coatings, the values used for TiO_2 (ZrO_2) are M_w = 79.87 (123.22) g/mol, Z = 4 and ρ = 4.23 (5.68) g/cm^3.

In this work, electrochemical tests were used as a first screening test of the electrochemical behavior of our materials systems. Immersion tests necessary to have a true vision of the long-term corrosion behavior were performed in a second step.

2.2.2 Immersion tests

Immersion tests were performed at CEA Saclay, NTU Singapore and CORRODYS platform in different environments:

- a 3.56 wt% NaCl solution standing for a simplified marine environment,
- a nitric acid solution simulating the evaporation stage of nuclear spent fuel reprocessing (2.5 mol/L HNO_3, 2.5 mol/L $NaNO_3$ and 2 g/L $Fe(NO_3)_3$),
- Singapore and French (Cherbourg) seawater for the study of coatings under service conditions.

For this purpose, three types of systems are used and detailed below (Figure 8, 9 and 11). A visual inspection before and after immersion was performed of all the immersion tests. Weight measurements were used to follow the evolution of the samples immersed in nitric acid, 3.56 wt.% NaCl and Singapore seawater while monitoring of corrosion potential over time was performed to assess the corrosion resistance of the samples in Cherbourg seawater. Additional analyses such as SEM/EDX on sample surface and cross-sections and Raman spectroscopy observations were carried out when deemed necessary.

CEA Saclay facility

Immersion tests at CEA Saclay were performed in a reactor filled with 2 L of the chosen solution (NaCl or nitric acid) and placed in a heating system (Figure 8a). The samples used for the tests in nitric acid (2 x 3 cm^2) are shown in Figure 8b and those for NaCl (5 x 5 cm^2) in Figure 8c. In the case of nitric solution, this solution is heated to 110°C to simulate the service conditions in an evaporator. The temperature measurement is performed using a thermocouple fixed in the reactor through the cover. In addition, a Dimroth condenser is placed on the cover to allow the system to be closed and maintain reflux conditions inside the reactor. The coated samples are placed on a sample holder and immersed in the reactor solution. The reactor is then closed with a chain. The heater is switched on and boiling occurs about 1 hour after warmup, signaling the beginning of the immersion test for nitric acid solution. For NaCl solution, the reactor is kept at room temperature (20°C) and the test begins immediately after closure. The typical immersion cycle performed in this work lasts 24 hours and several cycles (up to 5) can be performed. Note that at the end of each cycle, the solution is removed and a new one is put in the reactor for the next cycle in order not to accumulate corrosion products.

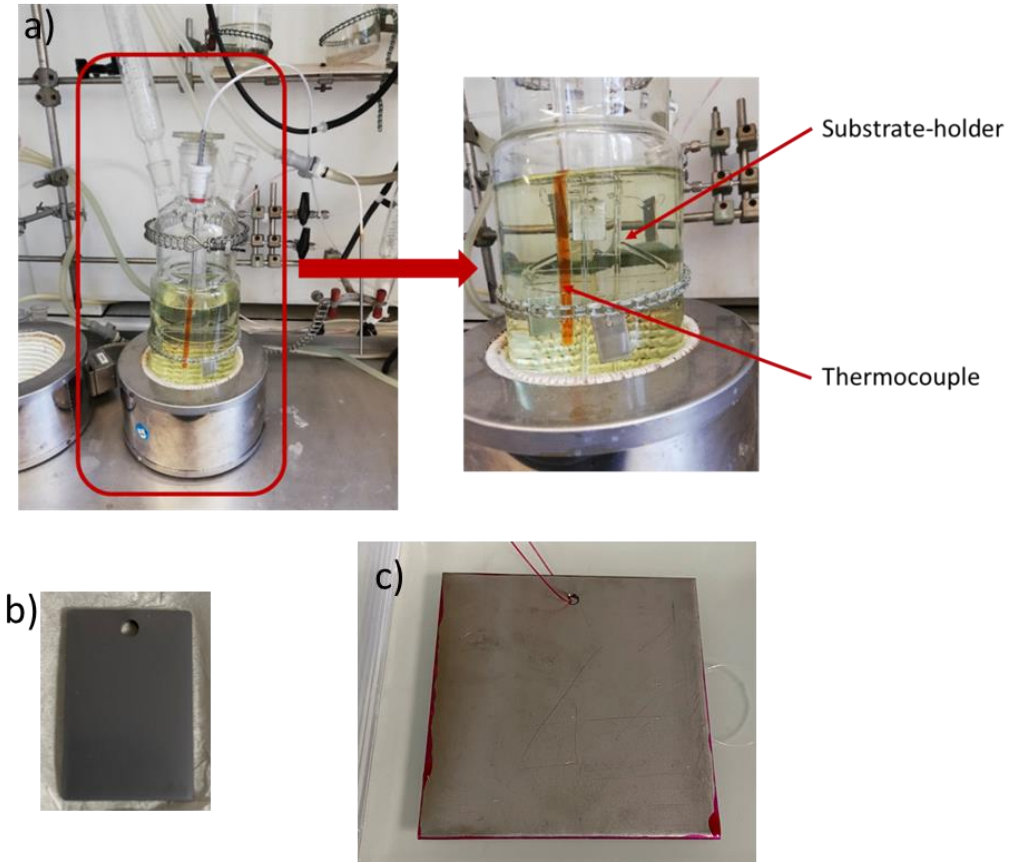

Figure 8: a) Immersion test facility at CEA Saclay, b) samples used for nitric acid and c) samples used for NaCl immersion tests.

NTU Singapore facility

The samples (5 x 5 cm²) were deployed at the Sentosa test site, south of Singapore (Figure 9a) to assess their corrosion resistance in service conditions. They were fixed inside a HDPE container using an acrylic plate, acrylic strips and stainless steel bolts. This container was covered with a thin acrylic sheet as shown in Figure 9b.

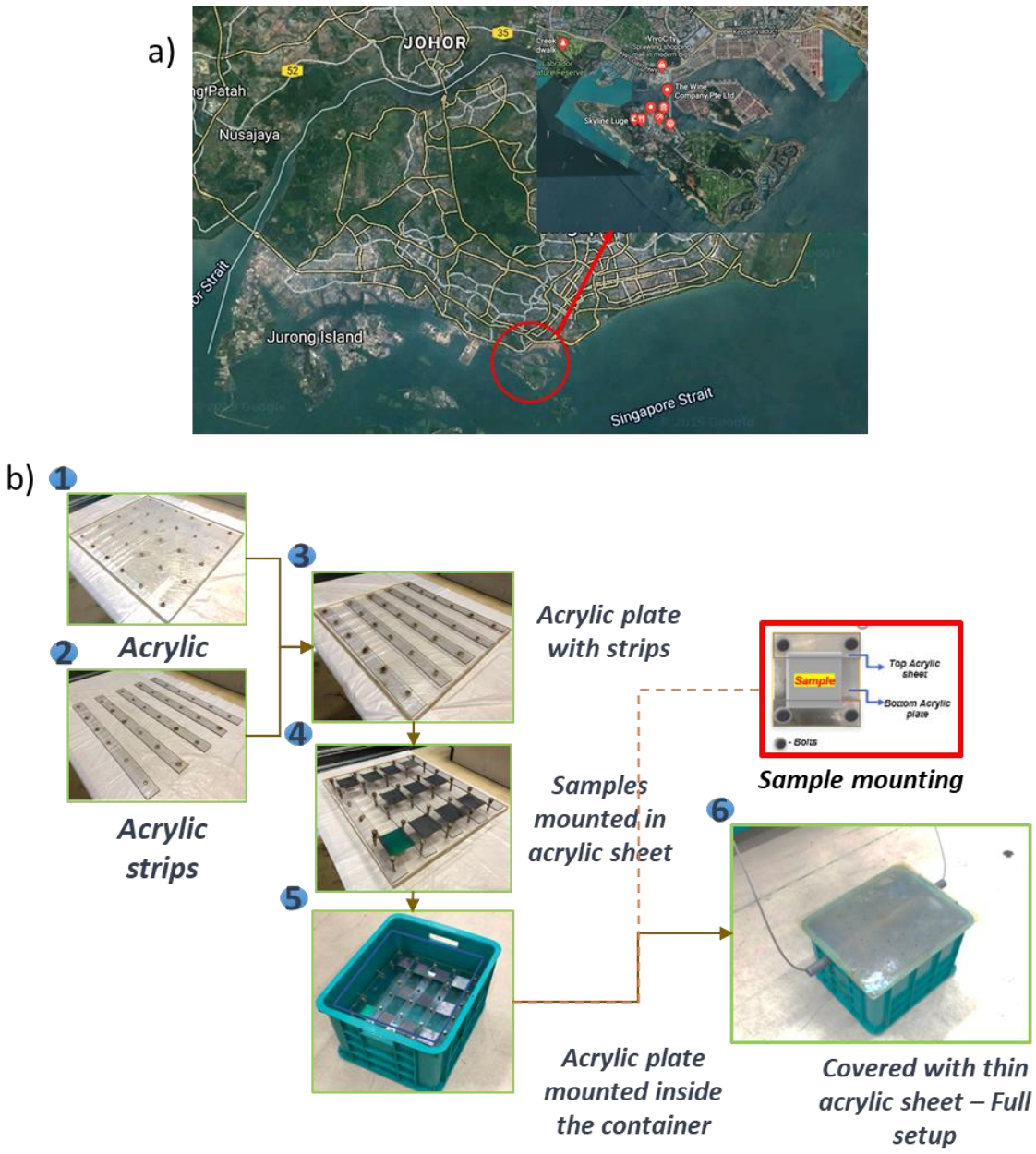

Figure 9: a) Sentosa test site location and b) sample mounting method.

This container is then immersed in seawater at a depth of 1 m during low tide so that the samples are immersed all the time, with a depth of 2 m at high tide (Figure 10). All samples were recovered every 15 days for weight and thickness measurements and then immersed back in seawater for a total reaction time of 60 days. During the immersion tests, temperature, conductivity, salinity, pH and dissolved oxygen (O_2) were measured (Table 4).

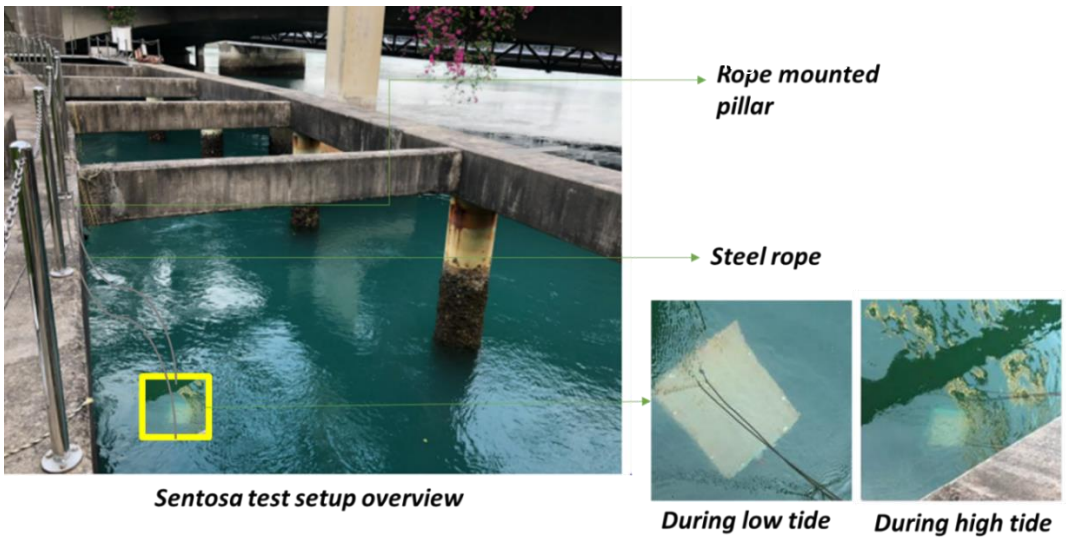

Figure 10: Immersion test facility at NTU Singapore.

Table 4: Seawater quality at the location where the samples were deployed at Sentosa.

Temperature (°C)	Conductivity (µS/cm)	Salinity (ppt)	pH	O_2 (mg/L)
29.7	51300	33.7	7.5	2.4

CORRODYS facility

Samples were also immersed in a 5 m^3 tank continuously supplied with natural seawater from the Port des Flamands in Cherbourg-en-Cotentin (Figure 11a) at a flow rate of 5 m^3/h. This tank serves as a plastic trail with a useful volume of 500 L in which the coupons were exposed. These coupons were previously prepared in order to establish an electrical connection allowing electrochemical monitoring and to protect the uncoated faces and edges of the samples by using an epoxy paint (Figure 11b). This paint was applied after cleaning the substrate surface with ethanol to isolate the 304L substrate in order to study only the coatings or implanted surfaces. The study surface was 4.6 cm^2 *i.e.* one exposed face of 20 x 23 mm. The natural seawater in the trail was continuously renewed at a rate of 360 L/h, which allowed a complete renewal rate of the trail higher than once a day (Figure 11c).

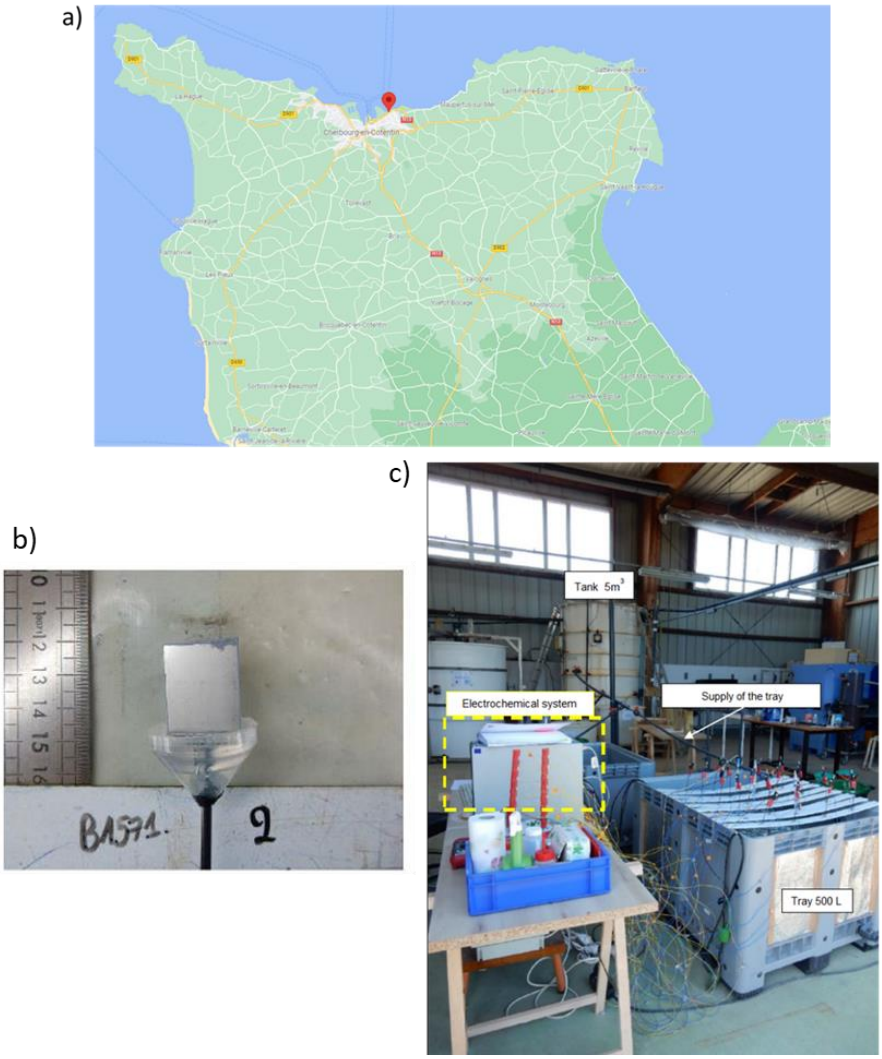

Figure 11: a) Port des Flamands location, b) samples used for immersion tests and c) immersion test facility.

Temperature, conductivity, salinity, pH and dissolved O_2 were measured continuously throughout the 8-week test and the average values are shown in Table 5. Note that the average pH of the seawater is between 7.5 and 8.4, the average conductivity is about 50 µS/cm and the salinity is 35 ppt. The values obtained for both seawaters are close to the averages but some vary such as the temperature and dissolved O_2. The temperature is much higher for the Singapore seawater due to the equatorial climate. Dissolved O_2 is lower for Singapore seawater than for Cherbourg seawater, indicating that only certain aquatic species can survive in Singapore seawater compared to Cherbourg one.

Table 5: Seawater quality at the samples deployed location in Cherbourg.

Temperature (°C)	Conductivity (µS/cm)	Salinity (ppt)	pH	O_2 (mg/L)
11.8	42835	27.6	8.1	10.2

The corrosion free potential was measured continuously on each of the coupons using a multiplexer and three saturated calomel reference electrodes (ECS), showing a potential $E^0_{Hg2Cl2/Hg}$ = 0.242 V/SHE. Each coupon was placed at an identical distance from the reference electrode. It is also important to note that the coating or implanted surface was facing the reference electrode. The coupons were visually inspected and photographed before and after the 8-week test (after biofilm sampling and surface cleaning). However, during this test there were no weight measurements of the samples. At the end of the tests, the samples were removed from seawater and the biofilm was swabbed for microbiological analysis. The following microbiological analyses were performed on the sample biofilm:

- the total aerobic heterotrophic flora (viable and cultivable microbial communities) was measured according to the NF EN ISO 7218 (*Microbiologie des aliments – Exigences générales et recommandations, 79 p., 2007*),
- the total biomass (dead and living microorganisms) was quantified by epifluorescence microscopy,
- the total number of microalgae was counted using a Malassez cell.

2.3 ROUGHNESS AND MECHANICAL PROPERTIES CHARACTERIZATION

2.3.1 Interferometric Microscopy

Interferometric microscopy is based on the principle of white light interferometry coupled with an optical microscope. An interferometer works by merging light sources to form an interference pattern. This interference pattern (fringes) contain information about the sample being studied and can be observed with an optical microscope when the sample is in focus. Two types of interferometer are used in interferometric microscopy depending on the objectives of the microscope: for the 5× objective, a Michelson interferometer and for the 20× objective, a Mirau interferometer. In both configurations, a beam splitter separates a source of white light directed towards the sample (Figure 12). One part is reflected by a reference mirror and the other is directed through the microscope objective towards the surface of the sample, placed at an angle of 90° with respect to the reference plane. Once reflected, the two light beams recombine and interference fringes are formed according to their phase shift. Unlike a Michelson type, the reference mirror of a Mirau interferometer is placed at the level of the beam splitter. The use of two types of objectives is essentially due to the working distance required depending on the desired magnification. During the vertical scan performed by the microscope, the alternation between the white (maximum intensity) and black (minimum) fringes measured by the CCD camera allow determining the relative height of each point on the surface. Therefore, this leads to the 3D mapping of the sample and the determination of the sample roughness. However, this technique can only characterize samples with good reflection (having a mirrored surface) and being flat. The tilted samples can affect the accuracy of the roughness measurements. Moreover, the results of the roughness determination are strongly influenced by the position of the measurement hence, the need to perform several measurements to average the roughness value.

In this study, the roughness of 304L ASS substrate and various coatings was determined using a Contour GT1 (Bruker). For this purpose, three measurements

were performed on each sample at different locations to obtain an average value of the roughness of the sample. If the samples have a high roughness, the surface exposed to the electrolyte during corrosion tests will be much larger than the expected surface. Moreover, a high roughness can create cavities or zones allowing accumulation of the corrosive medium and generate specific corrosion concerns. This can lead to a high uncertainty in electrochemical measurements for rough samples.

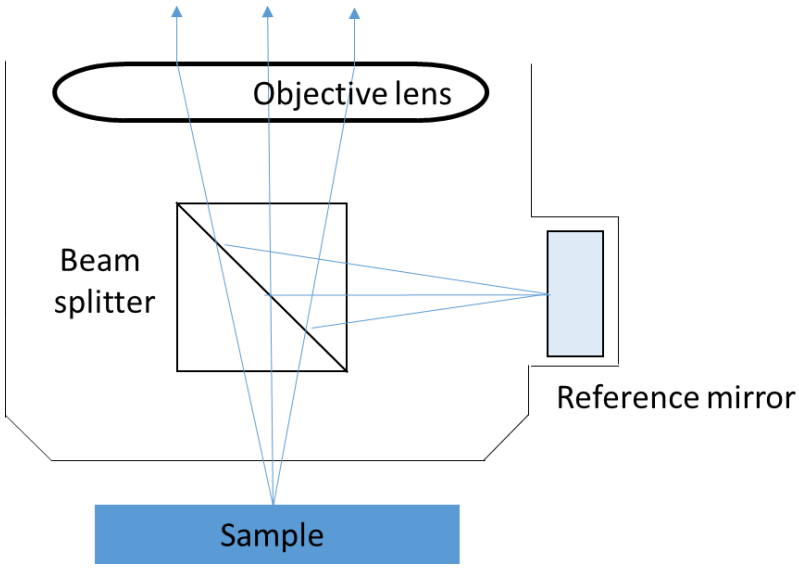

Figure 12: Diagram of an interferometer

2.3.2 Scratch-test

Scratch-test is a destructive method for evaluating the adhesion of a coating on a substrate *i.e.* substrate/coating interface. This technique consists in a diamond indenter (Rockwell tip, Berkovich tip, *etc.*) scratching a coated surface at a certain load and rate. During this displacement, an increasing normal force is applied to the tip until damage to the coating is observed [16, 17]. Various types of damage can be observed on the coating surface such as cracking, flaking and delamination. These types of damage depend mainly on the properties of the substrate, coating and substrate/coating interface [16]. In addition, critical loads (L_C) can be attributed to specific degradation phenomena, thanks to the tracking of normal and transversal loads and acoustic signal and to the observation of the samples. It should be pointed out that this technique does not quantify the fundamental adhesion bond strength of a substrate/coating system as the indenter penetration into the coating can cause high stresses and deformation in both substrate and coating. This technique is mechanically complex and presents an engineering evaluation of the adhesion strength between the coating and the substrate. Therefore, the scratch-test parameters must be chosen carefully.

In this work, the device used is a Fischerscope ST200 tester for analyzing the adhesion of substrate/coating interface. It is equipped with a Rockwell diamond indenter (radius of 200 µm, cone angle of 120°) and a high-resolution microscope with 5× and 20× magnification. The WIN-SCU software controls the measurement system

and records acoustic emission, forces and friction coefficient. The L_C measured in this work correspond to delamination across the entire width of the scratch and are estimated from signals measurements and optical observation. Two series of parameters were used depending on the samples tested:

- A loading speed of 10 N/min and progressive load varying from 0 to 10 N for the study of the etched + coated samples,
- A loading speed of 100 N/min and a progressive load varying from 0 to 50 N during the scratch test of the oxide and multilayer coatings.

3. CALCULATION OF ION IMPLANTATION (SRIM)

SRIM (Stopping Range of Ions into Matter) is a software calculating the ion penetration in materials using a quantum mechanical treatment of ion-atom collisions. This calculation program was developed by James F. Ziegler and Jochen P. Biersack in the 1980s. In addition, new experimental data allow significant improvements and corrections around every six years [18]. This calculation uses statistical algorithms and can be performed for several applications such as ion implantation and sputtering. The initial target parameters (material, composition and density) and the incident ions (nature, energy and angle of incidence) are defined by the user. In principle, the ion energy range is between 10 eV and 2 GeV. The choice of the number of incident particles defines the statistical quality of the calculation. A greater number of incident particles improves the statistics but increases the calculation time. Finally, the information available through this software is the implantation profile of the incident ion, the sputtering efficiency of the different chemical species and the energy exchange by nuclear shock and inelastic diffusion [18]. The SRIM calculation is based on several assumptions: the material is considered amorphous, the atoms are considered as immobile, which excludes recombination phenomena, and only one type of incident ion can be implanted at each calculation.

In this project, TRIM (the Transport of Ions in Matter) calculation program included in SRIM-2008 software is used and consists of a Monte-Carlo calculation following the ion into the target. In our case, the calculation enables estimating the implanted atomic percentage (at.%) of a sputtered species (Ar, Ti and Zr) and its implantation depth on a target material (304L simplified to 72Fe18Cr10Ni). Several simulations are performed to study all the cases *i.e.* different ionization degrees of the species (M^+ and M^{2+}) at a fixed bias voltage related to the ions energy (-900 V). This calculation only allows considering the implantation of one species with only one degree of oxidation according to a unique direction, consequently leading to strong uncertainty on the calculations.

4. CONCLUSIONS

The chemical composition of material chosen as substrate (304L) in this project was determined precisely using GDMS and ICP-OES techniques. In addition, 304L ASS microstructure was characterized by SEM/EBSD to identify the amount of austenite and ferrite phases. The etching and coating steps were performed with two deposition chambers (one in CEA and the other in DEPHIS company) using different deposition processes: HiPIMS and hybrid pulsed DCMS-HiPIMS. Therefore, comparison of the

properties of the substrate/coatings systems should be performed with caution. However, these techniques are complementary because the hybrid pulsed DCMS-HiPIMS method allows to take advantage of the highest ionized fraction of metal (attributed to the use of HiPIMS) and to reach a higher deposition rate (pulsed-DCMS).

Several physico-chemical and structural characterization techniques were used in order to study a large number of properties of the substrate/coating systems. SEM and XRD analyses were mainly performed to characterize the coatings microstructure and crystal phases. XPS was used to give information on thinner depths (up to 10 nm) than XRD (several hundred nm) such as ion etching pre-treated 304L ASS substrate. Atomic scale analyses using techniques such as TEM or APT were performed for the more detailed understanding of the interfaces of the systems: thickness, chemical elements at the interface, *etc*. Finally, the various techniques used are complementary, whether through their detection sensitivity, the area analyzed and the spatial resolution. This shows the interest of multiplying the characterization techniques to better understand the systems properties.

In this work, the behavior of various substrate/coating systems in two aggressive environments was studied: marine and spent nuclear fuel reprocessing environments. For this purpose, electrochemical methods were used to study the corrosion resistance properties of our systems in laboratory. The polarization curves allowed determining the corrosion current density and the corrosion potential. In addition, EIS measurements were carried out to study the evolution of the behavior of the systems over time. Moreover, immersion tests in laboratory but also in natural environment were performed to estimate the long-term corrosion resistance of samples in service conditions. Finally, further characterizations after electrochemical and immersion tests such as SEM observations and EDX profiles or mapping were carried out to allow an understanding of the phenomena involved.

Moreover, roughness of the samples can be estimated using interferometric microscopy technique. A rough sample can lead to a high uncertainty in corrosion tests measurements by modifying the surface exposed to the electrolyte. Scratch-test is used to estimate the substrate/coating adhesion but care must be taken in interpreting the results as the indenter penetration into the coating can cause high stresses and deformation in both substrate and coating. In parallel, calculations using SRIM software were performed to estimate the potential implantation depth and atomic percentage of the ions present during the etching step. In the end, the results obtained by these calculations will be compared with those of the experimental methods.

REFERENCES

[1] Fauvet P. (2012) “Chapter 19: Corrosion issues in nuclear fuel reprocessing plants.” Nuclear corrosion science and engineering (pp. 679-728), Woodhead Publishing, ISBN: 978-1845697655.

[2] Pokor C. (2003) “Caractérisation microstructurale et modélisation du durcissement des aciers austénitiques irradiés des structures internes des réacteurs à eau pressurisée.” CEA-R-6031.

[3] Euro Inox (2007) “Stainless steel: Tables of technical properties.” Materials and Applications Series, volume 5. ISBM 978-2-87997-242-8.

[4] Emery A. (2020) “Corrosion intergranulaire des aciers inoxydables austénitiques en milieu acide nitrique oxydant.“ Université Paris sciences et lettres. NNT : 2020UPSLM031. Tel-03097345.

[5] Prasad Rao K., Uma Maheshwar Rao A. & Gururaja G. J. (1988) “Effect of delta ferrite content on the corrosion resistance of type 316 clad metals.” Werkstoffe und Korrosion 39: 135-142.

[6] Balachandran U. & Eror N. G. (1982) “Raman spectra of titanium dioxide.” Journal of Solid State Chemistry 42: 276-282.

[7] Mazza T., Barborini E., Piseri P. & Milani P. (2007) “Raman spectroscopy characterization of TiO_2 rutile nanocrystals.” Physical Review B 75, 045416.

[8] Castrejon-Sanchez V. H., Camps E. & Camacho-Lopez M. (2014) “Quantification of phase content in TiO_2 thin films by Raman spectroscopy.” Superficies y Vacio 27: 88-92.

[9] Barberis P., Merle-Mejean T. & Quintard P. (1997) “On Raman spectroscopy of zirconium oxide films.” Journal of Nuclear Materials 246: 232-243.

[10] Basahel S. N., Ali T. T., Mokhtar M. & Narasimharao K. (2015) “Influence of crystal structure of nanosized ZrO_2 on photocatalytic degradation of methyl orange.” Nanoscale Research Letters 10:73.

[11] Blavette D., Bostel A., Sarrau J. M., Deconihout B. & Menand A. (1993) “An atom probe for three-dimensional tomography.” Nature 363: 432-435.

[12] Kelly T. F. & Miller M. K. (2007) “Invited review article: atom probe tomography.” Review of scientific instruments 78, 031101.

[13] Lee J. Y. & Ahn J.-P. (2016) “Focused ion beam-based specimen preparation for atom probe tomography.” Appl. Microsc. 46: 14-19.

[14] Noor N. M., Othman R., Mohd Hatta M. A. & Ani M. H. (2014) “Determination of linear Tafel region from piecewise linear regression analysis.” International Journal of Electroactive Materials 2:22-27.

[15] Etor A. (2009) “Electrochemical measurement of crevice corrosion of type AISI 304 stainless steel.” Master Thesis, University of Saskatchewan, Canada.

[16] Belov V. K., Gubarev E. V;, Papshev A. V., Gofman N. G. & Begletsov D. O. (2019) “Development of a scratch test method to determine adhesion and strength properties of coated steel sheets.” IOP Conf. Series: Materials Science and Engineering 597, 012012.

[17] Tlili B., Nouveau C., Benlatreche Y., Mustapha N. & Lambertin M. (2009) “Hardness and scratch response of PDV multilayer coatings.” 3eme Congres International Conception et Modelisation des Systemes Mecaniques CMSM’2009.

[18] Siad A. (2016) “Etude numérique et expérimentale de la croissance de couches minces déposées par pulvérisation réactive. ” Mécanique des matériaux. Ecole nationale supérieure d’arts et métiers. NNT : 2016ENAM0024. Tel-01418118.

Surface modification and interface engineering by HiPIMS pre-treatment

INTRODUCTION

304L austenitic stainless steels (ASS) are widely used for components in nuclear fuel reprocessing plants and marine environment, which can be subject to corrosion. One of the most promising solution studied in this work to improve the lifespan of ASS in service conditions is based on the use of a protective coating performed by PVD HiPIMS. However, the overall performance of the coating system not only depends on the coating itself but also on how it is bonded to the substrate, which relates to the substrate pre-treatment, and on the coating architecture (*i.e.* interlayer and/or multilayer). Therefore, a coating system has to be optimized step by step: etching pre-treatment, bond coat synthesis and coating deposition. Yet, it has been recognized that the corrosion is mainly initiated from coating defects (pores, pinholes or scratches) and species trapped at the substrate/coating system interfaces [1-3]. Thus, defect-free interfaces should improve adhesion and anticorrosive properties. In HiPIMS, the highly ionized metal vapour can be used for *in situ* surface preparation such as etching [4] by applying a high negative potential (bias voltage) to the substrate-holder. Both ionized Ar and ionized target material, which are accelerated by the substrate bias [5, 6], remove contaminants and impurities from the surface and may also be implanted in the substrate. Furthermore, when the substrate and coating materials have thermal expansion coefficients and crystal lattices that differ too much, an interlayer/bond coat is often required to allow coating adhesion [7-10]. Hence, working on the optimization of the substrate/coating interface is a processing route to improve the performance of the coated component under service conditions. The main objective is to form a clean, defect-free and as dense as possible interface, leading to the highest adhesion strength.

In this chapter, focus is placed on the influence of the etching step on the substrate/metallic bond coat system. For this purpose, different types of etchings were performed and their effect on the surface was analyzed using characterization techniques such as XRD, XPS, TEM and APT. In addition, ion implantation on the surface was calculated using SRIM software to estimate the implantation depth. This allows comparing the theoretical calculations with the experimental results. Then, substrate/metallic bond coat adhesion measurements were performed. Electrochemical investigations of the etched samples and etched and metallic bond coat deposited samples were performed in a nitric acid solution at boiling temperature representative of the end of evaporation stage of nuclear waste fuel reprocessing and in a NaCl solution at ambient temperature. The electrochemically investigated surface was characterized to assess the observed phenomena. Finally, immersion tests in media simulating the conditions of use or in natural environment were performed. Polished samples were used for the electrochemical measurements to better control the active surface and understand the corrosion mechanisms, whereas for immersion tests, unpolished samples were immersed in order to be closer of the real conditions of use. Note that some of the results presented in this chapter are the subject of a scientific paper submitted to the journal Surface and Coatings Technology.

1. ETCHING PRE-TREATMENT AND METAL COATING DEPOSITION

1.1 PROCESS PARAMETERS

1.1.1 Etching step

During the first year of study (Appendix 1) to investigate the influence of etching parameters on the substrate/coating interface, the presence of substrate elements (Cr and Fe mainly) contamination was observed at the interface due to resputtering of the substrate-holder and deposition chamber walls, limiting the conclusions that could be drawn on the final properties of the coated component. All the characterizations performed afterwards during this first year (microstructural observations, electrochemical measurements, immersion tests in CEA and NTU) were thus performed on these contaminated samples. Therefore, two different approaches were tested in order to reduce this contamination and to obtain etching parameters leading to efficient etching: change of the sample suspension method and modification of etching process parameters. The effectiveness of these etchings was verified by XPS analysis, allowing observing the chemical elements present at the extreme surface of the substrates. Noting that one estimates that an etching is effective when the elements of the substrate are mainly present in their metallic form in XPS analysis.

An efficient etching method was identified and consists on a three-hour treatment (seasoning) performed to cover the walls of the empty deposition chamber and the substrate-holder with the material to be deposited. The aim is to limit contamination from resputtering of the substrate-holder and/or the chamber walls. Note that seasoning is routinely performed on chemical vapor deposition (CVD) chambers [11, 12]. Then, the etching step is performed in a static configuration of the substrate-holder. The substrates (10 samples per batch) are suspended on the sample holder using stainless steel suspension wires. Three types of *in situ* plasma etching pre-treatments of the 304L substrate are studied in this work:

- argon ions using a diode or glow discharge (Ar^+),
- titanium and argon ions produced by a HiPIMS discharge over a titanium target (Ti^+),
- and zirconium and argon ions using a HiPIMS discharge over a zirconium target (Zr^+).

During these three etching experiments, the substrate-holder (bias) voltage is the same, while the target voltage varies for metal ion etchings (Table 1).

Table 1: Parameters of etchings using the new technique.

Parameters	**Ti^+ etching**	**Zr^+ etching**	**Ar^+ etching**
Pressure (Pa)	0.57	0.57	0.97
Argon flow (sccm)	100	100	100

Duration (min)	20	20	20
Target voltage (V)	600	400	X
Pulse width (µs)	20	20	X
Extinction time (µs)	1980	1980	X
Frequency (Hz)	250	250	X
Substrate-holder voltage (V)	-900	-900	-900
Substrate-holder power max (W)	2500	2500	2500

After the etching step, the substrates are left to cool down for one hour in the deposition chamber to prevent thermal stresses and shock. Note that the chamber temperature increases as the etching proceeds until it reached about 49°C at the end of the etching process. Then, the substrates are removed and weighed. The weight balance results from material loss via etching (an initial weighing was performed before putting the samples into the vacuum chamber). The thickness loss associated with the etching is calculated using the density of 304L, *i.e.* 7.93 g/cm^3 and shown in Table 2.

Table 2: Thickness loss calculated from weight measurements.

	Ti^+ etching	**Zr^+ etching**	**Ar^+ etching**
Average thickness loss (nm)	190 ± 120	450 ± 250	530 ± 200

The thickness losses obtained vary from one type of etching to another. In the case of diode discharge (Ar^+ etching), the cleaning effectiveness is increased since all the surfaces of the samples are immersed in the plasma, while only one side is exposed during metal ion etching. On the other hand, for Ti^+ etching, the lower thickness loss can be due to the back attraction of ionized metals species to the target, especially Ti^{2+} that mainly composed the Ti-HiPIMS discharge. This means that a lower amount of ions is available for etching [7]. Moreover, the standard variations show that the thickness losses change from one sample to another in the same batch. This can be related to edge effect, meaning that the more ions are drawn to the edges and corners of samples and leads to increase the etching rate [13].

1.1.2 Metal coating deposition

A metal coating (Ti or Zr) of a thickness of about 200 nm (called metallic bond coat in this chapter) is synthesized after *in situ* plasma etching. The bond coat will be used

as a metallic interlayer in the final architectural substrate/coating system to improve the adhesion of metallic or oxide coatings on the 304L ASS substrate. This thickness was chosen after performing a literature review showing the use of bond coat of about 200 nm [14, 15], as mentioned in section 1.2.2 of the chapter “Literature review”. This thickness is obtained in 100 minutes of deposition using the TriPros machine in threefold rotation and two targets of the material to be sputtered. This deposition time was calculated by carrying out preliminary coatings on a 304L substrate and analyzing them by SEM to determine the thickness deposited. All the parameters used for coating deposition are summarized in Table 3. After deposition, a two-hour rest allowed the samples to cool down and limit thermal stresses and shock. Then, they are removed from the vacuum chamber.

Table 3: Deposition parameters for all the metallic bond coats synthesized using the TriPros machine.

Pressure (Pa)	0.55
Ar flow (sccm)	100
Duration (min)	100
Target voltage (V)	900
Pulse width (µs)	50
Extinction time (µs)	950
Frequency (Hz)	500
Target power (W)	2000
Substrate-holder voltage (V)	-100
Substrate-holder power (W)	2000

The different parameters of etching and coating deposition are detailed in this section. Focus is now placed on the influence of the etching parameters on the substrate/metallic bond coat system, using various characterization techniques.

2. SURFACE MODIFICATION AND INTERFACE ENGINEERING

2.1 MODELING OF IMPLANTATION PROFILES

First, a modeling of the ion implantation is performed with the SRIM-2013 software in order to estimate the implantation depth and the amount of implanted ions into the surface. The calculated implantation profiles of Ar, Ti, and Zr using the SRIM-2013

software (Figure 1) all display Gaussian-like shapes with a tail penetrating deep into the solid. It should be noted that SRIM calculation is based on several assumptions: the material is considered amorphous, the atoms are considered as immobile, which excludes recombination phenomena, and only one type of incident ion can be implanted at each calculation. The heaviest ion Zr shows a narrower distribution (0-3.5 nm) than for the lighter ions Ti (0-4 nm) and Ar (0-4.5 nm), a mass dependence previously reported by Cano *et al.* [16]. The maximum concentration, corresponding to 10 at.% for Ti and Ar and around 12 at.% for Zr, is attained at a penetration depth of approximately 1.2 nm for Ti and Ar, and up to 1.4 nm for Zr. These calculations indicate that, under our conditions *i.e.* ions at 0.9 keV, these ions are implanted to a very shallow depth (from 0 up to 4.5 nm) that can be even more limited when taking into account the experimental conditions. Also, note that these calculations only allow considering the implantation of one species with only one degree of oxidation according to a unique direction. Consequently, the results obtained may be overestimated *i.e.* altering the actual localization and profile distribution of the elements in the substrate.

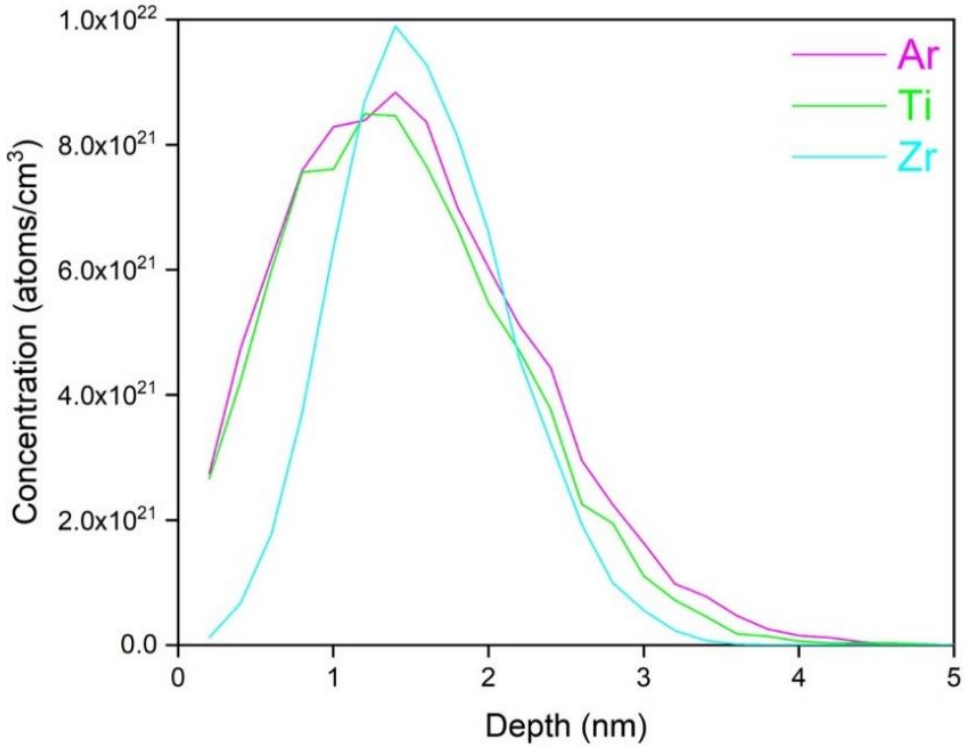

Figure 1: Concentration profiles of Ar, Ti, and Zr species on 304L stainless steel calculated using SRIM 2013 versus implantation depth for 10^4 ions.

2.2 STRUCTURAL AND CHEMICAL ANALYSES OF ETCHED SAMPLES

GAXRD patterns at 0.5° incident angle performed for the bare 304L substrate and etched specimens are shown in Figure 2. At an incident angle of 0.5°, the penetration depth of X-rays is estimated to about 95 nm in 304L according to calculations performed with the AbsorbDX software (Bruker). For the initial (unetched) 304L ASS substrate, austenite (γ) and ferrite (α) phases are observed. The austenite contributions at 43.8 (111), 50.9 (200), and 74.8°2θ (220) are more intense than the

ferrite ones at 44.7 (110), 65.1 (200), and 82.3°2θ (211). The XRD peaks of all etched samples are broader compared to the initial 304L substrate. For instance, the γ (200) contributions at 50.9°2θ for the Ar^+-, Ti^+- and Zr^+-etched samples are wider by about 6, 13 and 21%, respectively. Moreover, the amplitude of the austenite (γ) contribution decreases, and that of the ferrite (α) contribution almost disappears, with only two residual contributions at 44.7 and 82.3° 2θ, after metal ion etchings (Ti^+ and Zr^+).

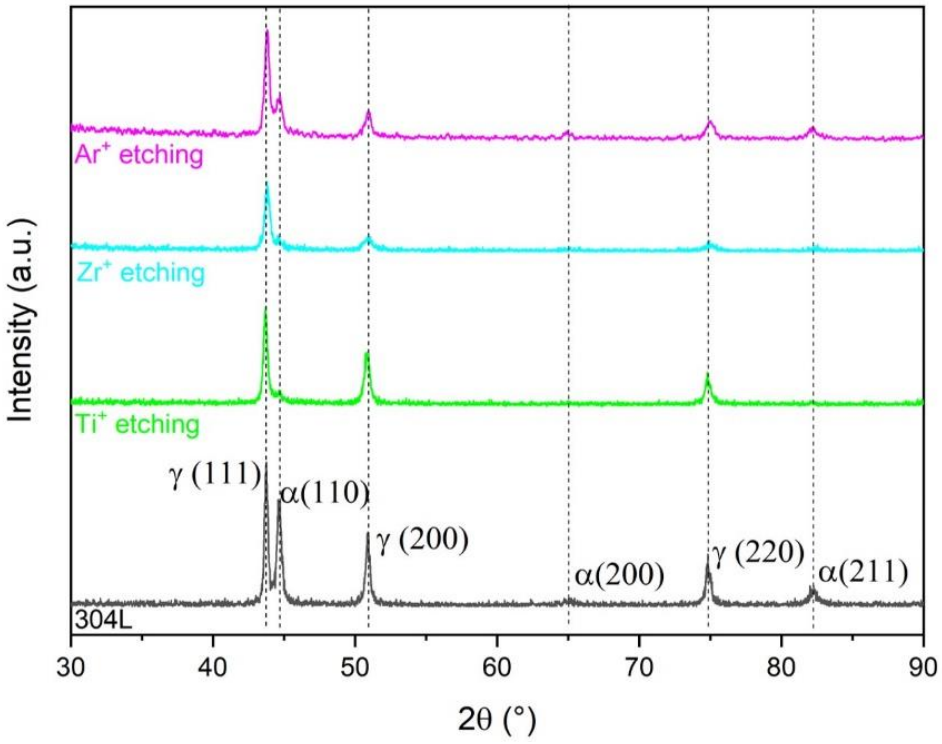

Figure 2: GAXRD patterns at 0.5° incident angle for the initial and etched (Ar^+, Zr^+ and Ti^+) 304L steel samples.

The three etchings do not trigger the formation of new phases, in accordance with previous results on implantations of Ti and Ar^+ in steels [17, 18] or of other elements in stainless steel [18, 19]. The increased in width and the decrease in amplitude of the XRD peaks for ferrite and austenite indicate an amorphisation after all etchings. Such phenomenon has been reported for ASS irradiated by 80 keV N_2^+, 170 keV Ag and 150 keV Mo ions because incident energetic ions are able to break the intrinsic stainless steel structure [19, 20]. These observations suggest that highly energetic incident ions create damages and deformations in the crystalline lattice, thereby reducing crystallinity [18, 20, 21]. Note that these ion energies are much higher than those used in etching (0.9 keV for M^+ and 1.8 keV for M^{2+}). This amorphisation is stronger for the Ti^+- and Zr^+-etched samples because of the simultaneous bombardment from metal and Ar^+ ions, and leads to the disappearance of the ferrite phase (1-2 % in initial 304L as mentioned in section 1.1 of the chapter “Materials and methods”). In comparison, Ar^+-etched samples undergo only Ar^+ bombardment, which decreases only the amount of ferrite. This could result in a different effect of metal (Ti^+ or Zr^+) and Ar^+ etchings on corrosion resistance.

Figure 3 shows the XPS (analyzed thickness from 1 to 10 nm) survey spectra of the initial and etched 304L steel substrates. In addition to C and O, all spectra display the

304L main elements, *i.e.* Fe, Cr and Ni. The signals from Ar, Ti, and Zr are observed for etched surfaces, indicating their presence on the extreme surface as implanted ions. Quantification of XPS spectra from the peak areas in spectra confirm the presence of substantial amounts of Ti (7 at.%) and Ar (5 at.%) after Ti^+ etching. Similarly, after Zr^+ etching, Zr and Ar amount each to 6 at.% at the extreme surface of the substrate. Finally, in the case of Ar^+ etching, Ar (4 at.%) and Zr (7 at.%) are significant. The surface compositions of the Ar^+- and Zr^+-etched samples are similar to one another according to the XPS analysis, whereas the XRD analysis (Figure 2) suggests that the samples have a different phase composition on the surface. The unexpected Zr contribution observed on Ar^+-etched samples can be attributed to resputtering effects from the vacuum chamber walls and substrate-holder.

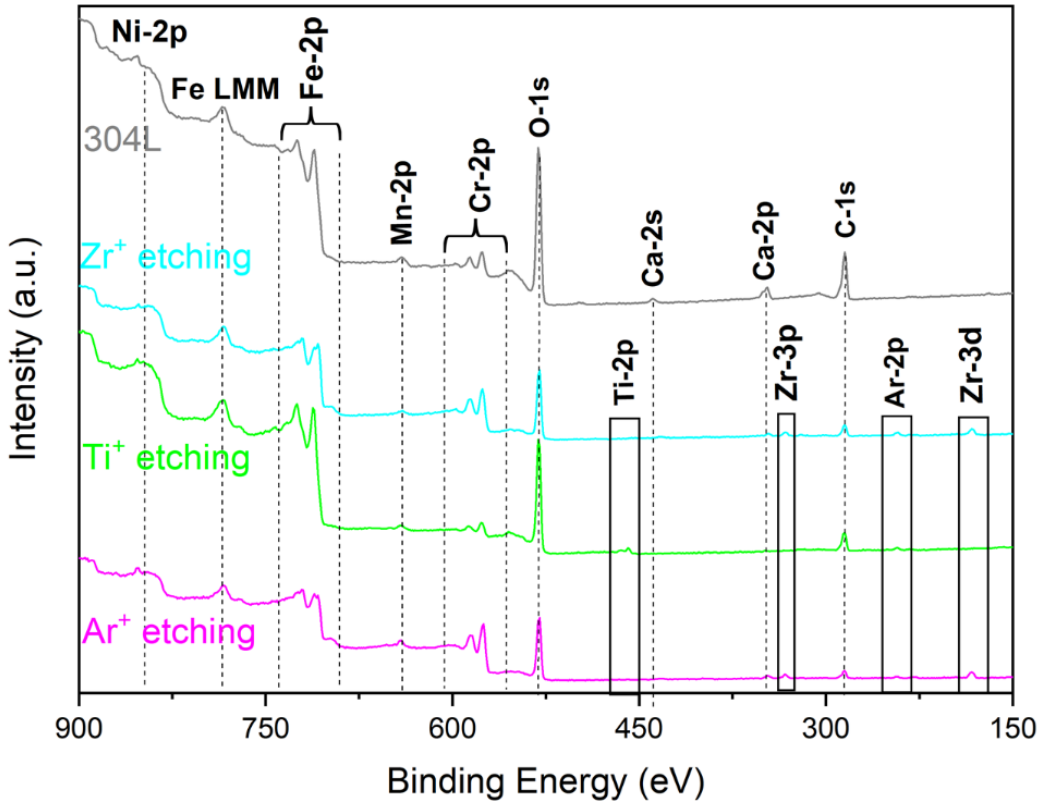

Figure 3: XPS survey spectra of the initial and etched 304L steel samples.

Figure 4 reveals differences between the XPS spectra of O 1s, Cr 2p, Fe 2p, Zr 3d, Ar 2p, Ti 2p, Ni 2p, and C 1s levels for the 304L steel and Ar^+-, Ti^+- or Zr^+-etched samples. For all samples, typical contributions from surface contamination are observed such as C (Figure 4h), as the analyses were performed without any *in situ* surface cleaning in the XPS chamber.

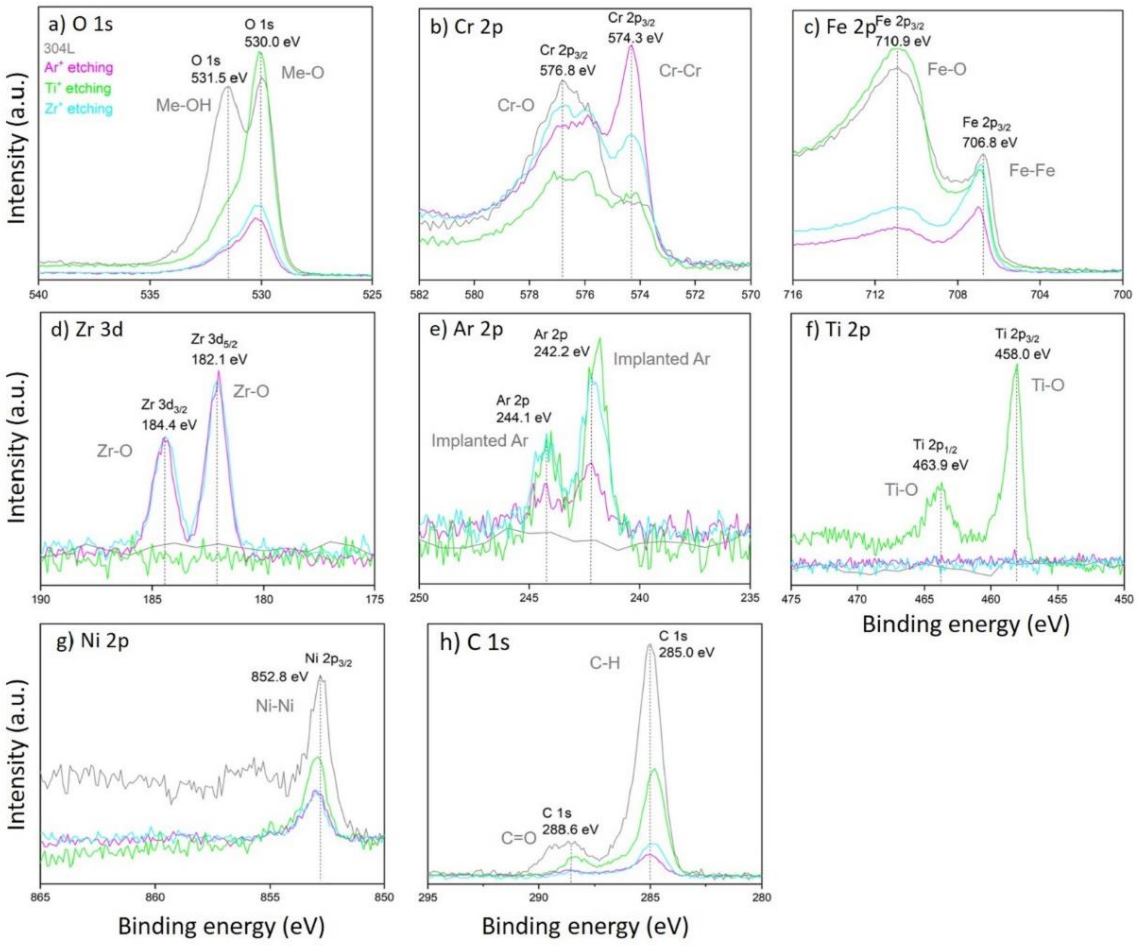

Figure 4: XPS region spectra of the 304L steel and etched samples.

Previous XPS analyses of the 304L steel substrate suggested the conspicuous presence of metal hydroxides (Fe or Cr hydroxides at 531.5 eV for O 1s) [16] and metal oxides (oxides at 530.0 eV for O 1s [16], Cr_2O_3 at 576.8 eV for Cr $2p_{3/2}$ [17, 20], and Fe_2O_3 at 710.9 eV for Fe $2p_{3/2}$) [16]), which is consistent with the literature. However, the contribution at 531.5 eV for O 1s can also be attributed to the surface contamination of the samples. Contributions at 574.3, 706.8, and 852.8 eV are attributed to metal Cr (Figure 4b), Fe (Figure 4c), and Ni (Figure 4g), respectively [17, 20, 22]. That only Ni is present in only metal form is explained by the preferential oxidation of Fe, Cr [23, 24]. These results indicate that the native passive layer formed on the 304L surface is mostly made of Fe and Cr species in oxide and hydroxide forms, which could be consistent with the formation of a mixed Fe(III) and Cr(III) oxy-hydroxide layer reported in the literature [23-26].

Etched samples exhibit similar contributions in shape and position for each electronic level but with distinct intensities. The hydroxides contribution at 531.5 eV for O 1s decreases in amplitude and becomes a shoulder of the oxide peak at 530 eV after Ar^+, Ti^+, or Zr^+ etching (Figure 4a). For Cr 2p, the peak at 576.8 eV assigned to Cr(III) oxide tends to decrease in intensity, especially for Ti^+ etching. On the other hand, the metal contribution at 574.3 eV increases after etching (Figure 4b), especially after Ar^+ and Zr^+ etchings (etched thicknesses of about 1050 nm for Ar^+ etching and 450 nm

for Zr^+ etching, as mentioned in Table 2). For Fe 2p, the signal associated with the Fe(III) oxide at 710.9 eV decreases after Ar^+ and Zr^+ etchings (Figure 4c). This decrease in intensity can indicate the decrease in the concentration of Cr(III) oxide *i.e.* Cr_2O_3, after Ti^+ etching, and Fe_2O_3 for Ar^+ and Zr^+ etchings, hinting at removal of the surface oxide layer. Moreover, TiO_2 and ZrO_2 form preferentially to Cr_2O_3 and Fe_2O_3 according to the Ellingham diagrams [27]. It is assumed that this oxidation occurred when the samples were removed from the deposition chamber and in contact with air. The metal contribution increases in intensity with etching, which could indicate that the surface oxide layer decreases in thickness with etching [28].

Figure 4d shows the Zr $3d_{3/2}$ (184.4 eV) and Zr $3d_{5/2}$ (182.1 eV) contributions attributed to Zr oxide, most likely ZrO_2 [20, 29], after Zr^+ and Ar^+ etchings. Note that the observation of the Zr oxide peak after Ar^+ etching is due to a Zr contamination from the vacuum chamber. The Ar 2p XPS spectrum (Figure 4e) reveals two bands at 242.2 eV and 244.1 eV corresponding to implanted Ar as already shown in [30] for all etchings. For Ti^+-etched substrates, two Ti 2p peaks are observed on the spectra (Figure 4f) at binding energies of 463.9 (Ti $2p_{1/2}$) and 458 eV (Ti $2p_{3/2}$), and are attributed to TiO_2 [31-33]. There is no identified contribution from metal Ti (454.1 eV) or Zr (178.9 eV). This suggests that, in addition to Fe and Cr, Zr and Ti formed oxides on the surface when samples were exposed to ambient air after being withdrawn from the deposition chamber, due to their affinity with O [34]. This formation of surface Ti or Zr oxide upon etching is an undisputable evidence of surface modification. In addition, the metal ions can be incorporated into the substrate by substituting lattice atoms (replacements) [6]. In our case, it can be assumed that Ti and Zr are implanted in the crystal lattice of ASS (in substitution) during etching then oxidation occurs promoting the formation of TiO_2 and ZrO_2, which are much more stable than Cr_2O_3 and Fe_2O_3.

A schematic drawing of the structure obtained in the substrate surface after the three types of etching is shown in Figure 5. For this purpose, the atomic percentages determined by XPS were used *i.e.* Ti (7 at.%) and Ar (5 at.%) after Ti^+ etching, Zr (6 at.%) and Ar (6 at.%) after Zr^+ etching and Ar (4 at.%) after Ar^+ etching (Figure 3). Note that the unexpected contribution of Zr in the Ar^+ etching was not considered for the modeling as it is due to resputtering effects from the vacuum chamber walls and substrate-holder and should not be usually observed. The atomic radii of the Fe (126 pm) and Cr (128 pm) substitution sites and the C (70 pm) interstitial site are used to make a simplified schematic drawing of FCC structure of 304L. As mentioned above, Ti (147 pm) can substitute to Cr and Zr (160 pm) can substitute to Fe in this structure. Moreover, Ar (71 pm) can be incorporated in interstitial sites [6].

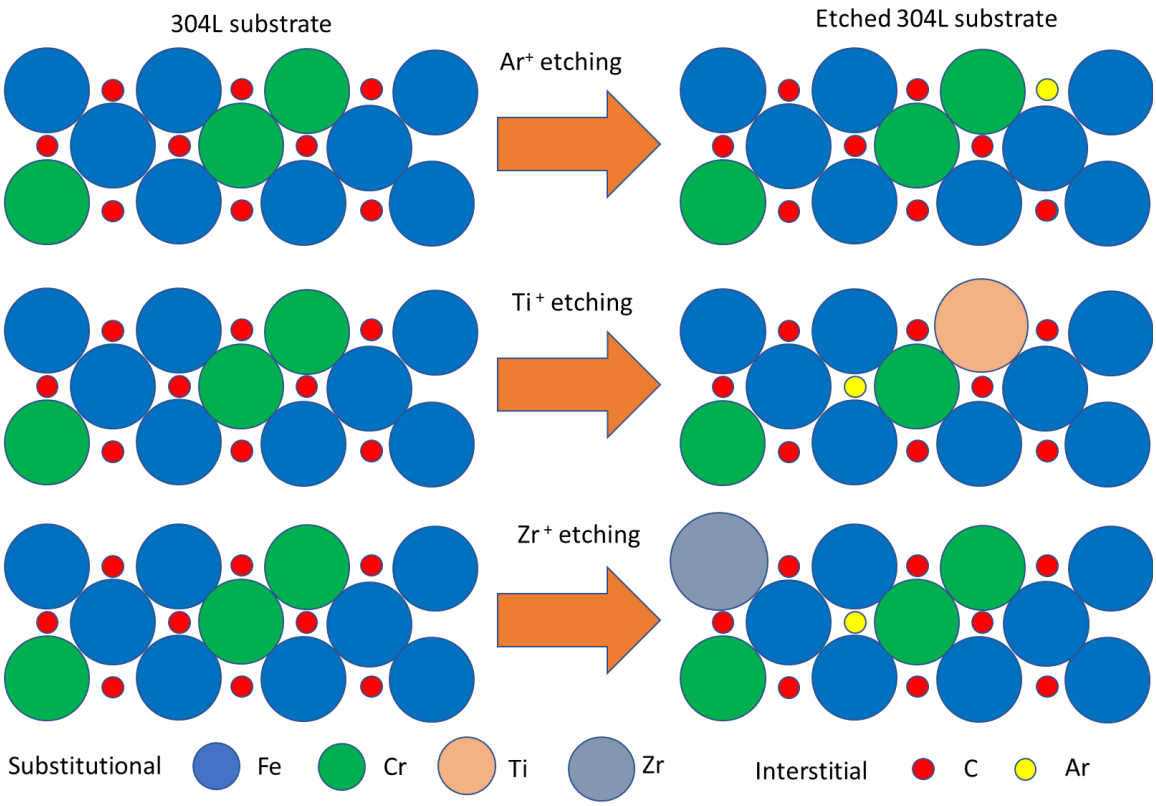

Figure 5: Schematic drawing in 1D of the substrate surface structure after a) Ar^+, b) Ti^+ and c) Zr^+ etching.

Figure 6 shows the XPS depth profiles of the initial substrate and for the Ti^+- and Zr^+-etched samples. It is not relevant to present the results for the Ar^+-etched sample since the XPS depth profiles are measured using a 1 keV Ar^+ ionic beam for surface erosion. The native surface layer is composed of a mixture of Fe(III) and Cr(III) oxides (up to around 70 at.% and 12 at.% at the surface, respectively; Figure 6a). In addition, a Ni enrichment is observed near the oxide/metal interface, which is due to the selective oxidation of Fe and Cr compared to Ni [22, 25, 26]. The oxide/metal interface seems broader after etching. Depth profiles also confirm that the amount of Fe(III) oxide decreases upon Ti^+ or Zr^+ etching (from around 70 at.% to 62 at.% for Ti^+ and 29 at.% for Zr^+). The depth profiles also confirm the presence of Ti and Zr in an oxidized state on the extreme surface after Ti^+ or Zr^+ etchings. However, the Ti and Zr depth profiles do not show Gaussian shapes, contrary to previous observations [24, 39] and SRIM calculations (Figure 1). In contrast, the amounts of metal Fe, Cr, and Ni increase along with the etched depth and reach stable levels corresponding to bulk 304L.

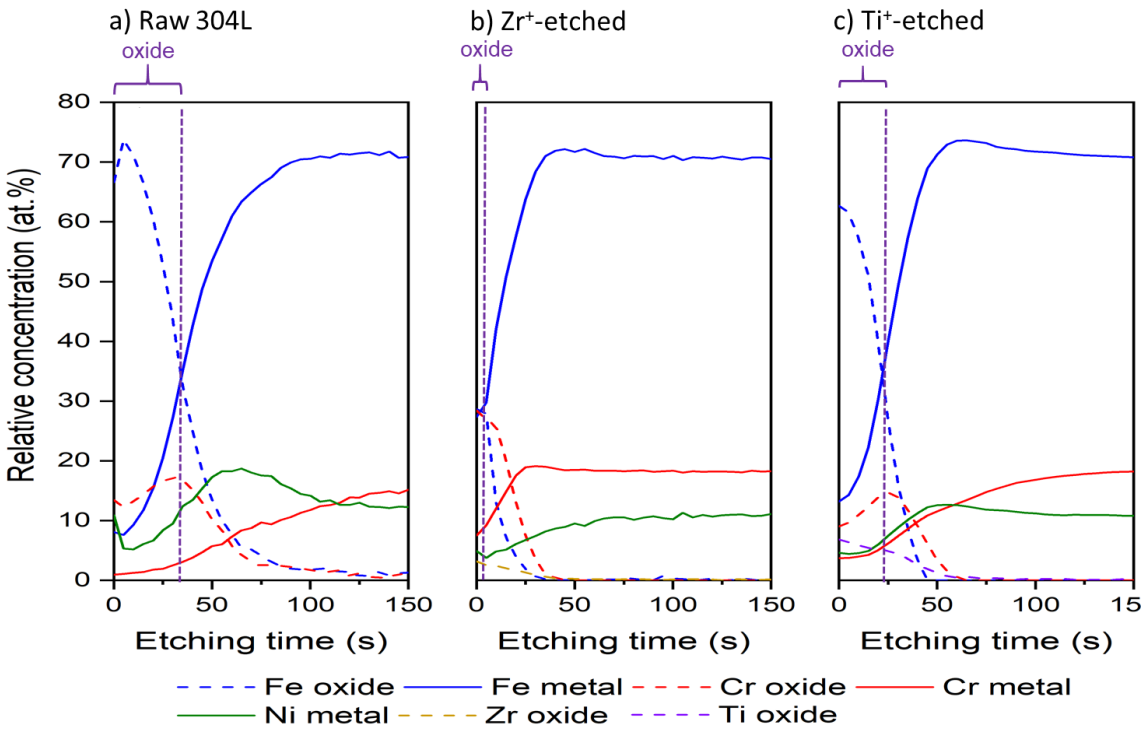

Figure 6: XPS depth profiles of (a) 304L steel and (b) Zr^+- and (c) Ti^+-etched samples.

As the erosion rate varies according to the nature of the layers (chemical composition), it is difficult to give an exact value of the thickness of each layer without prior calibration. Therefore, same thicknesses of different elements could be sputtered in different times. Further analyzes are needed such as GDOES to estimate the oxide layers thicknesses. However, by comparing the amount of Ti and Zr initially implanted with the amounts estimated by the depth profiles, it can be concluded that all Ti and Zr are oxidized in the oxide layer formed because similar amounts are observed at the extreme surface. Therefore, the thickness of the oxide layers formed in these two cases (Ti^+ and Zr^+ etchings) could be approximated to the implanted thickness estimated by the SRIM calculations (Figure 1) *i.e.* 3.5 nm for Zr and 4 nm for Ti. The XPS results show a higher metal contribution from the substrate elements for Zr^+- and Ti^+-etched samples than 304L ASS (Figure 4), which could indicate that these oxide layers are thinner than the native one of the 304L substrate.

The previous XPS results allow estimating the composition of the different surface layers (Figure 7). The native oxide layer of the 304L steel substrate is usually described as a mixture of Fe(III) and Cr(III) oxides and hydroxides (Figure 7a) [23, 25, 26]. For the etched samples (Figure 7b, c), the hydroxide species at the extreme surface disappear according to our XPS spectra analysis and a bilayer model seems to be present. The film shows an outer layer made of Fe(III), Cr(III) and Ti(IV)/Zr(IV) mixed oxides, and an inner layer of Ti(IV)/Zr(IV) and Cr(III) mixed oxides. Note that no further analysis was performed on these etched samples due to the need for a thin film (at least few nanometers) to carry out further characterizations such as TEM or APT.

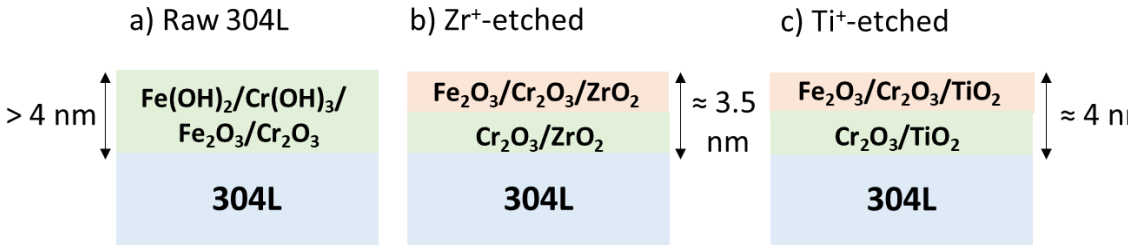

Figure 7: Surface layers of a) 304L steel, b) Zr^+-etched and c) Ti^+-etched samples.

2.3 INTERFACE CHARACTERIZATION

2.3.1 Chemical analyzes

First, crystalline structures of 200 nm-thick bond coats are investigated by glancing angle X-ray diffraction (GAXRD) with an incident angle of 0.5°. At an incident angle of 0.5°, the penetration depth of X-rays is estimated to about 95 nm for the 304L ASS, 220 nm for Ti and 227 nm for Zr according to calculations performed with the AbsorbDX software (Bruker). Therefore, the substrate is expected to be observed even at such a low incidence angle. For the Ti-coated sample diagram, contributions from the 304L substrate and metallic Ti are detected (Figure 8). Austenite (γ) phase from the substrate is observed for both Ti-based samples at 43.8 (111) and 50.7 (200). In addition, a γ contribution at 74.9 (220) is noticed for the Ti^+-etched and Ti-coated sample. The metallic Ti contributions are determined using the Joint Committee on Powder Diffraction Standards (JCPDS) database (PDF 00-044-1294) at 35.1 (100), 38.5 (002), 40.1 (101) and 62.9°2θ (110) for both Ti-based samples. Moreover, Ti contributions at 70.7 (103) and 76.2°2θ (112) are noticed for the Ar^+-etched and Ti-coated sample. The Ti^+-etched and Ti-coated sample shows a preferential orientation along the (101) axis compared to the Ar^+-etched and Ti-coated sample, which could indicate an effect of the Ti^+ etching on the crystalline structure of the Ti bond coat. Note that oxide contributions are absent, probably hidden in the baseline due to their too small thicknesses.

Austenite (γ) contributions from 304L are noticed for the Zr-coated samples (Figure 8) but ferrite (α) contributions are also observed at 44.6 (110) and 65.1°2θ (200) depending on the sample studied. The observation of the substrate below the bond coat is coherent with the penetration depths estimated for Ti and Zr. These ferrite contributions are not present on the GAXRD pattern of the Zr^+-etched and Zr-coated sample, which is consistent with the XRD results on the etched samples (Figure 2). In addition, peaks associated with metallic Zr (PDF 01-078-2921 for α-Zr reference) are noticed at 31.9 (100), 35.0 (002), 36.6°2θ (101) for the Zr-coated sample. A contribution at 65.8°2θ (103) is additionally observed for Zr^+-etched and Zr-coated. In comparison, the Ar^+-etched and Zr-coated shows less contribution from Zr metal and the peaks are wider, indicating that the coating is less crystallized than the others. Moreover, Ar^+-etched and Zr-coated and, unetched and Zr-coated samples are preferentially oriented along the (100) axis whereas there is no real preferential orientation observed for the Zr^+-etched and Zr-coated sample. This could indicate that Ar^+ etching and no etching have a similar effect on the crystal structure of the Zr bond

coat. In both cases, Ti and Zr bond coats are polycristalline (several diffraction planes).

Further analysis is required to understand if and how the etching type can influence the bond coat constitution and structure. Differences of the crystallization structures of the bond coat can be observed on these XRD patterns, which could indicate an influence of the type of etching on the growth mechanism of the coating. It can be assumed that the implanted metal species could act as preferential nucleation sites for the bond coat growth and promote an epitaxial film, at least on the first layers.

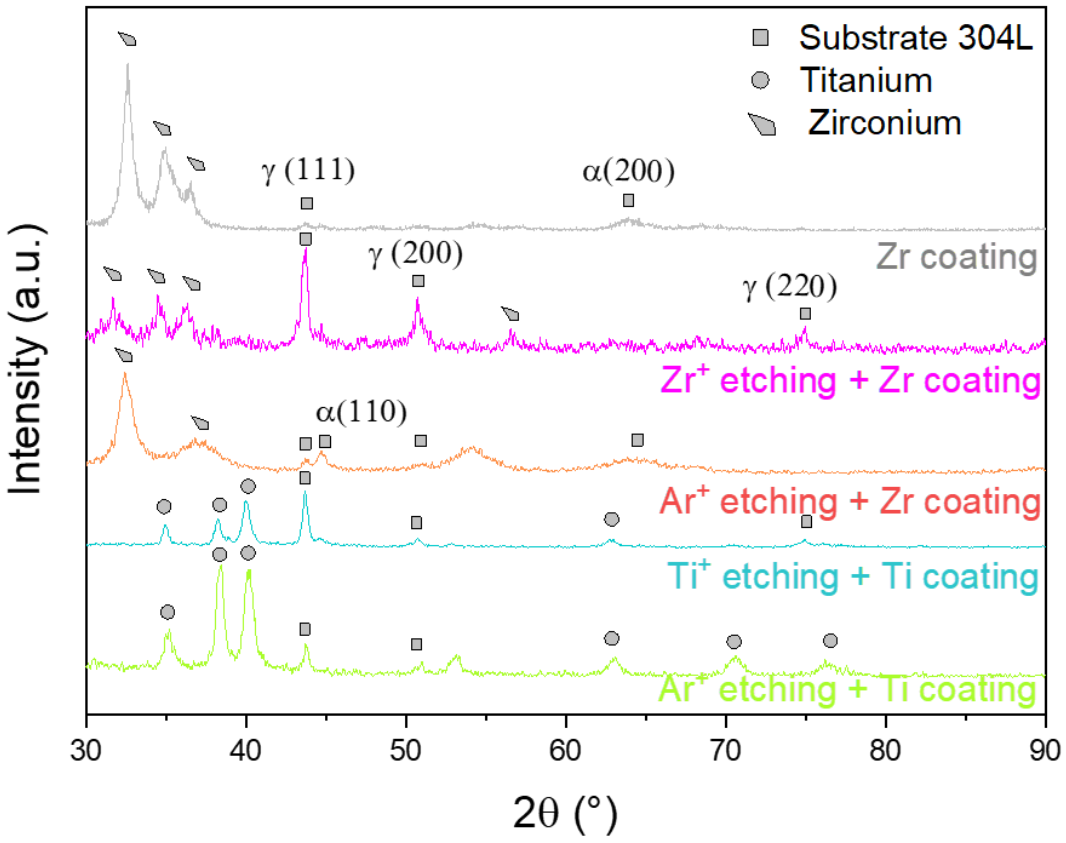

Figure 8: XRD patterns at 0.5° incident angle for Ti- and Zr-based samples synthesized using the TriPros machine.

Figure 9a, b shows the BSE micrographs of cross-sections of Ti and Zr bond coats deposited on 304L ASS substrate after metal ion etching. The microstructure of both coatings seems dense and defect-free. Moreover, Zr coating appears brighter than Ti because of the atomic number sensitivity of BSE mode (Figure 9b): Zr has a higher atomic number compared to Ti [40, 41]. The thickness of both coatings is usually around 200 nm but small variations mainly at the edges can be observed (± 31 nm), due to the shadowing effect and resputtering by highly energetic Ar ion bombardment. Moreover, the atomic percentages of the bond coats elements are estimated from EDX spectra performed on the cross-sections of Ti and Zr bond coats (Figure 9c). They are mainly made of Ti and Zr and substrate elements (Fe, Cr and Ni) are also observed in important quantities but far from the concentrations of the substrate. In fact, the resolution of EDX analysis (resolution of ≈ 1 µm² *i.e.* laterally and in depth)

should lead to higher levels of Fe, Cr and Ni with ratio close to the ones of the substrate. However, the EDX analysis is performed on a cross-section so the mounting resin is also analyzed, which may reduce the amount of detected substrate elements. Note that the results do not appear to vary with the type of etching given the scale analyzed by the EDX. That is why other analyses with finer resolutions such as GDOES could be used to study the influence of etching type on the structure of the bond coat more precisely. Some TEM characterizations are presented hereafter.

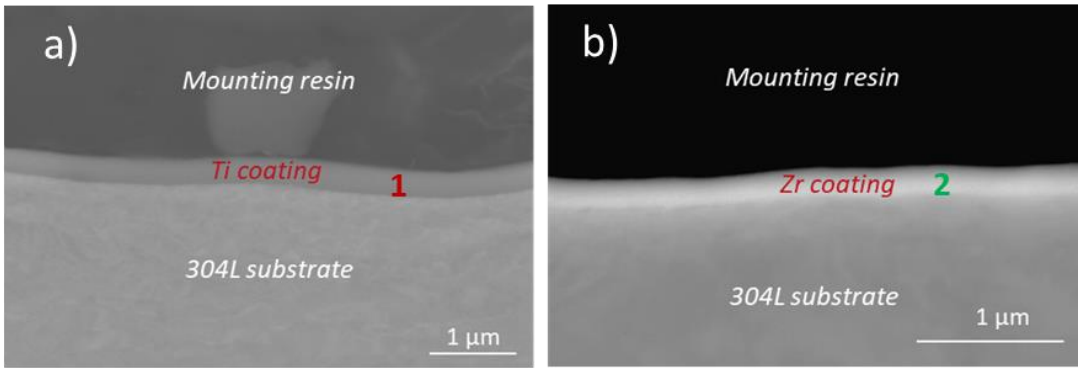

c)

Area	Ti (at.%)	Zr (at.%)	Cr (at.%)	Fe (at.%)	Ni (at.%)
1	73 ± 1	X	12 ± 1	13 ± 1	1 ± 1
2	X	72 ± 1	10 ± 1	16 ± 1	2 ± 1

Figure 9: SEM-BSE micrographs of cross-sections of synthetized a) Ti, b) Zr bond coats after metal ion etching in BSE mode and c) atomic percentages of elements obtained by EDX spectra.

The crystalline structure of Ti and Zr coatings is investigated in more detail using TEM micrographs and diffraction patterns. Figure 10a, b show the absence of impurities and defect at the substrate/metallic bond coat interface, hinting at a good adhesion of the coatings on the 304L substrate. Moreover, the deposited metallic bond coats show a columnar structure and are fully crystallized, probably due to the high energetic bombardment of the surface with ionized inert gas and metal plasma species present in the HiPIMS discharge. Generally, a columnar growth of dense and highly textured particles is observed, for coatings deposited by HiPIMS under sufficient energetic conditions [42]. In particular, it has been shown that dense good-quality films are synthesized when the ion energy is low (10-50 eV) or moderate (< 100 eV). According to our deposition parameters (substrate-holder voltage), the ion energy is approximated to about 100 eV. In comparison with Anders's structure zone model (see section 1.1.4 of "Literature review" chapter), it can be assumed that the growth of our bond coats takes place in zone 2 *i.e.* ion assisted epitaxial growth at low temperature and low energy, leading to a dense microstructure with columnar grains. At this scale of observation, no major differences can be observed on the structure of the bond coat as a function of the type of etching (Ar^+, Ti^+ and Zr^+).

In addition, electron diffraction patterns performed in different areas confirm a polycrystalline structure of the bond coats with nanosized grains, which differs from the µm-size of the substrate grains. In the interface area, a hybrid crystalline structure mixing that of the substrate and the bond coat is identified, probably due to ion implantation during etching step. Similar results were observed for all etched (Ar^+, Ti^+ and Zr^+) and metal bond coat deposited (Ti and Zr) samples (Figure 10b). This could indicate the formation of a pseudodiffusion-type interface (see section 1.1.2 of "Literature review" chapter) that is characterized by a gradient of composition between the substrate and the deposited bond coat, especially since the implantation of the etched species was observed (Figure 5).

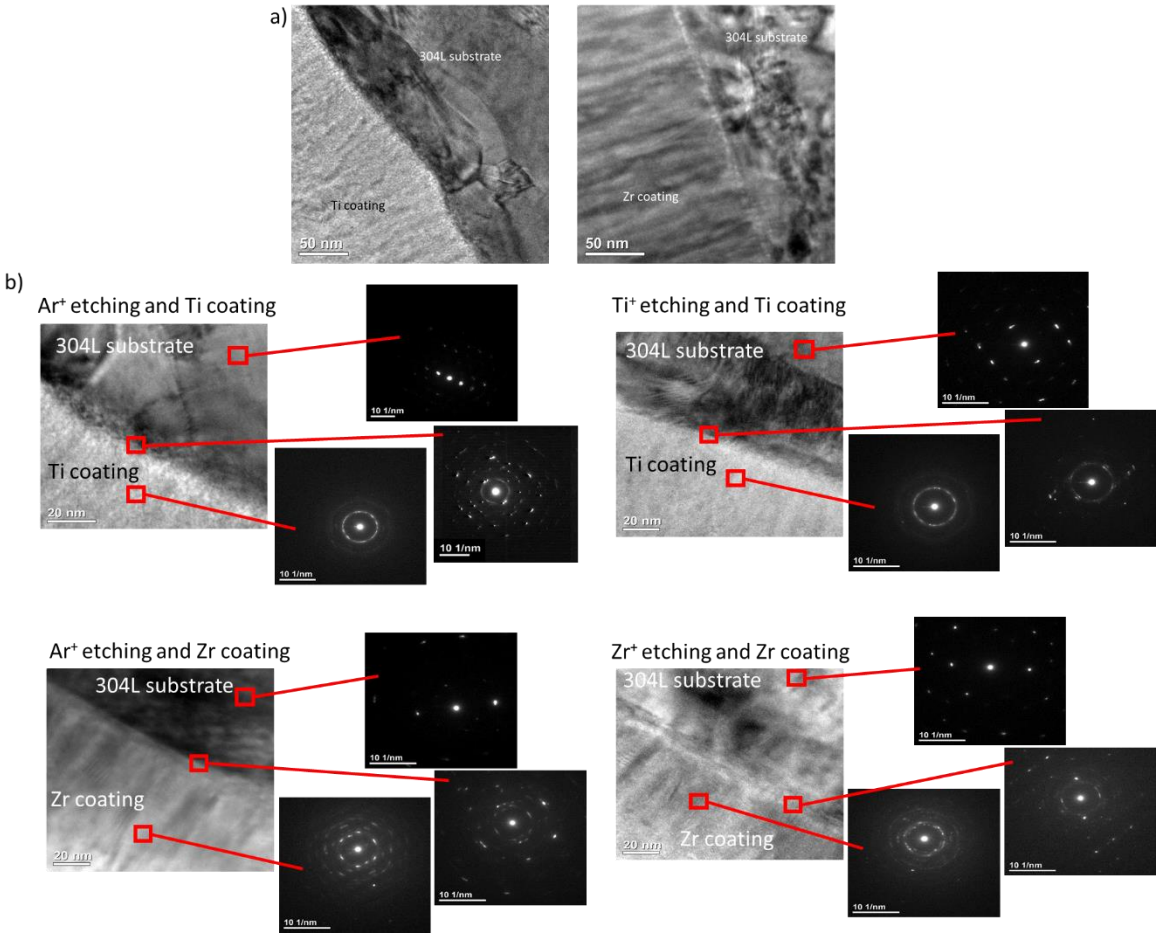

Figure 10: a) TEM images of Ar^+-etched and Ti-coated and Ar^+-etched and Zr-coated and b) TEM diffraction pattern for different areas of all etched and coated samples.

Figure 11 shows the XPS depth profiles of Ti^+-etched and Ti coated and, Zr^+-etched and Zr-coated samples. It is not relevant to do this measurement for the Ar^+-etched sample since the XPS depth profiles are measured using a 1 keV Ar^+ ionic beam for surface erosion. A solution could be to change the gas used for these analyses in order to study the Ar^+-etched and bond coat deposited samples. A Ti-based oxide layer is observed at the extreme surface of the Ti coating (Figure 11a), which is probably due to its high affinity with O when removed from the deposition machine and exposed to air. The same phenomenon is noticed for Zr (Figure11b). The depth

profiles also highlight the presence of O in the metal coatings (Ti and Zr). This can be explained by the presence of residual water vapour within the deposition chamber during the thin film growth. Moreover, the efficiency of etching can be confirmed by these profiles because Ti and Zr are present on the 304L substrate side (without O), indicating their incorporation in the substrate. This reinforces the hypothesis of the formation of a pseudodiffusion interface between the substrate and the bond coat. However, as the erosion rate varies according to the nature of the layers (chemical composition), it is difficult to give an exact value of the thickness of each layer without prior calibration.

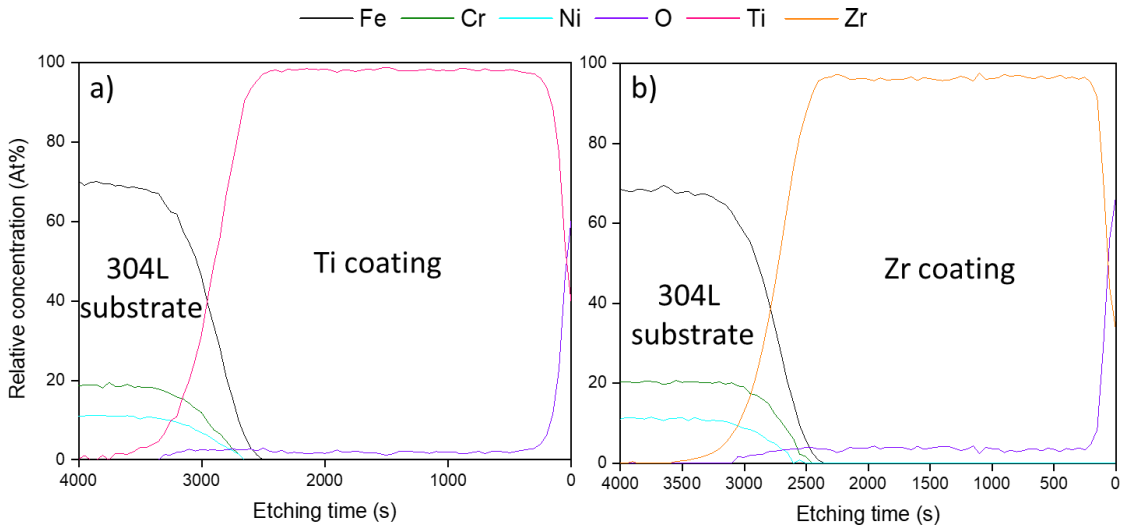

Figure 11: XPS depth profiles of (a) Ti-etched and Ti-coated and (b) Zr^+-etched and Zr-coated samples.

An interesting information given by the XPS profiles is the shift between the beginning of the etching times for Fe (around 2500 s) compared to Cr and Ni (between 2500 s and 3000 s). Indeed, if the interface between the coating and the substrate was sharp, one can assume that there would be no shift between these etching times. This result could show that there could be some kind of mixing between the elements occurring at the interface between Fe and Zr/Ti. A similar study of samples previously etched with Ar ions would reveal whether this mixing zone at the interface can also be observed for these samples.

The substrate/metallic bond coat interface after metal ion etching was studied in more detail by TEM (Figure 12). Note that the interfaces after Ar^+ etching were not analyzed by TEM as the number of samples was limited because I was not the one performing the analyses at NTU (due to the health crisis). However, it would be interesting to observe them for comparison with the metal ion-etched samples. For analytical reasons, deposition of a thin bond coat (200 nm-thick) directly followed the etching step for both etching ions. The interface is considered as the area where the crystal structure changes (from substrate to coating one) as shown in Figure 10 and is delimited by white dote lines in the bright field TEM images. These images reveal a clean, defect-free and contamination-free substrate/bond coat interface for both samples. The thickness of the interface, estimated from TEM observations, equals

about 2 nm for the Ti-based sample and 4 nm for Zr-based sample. The TEM profiles (Figure 12c, d) confirm the absence of contamination at the interface. In addition, no secondary or amorphous phase seems to have formed at this interface, suggesting a good adhesion between the bond coat and the substrate (Figure 12a, b). However, questions remain about the possible presence of a mixing zone between the substrate elements (mainly Fe) and the sputtered elements (Ti and Zr). Considering the existence of this mixing zone, the thickness of the interface estimated from the profiles would be around 10 nm for Ti-based sample and 13 nm for Zr-based sample. It should be noted that TEM profiles mainly depend on the microscope measurement parameters, which can lead to composition shift and broadening at the interface. To further check, APT analyzes were performed.

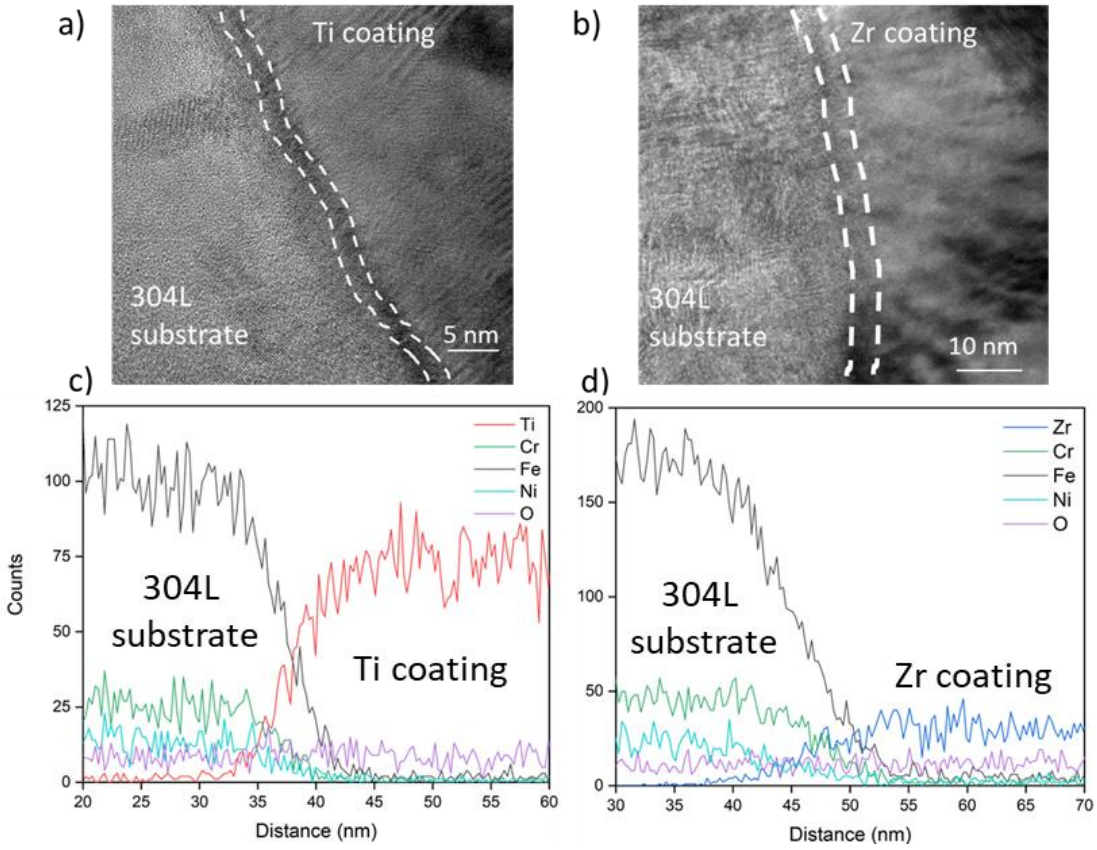

Figure 12: TEM observations of the substrate/bond coat interface of a) Ti^+-etched and Ti-coated and b) Zr^+-etched and Zr-coated samples and TEM profiles for c) Ti^+-etched and Ti-coated and d) Zr^+-etched and Zr-coated samples.

In parallel, two APT analyzes were performed at IRMA-ROUEN (electrical mode) and CEA/DMN (laser mode) to map the chemical composition near the substrate/metallic bond coat interface at the atomic scale and to estimate the thickness of the substrate/bond coat interface for the Zr^+-etched and Zr-coated sample. The number of samples to be studied was limited, that is why the Ar^+-etched and bond coat deposited samples were not analyzed by APT. On the other hand, the Ti^+-etched and Ti-coated sample was analyzed using APT but the tips broke off during the analysis and therefore, there are no usable results. Figure 13a, b show the distribution of Zr on the APT tip and the APT concentration profile obtained using an APT equipment in

electrical mode and a 3D reconstruction software that allows choosing the sampling volume. The objective is to have the best compromise between good spatial and statistical resolution to estimate the substrate/metallic bond coat interface thickness as accurately as possible. Figure 13c, d show the distribution of Zr on the APT tip and the APT concentration profile obtained using an APT device in laser mode and the software provided by the supplier. The substrate/metallic bond coat interface is plane but slightly inclined to the axis of the APT analysis, which means that the larger the sampling prism, the larger the apparent interface thickness. Fe and Cr are observed on the Zr bond coat side of the profile (Figure 13b, d). The thickness of the substrate/bond coat interface is estimated at about 2-5 nm, depending on whether the presence of Fe and Cr in the Zr coating is taken into account. For instance, a thickness of 1.9 nm is estimated if the interface is measured between the Zr and Cr signals but a thickness of 5.1 nm is obtained if the same measurement is done with Zr and Fe in Figure 13b.

The presence of Fe or Cr in the Zr bond coat could be due to a Fe/Zr and/or Cr/Zr mixing zone as the TEM and XPS results leave also some doubts about this. This mixing zone could be related to an elements' mixing due to the implantation of metallic ions during the etching step and/or to an interdiffusion of the elements of the substrate and the bond coat during its growth. However, it could be attributed to an artifact due to field effects during the APT analysis as the presence of these elements may depend on the evaporation mode used for the APT analysis (electrical or laser). Consequently, it is not possible for us to know if it is a clearly defined interface or a mixing zone between the elements from these analyses; that is why further investigations are required. Nonetheless, a mixing phenomenon is possible as already observed in the literature and generally leads to a better adhesion of the coating on the substrate [43]. Note that the same uncertainties remain for Ti-based sample.

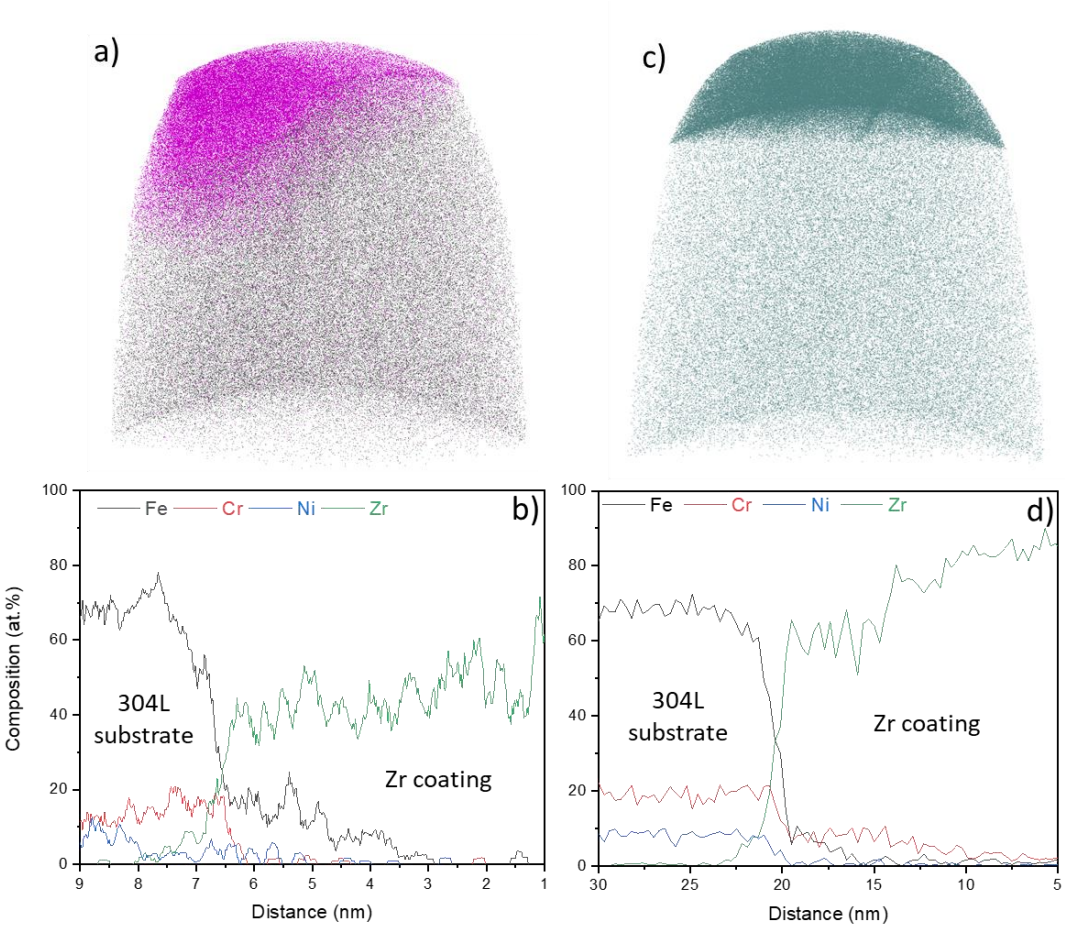

Figure 13: APT tip distribution of Zr and concentration profiles obtained for the Zr^+ etching + Zr coating sample performed a) and b) in electrical mode on IRMA GPM platform and c) and d) in laser mode in CEA platform, respectively.

2.3.2 Adhesion properties of the substrate/metallic bond coat system

Scratch-test measurements (from 0 to 10 N) were performed on the substrate/bond coat systems pre-treated by Ar^+ etching, metal ion etching, or not etched to study the influence of etching on the adhesion of the coating on the substrate. These measurements correspond to a scratch of 10 mm length on the sample surface (*i.e.* load increase of 1 N/mm). An example of scratch test results and the corresponding SEM observation in BSE mode of this scratch is shown in Figure 14 for the Ar^+-etched and Zr-coated sample. The curves plotted are those of the normal load (Fn), the tangential force (Ft), the friction coefficient (μ=Ft/Fn) and the penetration depth (Pd) of the indenter into the sample. SEM observation shows more or less dark areas along the scratch. The light areas are associated to the Zr coating and the dark areas to the 304L steel substrate. The delamination zones, *i.e.* showing the substrate, are visible on the curves mentioned above (zones represented with grey dotted lines).

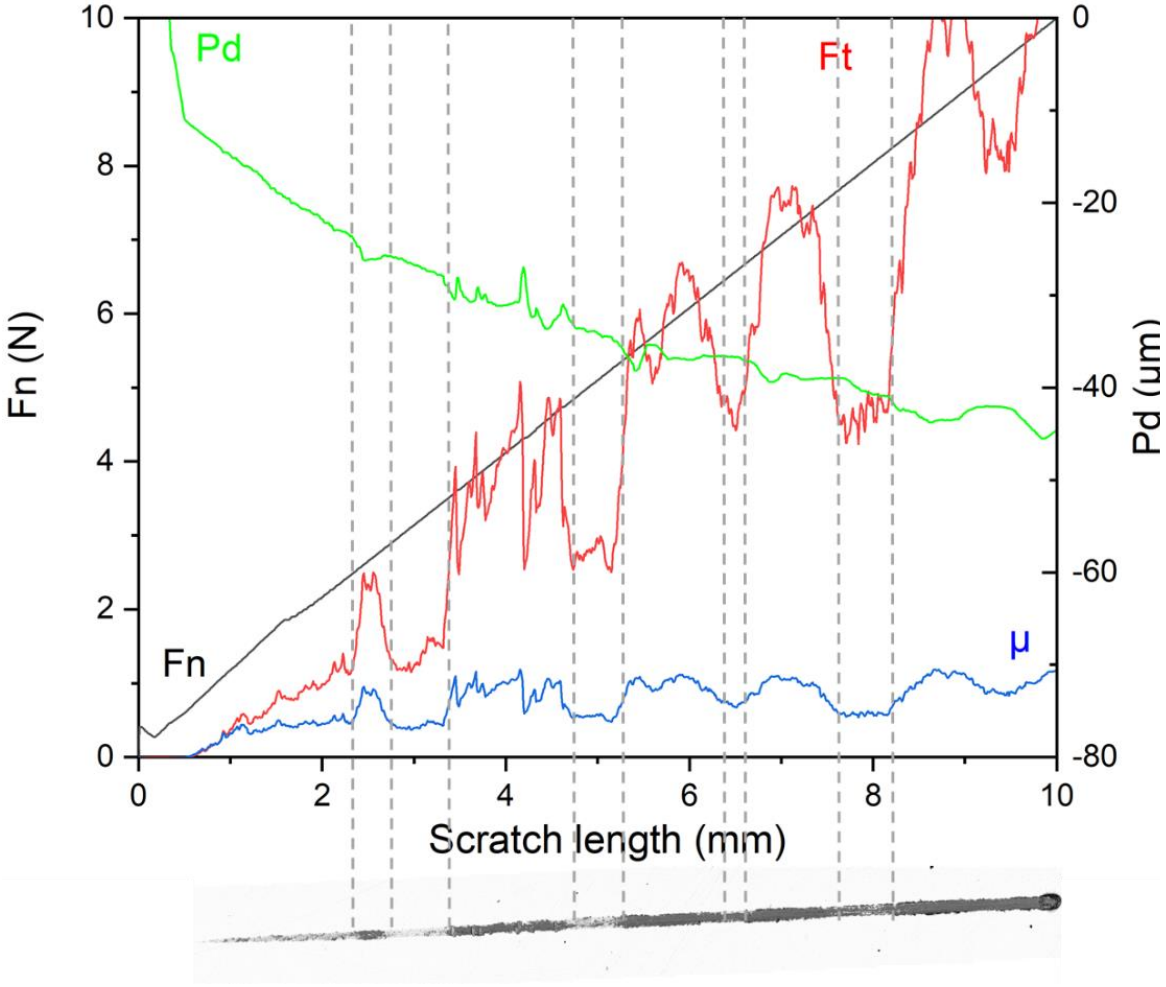

Figure 14: Evolution of the parameters (Fn, Ft, Pd and μ) vs. the scratch length and comparison with the SEM-BSE observation of this scratch performed on Ar^+-etched and Zr-coated sample.

By zooming in on the scratch (Figure 15, 16), the failure mode can be studied in more detail. Noted that the metal bond coats are much softer than the substrate, considerable plastic deformation occurs within the coating [39]. Conformal cracks are observed and open more and more in the scratch direction for Ar^+-etched and Zr-coated sample (Figure 15a). These cracks appear to be contained within the scratch as the edges of the groove are not damaged, likely due to high intrinsic stresses and a mismatch of bonding types in the substrate/bond coat interface. This behavior is commonly observed under high energy Ar^+ bombardment (*i.e.* -900 V), which introduces a large number of lattice defects in the substrate/bond coat interface and does not favor the formation of a gradual interface (implantation zone) [6]. In contrast, no cracks were observed for Zr bond coat deposited after metal ion HiPIMS pre-treatment (Figure 15b). It is well known that the origin of the observed differences in adhesion not only depend on the etching step but also on several other parameters. Some are directly related to the test itself (intrinsic parameters), while others are related to the substrate/coating combination properties (extrinsic parameters). Since the intrinsic and external stresses can be considered constant in our case, the differences in bond coat adhesion can thus be due to differences in the interfacial stresses and in pre-treatment processes. Consequently, here, this may be because

the Zr^+ etching first reduces the stress concentration [6] and then, results in an implantation zone at the substrate/bond coat interface. This greatly enhances adhesion of the deposited bond coat.

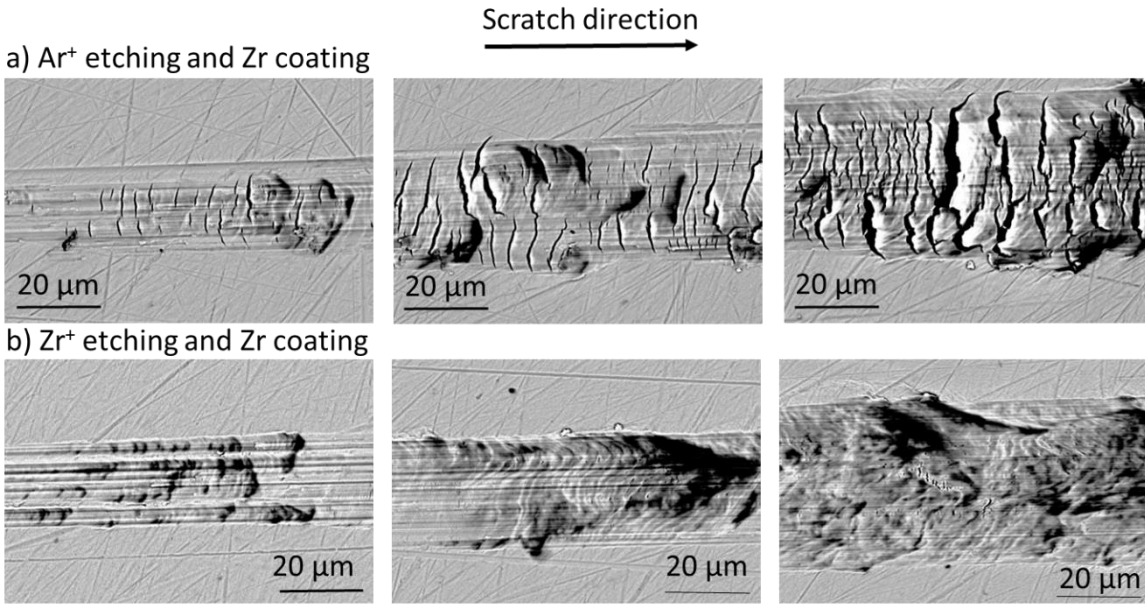

Figure 15: SEM-BSE micrographs of scratch testing track of a) Ar^+-etched and Zr-coated sample and b) Zr^+-etched and Zr-coated sample at different locations.

Apparently, the scratch-test reveals that the metal ion HiPIMS pre-treatment (Figure 16b) has no significant impact on the modification of failure modes of the Ti bond coat. This can be explained by extended (longer) etching of the substrate surface resulting in an increased substrate roughness, which decreases the adhesion of the bond coat [44, 45]. Another explanation can be the formation of a weak implantation zone preventing the formation of strong ionic or covalent bonds probably due to severe re-sputtering due to high fluxes of doubly-ionized metal species in the Ti HiPIMS discharge [7]. In our case, it is expected that high fluxes of Ti^{2+} in combination with a high negative substrate bias (- 900 V), meaning that Ti ions are accelerated towards the substrate with energy of 1800 eV, prevent any formation of strong interface. To conclude on this, a study of the etching time would be necessary to determine if there is an optimal duration leading to better properties of the substrate/bond coat system.

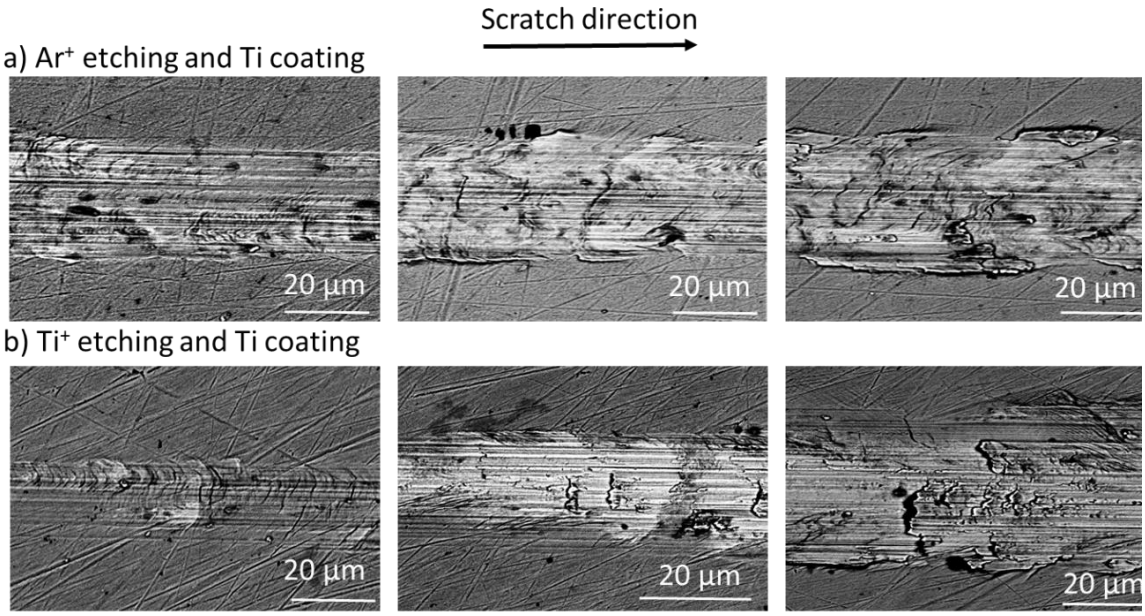

Figure 16: SEM-BSE micrographs of scratch testing track of a) Ar+-etched and Ti-coated sample and b) Ti+-etched and Ti-coated sample at different locations.

The critical loads values (Lc), corresponding to delamination across the entire width of the scratch, are estimated from the scratch-test measurements (curves and SEM observation) for all samples and shown in Figure 17. These values are the average of the three scratch-test measurements performed on each sample. It is worth noticing that the critical load values not only depend on the etching step but also on several other parameters. Some are directly related to the test itself (intrinsic parameters), while others are related to the substrate/coating combination properties (extrinsic parameters). However, in our case, an unambiguous adhesion improvement of the Zr bond coat is observed thanks to metal ion etching since the tests were performed in similar conditions (substrate material, film thickness, and test parameters).

Despite the similar failure modes of the Ar^+-etched and Ti-coated and the Ti^+-etched and Ti-coated samples, the Lc value for the Ti^+-etched and Ti-coated sample is slightly higher than for the Ar^+-etched and Ti-coated one, indicating a better adhesion after Ti^+ etching. The same behavior is observed for the Zr-based samples *i.e.* higher adhesion after metal ion etching. Moreover, the Zr-coated sample without pre-treatment shows the lowest Lc value for the Zr-based specimens. This indicates that a beneficial effect on substrate/bond coat adhesion is observed after etching, as expected, due to the formation of a clean and defect-free interface. On the other hand, Ar^+ etching shows a poor adhesion explained by the incorporation of Ar as interstitials in the crystal lattice, which increases the stresses and weakens the interface [6]. Consequently, etching using metal ions is better as they are incorporated as replacements in the crystal lattice, thus strengthening the interface [6].

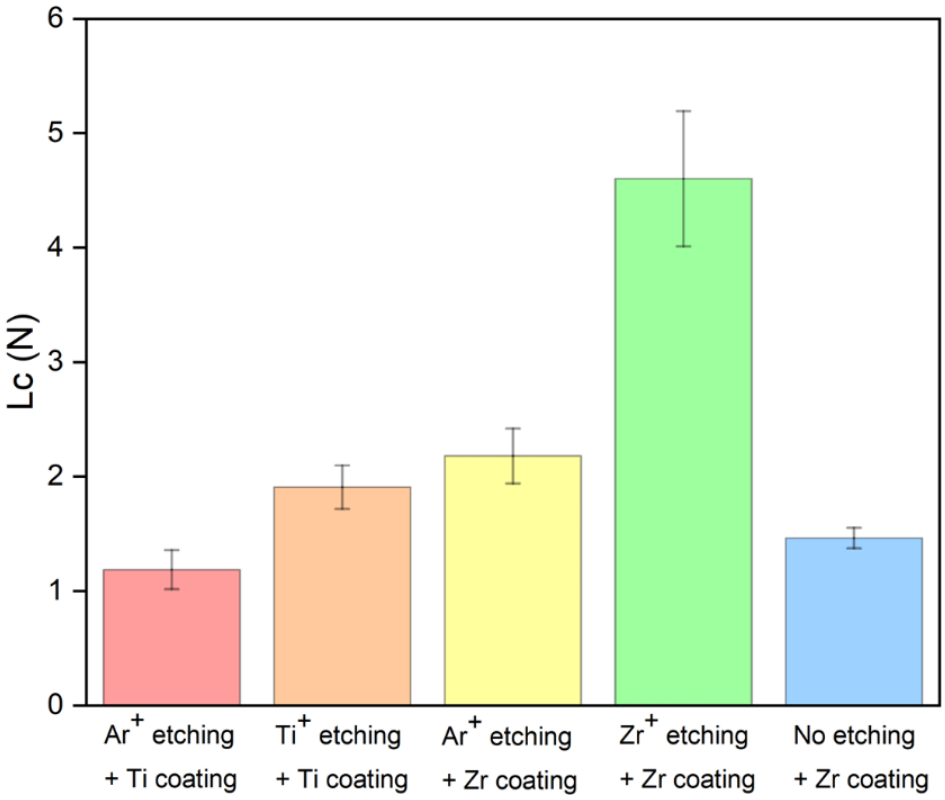

Figure 17: Adhesion properties of the substrate/metallic bond coat systems.

2.3.3 Modeling of the substrate/bond coat interface

Figure 5 shows the supposed structure obtained after etching. The aim is now to propose a model of substrate/bond coat interface from this modified structure (Figure 18). It is worth noticing that Ar, being an inert gas and incorporating into interstitial sites, is not involved in the creation of new bonds at the substrate/bond coat interface (Figure 18a, b). On the contrary, it can be assumed that the implanted metal ions (Ti and Zr) can help to form strong bonds and reduce the lattice mismatch at the substrate/bond coat interface [5, 6]. It can also be assumed that they could act as preferential nucleation sites for the bond coat growth and promote an epitaxial film, at least on the first layers, as lattice mismatch is decreased (see section 1.1.4 of the “Literature review” chapter). This could indicate the formation of a pseudodiffusion-type interface (see section 1.1.2 of “Literature review” chapter) that is characterized by a gradient of composition between the substrate and the deposited bond coat. In this representation, the possible mixing between Fe, Cr and Zr/Ti is not shown, but this possibility cannot be excluded at this stage.

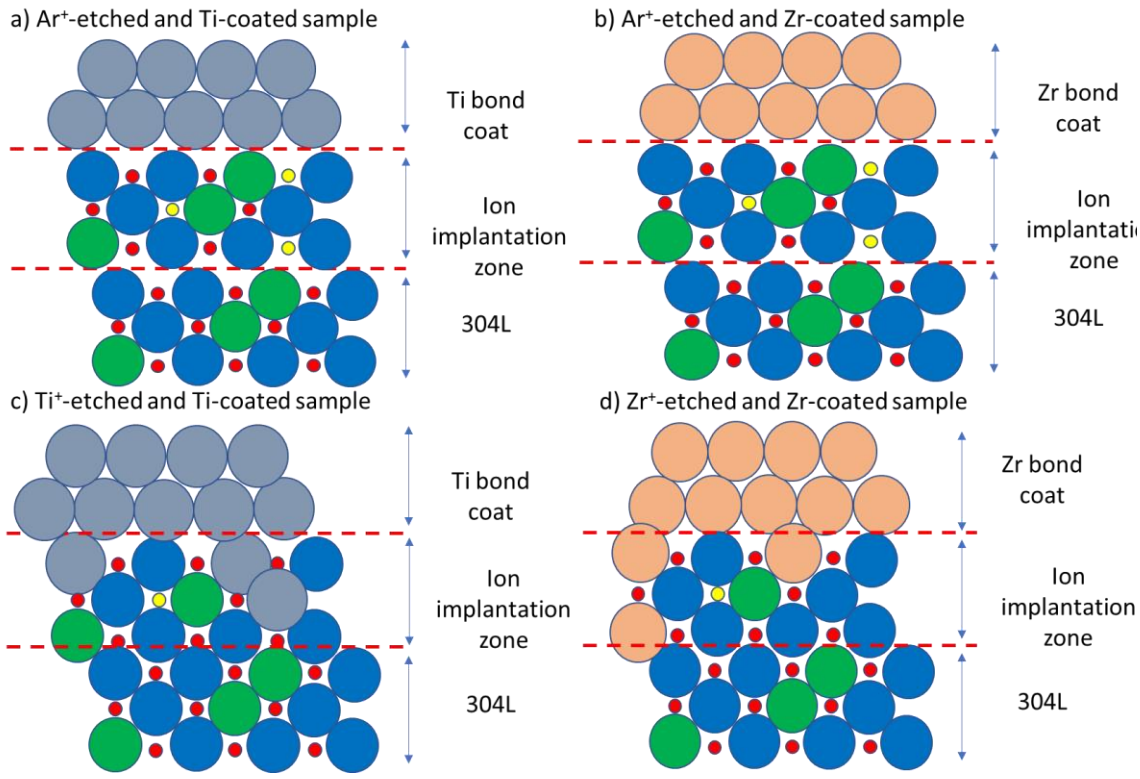

Figure 18: Model of the substrate/bond coat interface obtained for a) Ar^+-etched and Ti-coated, b) Ar^+-etched and Zr-coated, c) Ti^+-etched and Ti-coated and b) Zr^+-etched and Zr-coated samples.

2.4 CONCLUSION

In this work, 304L ASS substrates are etched using ionized vapour of Ar, Ti (Ar and Ti) and Zr (Ar and Zr) generated by HiPIMS. This ion etching pre-treatment results in the surface modification of the initial 304L by implantation of the sputtered species. The amount of these incorporated species differs slightly from one etching to another: Ti (7 at.%) and Ar (5 at.%) after Ti^+ etching, Zr (6 at.%) and Ar (6 at.%) after Zr^+ etching and Ar (4 at.%) and Zr (7 at.%) after Ar^+ etching. Noted that the unexpected Zr contribution observed after Ar^+ etching can be attributed to resputtering effects from the vacuum chamber walls and substrate-holder. These etchings do not trigger the crystallization of new phases but reduce the ferrite content and amorphize the 304L surface. This amorphisation is stronger for the Ti^+- and Zr^+-etched samples because of the simultaneous bombardment from metal and Ar^+ ions. A schematic drawing (Figure 5) has been proposed to have an idea of the structure obtained after these three types of etching. It assumes that Ti could replace Cr and Zr could replace Fe in the FCC structure of 304L ASS as the metal ions can be incorporated into the substrate by substituting lattice atoms (replacements). These preferential substitutions could be due to their similar radii that can induce a decrease in Cr_2O_3, after Ti^+ etching and air exposition and Fe_2O_3 after Zr^+ etching and air exposition as observed in XPS analysis. On the other hand, Ar, being an inert gas, can be incorporated in interstitial sites. The incorporation of sputtered species modifies the substrate extreme surface by modifying the nature and proportion of native oxides, promoting the formation of TiO_2 and ZrO_2, which are much more stable than Cr_2O_3

and Fe_2O_3. A more detailed study of the substrate surface etched by the metal ions indicates that the oxide layers formed could be estimated at about the implanted thickness. This implantation depth is estimated to 3.5 nm for Zr and 4 nm for Ti by SRIM calculation for ions at 0.9 keV. In addition, these oxide layers should be thinner than the native 304L substrate one. Further analyzes are needed such as GDOES to estimate the oxide layers thicknesses.

A 200 nm bond coat (Ti and Zr) has been deposited after the different types of etching in order to study the substrate/bond coat interface in more detail. The deposited metallic bond coats show a columnar structure and are fully crystallized, probably due to the high energetic bombardment of the surface with ionized inert gas and metal plasma species present in the HiPIMS discharge. Moreover, different crystalline orientations are observed depending on the type of etching performed. In fact, the Ti^+-etched and Ti-coated sample shows a preferential orientation along the (101) axis compared to the Ar^+-etched and Ti-coated sample. In addition, the Ar^+-etched and Zr-coated and, unetched and Zr-coated samples are preferentially oriented along the (100) axis, whereas there is no real preferential orientation observed for the Zr^+-etched and Zr-coated sample. This tends to indicate an effect of etching on the structure of the bond coat. However, further analysis is required to understand how the etching type can influence the bond coat growth mechanism and microstructure. Nonetheless, it can be assumed that the implanted metal species can act as preferential nucleation sites for the bond coat growth and promote an epitaxial film, at least on the first layers. This could indicate the formation of a pseudodiffusion-type interface that is characterized by a gradient of composition between the substrate and the deposited bond coat. As a result, the lattice mismatch can be reduced and strong bonds can be formed between the susbtrate and the bond coat. On the contrary, since Ar incorporates into the interstitial sites, it cannot form bonds at the substrate/bond coat interface. A model of the formation of the substrate/bond coat interface has been proposed (Figure 18) taking into account the 304L ASS structure modifications observed after etching to illustrate this hypothesis.

The more detailed investigation of the substrate/bond coat interface formed after metal ion etching indicates a 2-5 nm thick interface, which is clean, defect-free and free of contamination. In addition, no secondary or amorphous phase seems to have formed at this interface, suggesting a good adhesion between the bond coat and the substrate. However, questions remain about the possible presence of a mixing zone for both metal ion-etched and metal-coated samples after XPS, TEM and APT analyzes. These analyses were not performed on the Ar^+-etched and metal-coated samples, but it could help in determining whether or not this mixing zone is present. This mixing zone could be related to a mixing of the elements due to the implantation of metallic ions during the etching step and/or to an interdiffusion of the elements of the substrate and the bond coat during its growth. However, it could also be attributed to analyses artifacts. Therefore, it is not possible for us to know if it is a clearly defined interface or a mixing zone from these analyses; that is why further investigations are required. The adhesion of the substrate/bond coat interface has been investigated using scratch-test, showing a beneficial effect of etching related to the formation of a defect-free interface. Nonetheless, HiPIMS metal ion etching shows a better adhesion than inert gas. This is due to the formation of stronger bonds at the interface, resulting

from the substitution of lattice atoms by metal ions in the substrate structure. The more detailed investigation of the failure modes shows different results depending on the etching type studied. The comparison between Zr^+ and Ar^+ etchings shows that cracks are observed for Ar^+ etching, probably due to high intrinsic stresses and a mismatch of bonding types in the substrate/bond coat interface whereas no cracks are noticed for Zr^+ etching as it reduces the stress concentration and can result in an implantation zone at the interface. This reinforces the assumption of a mixing zone at the substrate/coating interface. On the other hand, no significant impact is observed on the modification of failure modes of the Ti bond coat after Ti^+ etching. This can be due the formation of a weak implantation zone preventing the formation of strong bonds probably due to high fluxes of doubly-ionized metal species in the Ti HiPIMS discharge that causes severe resputtering.

It can be assumed that HiPIMS metal ion etching has a beneficial effect on the corrosion resistance of the 304L ASS substrate as it changes the oxide film formed on the surface. In addition, metal ion-etched and bond-coated samples show higher adhesion, which may also lead to a better corrosion resistance by limiting the penetration of electrolyte into the substrate.

3. CORROSION RESISTANCE INVESTIGATIONS OF THE ETCHED SAMPLES

3.1 ELECTROCHEMICAL MEASUREMENTS

Electrochemical measurements are performed on a limited surface and instantaneous in time, using a three-electrodes configuration. Polarization and electrochemical impedance spectroscopy (EIS) are applied for measurements in nitric acid (2.5 mol/L HNO_3, 2.5 mol/L $NaNO_3$, 2 g/L $Fe(NO_3)_3$) solution at 110 °C while only polarization measurements are performed in 3.56 wt.% NaCl solution at ambient temperature. In the case of polarization measurements, Tafel extrapolation is a technique used to estimate the corrosion potential and corrosion current. This leads by extension to the estimation of the corrosion rate.

3.1.1 In nitric acid

3.1.1.1 Potentiodynamic polarization curves and EIS

Figure 19 shows the potentiodynamic polarization curves of the initial and etched substrates in a nitric acid solution at boiling temperature after 6 hours (h) and 2 days (d) of immersion. The corrosion potential (E_{corr}) and corrosion current density (J_{corr}) were derived from a Tafel extrapolation of the measured anodic polarization experiment performed to limit sample degradation. The Tafel extrapolation technique is described in the Materials and Methods chapter. Figure 19 shows that the E_{corr} value for the 304L steel equals 0.98 ± 0.01 V/SHE after 6 h and 0.96 ± 0.01 V/SHE after 2 d in nitric acid. As a comparison, E_{corr} of the etched substrates is shifted toward positive values. After 2 d, E_{corr} of Ti^+-, Zr^+-, and Ar^+-etched substrates stabilizes around 1.07 ± 0.01 V/SHE. The higher corrosion potentials can be attributed to the increase of the resistance to oxidation of the materials, which can be related to the reinforcement of the passive layer due to the respective presence of ZrO_2 and TiO_2 that are known to be highly resistant to corrosion in nitric acid [27, 46]. The variation

of E_{corr} between 6 h and 2 d shows that the stationary state may not have been reached.

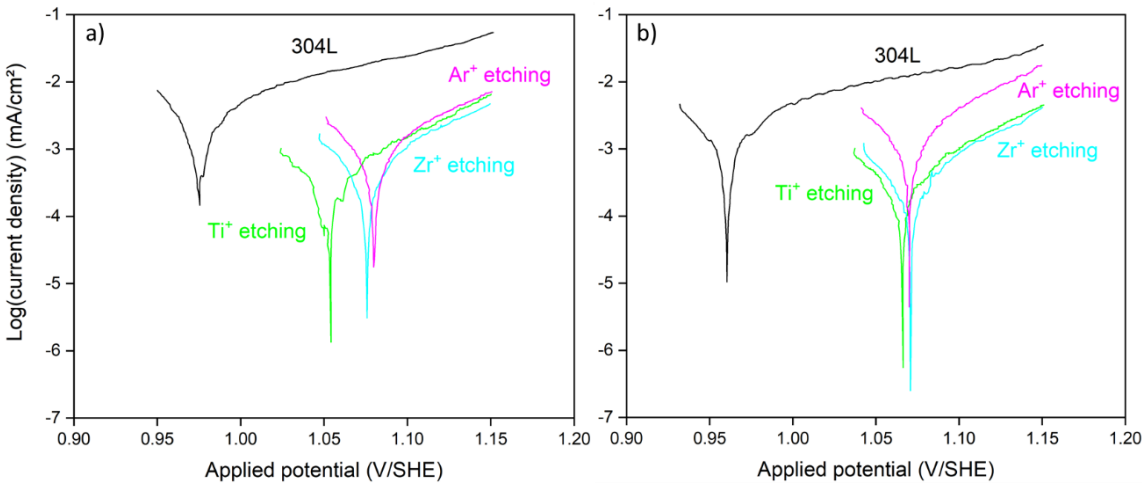

Figure 19: Potentiodynamic polarization curves of initial 304L and etched samples in a nitric acid (2.5 mol/L HNO_3, 2.5 mol/L $NaNO_3$ and 2 g/L $Fe(NO_3)_3$) solution at 110°C after (a) 6 h and (b) 2 d of immersion.

The effect of etchings is also observed on the corrosion currents. After 6 h, J_{corr} decreases by an order of magnitude for the etched samples down to 10^{-4} mA/cm², compared to 1×10^{-3} mA/cm² for the initial substrate (Figure 19a). However, after 2 d of immersion (Figure 19b), different behaviours are observed. J_{corr} for the initial substrate and Zr^+-etched sample slightly decreases to 6×10^{-4} mA/cm² and 9×10^{-5} mA/cm², respectively. On the other hand, J_{corr} is invariant for the Ti^+-etched samples (1×10^{-4} mA/cm²) and modestly increases for the Ar^+-etched samples to 6×10^{-4} mA/cm², a value similar to the 304L steel. The values obtained for the 304L differ from those observed in the literature that show a lower E_{corr} and a higher J_{corr} (0.447 V/SHE and 10×10^{0} µA/cm²) in a 1 mol/L HNO_3 solution at room temperature [47]. Moreover, the Tafel slopes obtained from the extrapolation can be used after 2 d to estimate the corrosion rate (see Materials and Methods chapter). After 2 d of immersion, the corrosion rate indicates a value of 6 µm/year for initial 304L and Ar^+-etched sample and around 1 µm/year for the Ti^+- and Zr^+-etched substrate (Table 4). These values are lower than the values allowed for the application in nitric acid service of 304L ASS (450 µm/year) [48, 49] and in a boiling condensed solution of 6.2 mol/L (95 µm/year) [50]. However, the 304L corrosion rate value is of the same order of magnitude as that calculated via mass loss from immersion tests in a 3.5 mol/L HNO_3 solution at 90 °C after 4 d of immersion (4.5 ± 4.5 µm/year) [51]. Note that the corrosion rate values calculated from the electrochemical tests are qualitative and limited to a uniform corrosion process considering the stationary state has been reached. It is also necessary that Tafel extrapolation begins at least 50-100 mV away from E_{corr} and that the anodic or cathodic regions are observed over at least a decade of current.

Table 4: Corrosion potential (E_{corr}) and current density (J_{corr}) values after 6 h and 2 d of immersion and corrosion rate after 2 d of immersion in a nitric acid (2.5 mol/L HNO_3, 2.5 mol/L $NaNO_3$ and 2 g/L $Fe(NO_3)_3$) solution at 110 °C.

	E_{corr} (V/SHE)		**J_{corr}** (mA/cm²)		**Corrosion rate** (µm/year)
	6 h	2 d	6 h	2 d	2 d
304L	0.98	0.96	1×10^{-3}	6×10^{-4}	6
Ar^+ etching	1.08	1.07	4×10^{-4}	6×10^{-4}	6
Ti^+ etching	1.05	1.07	1×10^{-4}	1×10^{-4}	1
Zr^+ etching	1.08	1.07	1×10^{-4}	9×10^{-5}	1

All etchings have a positive effect on the electrochemical behaviour of the 304L steel in nitric acid environment, but this effect is more pronounced for metal ion (Ti^+ and Zr^+) etchings than for Ar^+. A first hypothesis to explain this effect could be the reduction of the ferrite content and the amorphisation of the surface upon HiPIMS etching. In fact, ferrite can be preferentially attacked in nitric acid environments as reported in [52] for a minimum ferrite amount of 3.5 %. In addition, the quality of the passive film is higher for austenite compared to ferrite [23, 53]. Therefore, decreasing the amount of ferrite could improve the corrosion resistance of the steel. Also, potentiodynamic polarization curves of Ti^+- and Zr^+-etched samples reveal an increase in the corrosion potential which could be due to the decrease of the oxidation rate thanks to ion implantation [54] and improvement of the passive layer. In fact, the incorporation of Ti and Zr induces the formation of Ti and Zr oxides, which can reinforce the passive layer (Figure 9) and decrease the oxidation rate of 304L steel due to their stability in nitric acid environment. Moreover, a smaller corrosion current after 6 h and 2 d of immersion in boiling nitric acid is observed for these etchings leading to a lower corrosion rate [55, 56]. Consequently, the results hint at better corrosion resistance owing to structural modifications of the 304L surface and/or modification of the passive layer due to ion etching. In any case, immersion tests have to be performed to confirm this tendency and the corrosion mechanism of these modified materials for longer durations.

Figure 20 displays the Nyquist diagrams of the initial and etched 304L substrates at open potential (E_{corr}) after 6 h and 2 d of immersion in a nitric acid solution at boiling temperature. The Nyquist diagrams (Figure 20 a, b) show only one semicircle (capacitive loop) for all the samples, corresponding to a single time constant. The capacitive loop common to all samples is due to the charge transfer process [54, 57]. The increased loop diameter for the etched samples is related to the increasing of transfer resistance, which implies lower corrosion rates [54-56]. This decrease in corrosion rate can be related to the faster growth of a passive film on the surface of these samples [54-56]. However, in our case, it is difficult to conclude on the kinetics

of the layer formation without further analysis (modeling of impedance diagrams). Consequently, this may be due to the formation of a passive oxide layer that slows down the exchange of electrons with the surrounding environment. The presence of Ti and Zr in this layer could improve its passivity efficiency.

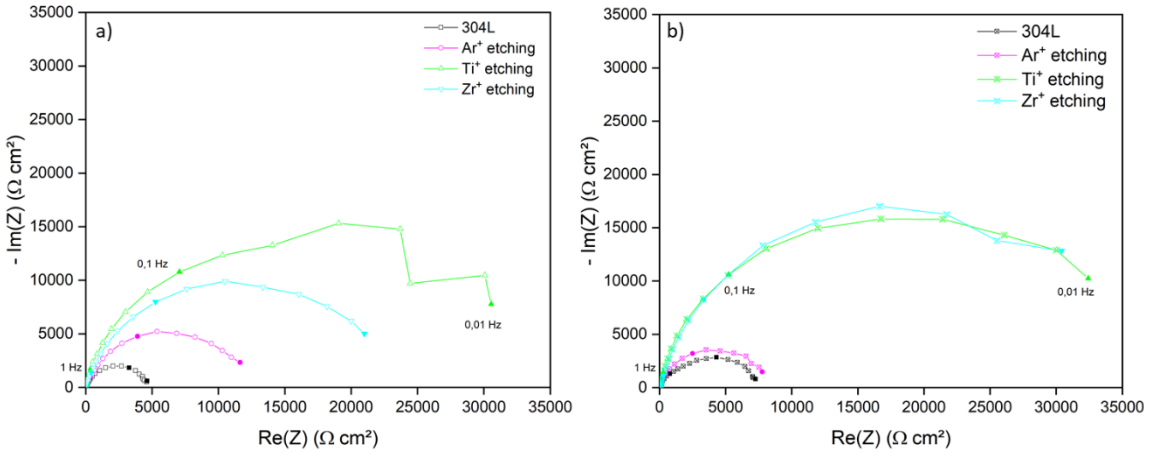

Figure 20: Nyquist diagrams at open potential after a) 6 h and b) 2 d in a nitric acid (2.5 mol/L HNO_3, 2.5 mol/L $NaNO_3$ and 2 g/L $Fe(NO_3)_3$) solution at 110 °C.

After 2 d of immersion, the diameter of the capacitive loops of the 304L ASS as well as Ti^+-, and Zr^+-etched substrates increases, and that of the Ar^+-etched sample is reduced (Figure 20b). Note that the increase is more pronounced for the Zr^+-etched substrate. The enlarged loop points to a decrease in corrosion rate over time for the Ti^+- and Zr^+-etched samples [54-56]. On the other hand, the reduced loop diameter of the Ar^+-etched sample suggests an increase in corrosion rate. The limitation of corrosion resistance by Ar^+ etching may be due to alteration of the surface crystallochemical properties compared to metal ion etchings. In fact, Ar ions only slightly modify the amount of ferrite and, consequently, the crystalline structure of the 304L substrate (Figure 5), as they are incorporated as interstitials in the crystal lattice [6]. This can limit the improvement in corrosion resistance. The decrease in corrosion rate over time for the Zr^+-etched susbtrate can be explained by the incorporation of ZrO_2 in the passive film during immersion, while for the Ti^+-etched sample, this effect is more limited. Several forms of Ti-based oxides can be formed before formation of a stable TiO_2 [47], especially Ti_3O_5 and Ti_2O_3 that have a lower enthalpy of formation compared to TiO_2. These non-stoichiometric oxides are porous and can dissolve in acid solution, whereas TiO_2 (stoichiometric oxide) is compact and stable. This could suggest that for Ti it would be the composition of the oxide layer that would influence the corrosion resistance, while for Zr it would be the thickness of the oxide layer.

The charge transfer resistance R_t is extracted from the Nyquist diagrams. After 6 h in nitric acid solution, the Ar^+-, Zr^+-, and Ti^+-etched substrates show R_t values about 2.5, 5, and 7 times larger than for initial 304L substrate, respectively (Table 5). The high resistance values confirms an improvement of corrosion resistance probably due to the formation of a more protective passive film [57]. These improved properties can result from modification of the passive layer by incorporation of Ti and Zr, leading to the formation of Ti and Zr oxides, which are more resistant in nitric acid environment.

Table 5: R_t values after 6 h and 2 d of immersion in a nitric acid (2.5 mol/L HNO_3, 2.5 mol/L $NaNO_3$ and 2 g/L $Fe(NO_3)_3$) solution at boiling 110 °C.

	R_t (kΩ cm²)	
	6 h	2 d
304L	5	8
Ar^+ etching	13	8
Ti^+ etching	32	37
Zr^+ etching	24	37

After a longer reaction time of 2 d in nitric acid at boiling temperature, identical R_t values are obtained for the initial 304L steel and Ar^+-etched sample (Table 5), whereas higher R_t values are obtained for Ti^+- and Zr^+-etched samples. Again, this improvement is likely due to modification of the passive surface layer that hinders the charge transfer process [55-57]. These results are consistent with the potentiodynamic polarization measurements (Figure 19a, b) even if variations are observed as between J_{corr} and R_t values for Ti^+-etched sample after 2 d of immersion. In fact, J_{corr} is invariant for the Ti^+-etched samples (1×10^{-4} mA/cm^2) whereas R_t increases from 6 h to 2 d of immersion (from 32 to 37 kΩ cm²). This shows the limitations of extrapolation from Tafel lines to determine J_{corr} as one would expected to observe the same trend for both electrochemical tests (polarization and EIS. A wrong selection of the Tafel slope lead to uncertainties and erroneous value of J_{corr}. It is necessary to ensure that the anodic or cathodic regions are observed over at least a decade of current, which is not always our case where the anodic and cathodic branches are sometimes limited

In conclusion, electrochemical measurements of corrosion in a boiling nitric acid solution indicate a decrease in the corrosion current density for the Ti^+- and Zr^+-etched samples after 2 d of immersion. In fact, HiPIMS metallic etching allows the decrease of the corrosion rate of the initial 304L steel by forming a more protective layer due to the presence of Ti and Zr that allows the formation of very stable oxides, which hinders the charge transfer process. Moreover, these modifications will provide additional protection in areas where coatings may fail.

3.1.1.2 Characterization of the electrochemically investigated etched surface

Figure 21 shows SEM images in secondary electrons (SE) mode of the initial 304L substrate and etched samples before and after 2 d in the nitric acid. The surfaces before electrochemical measurements show several scratches related to the preparation process (mechanical polishing using SiC abrasive discs). There does not seem to be any obvious difference between the surfaces of the samples before and after electrochemical measurements.

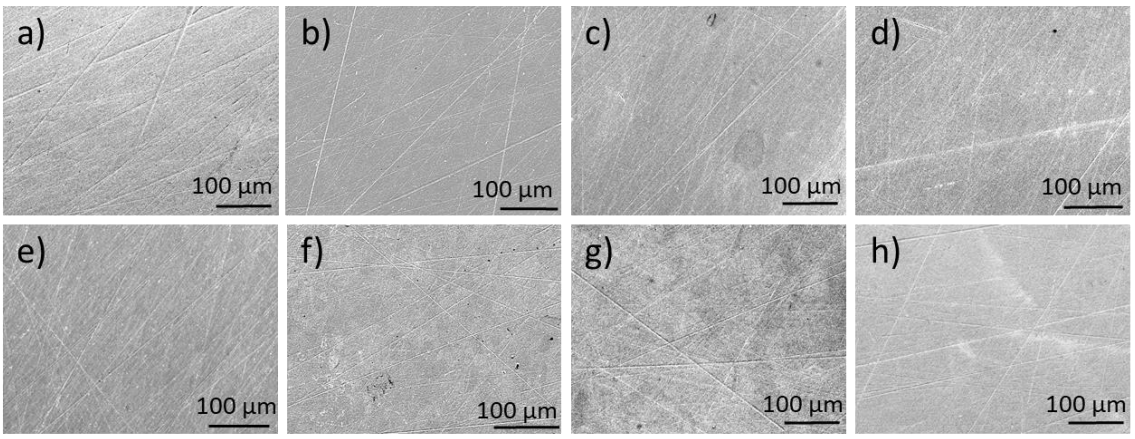

Figure 21: SEM-SE micrographs of the 304L as well as Ar^+-, Ti^+-, and Zr^+-etched samples before (a, b, c, d) and after (e, f, g, h) electrochemical measurements in a nitric acid (2.5 mol/L HNO_3, 2.5 mol/L $NaNO_3$ and 2 g/L $Fe(NO_3)_3$) solution at 110°C.

XPS region spectra of the main electronic levels of the initial and etched 304L steel samples are shown in Figure 22. Compared to spectra recorded before the electrochemical measurements (Figure 4a), the O 1s spectrum displays is made of a single large band containing two contributions at binding energies of 531.6 (metal hydroxides and surface contamination) and 530.7 eV (metal oxides) (Figure 22a) [16]. Moreover, one main Cr 2p peak at 576.8 eV associated to Cr(III) oxide (Cr_2O_3) and one minor peak at 574.4 eV, which is characteristic of Cr metallic binding, are observed for all samples (Figure 22b) [17, 20]. The Fe 2p spectra (Figure 22c) display the two peaks at 711.4 eV (Fe(III) oxide) and 706.9 eV (Fe metal) observed before electrochemical investigations of the etched samples [16]. A peak at 852.9 eV is attributed to metallic Ni (Figure 22g) as previously observed (Figure 4g). In addition, the contributions from surface contamination, mainly C (Figure 22h), are still observed after immersion in nitric acid but differ depending on the sample.

After electrochemical measurements, Ti and Zr contributions are no longer detected by XPS (Figure 22d, f) whereas the Ar^+-etched sample still exhibit traces of Ar (Figure 22e), although with only one remaining visible contribution at 242.2 eV. The absence of Ti and Zr suggests that these elements have actually dissolved in the electrolyte, which is coherent with the corrosion rate estimated of 1 µm/year (approximately 2-3 nm/day). Performing potentiodynamic measurements after a longer duration could have shown an increase of the corrosion current density due to the disparition of the passive layer enriched in Zr/Ti. The presence of Ar at the surface after 2 d of reaction can be explained by the different behaviour of Ar compared to Ti and Zr, which does not combine with the other surface elements and cannot oxidize.

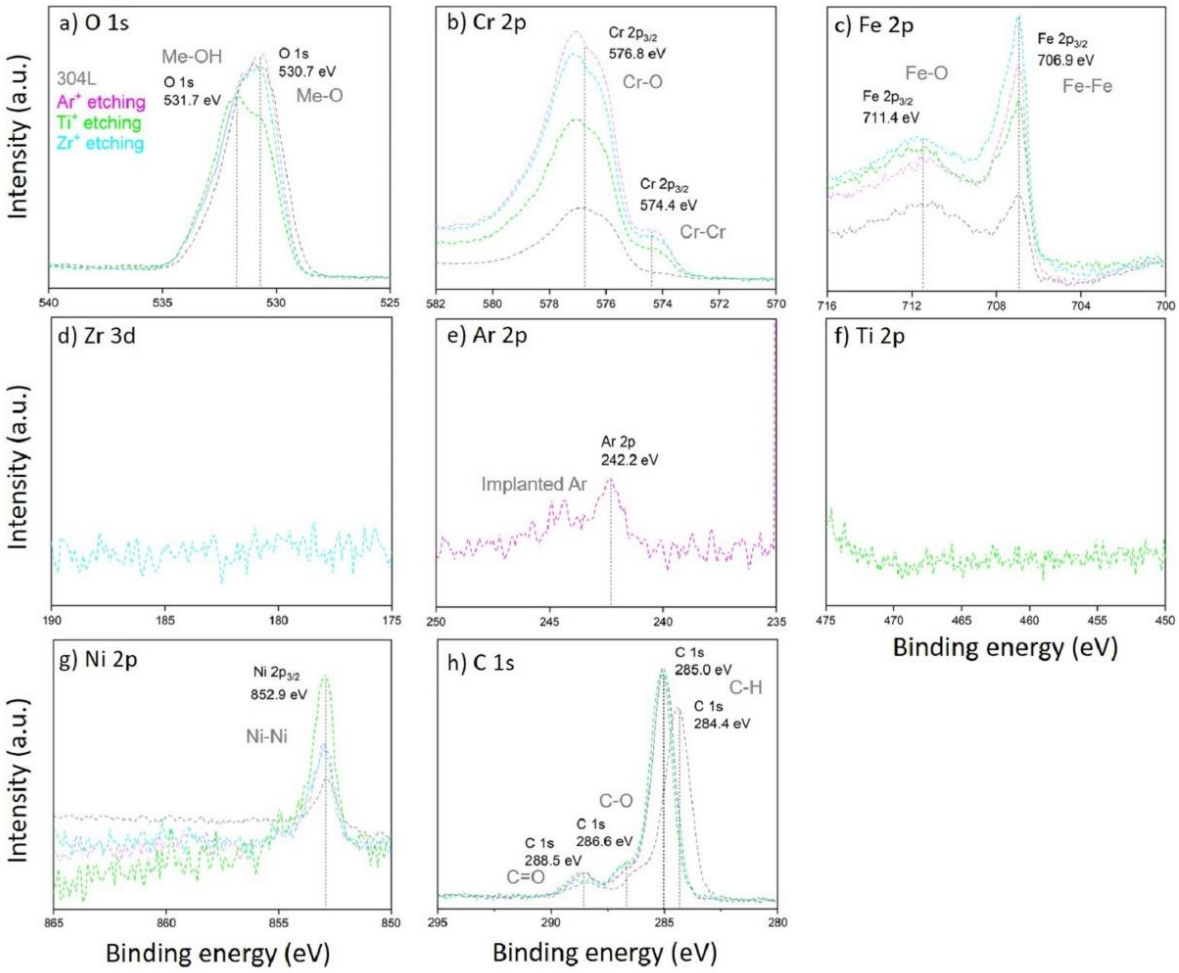

Figure 22: High-resolution XPS spectra of initial and etched 304L samples after 2 d in nitric acid (2.5 mol/L HNO_3, 2.5 mol/L $NaNO_3$ and 2 g/L $Fe(NO_3)_3$) solution at 110°C.

The XPS depth profiles were measured on the 304L steel and etched samples after electrochemical measurements (Figure 23). These measurements confirm that metal Ti and Zr contents significantly decreased at the extreme surface, down to respectively 0.9 and 0.4 at.% after electrochemical tests compared to 7 and 6 at.% before the immersion in nitric acid. Moreover, distinct XPS depth profiles were obtained for the 304L steel and Zr^+- and Ti^+-etched samples. The profile of the 304L steel shows a higher O penetration in the oxide and a broad oxide/metal interface compared to the etched samples. In addition, the Ni enrichment observed near the oxide/metal interface is greater for etched samples (Figure 23b, c) than for 304L steel due to the selective oxidation of Fe and Cr at the extreme surface. Metal ion etching induces a decrease in the thickness of the passive oxide film after electrochemical measurements. The passive layer formed in nitric acid is made of a mixture of Fe(III) and Cr(III) oxides for all samples. The amount of Fe(III) oxide seems to be the same in the extreme surface for all samples (around 10 at.% for 304L steel and Ti^+ and 9 at.% for Zr^+) and lower than in the initial layer (around 70 at.% for 304L steel, 62 at.% for Ti^+ and 29 at.% for Zr^+). On the other hand, the amount of Cr(III) oxide is slightly different between initial 304L and the etched samples (around 66 at.% for initial 304L, 54 at.% for Ti^+ and 53 at.% for Zr^+) but it is very high compared to the initial film (around

13 at.% for initial 304L, 9 at.% for Ti^+ and 29 at.% for Zr^+). The presence of this Cr-enriched passive layer is explained by the preferential dissolution of iron during passivation [23, 47] and the high stability of Cr(III) oxide. In fact, polarizing a steel in its passive state leads to the iron dissolution contained in the passive layer [58].

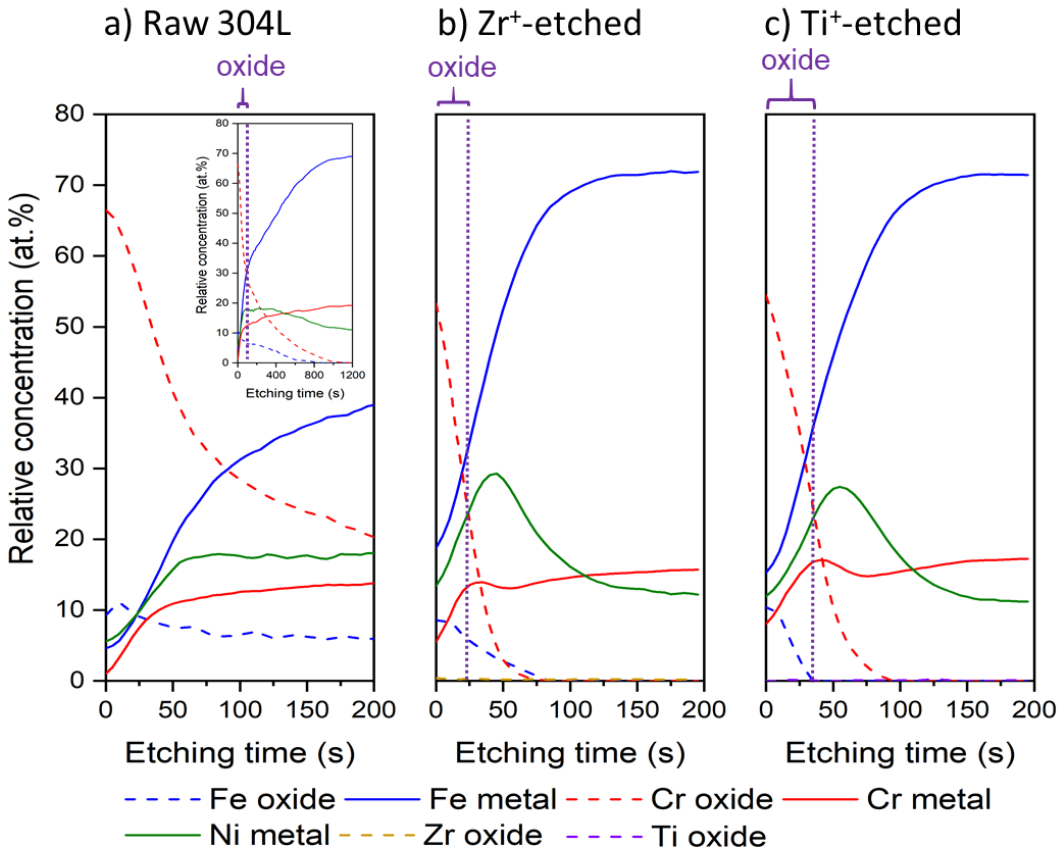

Figure 23: XPS depth profiles of (a) 304L steel and (b) Zr^+- and (c) Ti^+-etched samples after 2 d of immersion in nitric acid (2.5 mol/L HNO_3, 2.5 mol/L $NaNO_3$ and 2 g/L $Fe(NO_3)_3$) solution at 110 °C.

Ti and Zr almost disappeared from the sample surface after the electrochemical tests, which appears coherent with the corrosion rate estimated by electrochemical measurement (around 1µm/year) as Ti and Zr were estimated to be implanted at approximately 4 nm depth in the material. Electrochemical after longer immersion tests could thus be interesting to perform as well as immersion tests.

The composition of the passive films formed after reaction in nitric acid is illustrated in Figure 24. The passive film displays a bilayer structure. The outer layer is mostly made of a mixture of Cr(III) and Fe(III) oxides for all the samples. In contrast, the inner layer differs according to the sample under study: Cr(III) oxide for 304L steel and Ti^+-etched surfaces, and a mixed Fe(III) and Cr(III) oxides for the Zr^+-etched sample.

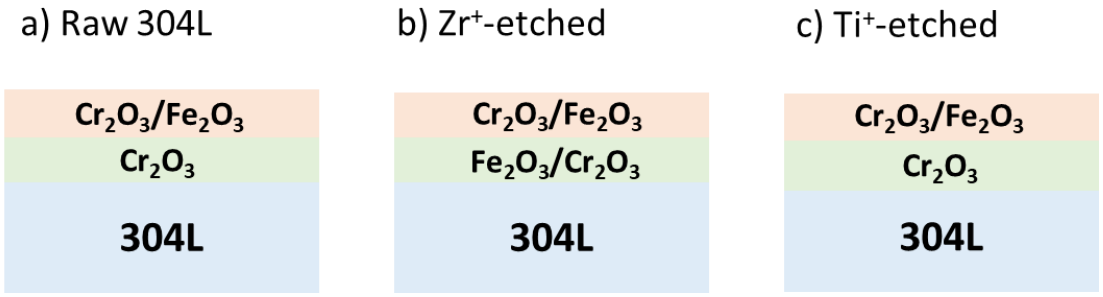

Figure 24: Passive surface layers of a) 304L steel, b) Zr^+-etched and c) Ti^+-etched samples after 2 d of immersion in nitric acid (2.5 mol/L HNO_3, 2.5 mol/L $NaNO_3$ and 2 g/L $Fe(NO_3)_3$) solution at 110 °C.

To summarize, electrochemical measurements and subsequent XPS surface analysis indicate that Ar^+ etching (inert gas) has a distinct impact than Ti and Zr (metal ions): Ar seems to slightly improve corrosion resistance of the 304L steel. In fact Ar^+ etching induces only small changes of 304L crystalline structure, which remains similar to the initial 304L steel, in contrast to metal ion etching (Figure 5). A similar effect was observed for the implantation of another inert gas (Ne) on 304L ASS, and was related to a high density of dislocations in the crystalline structure [59]. On the other hand, metal ion etching induces an extended modification of the crystalline structure (Figure 5) and leads to the formation of a modified and probably more passive layer compared to 304L due to the presence of Ti and Zr increasing the oxidation resistance of the material. This may explain their better corrosion resistance performance in nitric acid. This result should be confirmed by longer immersion tests.

3.1.2 In sodium chloride (NaCl) solution

3.1.2.1 Potentiodynamic polarization curves

Figure 25 compares the potentiodynamic polarization curves of the inital 304L steel and the etched samples in a 3.56 wt.% NaCl solution at ambient temperature after 6 h of immersion. Compared to nitric acid, only potentiodynamic polarization curves after 6 h of OCP are performed in 3.56 wt.% NaCl. Note that resistance to pitting corrosion was not studied in this work and therefore, pitting potentials were not determined. Table 6 shows that the E_{corr} value for the 304L steel reached 0.14 V/SHE after 6 h in NaCl. As a comparison, E_{corr} of the etched substrates is shifted toward positive values (> 0.23 V/SHE). After 6 h, E_{corr} of Ti^+-, Ar^+-, and Zr^+-etched samples stabilizes around 0.18, 0.22 and 0.25 ± 0.01 V/SHE. The effect of etchings, especially by metal ion, is also visible on the corrosion currents. After 6 h, J_{corr} for the Ti^+- and Zr^+-etched samples decreases by an order of magnitude down to 4×10^{-10} A/cm², compared to 3×10^{-9} A/cm² for 304L steel (Figure 25). However, J_{corr} for Ar^+-etched substrate is similar to initial 304L steel, showing a value of 2×10^{-9} A/cm² after 6 h in NaCl. Our values obtained for the 304L ASS differ from those observed in the literature that show a lower E_{corr} and a higher J_{corr} (-0.718 V/SHE and 7×10^{-7} A/cm²) in a 3 % NaCl solution at room temperature [60].

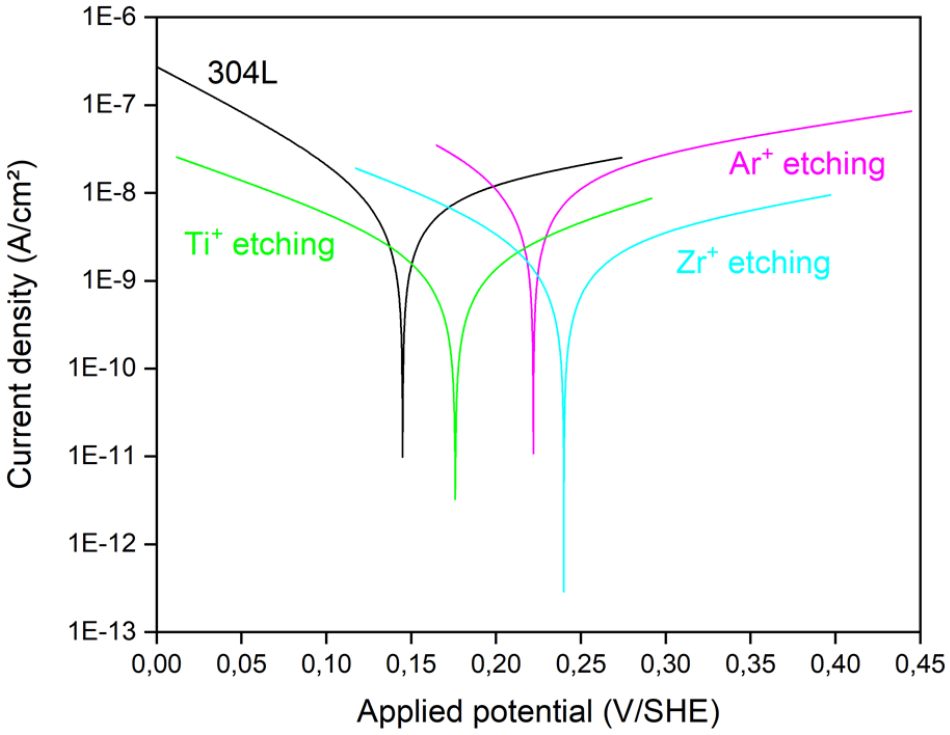

Figure 25: Potentiodynamic polarization curves of the initial and etched 304L steel samples and etched samples in a 3.56 wt.% NaCl solution at ambient temperature after 6 h of immersion.

Table 6: Corrosion potential (E_{corr}) and current density (J_{corr}) values after 6 h of immersion in a 3.56 wt.% NaCl solution at ambient temperature.

	E_{corr} (V/SHE)	**J_{corr}** (A/cm²)
304L	0.14	3×10^{-9}
Ar^+ etching	0.22	2×10^{-9}
Ti^+ etching	0.18	4×10^{-10}
Zr^+ etching	0.25	4×10^{-10}

These results clearly show that metal ion etching has a positive effect on the electrochemical behaviour of the 304L steel in 3.56 wt.% NaCl solution, as observed in nitric acid (Figure 19). This can be explained by the structural modifications of the 304L surface *i.e.* incorporation of sputtered species in the crystal lattice (Figure 5), inducing a modification of the passive layer formed in NaCl environment.

3.1.2.2 Characterization of the electrochemically investigated surface

Figure 26 shows SE micrographs of the surfaces of the 304L steel and etched samples after electrochemical measurements in a 3.56 wt.% NaCl solution. The surface shows some scratches from the mechanical polishing performed beforehand. No obvious degradation is observed after immersion in NaCl solution. This is due to the good

resistance to uniform corrosion of the 304L steel in this environment due to the formation of a stable passive layer [61-63]. The expected corrosion process in NaCl medium is pitting corrosion. Indeed, some pits are observed on the sample surfaces (Figure 26c). This may be due to the pitting potential of the samples being exceeded. However, as the pitting potential has not been determined beforehand, this assumption cannot be verified. Note that no cross-section analysis of these samples was performed due to time constraints.

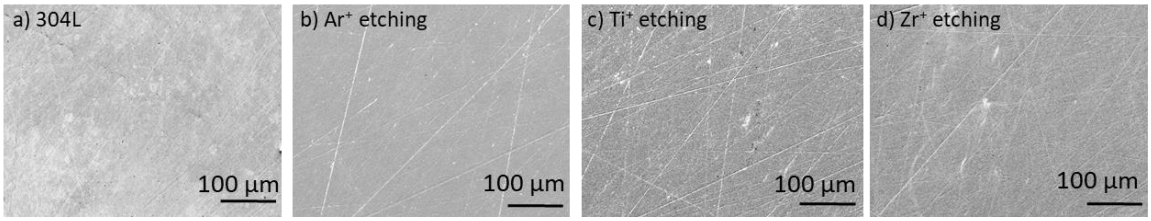

Figure 26: SEM-SE micrographs of the 304L and etched samples after electrochemical measurements in a 3.56 wt.% NaCl solution at ambient temperature.

In conclusion, as previously observed in nitric acid, metal ion etching improves the corrosion resistance properties of the 304L substrate in 3.56 wt.% NaCl solution compared to inert gas etching. This shows that metal ion etching is a good solution to modify the surface of 304L steel by forming stronger bonds at the substrate/bond coat interface, regardless of the environment in which this material is used.

3.2 IMMERSION TESTS

To complement the first elements given by electrochemical measurements, more representative immersion tests are performed in order to study the corrosion behavior on longer duration of the modified substrate surfaces in nitric acid solution at 110 °C and 3.56 wt.% NaCl solution at ambient temperature. Note that the initial surface of all the immersed samples were not polished to be close to the real use conditions. Immersion tests of different durations are performed according to the aggressiveness of the environment: 9 d for nitric acid solution and 60 d for NaCl. From these tests, the weight and thickness losses are calculated and the corrosion rate can be estimated. Moreover, immersion tests in natural seawater are performed on CORRODYS platform during 56 d to study the corrosion resistance of samples under service conditions. The corrosion free potential is measured continuously and visual inspection was performed before and after the 8-week test. Microstructural observations are performed as well. Note however that immersion tests were performed in Singapore seawater (NTU side) only on the contaminated samples (see Appendix 2).

3.2.1 In nitric acid

The immersion tests in nitric acid are performed only on the Zr^+-etched sample as it showed better behavior during the electrochemical measurements: increase in corrosion resistance with time and the lowest corrosion current density after 2 d of immersion (Table 4). Figure 27 shows the results of the immersion tests in a nitric acid solution at boiling temperature. The weight loss is measured by weighing the samples before and after immersion. As shown by the surface observations (Figure 28), a

homogeneous dissolution of the material occurs and a thickness loss (δ) can be estimated using the Equation 1:

Equation 1

$$\delta = \frac{10^4 \Delta w}{S\rho}$$

With δ: thickness (µm)

Δw: weight loss (g)

S: exposed surface (cm²)

ρ: metal density (g/cm^3)

The surface exposed to the nitric acid solution during these immersion tests is 1 cm² and the density used is that of 304L, *i.e.* 7.93 g/cm^3. Then, the corrosion rate (µm/year) can be estimated from the thickness loss calculation using Equation 2:

Equation 2

$$Corrosion\ rate = \frac{365\ \delta}{\Delta t}$$

With δ: thickness (µm)

Δt: immersion time (days)

The weight loss after 9 d of immersion is lower for the Zr^+-etched substrate (272 ± 2 mg/dm²) than for initial the 304L (311 ± 3 mg/dm²). The same tendency is observed for the thickness loss (Figure 27) and the corrosion rate. As the evolution of the weight loss is linear, we can assume a uniform corrosion process and determine the corrosion rates of both materials. The calculated corrosion rate indicates a value of 42 ± 3 µm/year for initial 304L and 36 ± 2 µm/year for the Zr^+-etched substrate, showing an improved corrosion resistance after Zr^+ etching that is consistent with the electrochemical results presented previously (Figure 19). However, the values obtained differ greatly from those estimated by electrochemical measurements (6 µm/year for initial 304L and 1 µm/year for Zr^+ etching after 2 d of immersion). These differences can be explained by the fact that the potential may not have stabilized as the stationary state was not reached. However, after 2 days the stationary state should have been reached. Another explanation can be the influence of the surface roughness of the samples, which can be different from one sample to another as they have not been polished for the immersion tests. If the samples have a high roughness, the real surface exposed to the electrolyte during corrosion tests will be much larger than the expected surface. Therefore, the weight losses related to the surface may be overestimated. These values are lower than the values allowed for the application in nitric acid service of 304L ASS (450 µm/year) [48, 49] and in a boiling condensed solution of 6.2 mol/L (95 µm/year) [50]. However, the 304L corrosion rate value is higher than that observed in a 3.5 mol/L HNO_3 solution at 90 °C after 10 d of immersion (7.5 ± 2.1 µm/year) [51]. As these results have been obtained at a lower temperature than boiling point this could explain this result. Moreover, in our case the composition

of the medium is more complex with the addition of nitrates (2.5 mol/L $NaNO_3$) and ferric ions (2 g/L $Fe(NO_3)_3$), which are detrimental for corrosion rates as shown in [63]. This may explain why our calculated corrosion rate for 304L ASS is higher than that reported in [51].

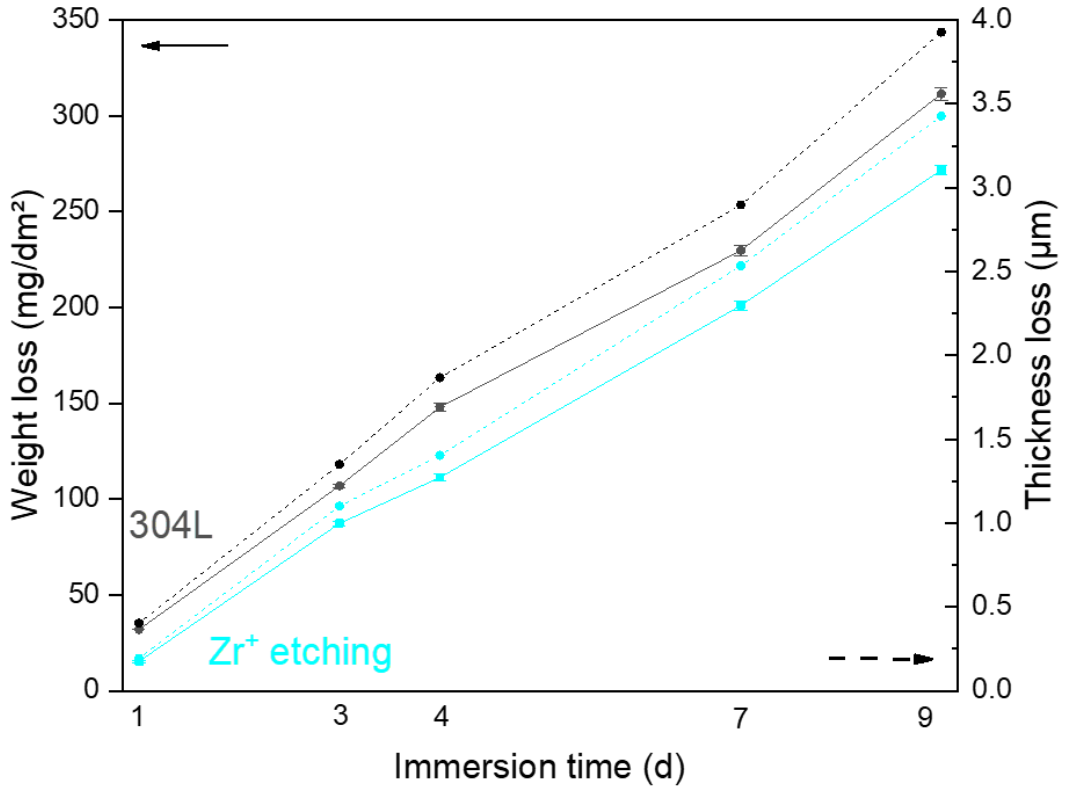

Figure 27: Weight loss measurements (lines) and thickness loss (dotted lines) estimation after 9 d of immersion in a nitric acid (2.5 mol/L HNO_3, 2.5 mol/L $NaNO_3$ and 2 g/L $Fe(NO_3)_3$) solution at 110 °C.

SE micrographs of the initial substrate and Zr^+-etched samples after 9 d of immersion in a nitric acid solution at boiling temperature are shown in Figure 28. Grain boundaries are evident, and appear to be hollowed out for the initial 304L steel (Figure 28a) compared to the Zr^+-etched substrate (Figure 28b). Intergranular corrosion, *i.e.* preferential corrosion along the grain boundaries, is the form of localized corrosion observed for 304L ASS in nitric acid in sufficiently oxidizing conditions to allow the steel to reach its transpassive domain [48, 49]. This intergranular corrosion occurs uniformly on the surface of the material and is related to the oxidizing ability of the medium and to the preferential sensitivity of the grain boundaries which can be attributed to a specific chemical composition of the grain boundary or to a particular crystalline structure [65]. The finer analysis of these grooves in terms of angle and depth could allow the determination of the specific corrosion rates of the grain boundary and of the grain surface.

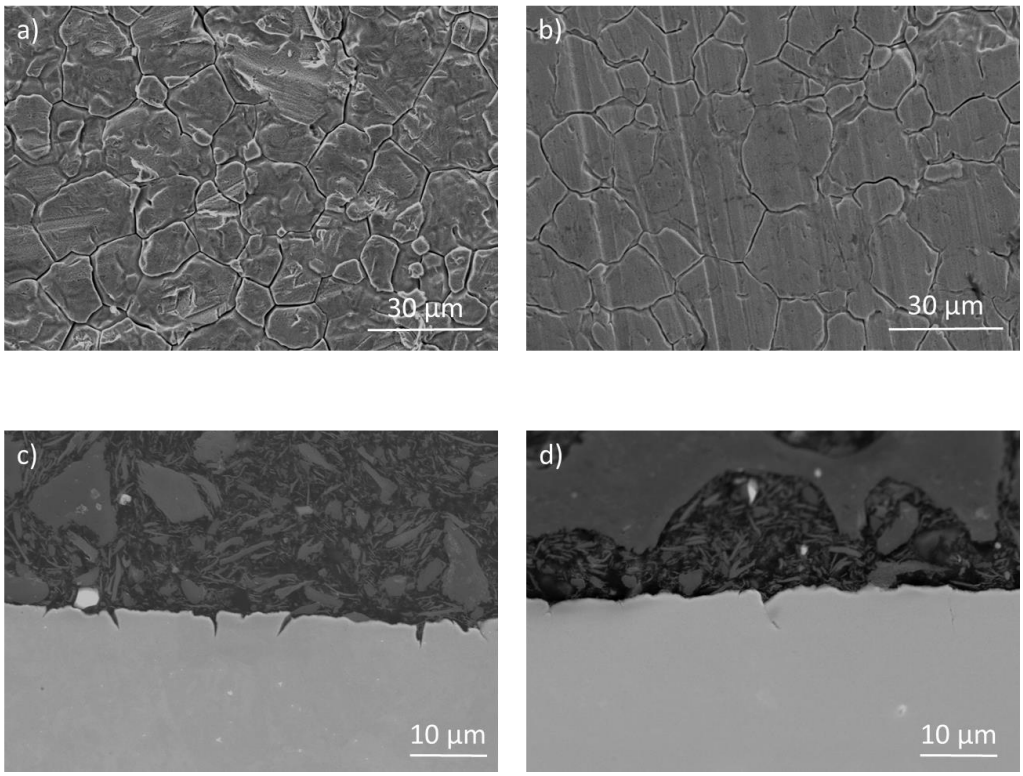

Figure 28: SEM-SE micrographs of surface of a) initial 304L steel and b) Zr^+-etched sample and cross-section of c) 304L steel and d) Zr^+-etched sample after 9 d of immersion in a nitric acid (2.5 mol/L HNO_3, 2.5 mol/L $NaNO_3$ and 2 g/L $Fe(NO_3)_3$) solution at 110 °C.

Cross-sections of these two samples confirm the occurrence of intergranular corrosion for the initial 304L, with grooves about of 3-3.5 µm deep (Figure 28c). The observation of the steel shows intergranular attack. For Zr^+-etched substrates, grooves are tighter and shallower (Figure 28d). This indicates a reduced intergranular corrosion rate for the modified substrate surface which could be attributed to the better passivity of the material due to the presence of zirconium oxide as observed in previous XPS analyses (Figure 6).

3.2.2 In NaCl solution

Figure 29 shows the weight and thickness losses of 304L steel and etched substrates immersed in a 3.56 wt.% NaCl solution at ambient temperature. The surface exposed to NaCl environment during these immersion tests is 53 cm^2 (sample size of 5 x 5 cm^2) and the density used is that of 304L (7.93 g/cm^3). The weight (Figure 29a) and thickness (Figure 29b) losses increase with immersion time, except for the values at 30 d of immersion. The drop in temperature within the laboratory during the 15-30 d immersion period may explains this behavior, leading to weighing errors. The weight loss reached after 60 d of immersion is lower for the Ti^+-etched substrate (6.05 ± 0.10 mg/dm^2) than for initial 304L (7.61 ± 0.13 mg/dm^2) and for others etched samples (9.14 ± 0.08 mg/dm^2 for Zr^+ and 9.15 ± 0.11 mg/dm^2 for Ar^+). As shown by the SEM observations (Figure 30), a homogeneous dissolution of the material occurs and the thickness loss can be estimated using the Equation 1. Then, the corrosion rate can be calculated from the thickness loss calculation using Equation 2. Note that the 30-day

values are excluded for the calculation of the corrosion rate. The evaluated corrosion damage (corrosion rate) indicates a value of 0.51 µm/year for the Ti^+-etched substrate, 0.58 µm/year for 304L steel and 0.70 µm/year for the others etched samples. Attention must be also paid to the surface roughness of the samples, which is probably not the same as they have not been polished for the immersion tests. Indeed, if the samples have a high roughness, the real surface exposed to the electrolyte during corrosion tests will be much larger than the expected surface. Therefore, the weight losses related to the surface could be overestimated.

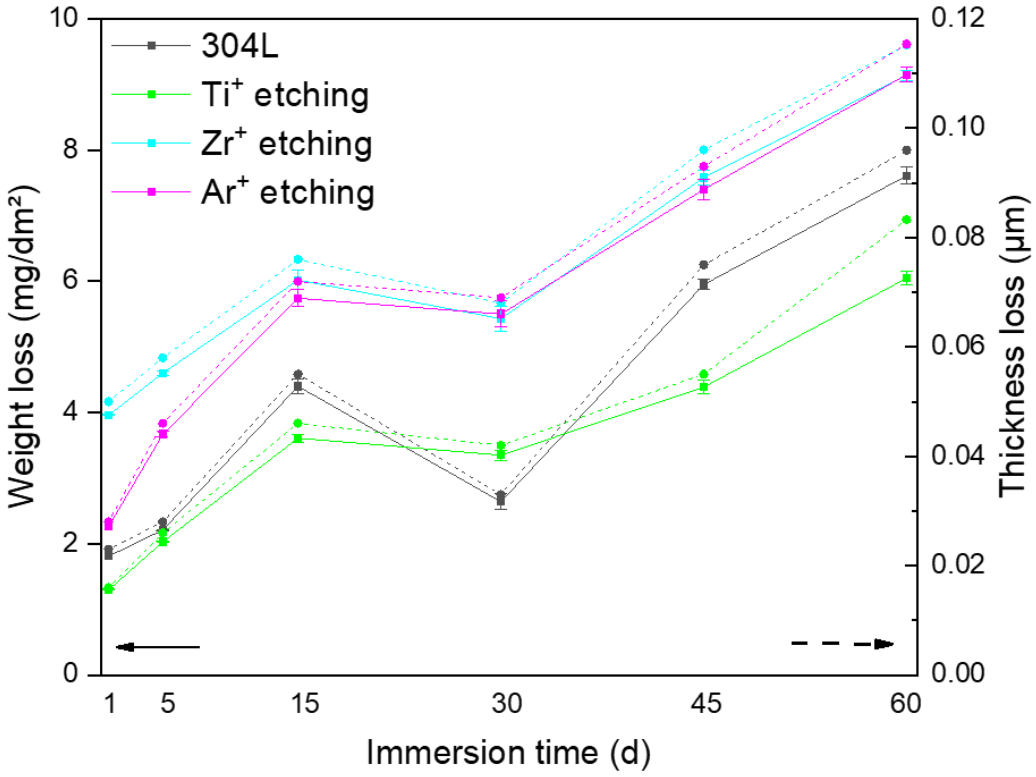

Figure 29: a) Weight loss measurements and b) thickness loss estimation after 60 d of immersion in a 3.56 wt.% NaCl solution at ambient temperature.

Figure 30 shows SE micrographs of initial and etched 304L surface after 60 d of immersion in 3.56 wt.% NaCl solution. All the samples have a similar surface, where the grains are visible. Note that the initial surface were not polished to be close to the real use conditions. In addition, pitting, which appears to be shallow, is observed on the surface of the substrates. This indicates the presence of pitting corrosion after 60 d of immersion in 3.56 wt.% NaCl, as reported on [62].

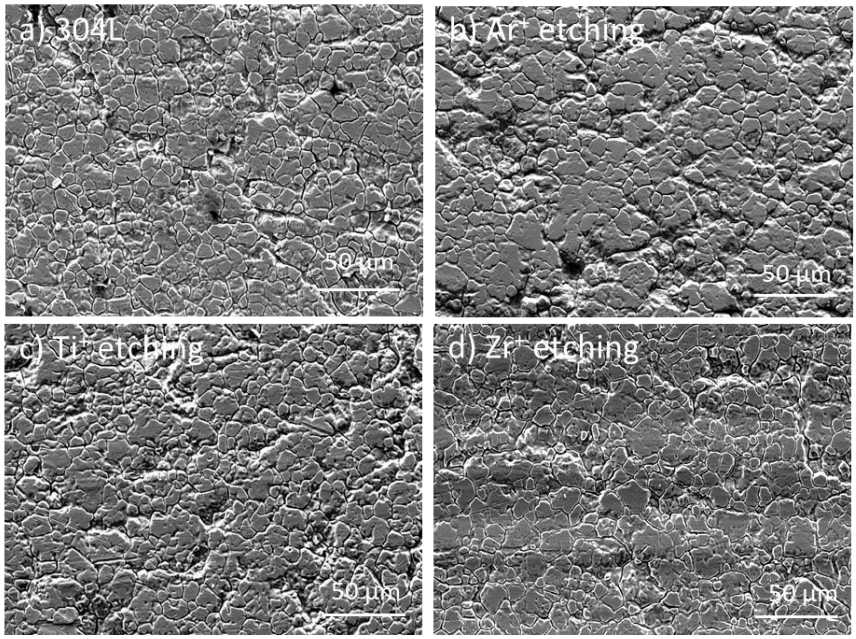

Figure 30: SEM-SE observations of a) 304L steel, b) Ar^+-, c) Ti^+- and d) Zr^+-etched samples surface after 60 d of immersion in a 3.56 wt.% NaCl solution at ambient temperature.

Close visual inspection of pits (Figure 31a) and cross-sections (Figure 31b) allow to measure the average size of the pits. An example is shown in Figure 31 for the 304L steel. The diameter of the pit is estimated at 21 µm and its depth at about 6 µm if the sample cut was performed in the center of the pit. The overall observation of the substrate surfaces indicates that the diameter of the pits seems to be of the same order of magnitude for all the samples.

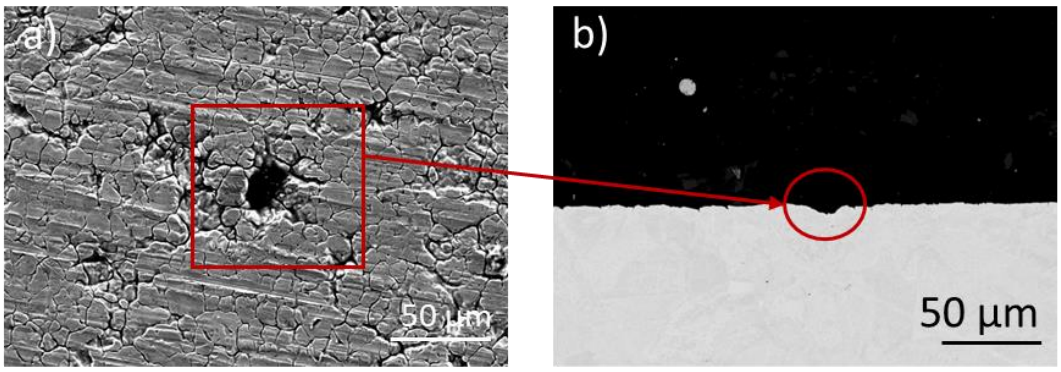

Figure 31: a) surface and b) cross-section observation by SEM of a pit in the raw 304L steel after 60 d of immersion in a 3.56 wt.% NaCl solution at ambient temperature.

3.2.3 In Cherbourg natural seawater

Immersion tests were performed in Singapore seawater only on the contaminated samples (see Appendix 2). Consequently, this section focuses on immersion tests performed on CORRODYS platform in natural seawater from the Port des Flamands in Cherbourg-en-Cotentin during 56 d (from April to June 2021) to study the corrosion resistance of samples under service conditions. A protective paint was applied after

cleaning the substrate surface with ethanol to isolate the 304L substrate in order to study only the coatings or implanted surfaces. The corrosion free potential was measured continuously and visual inspection was performed before and after the 8-week test.

The immersion tests in natural environment were first performed on the metal ion-etched samples, as electrochemical measurements suggested that this treatment was best suited to improve the corrosion resistance. In addition, the number of samples were limited to perform these immersion tests on CORRODYS platform. The monitoring of the evolution of the corrosion potential as a function of immersion time for initial 304L steel and metal ion-etched samples is shown in Figure 32. The curve obtained for initial 304L steel shows that the corrosion potential changes over time. First, an increase in E_{corr} is observed from -0.100 V/ECS up to of 0.168 V/ECS, which is consistent with the literature [66, 67]. Then, the potential drops to -0.200 V/ECS and increase slightly again to stabilize at about -0.120 V/ECS after 56 d of immersion in natural seawater. A similar trend is observed for the metal ion-etched samples, with an increase in potential (up to 0.169 V/ECS for Zr^+-etched and 0.288 V/ECS for Ti^+-etched samples), then a decrease (down to -0.155 V/ECS for Zr^+-etched and -0.144 V/ECS for Ti^+-etched samples) and finally a stabilization around -0.120 V/ECS.

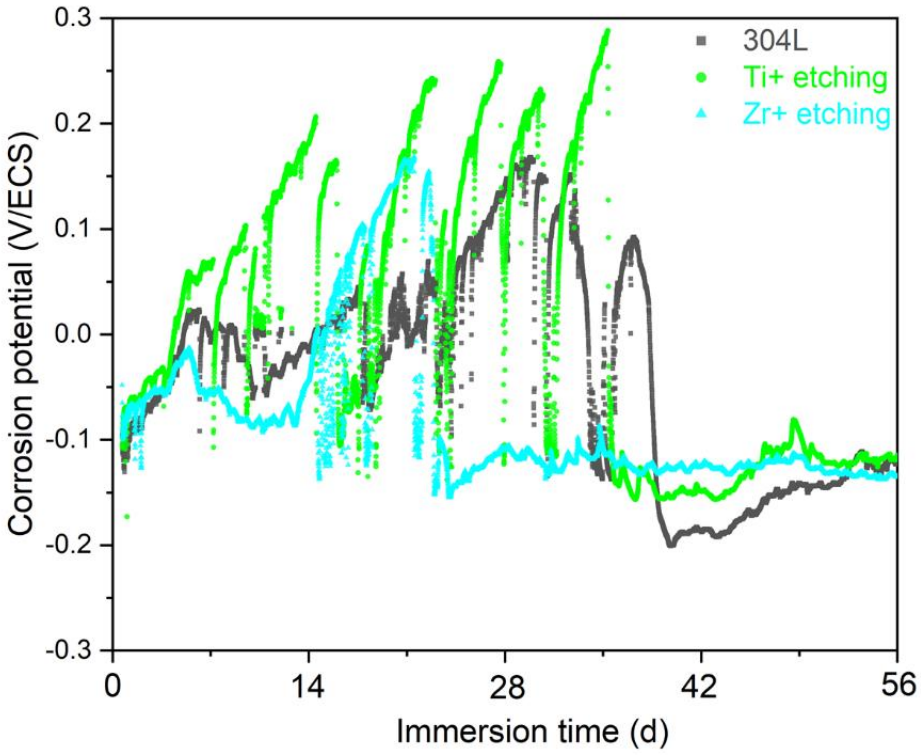

Figure 32: Monitoring of the corrosion potential vs. immersion time in natural seawater in Cherbourg.

The increase in corrosion potential is related to the formation and development of biofilm on the surface of the material. This generally involves an increase in the cathodic reaction rate [66, 67]. The algae, which are the main microorganisms present in biofilm, are able to modify the physico-chemical properties of the surface and lead to an increase of the corrosion potential [66, 67]. It should be noted that this increase

can be detrimental if the value of the corrosion potential is higher than the pitting potential. On the other hand, sudden decreases in corrosion potential observed after some immersion time may be due to an abrupt change in the surface of the samples such as biofilm removal or degradation. Note that the evolution of the corrosion potential shows cyclic instabilities, which can be due to electrical contact losses and/or to local biofilm removals. In addition, oscillations with a period of about 24 h can be observed and are attributed to circadian cycles, *i.e.* lower temperatures during the night [66].

Microbiological analyses were performed on the biofilm collected from the surface of the samples to study their antifouling properties. The total biomass is relatively similar for all the samples and is in the order of 1×10^7 microorganisms/cm². Figure 33 shows the total microalgae biomass and total aerobic heterotrophic flora (viable and cultivable microbial communities) counted after 56 d of immersion in Cherbourg natural seawater. The total microalgae biomass (Figure 33a) is lower for the Zr^+-etched substrate (6.5×10^3 microorganisms/cm²) compared to initial 304L (1.1×10^5 microorganisms/cm²) and Ti^+-etched sample (1.3×10^5 microorganisms/cm²). On the other hand, the total aerobic heterotrophic flora (Figure 33b) is lower for the Ti^+-etched substrate (1.8×10^4 [1]UFC/cm²) compared to 304L steel (5.7×10^4 UFC/cm²) and Zr^+-etched sample (6.0×10^4 UFC/cm²). These results seem to indicate a different behavior of the etched samples compared to 304L steel. Zr^+ etching tends to reduce the amount of microalgae on the biofilm, whereas Ti^+ etching affects the amount of bacteria. Further analysis of the biofilms would be required to confirm these observed tendencies.

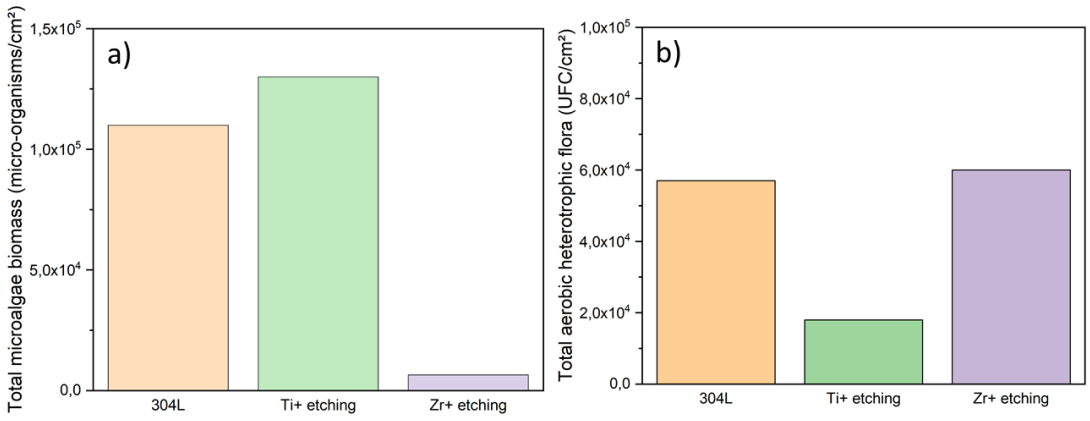

Figure 33: Results of microbiological analyses indicating the a) total microalgae biomass and b) total aerobic heterotrophic flora after 56 d of immersion in Cherbourg natural seawater.

BSE images of two areas of the surfaces of 304L steel and metal ion-etched substrates immersed during 56 d in Cherbourg natural seawater are shown in Figure 34. These observations were performed after biofilm removal for microbiological analyses. The 304L steel surface (Figure 34a) is differs from that of the etched samples, *i.e.* the grains are more visible. Two distinct areas of the sample surface are

[1]UFC: Unités formant colonies (French) or colony forming units (English)

studied. Only small residues of biofilms seem to be visible in area 1, while in area 2, a remaining part of the biofilm is clearly observed.

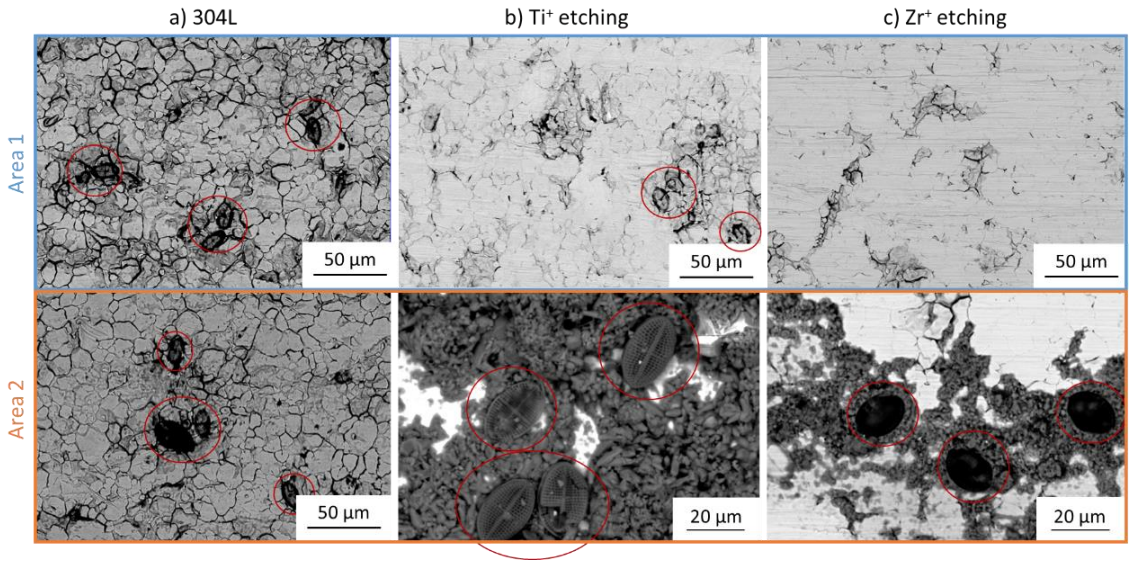

Figure 34: SEM-BSE micrographs on two different areas of the surface of the a) 304L steel, b) Ti^+- and c) Zr^+-etched substrates after 56 d of immersion in Cherbourg natural seawater.

Biofilm are made of macromolecules and microorganisms [66]. The microorganisms are mainly microalgae and more particularly diatoms as observed on Figure 34 (red circle). The diatoms are microscopic and unicellular algae that typically range in size from 10 to 100 µm [68, 69]. They only need carbon dioxide and nutrients to growth, which is why they are considered as the initial colonizing biomass on the surfaces immersed in the marine environment [68]. It seems that the species present on the surface of our samples is a pennate diatom called *cocconeis placentula* [69]. It is an abundant form of the fouling diatom community on 304L as it easily attaches to any surface [69].

3.3 CONCLUSIONS

Electrochemical measurements are performed in nitric acid (2.5 mol/L HNO_3, 2.5 mol/L $NaNO_3$, 2 g/L $Fe(NO_3)_3$) solution at 110 °C and in 3.56 wt.% NaCl solution at ambient temperature in order to estimate the corrosion resistance of the 304L ASS modified by etching.

In nitric acid solution, electrochemical measurements and subsequent XPS surface analysis indicate that Ar^+ etching (inert gas) has a lower impact than Ti and Zr (metal ions) on corrosion resistance on the 304L ASS. Ar^+ etching induces only small changes of 304L crystalline structure (incorporated in interstitial sites), which remains similar to the initial 304L steel. In contrast, metal ion etching that can substitute to 304L ASS atoms, leads to lattice mismatch decrease and the formation of stronger bonds at the substrate/bond coat interface. HiPIMS metallic etching decreases the corrosion rate of the initial 304L steel by forming a modified and probably more protective passive layer, which hinders the charge transfer process. In addition, these

modifications will provide additional protection in areas where coatings may fail. The positive effect of metal ion etching on the electrochemical behaviour of the 304L ASS is also observed in NaCl solution. This can be due to the structural modifications of the 304L surface, inducing the formation of stronger bonds at the substrate/bond coat interface and leading to the growth of an epitaxial film. Moreover, metal ion etching can lead to the modification of the passive layer formed in this environment by promoting TiO_2 and ZrO_2 formation on the sample surface. Longer immersion tests are necessary to confirm these tendencies for longer durations and observe the corrosion behaviors of the etched samples as well as of the samples with etching and bond coats.

Immersion tests are performed to study the corrosion behavior on longer duration of the 304L ASS modified by etching. These tests are performed in nitric acid (2.5 mol/L HNO_3, 2.5 mol/L $NaNO_3$, 2 g/L $Fe(NO_3)_3$) solution at 110 °C, in 3.56 wt.% NaCl solution at room temperature and in Cherbourg natural seawater at ambient temperature.

In nitric acid solution, immersion tests and SEM surface analysis indicate that Zr^+-etched sample improves the corrosion resistance of the 304L ASS. Intergranular corrosion is noticed on 304L surface in this environment showing that due to the oxidizing power of the medium, the steel is in its transpassive state. Its surface modification by etching for the duration of the test leads to a reduction of the intergranular grooves. Longer tests should be performed to see the evolution of the corrosion mechanism. Although the corrosion rate values obtained differ from those of the electrochemical measurements, the same trend is observed *i.e.* Zr^+ etching decreases the corrosion rate of 304L. Moreover, immersion tests performed in NaCl show that only Ti^+ etching improves the corrosion resistance of 304L ASS and not both types of metal ion etching. No major differences are obtained between these different samples regarding their corrosion rate. Moreover, the presence of pitting corrosion is noticed after 60 d of immersion in NaCl solution, which could be studied in more detail. Finally, immersion tests performed under service conditions (natural seawater) show a similar behaviour of etched samples and 304L ASS. This suggests that these samples do not have a pronounced beneficial effect on the corrosion resistance of 304L. Nonetheless, they seem to influence the biofilm population by decreasing bacteria and/or microalgae.

4. CORROSION RESISTANCE INVESTIGATIONS OF THE ETCHED AND BOND COAT DEPOSITED SAMPLES

4.1 ELECTROCHEMICAL MEASUREMENTS

Electrochemical measurements are performed on a limited surface and instantaneous in time, using a three-electrodes configuration. Polarization and electrochemical impedance spectroscopy (EIS) are applied for measurements in nitric acid (2.5 mol/L HNO_3, 2.5 mol/L $NaNO_3$, 2 g/L $Fe(NO_3)_3$) solution at 110 °C while only polarization measurements are performed in 3.56 wt.% NaCl solution at ambient temperature. In the case of polarization measurements, Tafel extrapolation is a technique used to estimate the corrosion potential and corrosion current.

4.1.1 In nitric acid

4.1.1.1 Potentiodynamic polarization curves and EIS

Figure 35 shows the potentiodynamic polarization curves of the initial substrate and, etched and metallic bond coat deposited samples in a nitric acid solution at boiling temperature after 6 h of immersion. The polarization curves were not shown after 2 d of immersion as there were experimental problems, particularly leakage in the electrochemical cell. Table 7 shows that the E_{corr} value for the initial 304L steel equals 0.98 V/SHE after 6 h in nitric acid. In comparison, a dispersion of E_{corr} of the etched and bond coat deposited samples is observed. Only E_{corr} of Ar^+-etched and Zr-coated and, unetched and Zr-coated samples are shifted toward positive values to equal 1.02 and 1.03 V/SHE, respectively. A similar E_{corr} values tendency is observed for Zr bulk with a value of 0.7 V/SHE in a 3.1 mol/L HNO_3 solution at boiling temperature after 24 h of immersion [64] compared to 0.82 V/SHE for the Zr^+-etched and Zr-coated sample. In the case of 1 µm-thick Ti coating, a lower E_{corr} (0.527 V/SHE) is observed in 1 mol/L HNO_3 solution at room temperature [47]. The observed dispersion of E_{corr} could be due to kinetic limitations *i.e.* the potential may not be stabilized after 6 h and the stationary state not be reached. Another hypothesis could be that the decrease of Ecorr, especially observed for the Zr^+-etched and Zr-coated sample, could be due to the decrease of the reduction rate of nitric acid attributed to the growth of the zirconia layer [70]. The effect of bond coats is also observed on the corrosion currents. After 6 h of immersion, J_{corr} decreases by an order of magnitude for all the etched and metallic bond coat deposited samples down to 10^{-4} mA/cm² and even by almost two orders of magnitude for the Zr^+-etched and Zr-coated samples (10^{-5} mA/cm²), compared to 1×10^{-3} mA/cm² for initial 304L steel.

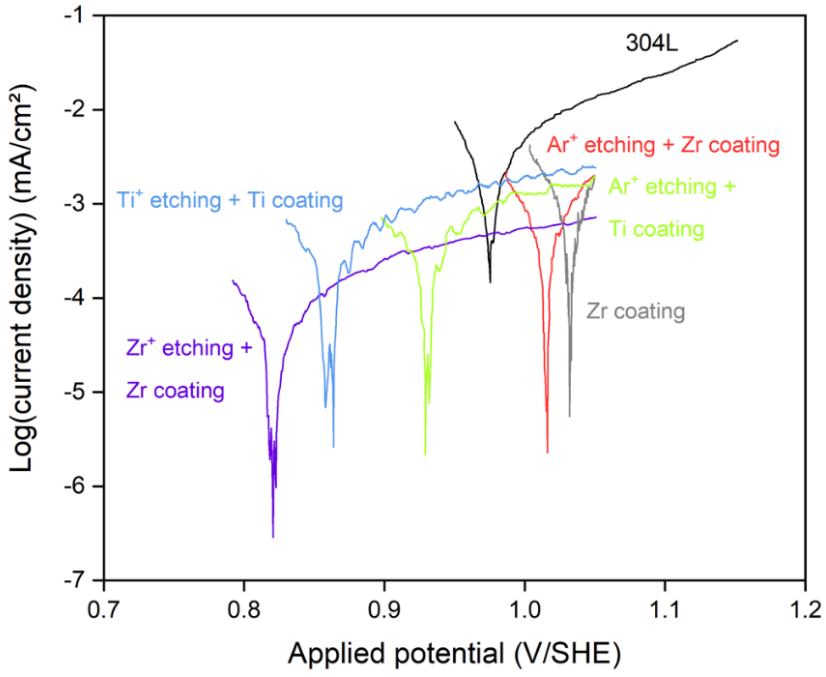

Figure 35: Potentiodynamic polarization curves of the 304L steel and the etched and metallic bond coat deposited samples in a nitric acid (2.5 mol/L HNO_3, 2.5 mol/L $NaNO_3$ and 2 g/L $Fe(NO_3)_3$) solution at 110 °C after 6 h of immersion.

To summarize, all the samples show a decrease of the corrosion current density compared to bare 304L, the most important decrease being obtained for the Zr^+-etched and Zr-coated sample. It could have been interesting to observe the behavior of our samples in the transpassive domain but this was not done to limit sample degradation for the characterizations after electrochemical tests.

Table 7: Corrosion potential (E_{corr}) and current density (J_{corr}) values after 6 h of immersion in a nitric acid (2.5 mol/L HNO_3, 2.5 mol/L $NaNO_3$ and 2 g/L $Fe(NO_3)_3$) solution at 110 °C.

	E_{corr} (V/SHE)	**J_{corr}** (mA/cm²)
304L	0.98	1×10^{-3}
Ar^+ etching + Ti coating	0.93	1×10^{-4}
Ti^+ etching + Ti coating	0.86	1×10^{-4}
Ar^+ etching + Zr coating	1.02	1×10^{-4}
Zr^+ etching + Zr coating	0.82	2×10^{-5}
Zr coating	1.03	3×10^{-4}

It is interesting to note that etching followed by metallic bond coat deposition has a positive effect on the electrochemical behaviour of 304L steel in nitric acid environment. Note that this effect seems to be more pronounced for Zr^+-etched and Zr-coated samples than for the other ones. This tends to indicate that beneficial effect of Zr^+ etching compared to the Ar^+ one is still observed after the bond coat deposition. Of course, this first observation has to be confirmed by immersion tests performed for longer durations.

The substrate/bond coat interface forms differently depending on the used etching type (Zr^+ or Ar^+), as illustrated in Figure 5. Zr can substitute to atoms of the 304L structure, whereas Ar is incorporated into the interstitial sites, leading to a decrease of the lattice mismatch and formation of stronger bonds at the substrate/bond coat interface after Zr^+ etching. However, even if this improvement of the bonding between the substrate and the bond coat due to metal etching can induce an improvement of the adhesion of the substrate (Figure 17), it cannot explain the modification of the surface properties of the bond coat except if the bond coat has delaminated. In that case, the higher adhesion may confer a better protection by the coating in aggressive environment by preventing the bond coat from delaminating. This evolution could also be related to a modification of the structure of the bond coat. As previously shown, differences between the different etchings have been observed in the XRD patterns (Figure 8), which show a modification of the crystallization of the bond coat. This could be due to metal ion species incorporation on the 304L ASS substrate that could act as preferential nucleation sites for the bond coat growth and promote an epitaxial film, at least on the first layers. As a result, a denser film could be formed. However, no

major differences were observed between the bond coats with TEM observations. Other characterizations should be performed on the bond coats obtained with the different etchings to determine structural modifications induced by the etching type.

Figure 36 displays the Nyquist diagrams of the etched and metallic bond coat deposited samples and the initial 304L substrate at E_{OCP} after 6 h and 1 d of immersion in a nitric acid solution at boiling temperature. The polarization curves were not shown after 2 d of immersion as there were experimental problems, particularly leakage in the electrochemical cell. This also explains why the Nyquist diagrams are shown after only 1 d and not 2 d of immersion as for the etched samples (Figure 20). The Nyquist diagrams (Figure 36a, b) show only one semicircle (capacitive loop) for all the samples, corresponding to a single time constant. The increasing loop diameter for all the samples after 6 h of immersion compared to initial 304L steel is related to the increase in transfer resistance, which means improved corrosion resistance [54-56]. This indicates a decrease in corrosion rate, again possibly related to the growth of a passive film that limits the electron transfer between our system and the environment. Another explanation is a better passivity of this film due to the presence of Ti and Zr that oxidize rapidly and are stable in this environment. A maximum loop diameter is reached for the Zr^+-etched and Zr-coated substrate after 6 h in nitric acid environment (Figure 36a), which is consistent with the electrochemical measurements (Figure 35). After 1 d of immersion, the diameter of the capacitive loops of all the samples increases, except for the Ar^+-etched and Zr-coated substrate (Figure 36b). Note that this phenomenon is more pronounced for the Zr^+-etched and Zr-coated sample, indicating the higher decrease in corrosion rate over time.

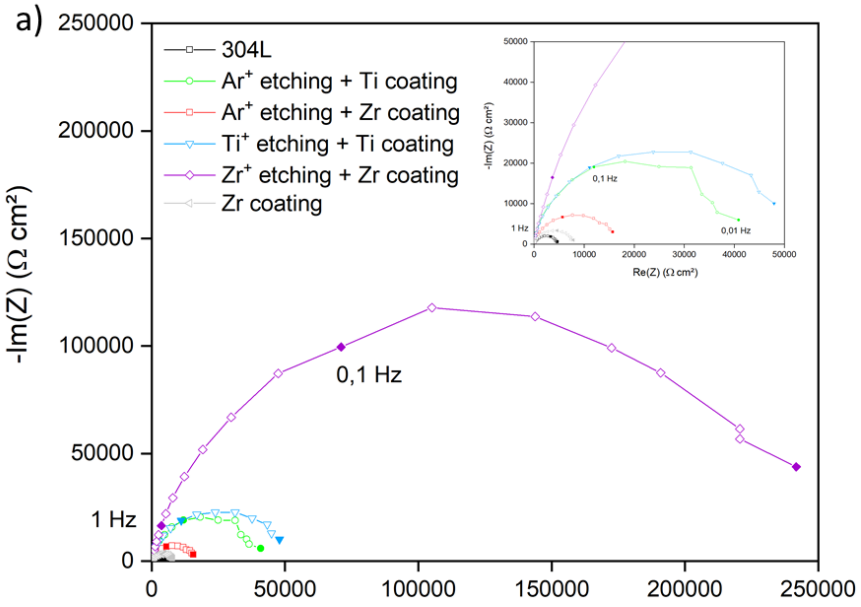

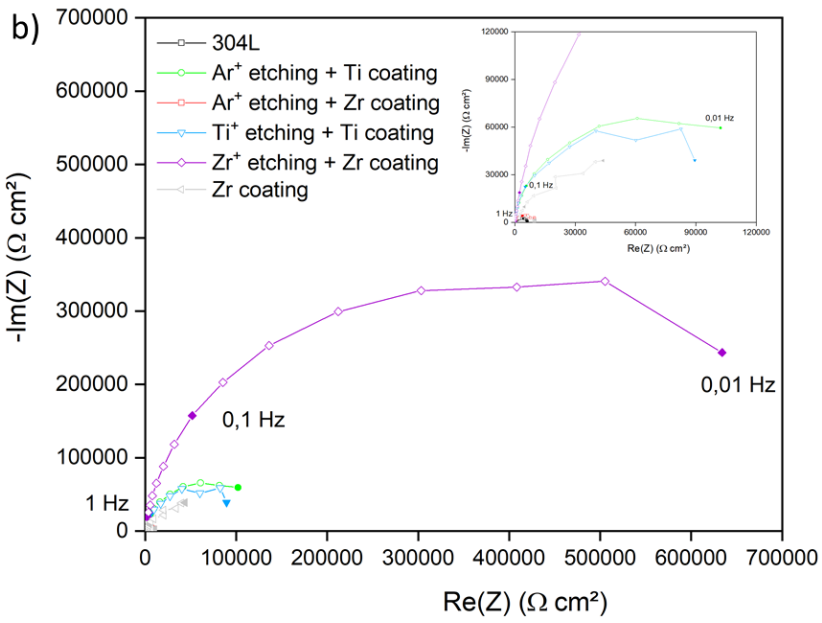

Figure 36: Nyquist diagrams at open circuit potential of etched and coated samples after a) 6 h and b) 1 d in a nitric acid (2.5 mol/L HNO_3, 2.5 mol/L $NaNO_3$ and 2 g/L $Fe(NO_3)_3$) solution at 110°C.

EIS measurements show a different behavior of Ti-based samples compared to Zr ones depending on the etching type performed prior to deposition. Metal ion etching appears to have a beneficial effect on the corrosion resistance properties of the substrate/Zr bond coat system while Ar^+ etching does not. These results are consistent with those obtained on etched-only surfaces (Figure 20). Indeed, Zr can substitute to atoms of the 304L structure, whereas Ar is incorporated into the interstitial sites, leading to a decrease of the lattice mismatch and formation of stronger bonds at the substrate/bond coat interface after Zr^+ etching. The metal ion species incorporated on the 304L ASS substrate could act as preferential nucleation sites for the bond coat growth and promote an epitaxial film, at least on the first layers. As a result, a denser film could be formed compared to the bond coat formed after Ar^+ etching. On the other hand, this effect is not observed for the Ti-based coating system. This may be due to high fluxes of doubly-ionized metal species in the Ti HiPIMS discharge that can cause severe back attraction to the target and also re-sputtering, which can prevent the formation of strong ionic and covalent bonds [7]. In our case, it is expected that high fluxes of Ti^{2+} in combination with a high negative substrate bias (- 900 V), meaning that Ti ions are accelerated towards the substrate with energy of 1800 eV, prevent any formation of strong interface by reducing the number of Ti incorporated on the 304L ASS. This could lead to fewer preferential nucleation sites compared to Zr and therefore, affect the bond coat growth.

The EIS data can be fitted with a model of an equivalent electrical circuit using an in-lab software based on a simplex algorithm [71]. The used model obtained is shown in Figure 37, and best-fit values obtained for the model parameters are listed in Table 8.

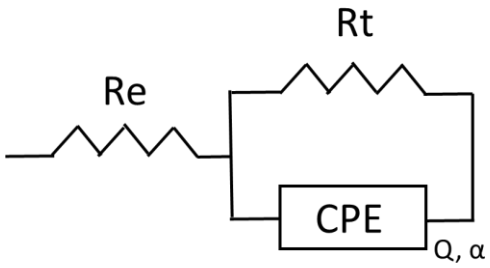

Figure 37: Equivalent electrical circuit of the initial and etched and metallic bond coat deposited samples in a nitric acid (2.5 mol/L HNO_3, 2.5 mol/L $NaNO_3$ and 2 g/L $Fe(NO_3)_3$) solution at 110°C.

In this model, R_e is the resistance of the electrolyte and R_t is the charge transfer resistance. The constant phase element (CPE) consists of a non-ideal capacitance and reflects the heterogeneities of the surface; it is characterized by parameters α and Q [72]. The α parameter is determined from the representation of the imaginary part of the impedance (Im(Z)) as a function of frequency (f): the slope at high frequency is – α [73]. In addition, the CPE coefficient (Q) is defined from the imaginary part of the impedance by:

$$Q_{eff} = \sin(\frac{\propto \pi}{2}) \frac{-1}{Im(Z)(2\pi f)^{\alpha}}$$

The main differences between the initial 304L substrate and the other samples lie in the values of the CPE parameters (α and Q) and the charge transfer resistance R_t, which is associated with the capacitive loop of the Nyquist diagram (Figure 36b). After 6 h in nitric acid solution, all the coated substrates show R_t values larger than for initial 304L steel (Table 8). The high resistance values suggest an improvement of corrosion resistance due to the formation of a more protective passive film than on the initial 304L [34]. These improved properties could be explained by the modification of the composition of the passive layer: presence of oxidized Ti or Zr that increases the resistance in this environment. In addition, $\alpha < 1$ for all samples, which indicates surface heterogeneities [72] or continuous distribution of time constants for charge-transfer reactions [73]. This is especially observed for the unteched and Zr-coated sample that displays the lowest α value (0.708), which may be related to the presence of the native oxide layer under the Zr bond coat probably leading to a higher surface roughness of this sample. The CPE parameter Q_{eff} is determined using α and it shows an inverse trend.

Table 8: Rt, α and Qeff values after 6 h and 1 d of immersion in a nitric acid (2.5 mol/L HNO_3, 2.5 mol/L $NaNO_3$ and 2 g/L $Fe(NO_3)_3$) solution at 110°C.

	R_t (kΩ cm²)		**α** (dimensionless)		**Q_{eff}** (s^{α}/Ω cm²)	
	6 h	1 d	6 h	1 d	6 h	1 d
304L	5	8	0.841 ± 0.015	0.822 ± 0.009	2.05×10^{-4} ± 8.77×10^{-6}	2.00×10^{-4} ± 5.52×10^{-6}
Ar^+ etching + Ti coating	41	102	0.897 ± 0.008	0.887 ± 0.008	8.18×10^{-5} ± 1.28×10^{-6}	9.41×10^{-5} ± 1.78×10^{-6}
Ti^+ etching + Ti coating	48	89	0.912 ± 0.012	0.893 ± 0.011	7.39×10^{-5} ± 1.57×10^{-6}	9.15×10^{-5} ± 1.95×10^{-6}
Ar^+ etching + Zr coating	16	10	0.845 ± 0.008	0.830 ± 0.008	1.37×10^{-4} ± 1.99×10^{-6}	1.92×10^{-4} ± 2.86×10^{-6}
Zr^+ etching + Zr coating	242	634	0.893 ± 0.011	0.797 ± 0.005	1.37×10^{-5} ± 4.12×10^{-7}	1.64×10^{-5} ± 4.25×10^{-7}
Zr coating	8	44	0.708 ± 0.007	x	3.85×10^{-4} ± 9.59×10^{-6}	x

After a longer reaction time of 1 d in nitric acid at boiling temperature, close R_t values are obtained for the 304L steel and the Ar^+-etched and Zr-coated sample (Table 8), while higher R_t values are obtained for all other coated samples. On the other hand, a decrease in α with immersion time is observed for all the samples. This may be due to surface heterogeneity [74]. Lower Q_{eff} values (10^{-5} s^{α}/Ω cm²) are obtained for all coated substrates, especially for the Zr^+-etched and Zr-coated sample, compared to the initial 304L steel and to the Ar^+-etched and Zr-coated sample. Nonetheless, Q_{eff} value obtained for Ar^+-etched and Zr-coated is lower than for initial 304L steel. The Q_{eff} values could be used to determine the oxide or double layer capacitance values, which would lead to an estimation of the active surface and/or the thickness of the oxide layer. These results confirm the previous potentiodynamic polarization measurements, indicating the better corrosion resistance of the Zr^+-etched and Zr-coated substrate. This could be due to metal ion species incorporation on the 304L ASS substrate that could act as preferential nucleation sites for the bond coat growth and promote an epitaxial film, at least on the first layers. As a result, a denser film

could be formed. The higher adhesion of the bond coat for these samples, which is attributed to the stronger bond formation at the substrate/bond coat interface compared to Ar^+-etched and unetched samples could explain the fact that no delamination is observed. Note that the values of the CPE parameters could not be determined using this method for the unetched and Zr-coated sample due to a leakage problem during the measurement.

To sum up, the combination of etching and bond coat deposition has a positive effect on the corrosion resistance of 304L ASS, especially for the Zr^+-etched and Zr-coated sample. This confirms the beneficial effect of Zr^+ etching compared to Ar^+ etching due to the formation of stronger bonds, the reduction of the lattice mismatch at the substrate/bond coat interface and possibly to a modification of the bond coat growth mechanism leading for example to a higher density of the bond coat. This can also be related to the higher adhesion of this sample that allow preventing the bond coat from delaminating. On the other hand, this effect is not observed for the Ti-based coating system, which could be due to high fluxes of doubly-ionized metal species in the Ti HiPIMS discharge that can cause severe back attraction to the target and also re-sputtering. This could prevent the formation of strong ionic and covalent bonds by reducing the number of Ti incorporated on the 304L ASS, probably leading to fewer preferential nucleation sites than for Zr. Therefore, this could affect the bond coat growth.

4.1.1.2 Characterization of the electrochemically investigated etched and bond coat-deposited surface

Figure 38 shows SE images of the etched and metallic bond coat-deposited samples after electrochemical measurements in the nitric acid. The surface shows some scratches from the mechanical polishing performed beforehand. No obvious degradation is observed on the samples surface after immersion in nitric acid solution. Moreover, the atomic percentages of the bond coats elements are estimated from EDX spectra after electrochemical measurements in nitric acid. Compared to the initial values shown in Figure 9, the amounts of Ti have decreased (73 at.% Ti for Ti bond coat down to 35 at.% for Ti^+-etched and Ti-coated and 25 at.% for Ar^+-etched and Ti-coated samples after immersion), Nonetheless, the Ti-based samples show similar results indicating that the Ti bond coat is still present after immersion. The substrate elements (Fe, Cr and Ni) are also observed because of the limited resolution of EDX analysis (spot size). However, only the Zr^+-etched and Zr-coated sample shows the presence of Zr after immersion in nitric acid (down to 22 at.% Zr for Zr^+-etched and Zr-coated sample after immersion compared to 72 at.% Zr before immersion), suggesting that the other bond coats have delaminated. This may be due to the higher adhesion of this bond coat compared to the Ar^+-etched and unetched ones, resulting from the formation of stronger bonds and the reduction of lattice mismatch at the substrate/bond coat interface. No cross-section analysis of these samples was performed due to time constraints.

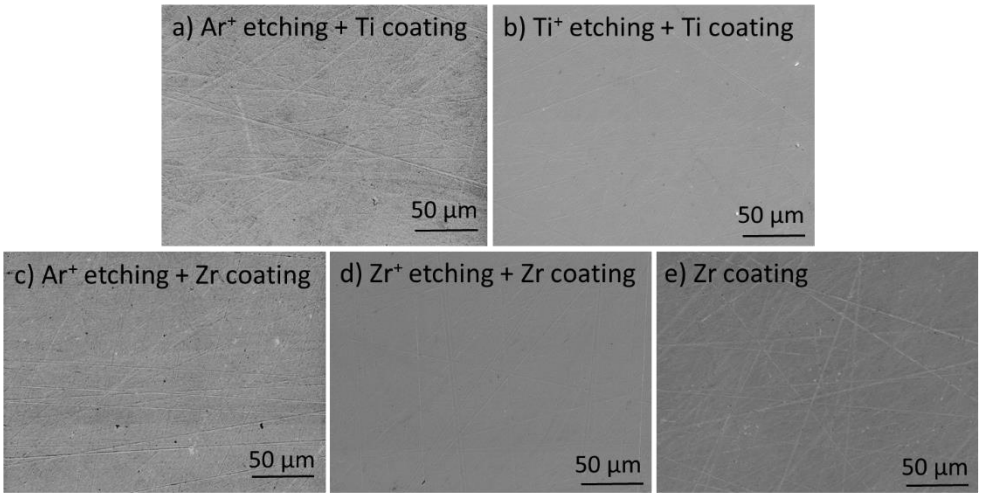

Samples	Fe (at.%)	Cr (at.%)	Ni (at.%)	O (at.%)	Ti (at.%)	Zr (at.%)
Ar^+ etching + Ti coating	48 ± 2	15 ± 1	7 ± 1	5 ± 1	25 ± 1	X
Ti^+ etching + Ti coating	42 ± 1	13 ± 1	5 ± 1	5 ± 1	35 ± 1	X
Ar^+ etching + Zr coating	68 ± 1	20 ± 1	10 ± 1	1 ± 1	X	1 ± 1
Zr^+ etching + Zr coating	52 ± 1	16 ± 1	7 ± 1	3 ± 1	X	22 ± 1
Zr coating	66 ± 3	19 ± 1	11 ± 1	2 ± 1	X	2 ± 1

Figure 38: SEM-SE micrographs of a) Ar^+-etched and Ti-coated, b) Ti^+-etched and Ti-coated, c) Ar^+-etched and Zr-coated, d) Zr^+-etched and Zr-coated and e) Zr-coated samples and atomic percentages of elements obtained by EDX spectra after electrochemical measurements in a nitric acid (2.5 mol/L HNO_3, 2.5 mol/L $NaNO_3$ and 2 g/L $Fe(NO_3)3$) solution at 110°C.

GAXRD patterns at 0.5° incident angle performed for the etched and bond coat deposited-samples before and after electrochemical measurements in nitric acid solution at 110 °C are shown in Figure 39. In the Ti (Zr)-coated sample diagram, contributions from the 304L steel substrate and metallic Ti (Zr) are detected before (Figure 39a) and after (Figure 39b) immersion in nitric acid. However, some differences are observed between the patterns before and after the electrochemical measurements. For instance, the Zr contribution at 35.0°2θ and 36.6°2θ disappears for the Zr bond coat-deposited sample after immersion. Similarly, the Zr contribution at 36.6°2θ disappears for the Ar^+-etched and Zr-coated sample. Moreover, the Ti contribution at 76.2°2θ disappears after immersion for the Ar^+-etched and Ti-coated sample. Other differences in 304L substrate contributions are observed, such as the disappearance of the γ(200) phase at 50.7°2θ for all the samples and the disappearance of the γ(220) phase at 74.9°2θ for the metal ion-etched and coated samples (Zr^+-etched and Zr-coated and Ti^+-etched and Ti-coated samples). The disappearance of the α(200) peak is also noticed for unetched and Zr-coated sample after immersion in nitric acid. The appearance of the α(110) peak at 44.6°2θ is observed for the metal ion-etched and unetched samples (Zr^+-etched and Zr-coated and unetched and Zr-coated samples).

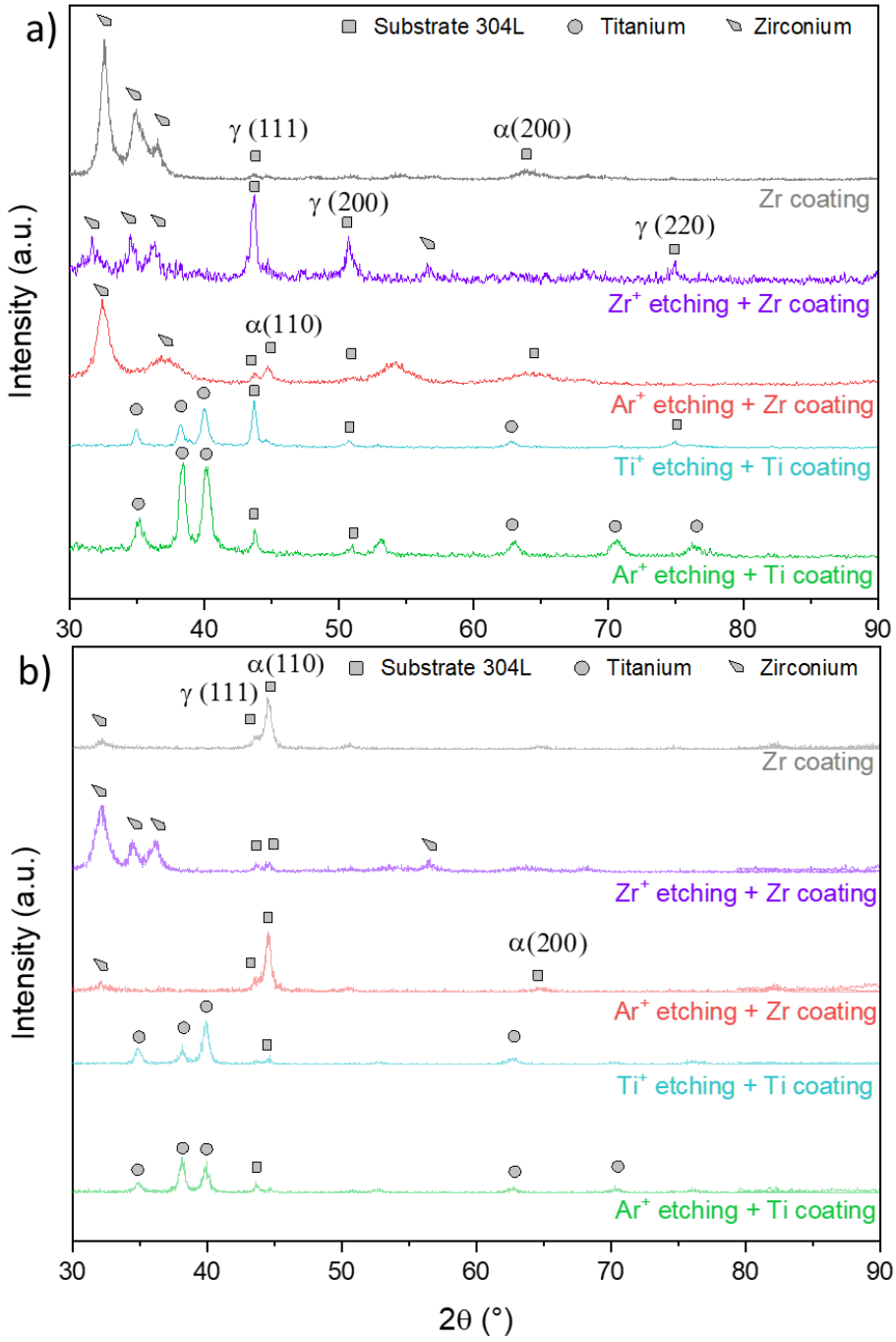

Figure 39: GAXRD patterns at 0.5° incident angle for the 304L steel and, the etched and metallic bond coat deposited samples a) before and b) after immersion in nitric acid (2.5 mol/L HNO_3, 2.5 mol/L $NaNO_3$ and 2 g/L $Fe(NO_3)_3$) solution at 110 °C.

The decrease in amplitude or even the disappearance of Zr contributions metallic XRD peak for the Ar^+-etched and Zr-coated samples and unetched and Zr-coated samples may be due to their poor adhesion, resulting in their delamination compared to the Zr^+-etched and Zr-coated sample. These results are in agreement with the electrochemical measurements showing a lower corrosion resistance for these samples (Figure 35) and the SEM analysis indicating a very low amount of Zr on the surface.

Focus is now placed on the Zr^+-etched and Zr-coated sample as it offers the best corrosion resistance properties according to electrochemical measurements. Figure 40 shows the XPS depth profiles of this sample before and after electrochemical measurements in nitric acid. These measurements indicate that a Zr-based oxide layer is present at the extreme surface of the Zr coating (bond coat) before immersion in a nitric acid solution (observed up to an erosion time of 60 s). Figure 40b shows that this oxide film is present over a longer erosion time after 2 d of immersion in nitric acid (until 220 s of erosion), indicating that its thickness has increased. However, since the erosion rate varies according to the nature of the layers (chemical composition), it is difficult to give an exact value of the thickness of each layer without prior calibration. Further analyzes are needed such as GDOES to estimate the oxide layers and bond coat thicknesses.

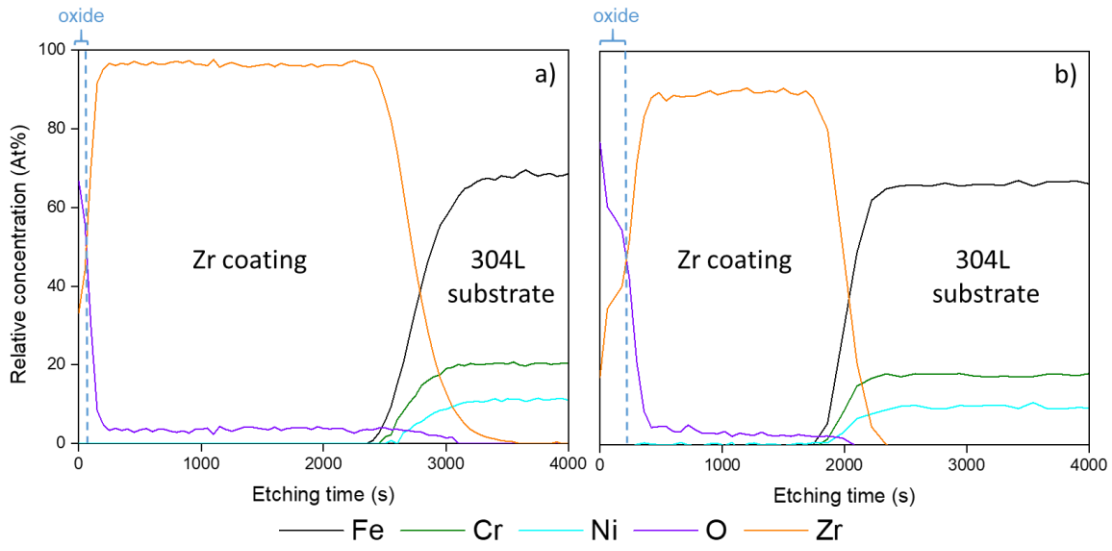

Figure 40: XPS depth profiles of (a) Zr^+-etched and Zr-coated sample before and (b) Zr^+-etched and Zr-coated sample after 2 d of immersion in nitric acid (2.5 mol/L HNO_3, 2.5 mol/L $NaNO_3$ and 2 g/L $Fe(NO_3)_3$) solution at 110 °C.

The oxide layer present before the electrochemical measurements probably formed when the samples were removed from the deposition chamber, and is due to the high affinity of Zr for O. This Zr-based oxide film formed in air is very stable as shown by the Ellingham diagrams [27]. This oxide film chemical composition is not modified during the nitric acid immersion unlike the initial layer observed on the etched samples (Figure 7). This is due to the high amount of Zr, which allows the Zr oxide layer to grow during the immersion in nitric acid (passivation). This has already been reported in a 6 mol/L HNO_3 solution at 100 °C, where the native film on the Zr surface in air, estimated at 6 nm, increases to 10-12 nm after several hundred hours in this environment [64].

This beneficial effect is still observed after deposition of the metallic bond coat, especially for the Zr^+-etched and Zr-coated sample. This could be due to the epitaxial growth of the bond coat due to metal species that act as preferential nucleation sites. As a result, a denser film could be formed, which improves the corrosion resistance

compared to the bond coat formed after Ar^+ etching. Moreover, the stronger bonds at the substrate/bond coat interface compared to Ar^+-etched one and the reduction of lattice mismatch that lead to the formation of a more adherent bond coat could prevent it from delamination.

4.1.2 In sodium chloride (NaCl) environment

4.1.2.1 Potentiodynamic polarization curves

Figure 41 compares the potentiodynamic polarization curves of the inital 304L steel and, the etched and bond coated samples in a 3.56 wt.% NaCl solution at ambient temperature after 6 h of immersion. Compared to nitric acid, only potentiodynamic polarization curves after 6 h of OCP are performed in 3.56 wt.% NaCl. Note that resistance to pitting corrosion was not studied in this work and therefore, pitting potentials were not determined. Table 9 shows that the E_{corr} value for the 304L steel reached 0.14 V/SHE after 6 h in NaCl. As a comparison, E_{corr} values of the etched and metallic bond coat deposited samples disperse over 0.4 V. Only E_{corr} of Ar^+-etched and Ti-coated and Ti^+-etched and Ti-coated samples are shifted toward positive values to reach 0.32 and 0.31 V/SHE, respectively. The observed dispersion of E_{corr} could be explained by the non stabilization of the potential after 6 h due to kinetic limitations. The effect of bond coat deposition is visible on the corrosion currents. After 6 h of immersion, J_{corr} decreases by an order of magnitude for all the metal ion-etched, bond coat- deposited and only metallic bond coat-deposited samples down to 10^{-10} A/cm², compared to 3×10^{-9} A/cm² for initial 304L. In contrast, J_{corr} for Ar^+-etched and Ti-coated and Ar^+-etched and Zr-coated substrates after 6 h in NaCl are similar to initial 304L, with values of 2×10^{-9} A/cm² and 1×10^{-9} A/cm², respectively (Table 9).

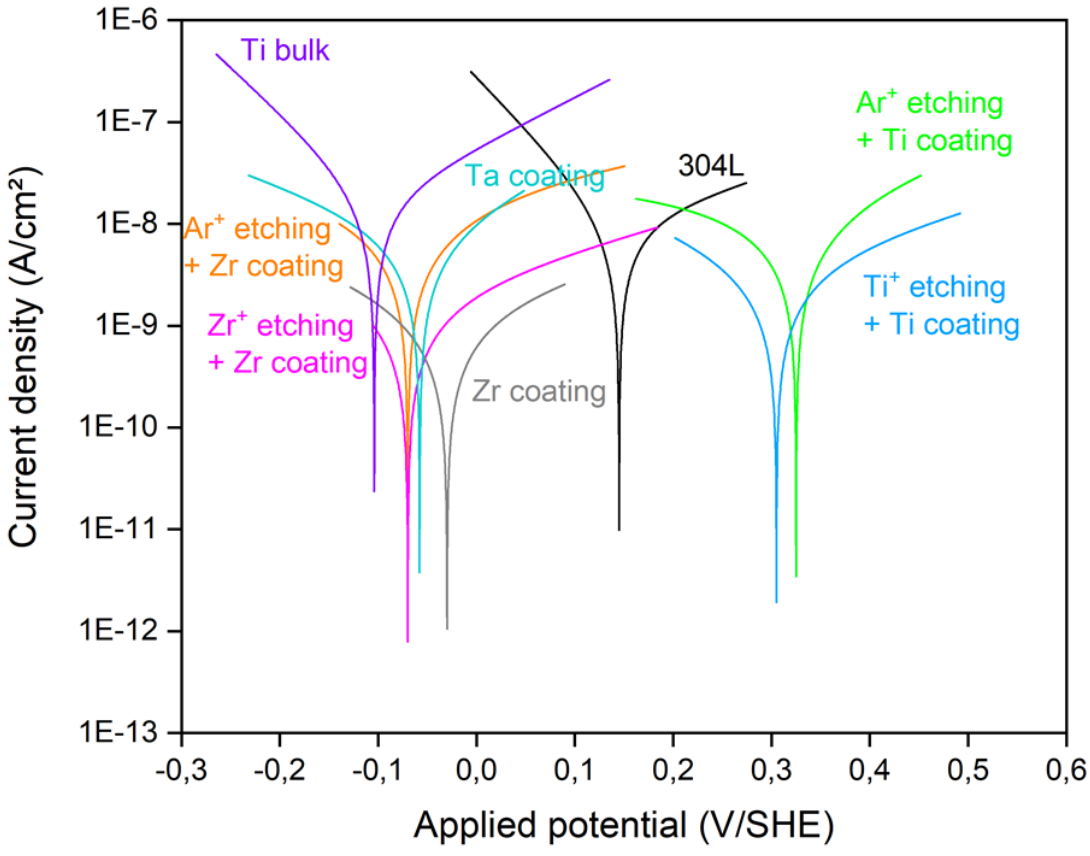

Figure 41: Potentiodynamic polarization curves of the initial and etched 304L steel samples and, the etched and metallic bond coat deposited samples in a 3.56 wt.% NaCl solution at ambient temperature after 6 h of immersion.

Table 9: Corrosion potential (E_{corr}) and current density (J_{corr}) values after 6 h of immersion in a 3.56 wt.% NaCl solution at ambient temperature.

	E_{corr} (V/SHE)	**J_{corr}** (A/cm²)
304L	0.14	3×10^{-9}
Ar^+ etching + Ti coating	0.32	2×10^{-9}
Ti^+ etching + Ti coating	0.31	6×10^{-10}
Ar^+ etching + Zr coating	-0.07	1×10^{-9}
Zr^+ etching + Zr coating	-0.07	3×10^{-10}
Zr coating	-0.03	2×10^{-10}

The positive effect of the metal ion etching is still visible after deposition of the metallic bond coat, indicating that the interface constitution first depends on the etching type (Ar^+ or Ti^+/Zr^+). In fact, it can be assumed that the implanted metal species can act as preferential nucleation sites for the bond coat growth and promote an epitaxial film, at least on the first layers. As a result, a denser film could be formed. However, direct coating of the 304L steel without etching (unetched and Zr-coated sample) also seems to offer a corrosion protection in this environment. Consequently, Ar^+ etching shows a limited effect on the substrate/metallic bond coat system. This can be due to the incorporation of Ar as interstitials in the crystal lattice, which cannot act as preferential nucleation site and therefore, cannot modify the coating growth mechanism. Moreover, it induces an increase in stress in the lattice [6] and may degrade the adhesion of the coating on the substrate.

4.1.2.2 Characterization of the electrochemically investigated surface

Figure 42 shows SE micrographs of the surfaces of the 304L steel and, etched and metallic bond coat-deposited, after electrochemical measurements in a 3.56 wt.% NaCl solution. The surface shows some scratches from the mechanical polishing performed beforehand. No obvious degradation is observed after immersion in NaCl solution. This is due to the good resistance to uniform corrosion of the 304L steel in this environment due to the formation of a stable passive layer [61-63]. The expected corrosion process in NaCl medium is pitting corrosion. Indeed, some pits are observed on the sample surfaces (Figure 42d). This may be due to the pitting potential of the samples being exceeded. However, as the pitting potential has not been determined beforehand, this assumption cannot be verified. Note that no cross-section analysis of these samples was performed due to time constraints.

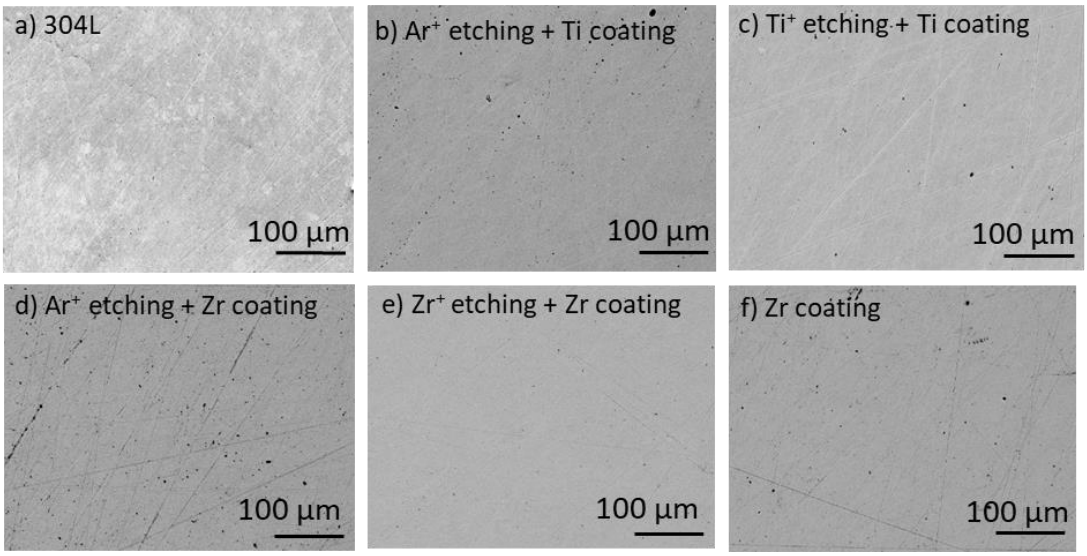

Figure 42: SEM-SE micrographs of the 304L and, etched and metallic bond coat deposited samples after electrochemical measurements in a 3.56 wt.% NaCl solution at ambient temperature.

GAXRD patterns at 0.5° incident angle performed for the initial or etched and metallic bond coat deposited 304L before and after electrochemical measurements in 3.56 wt.% NaCl solution at ambient temperature are shown in Figure 43. In the Ti (Zr)-coated sample diagram, contributions from the 304L steel substrate and metallic Ti (Zr) are detected before (Figure 43a) and after (Figure 43b) immersion in 3.56 wt.% NaCl solution. However, some differences are observed between the patterns before and after the electrochemical measurements. For instance, the Zr contribution at 36.6°2θ almost disappears for the Ar^+-etched and Zr-coated sample after immersion. Similarly, the Ti contribution at 76.2°2θ disappears after immersion for the Ar^+-etched and Ti-coated sample. Other differences in 304L substrate contributions are observed, such as the disappearance of the γ(220) phase at 74.8°2θ and the appearance of the α(110) peak at 44.6°2θ for the metal ion-etched and coated samples (Zr^+-etched and Zr-coated and Ti^+-etched and Ti-coated samples). The α(110) peak is also noticed for the Ar^+-etched and Ti-coated sample after immersion in 3.56 wt.% NaCl solution.

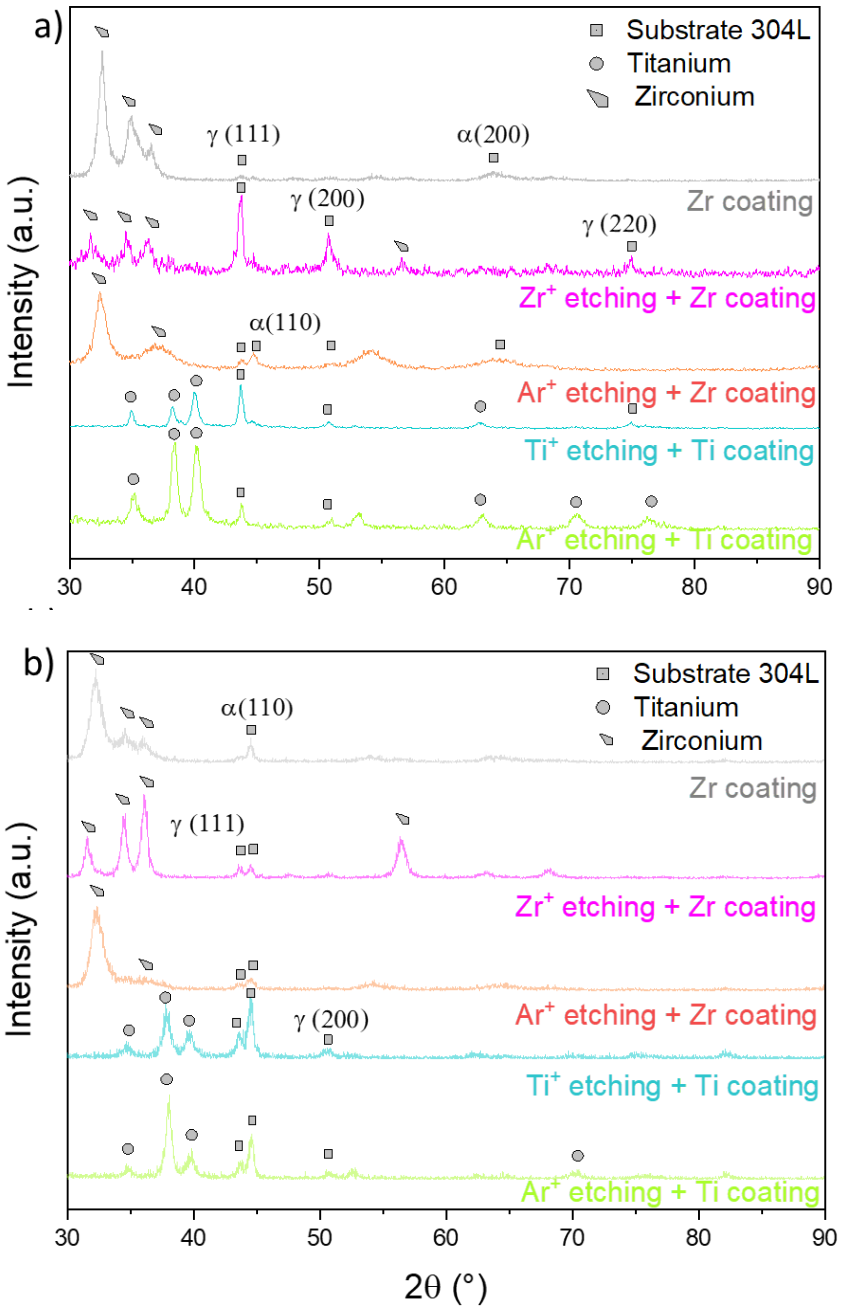

Figure 43: GAXRD patterns at 0.5° incident angle for the 304L steel and, the etched and metallic bond coat deposited samples a) before and b) after immersion in a 3.56 wt.% NaCl solution at ambient temperature.

The decrease in amplitude, or even the disappearance of Zr and Ti contributions metallic XRD peak for the Ar^+-etched and metallic bond coat-deposited samples may be due to the onset of coating dissolution, or at least its degradation. These results are in agreement with electrochemical measurements showing a lower corrosion resistance for these samples (Figure 41). On the other hand, the modifications observed for the contributions of the 304L steel *i.e.,* the decrease of austenite amount and the increase of the ferrite one can be explained by a selective corrosion of austenite, likely because of pitting and subsequent preferential dissolution [75].

After the deposition of a metallic bond coat, the metal ion etching beneficial effect is observed for both types of metal ion in NaCl environment unlike nitric acid (only Zr^+-etched and Zr-coated sample improves significantly corrosion resistance). These differences could be explained by the aggressiveness of nitric acid compared to NaCl, where Zr is more resistant than Ti due to the formation of a dense and insulating oxide layer (ZrO_2) on its surface [76].

4.2 IMMERSION TESTS

To complement the first elements given by electrochemical measurements, more representative immersion tests are performed in order to study the corrosion behavior on longer duration of the etched and bond coat deposited smaples in a 3.56 wt.% NaCl solution at ambient temperature. Note that the initial surface of all the immersed samples were not polished to be close to the real use conditions. Immersion tests duration is 60 d for NaCl. From these tests, the weight and thickness losses are calculated and the corrosion rate can be estimated. No immersion tests were performed on etched samples with a bond coat due to lack of time. However, it should be done in order to evaluate the long-term behavior of the bond coat and to study whether the effect of etching type is visible after bond coat deposition as appears to be the case in electrochemical measurements. Moreover, immersion tests in natural seawater are performed on CORRODYS platform during 56 d to study the corrosion resistance of samples under service conditions. The corrosion free potential is measured continuously and visual inspection was performed before and after the 8-week test. Microstructural observations are performed as well. Note however that immersion tests were performed in Singapore seawater (NTU side) only on the contaminated samples (see Appendix 2).

4.2.1 In NaCl solution

Figure 44 shows the weight and thickness losses of initial 304L and, etched and metallic bond coat-deposited samples immersed in a 3.56 wt.% NaCl solution at ambient temperature. The surface exposed to NaCl solution during these immersion tests is 53 cm^2. Assuming a homogeneous dissolution of the material, the thickness loss can be estimated using Equation 1. Then, the corrosion rate can be calculated from the thickness loss calculation using Equation 2. Knowing the thickness of the bond coats, their weight can be calculated and compared to the total weight loss. The results of these calculations show that the only dissolution of the bond coat can be considered and therefore, the densities of Ti and Zr can be used for our thickness loss calculations. The densities used are those of 304L (7.93 g/cm^3), Ti (4.51 g/cm^3) and Zr (6.52 g/cm^3), depending on the sample considered. The weight (Figure 44a) and thickness (Figure 44b) losses increase with the immersion time (again except for the point at 30 days). These immersion tests were performed at the same time and in the same building as the immersion tests on etched samples, which explains the same trend (decrease/stagnation) for the values at 30 d of immersion.

The weight loss after 60 d of immersion is lower for the Zr^+-etched and Zr-coated (6.45 ± 0.07 mg/dm^2), unetched and Zr-coated (6.34 ± 0.03 mg/dm^2) and, Ar^+-etched and Ti-coated samples (7.42 ± 0.04 mg/dm^2) compared to 304L steel (7.61 ± 0.13 mg/dm^2). The thickness loss does not follow the same trend as the weight loss due to the

different material densities. The results show that the thickness loss is similar for initial 304L steel, Zr^{+}-etched and Zr-coated and, unetched and Zr-coated samples. The calculated corrosion rate equals 0.58 µm/year for initial 304L steel, 0.59 µm/year for not etched and Zr-coated and, 0.60 µm/year for Zr^{+}-etched and Zr-coated sample, indicating similar behavior of these three samples in NaCl after 60 d of immersion. As it was already said before, attention must be paid to the roughness of the samples, if they have a high roughness, the real surface exposed to the electrolyte during corrosion tests will be much larger than the expected surface. Therefore, the weight losses related to the surface may be overestimated. Note that these values are lower than the values observed for a 304L ASS in 3.5% NaCl at room temperature after 360 h of immersion (1.271 mpy *i.e.* 32.3 µm/y) [77]. This can be due to the higher concentration of corrosion products in [77] due to a lower amount of NaCl used (200 mL) compared to our case (2L).

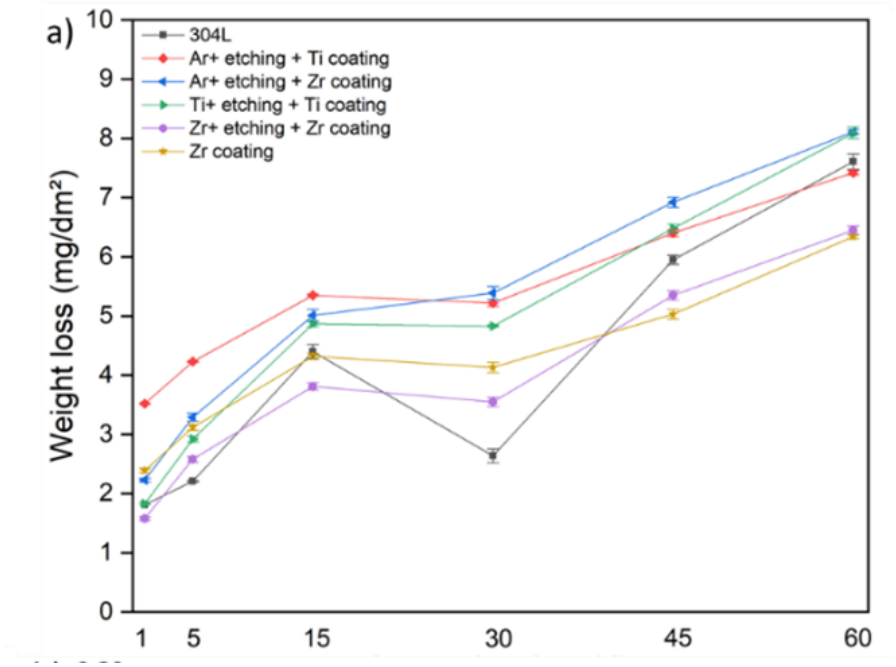

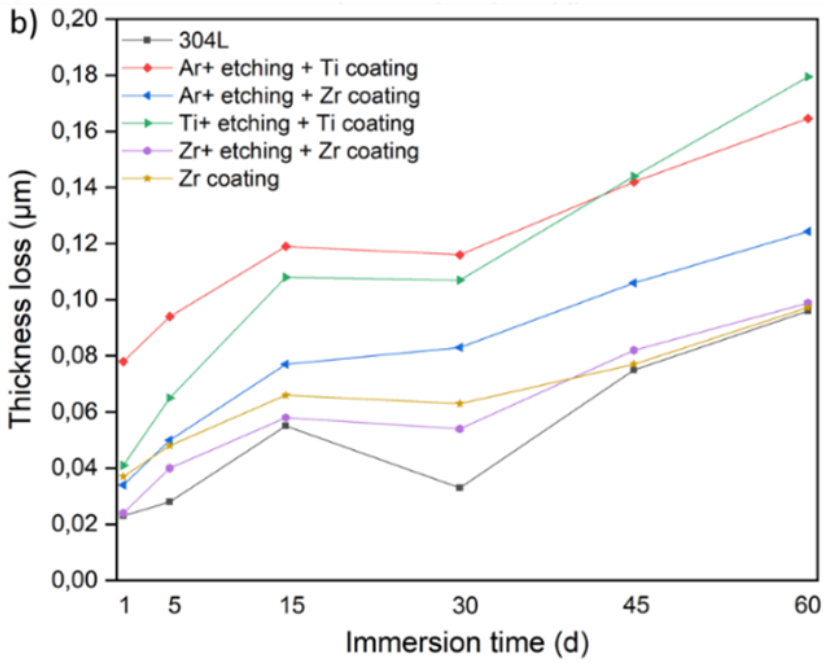

Figure 44: a) Weight loss measurements and b) thickness loss estimation after 60 d of immersion in a 3.56 wt.% NaCl solution at ambient temperature.

SE micrographs of initial 304L steel and etched and metallic bond coat deposited samples surface after 60 d of immersion in 3.56 wt.% NaCl solution are shown in Figure 45. The grain boundaries are clearly visible on all micrographs as the initial surface were not polished to mimic service conditions. In addition, pitting, which appears to be shallow, is observed on the substrate surfaces. This indicates the presence of pitting corrosion after 60 d of immersion in 3.56 wt.% NaCl environment, as reported on [64]. These results are similar to those obtained for the etched samples only in Figure 30.

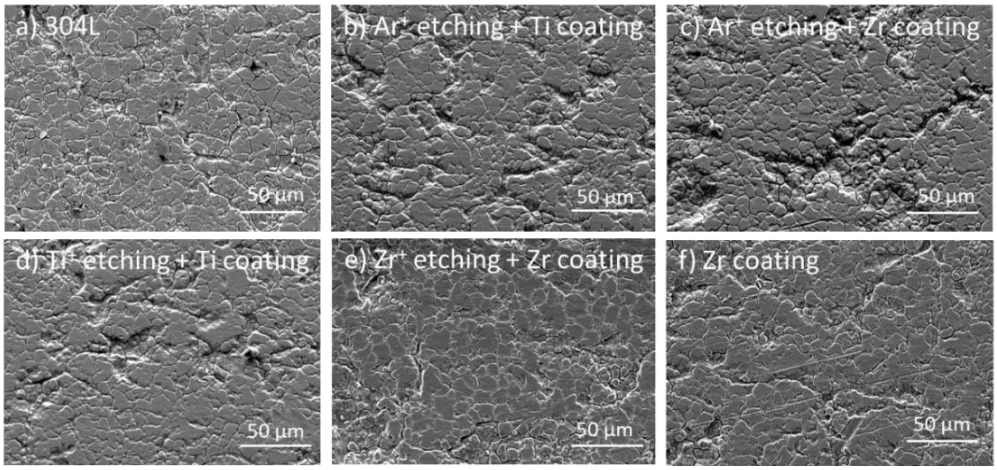

Figure 45: SEM-BE surface observation of a) 304L steel, b) Ar^+-etched + Ti-coated, c) Ar^+-etched + Zr-coated, d) Ti^+-etched + Ti-coated, e) Zr^+-etched + Zr-coated and f) Zr-coated samples after 60 d of immersion in a 3.56 wt.% NaCl solution at ambient temperature.

4.2.2 In Cherbourg natural seawater

Immersion tests were performed in Singapore seawater only on the contaminated samples (see Appendix 2). Consequently, this section focuses on immersion tests performed on CORRODYS platform in natural seawater from the Port des Flamands in Cherbourg-en-Cotentin during 56 d (from April to June 2021) to study the corrosion resistance of samples under service conditions. A protective paint was applied after cleaning the substrate surface with ethanol to isolate the 304L substrate in order to study only the coatings or implanted surfaces. The corrosion free potential was measured continuously and visual inspection was performed before and after the 8-week test.

The immersion tests in natural seawater were performed only on the metal ion-etched and metallic bond coat deposited samples as the number of samples were limited to perform these immersion tests on CORRODYS platform. Figure 46 shows the evolution of the corrosion potential as a function of immersion time for initial 304L, and for metal ion-etched and metallic bond coat deposited samples. A similar trend to that of 304L steel is observed for these two samples. An increase in corrosion potential is visible (up to 0.273 V/ECS for Ti^+-etched and Ti-coated and 0.168 V/ECS for Zr^+-etched and Zr-coated samples) followed by a decrease tending towards a stabilization around -0.170 V/ECS for Ti^+-etched and Ti-coated and -0.099 V/ECS for Zr^+-etched and Zr-coated samples. These results are comparable with those obtained for the etched samples (Figure 32): an increase in potential (up to 0.169 V/ECS for Zr^+-etched and 0.288 V/ECS for Ti^+-etched samples), then a decrease (down to -0.155 V/ECS for Zr^+-etched and -0.144 V/ECS for Ti^+-etched samples) and finally a stabilization around -0.120 V/ECS. As mentioned for the etched samples, oscillations with a period of 24 h are observed and attributed to circadian cycles [66]. On the other hand, the increase in the corrosion potential indicates the formation and development of a biofilm, and the sudden decrease suggests a change in the surface such as biofilm degradation.

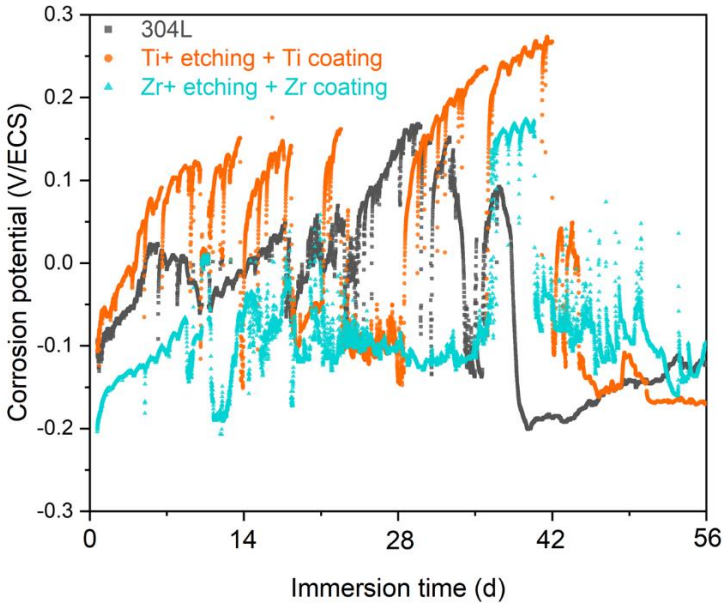

Figure 46: Monitoring of the corrosion potential vs. immersion time in natural seawater in Cherbourg.

The total microalgae biomass and total aerobic heterotrophic flora counted after 56 d of immersion in Cherbourg natural seawater are depicted in Figure 47. The total microalgae biomass (Figure 47a) is lower for the Ti^+-etched and Ti-coated substrate (5.2×10^4 micro-organisms/cm²) compared to Zr^+-etched and Zr-coated sample (1.0×10^5 micro-organisms/cm²) and initial 304L (1.1×10^5 micro-organisms/cm²). The results obtained for the Zr^+-etched and Zr-coated sample as comparable to the Ti^+-etched sample (1.3×10^5 microorganisms/cm²). On the other hand, the Zr^+-etched sample shows the lowest total microalgae biomass value (6.5×10^3 microorganisms/cm²). On the other hand, the total aerobic heterotrophic flora (Figure 47b) is lower for Zr^+-etched and Zr-coated substrate (3.5×10^4 UFC/cm²) compared to initial 304L (5.7×10^4 UFC/cm²) and Ti^+-etched and Ti-coated sample (9.3×10^4 UFC/cm²). The Ti^+-etched sample shows the lowest total aerobic heterotrophic flora (1.8×10^4 [2]UFC/cm²), whereas the value of the Zr^+-etched sample (6.0×10^4 UFC/cm²) is comparable to that of 304L. The Ti^+-etched and Ti-coated substrate tends to reduce the amount of microalgae on the biofilm while the Zr^+-etched and Zr-coated sample affects the amount of bacteria. These results differ from the etched samples where Zr^+ etching tends to reduce the amount of microalgae on the biofilm, and Ti^+ etching affects the amount of bacteria. Further analysis is required to conclude on these observations.

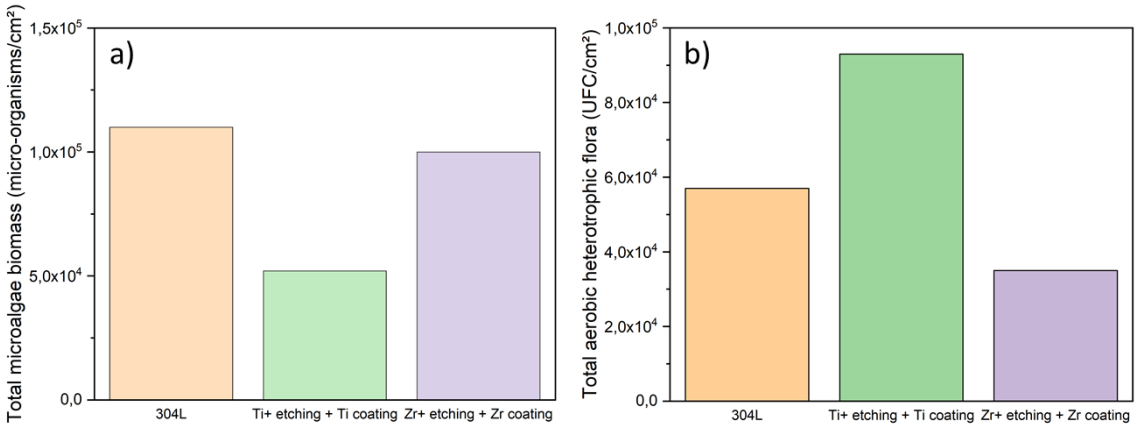

Figure 47: Results of microbiological analyses indicating the a) total microalgae biomass and b) total aerobic heterotrophic flora after 56 d of immersion in Cherbourg seawater.

Figure 48 shows BSE images of two areas of the surfaces of metal ion-etched and metallic bond coat-deposited samples immersed during 56 d in Cherbourg natural seawater. There are no differences observed between these two areas for the Ti^+-etched and Ti-coated sample while for the Zr^+-etched and Zr-coated sample, biofilm residues are visible in area 2 (diatoms).

[2]UFC: Unités formant colonies (French) or colony forming units (English)

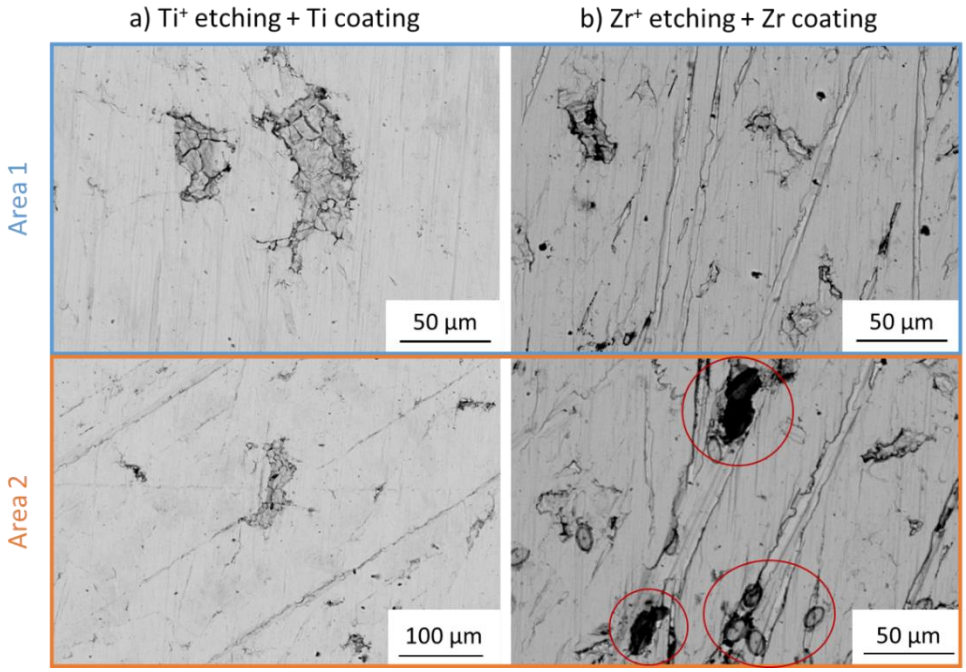

Figure 48: SEM-BSE micrographs on two different areas of the surface of a) Ti+-etched + Ti-coated and b) Zr+-etched and Zr-coated samples after 56 d of immersion in Cherbourg natural seawater.

The biofilm present at the surface of the coated samples is mostly made of diatoms (*cocconeis placentula*) as for the 304L steel. EDX spectra and maps acquired in two areas on the Zr^+-etched and Zr-coated substrate surface after 56 d of immersion in Cherbourg natural seawater are shown in Figure 49. Spectrum 1 is recorded on the Zr-coated surface and spectrum 2 on a diatom. Major differences are observed according to the quantification of these two spectra, especially the presence of a higher amount of silicon and oxygen for area 2. This is confirmed by the EDX mapping, which shows that these elements are mainly present on the diatoms. This higher amount of silicon detected for diatoms is explained by their skeleton, which is mainly composed of silicon [66, 69].

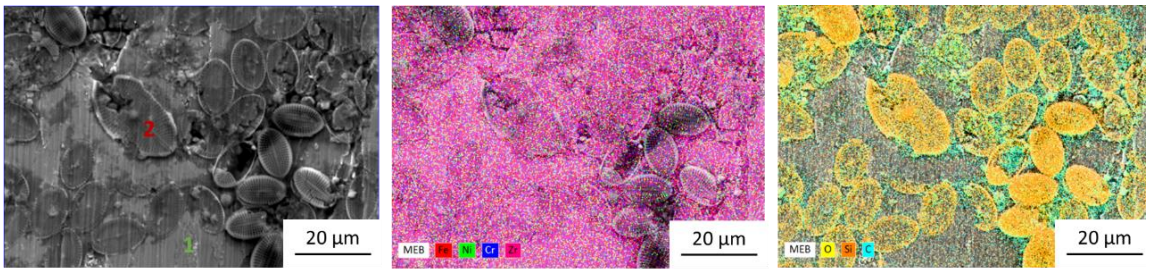

Area	Fe (at.%)	Cr (at.%)	Ni (at.%)	Zr (at.%)	O (at.%)	Si (at.%)	C (at.%)
1	45	13	6	19	5	1	11
2	18	6	2	10	43	7	14

Figure 49: SEM-SE EDX analysis at an area of the Zr^+-etched + Zr-coated sample showing biofilm residue after 56 d of immersion in Cherbourg seawater.

In conclusion, the etched and metallic bond coat-deposited samples show evolution in corrosion potential similar to that of initial 304L steel in Cherbourg natural seawater. However, different behaviors can be observed in microbiological analyses, indicating that the surface pre-treatment influences the biofilm population by reducing microalgae and/or bacteria. No study dealing with this phenomenon has been found in the literature so far. Note that in all cases, diatoms are present in the biofilm that forms on the surface of the samples.

4.3 CONCLUSIONS

Electrochemical measurements are performed in nitric acid (2.5 mol/L HNO_3, 2.5 mol/L $NaNO_3$, 2 g/L $Fe(NO_3)_3$) solution at 110 °C and in 3.56 wt.% NaCl solution at ambient temperature in order to estimate the corrosion resistance of the 304L ASS modified by etching and the addition of a metallic bond coat.

In nitric acid solution, the beneficial effect of metal ion etching is still observed after deposition of the metallic bond coat, indicating that the combination of etching and bond coat deposition is a good method to improve the corrosion resistance of 304L ASS, especially for the Zr^+-etched and Zr-coated sample. In fact, the metal species incorporated in the 304L ASS substrate could act as nucleation sites, which promote an epitaxial growth of the bond coat leading to a denser layer. As a result, a higher adhesion is reached, limiting delamination of the coating. Specific characterizations should be performed to characterize finely the nature of the bond coat depending on the etching species such as TEM and APT analyses. In addition, for the Zr-based sample, the formation of a stable and resistant ZrO_2 layer at its surface further increases its corrosion resistance. This effect is more limited for the Ti-based coating system, probably due to the limited formation of strong bonds in the case of Ti^+ etching. Moreover, the positive effect of metal ion etching after the deposition of a metallic bond coat on the electrochemical behaviour of the 304L ASS is also observed in NaCl solution. However, this effect is noticed for both types of metal ion etchings unlike nitric acid. This can be related to the aggressiveness of nitric acid compared to NaCl, where Zr is more resistant than Ti due to the formation of a dense and insulating ZrO_2 layer on its surface. Longer immersion tests are necessary to confirm these tendencies for longer durations and observe the corrosion behaviors of the etched samples as well as of the samples with etching and bond coats.

Immersion tests are performed to study the corrosion behavior on longer duration of the 304L ASS modified by etching and the addition of metallic bond coat. These tests are performed in 3.56 wt.% NaCl solution at room temperature and in Cherbourg natural seawater at ambient temperature.

Immersion tests performed in NaCl show that only Ti^+ etching improves the corrosion resistance of 304L ASS and not both types of metal ion etching. After the deposition of metallic bond coat, the lower corrosion rate is observed for 304L ASS, Zr^+-etched and Zr-coated and unetched and Zr-coated samples. No major differences are obtained between these different samples regarding their corrosion rate. Moreover, the presence of pitting corrosion is noticed after 60 d of immersion in NaCl solution, which could be studied in more detail. Moreover, immersion tests performed under service conditions (natural seawater) show a similar behaviour of etched and metallic

bond coat-deposited samples and 304L ASS. This suggests that these samples do not have a pronounced beneficial effect on the corrosion resistance of 304L. Nonetheless, they seem to influence the biofilm population by decreasing bacteria and/or microalgae.

CONCLUSIONS

This chapter presents the HiPIMS etching pre-treatment method and its effect on a substrate/metallic bond coat system.

First, the influence of three types of ion etching (Ar^+, Ti^+ and Zr^+) on the properties of the 304L ASS substrate was investigated. The XRD results indicate an alteration of the crystalline structure at the substrate surface due to the incorporation of elements on the first nanometers. These etchings reduce the ferrite content and amorphize the 304L surface. This amorphisation is stronger for the Ti^+- and Zr^+-etched samples because of the simultaneous bombardment from metal and Ar^+ ions. In fact, the metal ions (at 0.9 keV) can be incorporated into the solid by substituting lattice atoms (replacements), *i.e.* Ti could replace Cr while Zr could replace Fe in the FCC structure of 304L ASS. On the other hand, Ar, being an inert gas, can be incorporated in interstitial sites. Moreover, the amount of these incorporated species estimated by XPS analysis differs slightly from one etching to another: Ti (7 at.%) and Ar (5 at.%) after Ti^+ etching, Zr (6 at.%) and Ar (6 at.%) after Zr^+ etching and Ar (4 at.%) and Zr (7 at.%) after Ar^+ etching. Unexpected Zr contribution was also observed after Ar^+ etching due to resputtering effects of the vacuum chamber walls and substrate-holder triggered by the high energetic bombardment of their surface. These changes in atomic compositions at the substrate surface lead to a modification of the composition of the native layer formed on the surface of the 304L substrate during its exposure to air, promoting the formation of TiO_2 and ZrO_2, which are much more stable than Cr_2O_3 and Fe_2O_3. The substrate surface etched by the metal ions indicates that the oxide layers formed could be estimated at about the implanted thickness, *i.e.* 3.5 nm for Zr and 4 nm for Ti calculated according to SRIM calculation for ions at 0.9 keV. Further analyzes are required such as GDOES to estimate the oxide layers thicknesses.

Then, the influence of etching on the substrate/bond coat interface was studied thanks to the deposition of Ti and Zr metallic bond coats of about 200 nm-thick (± 31 nm) on the etched substrates. The deposited metallic bond coats show a columnar structure and are fully crystallized, probably due to the high energetic bombardment of the surface with ionized inert gas and metal plasma species present in the HiPIMS discharge. Moreover, different crystalline orientations are observed depending on the type of etching performed, which tends to indicate an effect of etching on the growth mechanism and structure of the bond coat. Although further analysis is required to understand how the etching type can exactly influence on the bond coat microstructure, a mechanism for the formation of the substrate/bond coat interface is proposed, suggesting that metal species can act as nucleation site for the growth of the bond coat and promote an epitaxial film, at least on the first layers. This could indicate the formation of a pseudodiffusion-type interface that is characterized by a gradient of composition between the substrate and the deposited bond coat. Moreover, this leads to a decrease of lattice mismatch and results in the formation of strong bonds. On the contrary, since Ar incorporates into the interstitial sites, it cannot form bonds at the substrate/bond coat interface. The substrate/bond coat interface formed after metal ion etching is 2-5 nm thick, clean, defect-free and free of contamination. In addition, no secondary or amorphous phase seems to have formed at this interface, suggesting a good adhesion between the bond coat and the

substrate. However, questions remain about the possible presence of a mixing zone for both metal ion-etched and metal-coated samples after XPS, TEM and APT analyzes. This mixing zone could be related to a mixing of the elements due to the implantation of metallic ions during the etching step but it could also be attributed to analyses artifacts. Therefore, it is not possible for us to know if it is a clearly defined interface or a mixing zone from these analyses. Consequently, further investigations are required. For this purpose, a bond coat of another material that does not interact with our implanted elements could be deposited to perform the observations. In addition, the substrate/bond coat interface show better adhesion properties after etching, which is associated with the formation of a defect-free interface. The best adhesion is observed after HiPIMS metal ion etching due to the formation of stronger bonds at the interface, resulting from the substitution of lattice atoms by metal ions in the substrate structure. In comparison, diode (Ar) etching leads to poor adhesion of bond coats either because of contamination induced by the re-sputtering effect of substrate-holder and chamber walls or because of the incorporation of Ar as interstitials in the crystal lattice, which increases the stresses and weakens the interface. The more detailed investigation of the failure modes shows different results depending on the etching type studied. The comparison between Zr^+ and Ar^+ etchings shows that cracks are observed for Ar^+ etching, probably due to high intrinsic stresses and a mismatch of bonding types in the substrate/bond coat interface whereas no cracks are noticed for Zr^+ etching as it reduces the stress concentration and can result in an implantation zone at the interface. This reinforces the assumption of a mixing zone at the substrate/coating interface. On the other hand, no significant impact is observed on the modification of failure modes of the Ti bond coat after Ti^+ etching. This can be due the formation of a weak implantation zone preventing the formation of strong bonds probably due to high fluxes of doubly-ionized metal species in the Ti HiPIMS discharge that causes severe resputtering.

Corrosion investigations in nitric acid (2.5 mol/L HNO_3, 2.5 mol/L $NaNO_3$, 2 g/L $Fe(NO_3)_3$) solution at 110 °C and 3.56 wt.% NaCl solution at ambient temperature were performed on etched samples. Electrochemical measurements show a beneficial effect of metal ion etchings on corrosion resistance of the 304L ASS by shifting the E_{corr} to positive values (1.07 ± 0.01 V/SHE compared to 0.96 ± 0.01 V/SHE for 304L) and decreasing J_{corr} values (down to 9×10^{-5} mA/cm^2 for Zr^+ etching compared to 6×10^{-4} mA/cm^2 for 304L) after 2 d of immersion. This leads to a corrosion rate of 6 µm/year for initial 304L and Ar^+-etched sample and around 1 µm/year for the Ti^+- and Zr^+-etched substrate. Note that the corrosion rate values calculated from the electrochemical tests are qualitative and limited to a uniform corrosion process as long as the stationary state is reached. It is also necessary that Tafel extrapolation begin at least 50-100 mV away from E_{corr} and that the anodic or cathodic regions are observed over at least a decade of current. This enhancement of the corrosion current density is attributed to the modified crystalline structure by the substitution of 304L atoms by metal species (Zr, Ti), leading to the formation of a more protective passive layer containing TiO_2 and ZrO_2. Moreover, the positive effect of metal ion etching on the electrochemical behaviour of the 304L ASS is also observed in NaCl solution. After 6 h of immersion, J_{corr} for the Ti^+- and Zr^+-etched samples decreases by an order of magnitude down to 4×10^{-10} A/cm², compared to 3×10^{-9} A/cm² for 304L steel. As in nitric acid, metal ion etching can lead to the modification of the passive layer formed

in NaCl by promoting TiO_2 and ZrO_2 formation that are more stable than Cr_2O_3 and Fe_2O_3. However, some pits are observed on the etched sample surfaces. This may be due to the pitting potential of the samples being exceeded. However, as the pitting potential has not been determined beforehand, this assumption cannot be verified.

After the deposition of metallic bond coat, the beneficial effect of metal ion etching is still observed compared to initial 304L. After 6 h of immersion, J_{corr} decreases by an order of magnitude for all the etched and metallic bond coat deposited samples down to 10^{-4} mA/cm² and even by almost two orders of magnitude for the Zr^+-etched and Zr-coated samples (10^{-5} mA/cm²), compared to 1×10^{-3} mA/cm² for initial 304L steel. This could be due to the epitaxial growth of the bond coat due to metal species that act as preferential nucleation sites. As a result, a denser film could be formed, which improves the corrosion resistance compared to the bond coat formed after Ar^+ etching that would be more porous. This effect is more pronounced for the Zr^+-etched and Zr-coated sample compared to Ti-based samples, which can be additionally related its higher adhesion that limits delamination of the coating. Finally, a denser film prevents also the electrolyte from reaching the 304L substrate and the formation of a stable and resistant ZrO_2 layer increases the resistance of the passive layer. The positive effect of metal ion etching after the bond coat deposition on the electrochemical behaviour of the 304L ASS is also observed in NaCl solution. After 6 h of immersion, J_{corr} decreases down to 6×10^{-10} mA/cm² for Ti^+-etched and Ti-coated sample and 3×10^{-10} mA/cm² for Zr^+-etched and Zr-coated sample compared to 3×10^{-9} mA/cm² for initial 304L steel. The explanation is the same as before *i.e.* the epitaxial growth of bond coat after metal ion etching. However, some pits are observed on the etched sample surfaces. In any case, immersion tests have to be performed to confirm this tendency and the corrosion mechanism of these modified materials for longer durations.

Immersion tests in nitric acid (2.5 mol/L HNO_3, 2.5 mol/L $NaNO_3$, 2 g/L $Fe(NO_3)_3$) solution at 110 °C for 9 days and in 3.56 wt.% NaCl solution at ambient temperature for 60 days were performed on etched samples. The results obtained in nitric acid show a uniform corrosion process and the same tendency that the electrochemical measurements presented previously with calculated corrosion rates indicating values of 42 ± 3 µm/year for initial 304L and 36 ± 2 µm/year for the Zr^+-etched substrate. The SEM analysis performed after the immersion tests confirms that the intergranular corrosion of the 304L ASS decreases after Zr^+ etching. This could be attributed to the better passivity of the material due to the presence of ZrO_2 layer on the sample surface. No immersion tests were performed on etched samples with a bond coat due to lack of time. However, it should be done in order to evaluate the long-term behavior of the bond coat and to study whether the effect of etching type is visible after bond coat deposition as appears to be the case in electrochemical measurements. In addition, longer immersion tests could be performed to show the effect of etching and, etching and bond coat deposition on the intergranular corrosion. The results of etched samples immersed in 3.56 wt.% NaCl indicate that only Ti^+ etching seems to have a positive effect on the decrease of corrosion rate, which differs from the electrochemical measurements in the NaCl solution. In addition, immersion tests in 3.56 wt.% NaCl solution at ambient temperature were performed on etched and bond coat deposited samples. They show that the lower corrosion rate is observed for 304L ASS, Zr^+-etched and Zr-coated and unetched and Zr-coated samples. No major

differences are obtained between these different samples regarding their corrosion rate. Moreover, the presence of pitting corrosion is noticed after 60 d of immersion in NaCl solution, which could be studied in more detail.

Finally, immersion tests were performed under service conditions i.e. in natural seawater. The results obtained in Cherbourg natural seawater do not allow us to conclude on the improvement of the corrosion resistance after only etching, or after etching and metallic bond coat deposition. However, they give us information on the fouling and type of biofilm formed on the surface of our samples. In fact, this biofilm is mainly composed of microalgae such as diatoms (*cocconeis placentula*) whose skeleton is made of silicon. The Ti-based system seems to decrease the amount of microalgae while Zr reduces the amount of bacteria. Further analysis is needed to confirm these observations.

The study of the substrate/metallic bond coat system allowed us to obtain information on the influence of the etching step on interface constitution, especially corrosion tests (electrochemistry and immersion). It is now possible to use the most relevant studied etching procedure in terms of corrosion resistance improvement for our coating system. In addition, the 200 nm-thick bond coat used for the substrate/metallic bond coat system studied in this chapter will be the interlayer in the final coating system.

This final system consisting of substrate/metal bond coat/oxide coating as well as its anticorrosion properties are presented in the next chapter. Nonetheless, it should be noted that no step of our system could be optimized as each of them requires a precise parametric study, which indicates that improvements of the substrate/coating system (microstructure, adhesion, *etc*.) are clearly possible.

REFERENCES

[1] Kazazi M., Haghighi M., Yarali D. & Zaynolabedini M.H. (2018) “Improving Corrosion Resistance of 316L Austenitic Stainless Steel Using ZrO_2 Sol-Gel Coating in Nitric Acid Solution.” Journal of Materials Engineering and Performance 27: 1093-1102.

[2] Reinhard C., Ehiasarian A. P. & Hovsepian P. Eh. (2007) “CrN/NbN superlattice structured coatings with enhanced corrosion resistance achieved by high power impulse magnetron sputtering interface pre-treatment.” Thin Solid Films 515: 3685-3692.

[3] Wang Q.-Y., Xi Y.-C., Liu X.-Y., Liu S., Bai S.-L. & Liu Z. D. (2017) “Microstructure and mechanical properties of interface between laser cladded Hastelloy coating and steel substrate.” Transactions of Nonferrous Metal Society of China 27: 733-740.

[4] Alami J., Bolz S. & Sarakinos K. (2009) “High power pulsed magnetron sputtering: Fundamentals and applications.” Journal of Alloys and Compounds 483: 530-534.

[5] Santiago J. A., Fernandez-Martinez I., Wennberg A., Molina-Aldareguia J. M., Castillo-Rodriguez M., Rojas T. C., Sanchez-Lopez J. C., Gonzalez M. U., Garcia-Martin J. M., Li H., Bellido-Gonzalez V., Monclus M. A. & Gonzalez-Arrabal R. (2018) “Adhesion enhancement of DLC hard coatings by HiPIMS metal ion etching.” Surface and Coatings Technology 349: 787-796.

[6] Ehiasarian A. P., Wen J. G. & Petrov I. (2007) “Interface microstructure engineering by high power impulse magnetron sputtering for the enhancement of adhesion.” Journal of Applied Physics 101: 054301.

[7] Bakoglidis K. D., Schmidt S., Greczynski G. & Hultman L. (2016) “Improved adhesion of carbon nitride coatings on steel substrates using metal HiPIMS pretreatments.” Surface and Coatings Technology 302: 454-462.

[8] Bull S. J. (1992) “Techniques for improving thin film adhesion.” Vacuum 43: 517-520.

[9] Vassallo E., Caniello R., Cremona A., Dellasega D. & Miorin E. (2013) “Titanium interlayer to improve the adhesion of multilayer amorphous boron carbide coating on silicon substrate.” Applied Surface Science 266: 170-175.

[10] Pischow K. A., Eriksson L., Harju E., Korhonen A. S. & Ristolainen E. O. (1993) “The influence of titanium interlayers on the adhesion of PVD TiN coatings on oxidized stainless steel substrates.” Surface and Coatings Technology 58: 163-172.

[11] Qiao J., Chan C., Chan D., Leung C. S. & Sahin T. “Method and apparatus for seasoning a substrate processing chamber.” EP 0 892 083 A1, 20.01.1999.

[12] Rossman K., Sahin T., M’Saas H. & Nowak R. “Reduction of mobile ion and metal contamination in HDP-CVD chambers using chamber seasoning film depositions.” US 6121161, 19.09.2000.

[13] Bohlmark J., Blomqvist H., Landälv L., Amerioun S. & Ahlgren M. (2011) “Evaluation of arc evaporated coatings on rounded surfaces and sharp edges.” Materials Science Forum 681: 145-150.

[14] Cheng Y. & Zheng Y. F. (2006) “A study of ZrN/Zr coatings deposited on NiTi alloy by PIIID technique.” IEEE Transactions on Plasma Science 34: 1105-1108.

[15] Huang J.-H., Ouyang F.-Y. & Yu G.-P. (2007) “Effect of film thickness and Ti interlayer on the structure and properties of nanocrystalline TiN thin films on AISI D2 steel.” Surface and Coatings Technology 201: 7043-7053.

[16] Cano E., Martinez L., Simancas J., Perez-Trujillo F. J., Gomez C. & Bastidas J. M. (2006) “Influence of N, Ar and Si ion implantation on the passive layer and corrosion behavior of AISI 304 and 430 stainless steels.” Surface and Coatings Technology 200: 5123-5131.

[17] Qiu Z., Wang F., Li Q., Zleng L., Zhang F. & Zhang H. (2020) “Corrosion and mechanical properties for Cr-coated CSS-42L bearing steel after Ti and C ions co-implantation.” Applied Surface Science 509, 145293.

[18] Martinez L., Gomez C. & Perez F. J. (2005) “Synergistic effect of ion implantation as a surface modification technique to improve localized corrosion of AISI 304 austenitic stainless steel.” Surface and Coatings Technology 195: 70-80.

[19] Dudognon J., Vayer M., Pineau A. & Erre R. (2008) “Mo and Ag ion implantation in austenitic, ferritic and duplex stainless steels: A comparative study.” Surface and Coatings Technology 203: 180-185.

[20] Chang G. S., Son J. H., Kim S. H., Chae K. H., Whang C. N., Menthe E., Rie K.-T. & Lee Y. P. (1999) “Electronic structures and nitride formation of ion-implanted AISI 304L austenitic stainless steel.” Surface and Coatings Technology 112: 291-294.

[21] Pelletier H., Mille P., Cornet A., Grob J. J., Stoquert J. P. & Muller D. (1999) “Effects of high energy nitrogen implantation on stainless steel microstructure.” Nuclear Instruments and Methods in Physics Research B 148: 824-829.

[22] Feng K., Wang Y., Li Z. & Chu P. K. (2015) “Characterization of carbon ion implantation induced graded microstructure and phase transformation in stainless steel.” Materials Characterization 106: 11-19.

[23] Gardin E., Zanna S., Seyeux A., Allion-Maurer A. & Marcus P. (2019) “XPS and ToF-SIMS characterization of the surface oxides on lean duplex stainless steel – Global and local approaches.” Corrosion Science 155: 121-133.

[24] Olsson A.-O. A. & Landolt D. (2003) “Passive films on stainless steels – chemistry, structure and growth.” Electrochimica Acta 48: 1093-1104.

[25] Maurice V., Yang W. P. & Marcus P. (1998) “X-ray photoelectron spectroscopy and scanning tunneling microscopy study of passive films formed on (100) Fe-18Cr-13Ni single-crystal surfaces.” Journal of The Electrochemical Society 145: 909-919.

[26] Ma L., Pascalidou E.-M., Wiame F., Zanna S., Maurice V. & Marcus P. (2020) “Passivation mechanisms and pre-oxidation effects on model surfaces of FeCrNi austenitic stainless steel.” Corrosion Science 167, 108483.

[27] Sahin E. O. (2016) “Development of rare earth-free negative electrode materials for NiMH batteries.” PhD thesis, Middle East Technical University, Turkey.

[28] Tcharkhtchi-Gillard E., Benoit M., Clavier P., Gwinner B., Miserque F. & Vivier V. (2016) “Kinetics of the oxidation of stainless steel in hot and concentrated nitric acid in the passive and transpassive domains.” Corrosion Science 107: 182-192.

[29] Vigen Karimi M., Sinha S. K., Kothari D. C., Khanna A. K. & Tyagi A. K. (2002) “Effect of ion implantation on corrosion resistance and high temperature oxidation resistance of Ti deposited 316 stainless steel.” Surface and Coatings Technology 158-159: 609-614.

[30] Vincent Crist B. (1992) “Argon implanted into Graphite, by XPS.” Surface Science Spectra 1: 376-380.

[31] Peng D. Q., Bai X. D., Pan F., Sun H. & Chen B. S. (2005) “Influence of titanium ion implantation on the corrosion behavior of zircalloy-4 in 1 M H_2SO_4.” Materials Chemistry and Physics 92: 443-447.

[32] Lee H., Lee S. M., Ada E. T., Kim B., Weiss M., Perry S. S. & Rabalais J.W. (1999) “Shallow implantation of Ti^+ ions in sapphire [α-Al_2O_3(0001)].” Nuclear Instruments and Methods in Physics Research B 157: 226-232.

[33] Liu C., Xin Y., Tian X., Zhao J. & Chu P. K. (2007) “Corrosion resistance of titanium ion implanted AZ91 magnesium alloy.” Journal of Vacuum Science & Technology A 25: 334-339.

[34] Arenas M. A., Garcia I. & de Damborenea J. (2004) “X-ray photoelectron spectroscopy study of the corrosion behaviour of galvanized steel implanted with rare earths.” Corrosion Science 46: 1033-1049.

[35] Maldonado F., Novillo C. & Stashans A. (2012) “Ab initio calculation of chromium oxide containing Ti dopant.” Chemical Physics 393: 148-152.

[36] Kaspar T. C., Sushko P. V., Bowden M. E., Heald S. M., Papadogiani A., Tschammer C., Bierwagen O. & Chambers S. A. (2016) “Defect compensation by Cr vacancies and oxygen intrstitials in Ti^{4+}-doped Cr_2O_3 epitaxial thin films.” Physical Review B 94, 155409.

[37] Wang D., Jin L., Li Y. & Hu H. (2017) “Partial oxidation of vacuum residue over Al and Zr-doped α-Fe_2O_3 catalysts.” Fuel 210: 803-810.

[38] Benjelloun D., Bonnet J. P., Doumerc J. P., Launay J. C. & Onillon M. (1988) “Anisotropy in the electrical properties of zirconium doped α-Fe_2O_3 single crystals.” Materials Chemistry and Physics 20: 1-12.

[39] Li J. & Beres W. (2007) “Scratch Test for Coating/Substrate Systems – A Literature Review.” Canadian Metallurgical Quarterly 46: 155-173.

[40] Lloyd G. E. (1987) “Atomic number and crystallographic contrast images with the SEM: a review of backscattered electron techniques.” Mineralogical Magazine 51: 3-19.

[41] Kowol T., Müller E., Fritsch-Decker S., Hettler S., Störmer H., Weiss C. & Gerthsen D. (2017) “Contrast of backscattered electron SEM images of nanoparticles on substrates with complex structure.” Hindawi 4907457.

[42] Avila P. R. T., da Silva E. P., Rodrigues A. M., Aristizabal K., Pineda F., Coelho R. S., Garcia J. L., Soldera F., Walczak M. & Pinto H. C. (2019) “On manufacturing multilayer-like nanostructures using misorientation gradients in PVD films.” Scientific Reports 9, 15898.

[43] Jain I.P. & Agarwal G. (2011) “Ion beam induced surface and interface engineering.” Surface Science Reports 66: 77-172. doi:10.1016/j.surfprep.2010.11.001

[44] Drabik M., Truchly M., Ballo V., Roch T., Kvetkova L. & Kus P. (2018) “Influence of substrate material and its plasma pretreatment on adhesion and properties of WC/a-C:H nanocomposite coatings deposited at low temperature.” Surface and Coatings Technology 333: 138-147.

[45] Drabik M., Ballo V., Truchly M., Frkan J., Roch T., Kvetkova L., Satrapinskyy L. & Kus P. (2016) “Influence of plasma pretreatment on the performance of industrial tungsten carbide coatings deposited at low temperature on 100Cr6 bearing steel substrates.” Surface and Coatings Technology 293: 2-9.

[46] Pinard Legry G. (1990) “Corrosion resistance of zirconium: general mechanisms, behaviour in nitric acid.” Communication aux Journées d’Etudes sur le zirconium, Lyon, 10-11/10.

[47] Padhy N., Kamachi Mudali U., Chawla V., Chandra R. & Raj B. (2011) “Corrosion behavior of single (Ti) and duplex (Ti-TiO_2) coating on 304L stainless steel in nitric acid medium.” Materials Chemistry and Physics 130: 962-972.

[48] Raj B. & Kamachi Mudali U. (2006) “Materials development and corrosion problems in nuclear fuel reprocessing plants.” Progress in Nuclear Energy 48: 283-313.

[49] Bhise S. & Kain V. (2012) “Methodology based on potential measurement for predicting corrosion behaviour of SS 304L in boiling nitric acid containing oxidizing ions.” Corrosion Engineering, Science and Technology 47: 61-69.

[50] Furuya T., Kawafuku J., Satoh H., Shimogori K., Aoshima A. & Takeda S. (1991) “A corrosion testing method for titanium in nitric acid environments.” ISIJ International 31: 189-193.

[51] Badet H. & Poineau F. (2020) “Corrosion studies of stainless steel 304L in nitric acid in the presence of uranyl nitrate: effect of temperature and nitric acid concentration.” SN Applied Sciences 2:459.

[52] Prasad Rao K., Uma Maheshwar Rao A. & Gururaja G. J. (1988) “Effect of delta ferrite content on the corrosion resistance of type 316 clad metals.” Werkstoffe und Korrosion 39: 135-142.

[53] Ornek C., Leygraf C. & Pan J. (2019) “Passive film characterization of duplex stainless steel using scanning Kelvin probe force microscopy in combination with electrochemical measurements.” npj Materials Degradation 3:8.

[54] Zhu S., Huang N., Shu H., Wu Y. & Xu L. (2009) “Corrosion resistance and blood compatibility of lanthanum ion implanted pure iron by MEVVA.” Applied Surface Science 256: 99-104.

[55] Wu H., Xi K., Xiao S., Qasim A. M., Fu R. K. Y., Shi K., Ding K., Chen G., Wu G. & Chu P. K. (2020) “Formation of self-layered hydrothermal coating on magnesium aided by titanium ion implantation: Synergistic control of corrosion resistance and cytocompatibility.” Surface and Coatings Technology 401: 126251.

[56] Jamesh M., Wu G., Zhao Y. & Chu P. K. (2013) “Effects of silicon plasma ion implantation on electrochemical corrosion behavior of biodegradable Mg-Y-RE Alloy.” Corrosion Science 69: 158-163.

[57] Jamesh M. I., Wu G., Zhao Y., McKenzie D. R., Bilek M. M. M. & Chu P. K. (2014) “Effects of zirconium and oxygen plasma ion implantation on the corrosion behavior of ZK60 Mg alloy in simulated body fluids.” Corrosion Science 82: 7-26.

[58] Robin R., Miserque F. & Spagnol V. (2008) “Correlation between composition of passive layer and corrosion behavior of high Si-containing austenitic stainless steels in nitric acid.” Journal of Nuclear Materials 375: 65-71.

[59] Sabot R., Devaux R., De Becdelievre A. M. & Duret-Thual C. (1992) “The resistance to localized corrosion in neutral chloride medium of an AISI 304L stainless steel implanted with nitrogen and neon ions.” Corrosion Science 33: 1121-1134.

[60] Shan C. X., Hou X. & Choy K.-L. (2008) “Corrosion resistance of TiO_2 films grown on stainless steel by atomic layer deposition.” Surface and Coatings Technology 202: 2399-2402.

[61] Saefuloh I., Kanani N., Gumetal Ramadhan F., Rukmayadi Y., Yusuf Y., Abdullah S. & Susilo S. (2020) “The study of corrosion behavior and hardness of AISI stainless steel 304 in concentration of chloride acid solution and temperature variations.” Journal of Physics: Conference Series 1477, 052058.

[62] Asaduzzaman MD., Mustafa C. M. & Islam M. (2011) “Effects of concentration of sodium chloride solution on the pitting corrosion behavior of AISI-304L austenitic stainless steel.” Chemical Industry & Chemical Engineering Quaterly 17: 477-483.

[63] Loto R. T. (2017) “Study of the corrosion resistance of type 304L and 316 austenitic stainless steels in acid chloride solution.” Oriental Journal of Chemistry 33: 1090-1096.

[64] Fauvet P. (2012) “Chapter 19: Corrosion issues in nuclear fuel reprocessing plants.” Nuclear corrosion science and engineering (pp. 679-728), Woodhead Publishing, ISBN: 978-1845697655.

[65] Emery A. (2020) “Corrosion intergranulaire des aciers inoxydables austénitiques en milieu acide nitrique oxydant.“ Université Paris sciences et lettres. NNT : 2020UPSLM031. Tel-03097345.

[66] Marconnet C., Dagbert C., Roy M. & Feron D. (2008) “Stainless steel ennoblement in freshwater: From exposure tests to mechanisms.” Corrosion Science 50: 2342-2352.

[67] Landoulsi J., Kirat K. El, Richard C., Feron D. & Pulvin S. (2008) “Enzymatic approach in microbial-influenced corrosion: A review based on stainless steels in natural waters.” Environmental Science & Technology 42: 2233-2242.

[68] Landoulsi J., Cooksey K. E. & Dupres V. (2011) “Review – Interactions between diatoms and stainless steel: focus on biofouling and biocorrosion.” Biofouling 27: 1105-1124.

[69] Richard C., Mitbavkar S. & Landoulsi J. (2017) “Diagnosis of the diatom community upon biofilm development on stainless steels in natural freshwater.” Scanning, 5052646.

[70] Meisterjahn P., Hoppe H. W. & Schultze J. W. (1987) “Electrochemical and XPS measurements on thin oxide-films on zirconium.” Journal of electroanalytical chemistry 217: 159-185.

[71] Agullo J., Bataillon C. & Michau N. (2017) “Preliminary electrochemical corrosion monitoring of iron in mixture cement paste-bentonite.” Corrosion Engineering, Science and Technology 52: 155-161.

[72] Alexander C. L., Tribollet B. & Orazem M. E. (2015) “Contribution of surface distributions to constant-phase-element (CPE) behavior: 1. Influence of roughness.” Electrochimica Acta 173: 416-424.

[73] Orazem M. E., Pébère N. & Tribollet B. (2006) “Enhanced graphical representation of electrochemical impedance data.” Journal of The Electrochemical Society 153: B129-B136.

[74] Zhang Z., Ter-Ovanessian B., Marcelin S. & Normand B. (2020) “Investigation of the passive behavior of a Ni-Cr binary alloy using successive electrochemical impedance measurements.” Electrochimica Acta 353: 136531.

[75] Ornek C., Davut K., Kocabas M., Bayath A. & Urgen M. (2021) “Understanding corrosion morphology of duplex stainless steel wire in chloride electrolyte.” Corrosion and Materials Degradation 2: 397-411.

[76] Gwinner B., Badji H., Benoit M., Brijou-Mokrani N., Fauvet P., Gruet N., Laghoutaris P., Miserque F., Robin R. & Tabarant M. (2015) ”Corrosion of zirconium in the context of the spent nuclear fuel reprocessing plant.” Proceedings of Global 2015 – 21st International Conference and Exhibition Nuclear Fuel Cycle for a Low-Carbon Future, Paris, France.

[77] Pourriahi M., Nasr-Esfahani M. & Motalebi A. (2014) “Effect of Henna and Rosemary Extracts on the corrosion of 304L stainless steel in 3.5% NaCl solution.” Surface Engineering and Applied Electrochemistry 50: 525-533.

Preliminary assessment of anticorrosion performance of an architectured substrate/coating system

INTRODUCTION

The previous chapter presented results on the characterization and analysis of ion etching pre-treatments and bond coat deposition and their corrosion performance evaluation in two corrosive environments: hot concentrated nitric acid for nuclear waste fuel reprocessing and marine environment. The 304L ASS substrates were etched using ionized vapour of Ar, Ti (Ar and Ti) and Zr (Ar and Zr) generated by HiPIMS. This ion etching pre-treatment resulted in the surface modification of the initial 304L by implantation of the sputtered species on the first nanometers. We can assume that Ar was incorporated in interstitial sites and metal (Ti and Zr) species were substituted to 304L lattice atoms (Cr and Fe). The incorporation of sputtered species modified the 304L substrate extreme surface by modifying the nature and proportion of native oxides. This led to increased corrosion resistance of the modified 304L in nitric acid and NaCl solutions according to electrochemical measurements, probably due to modification of the passive layer due to the presence of ZrO_2 and TiO_2. Then, a metallic bond coat (Zr or Ti) was deposited after the etching. We can assume that the metal species implanted during the etching process could act as preferential nucleation site for the growth of the bond coat, resulting in a decrease of the lattice mismatch, formation of strong bonds between the susbtrate and the bond coat. The growth process of the coating could be as well modified to lead to an epitaxial growth of the bond coat that result in a denser coating. This could lead to a higher density of the bond coat, higher adhesion strength between the substrate and the bond coat and, improved corrosion resistance from metal ion-etched samples. The best corrosion behavior was observed for the Zr^+-etched and Zr-coated sample.

From these encouraging results, an architectured coating system can be proposed to further increase the lifespan of 304L ASS in nitric acid and marine environments. As the bond coat is very thin (200 nm), increasing the duration of the corrosion tests would lead to its dissolution. That is why it is necessary to continue the studies on more “industrial” coating systems. Several studies show that a multilayer coating can offer a better corrosion resistance by limiting propagation from defects and preventing the electrolyte from reaching the substrate though these multiple interfaces [1-3]. Thus, the basis of the architectured system is the one studied in the previous chapter *i.e.* the 304L substrate is pre-treated by HiPIMS metal ion etching and the 200 nm-thick metal bond coat is deposited on the modified substrate. Unfortunately, no comparative test with Ar^+ etching were performed due to time limitation. Nonetheless, this would be interesting to perform this test to see if the tendency observed at the scale of the bond coat is still observed at larger scales. Then, an oxide (ceramic) coating is deposited on the bond coat. Various ceramics coatings are being investigated for anticorrosion properties, such as ZrO_2 [4, 5] and TiO_2 [6-8], as a result of the unique chemical, thermal and mechanical properties of these compounds [9]. For instance, a ZrO_2 coating deposited on 316L steel decreases the corrosion current density in 1 mol/L HNO_3 solution (9.8×10^{-1} µA/cm^2 compared to 4.1×10^{1} µA/cm^2 for uncoated 316L) [4]. A similar trend is observed after the deposition of a TiO_2 coating on 304L steel in 1 mol/L HNO_3 solution (5×10^{-1} µA/cm^2 compared to 10×10^{0} µA/cm^2 for initial 304L) [6]. In fact, ZrO_2 thin films are used as corrosion protective barriers for various metals [10-14] due to ZrO_2 chemical inertness [10-12, 14] and a thermal expansion coefficient close to that of metals [10, 11]. TiO_2 coatings are also applied

owing to reasonable electrochemical stability [15], high durability [15] and insulating properties [7]. Additionally, TiO_2 coatings are also under development for other applications, *i.e.* antifouling. These coatings can be deposited by a variety of techniques, including, recently, HiPIMS [16].

In this chapter, the focus is placed on the properties of a complete but non-optimized architectured system *i.e.* substrate/metallic bond coat/oxide coating. Note that the bond coat is synthesized with the metal of the oxide that is then deposited: Ti bond coat and TiO_2 coating for example. For this purpose, deposition of oxide and metal/oxide multilayer coatings were performed. In this study, four architectured systems were studied as shown in Figure 1: substrate/oxide coating, substrate/bond coat/oxide coating, substrate coated with five (bond coat/oxide layer) successive layers, and substrate coated with 10 (bond coat/oxide layer) successive layers. Note that a very thin metal bond coat about 100 nanometers thick is also deposited before monolayer ZrO_2 as well TiO_2 coating and is attributed to the transition from metallic towards poisoned target state after etching step. The properties (structural, chemical and adhesion) of the architectured substrate/(bond coat/)coating systems were studied using experimental techniques such as SEM, XRD and scratch test. Finally, electrochemical measurements and immersion tests were performed in nitric acid solution at boiling temperature, in Cherbourg natural seawater at an average temperature of 12 °C and in Singapore natural seawater at an average temperature of 29-30 °C. Note that the corrosion resistance of our systems are compared to those of their bulk form when possible (e.g. bulk Ti) but also to other materials currently studied to improve the durability of components as tantalum (Ta) in nitric acid, which is known to be highly resistant to corrosion but shows a high cost, a high density (16.4 g/cm^3). This can be a limitation for the building of industrial components [17]. Moreover, Ta is a critical element and thus its use should be limited e.g. with the use of a thin coating instead of a massive material.

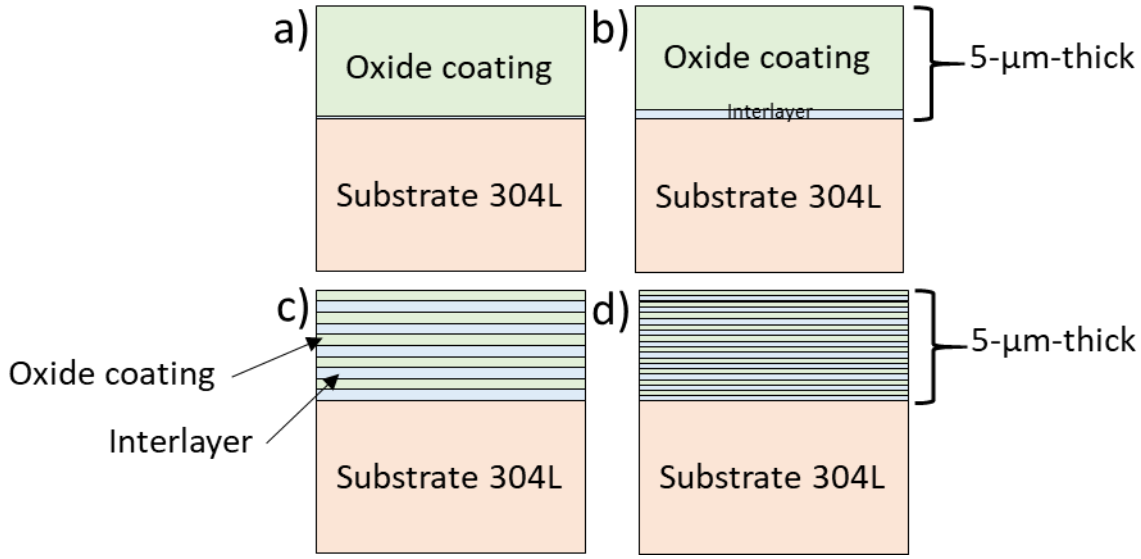

Figure 1: Drawing of the four system architectures studied in this chapter: a) substrate/oxide coating, b) substrate/metal /oxide coating, c) substrate/metal bond coat/oxide coating 5 layers and d) substrate/metal bond coat/oxide coating 10 layers.

1. DEPOSITION OF OXIDE AND MULTILAYER THIN FILMS

1.1 PROCESS PARAMETERS

Oxide and multilayer thin films have been synthesized by the company DEPHIS in a deposition machine using two metallic targets facing each other. One of the targets operates in pulsed DC mode and the other in HiPIMS mode. The difference between these two techniques is the type of power supply: shorter pulses of higher peak power leading to a highly ionized plasma characterize HiPIMS. As observed in [18-20], the simultaneous use of these two techniques should result in denser thin films with lower residual stresses because of the increased adatom mobility thanks to metal ion bombardment, in combination with a higher deposition rate than HiPIMS alone. The metal ion etchings (Ti^+ or Zr^+) investigated in the previous chapter have been chosen as a substrate pre-treatment because they seemed to be efficient in improving corrosion resistance properties compared to Ar^+ etching. Due to time limitation, we have not yet assessed comparative test with Ar^+ etching but this would be important to see if the tendency observed at the scale of the bond coat is still observed at larger scales. Metal ion etching is performed during three minutes using a substrate-holder (bias) voltage of – 900 V (Table 1). The specific etching parameters were chosen to assure the same parameters as those used in the previous chapter. Here, it can be pointed out that etching parameters can be optimized in such way that the bias voltage can be adjusted to obtain fully dense substrate/coating interfaces without contaminants. However, contrary to the study of the substrate/metal coating system, the substrate-holder is in a double rotation configuration to allow the etching and the deposition on all the substrate faces. The substrates are suspended on the sample holder using stainless steel suspension wires as in the TriPros deposition chamber.

Table 1: Parameters of etchings, metal interlayers and oxide coatings deposition.

		Etching (Ti/Zr)	Metal coating (Ti/Zr)	Oxide coating (Ti/Zr)
DC pulsed mode	Intensity (A)	/	5	5
	Target Voltage (V)		260/230	300/260
	Pulse width (µs)		16	16
	Extinction time (µs)		4	4
	Frequency (kHz)		50	50

HiPIMS mode	Intensity (A)	3.5	3.5	3.5
	Target Voltage (V)	870/860	870/820	820/830
	Pulse width (µs)	500	500	500
	Extinction time (µs)	500	500	500
	Frequency (kHz)	1	1	1
	Current peak (A)	800/700	400/360	400/440
Substrate-holder bias (V)		900	50	50

The Ti/TiO_2 and Zr/ZrO_2 multilayer coatings were prepared according to the previous chapter, *i.e.* a 200 nm-thick metal (Ti or Zr) layer was first deposited as bond coat between the substrate and the oxide coating to improve adhesion [21, 22]. Then, alternate metal (Ti or Zr) and oxide layers were deposited by controlling the oxygen flow within the chamber. Coating structures and thicknesses for each sample are provided in Table 2. Note that a very thin metal bond coat about 100 nanometers thick is also deposited before monolayer ZrO_2 as well TiO_2 coating and is attributed to the transition from metallic towards poisoned target state after etching step. To prevent this, an optical monitoring behind the shutter should be preferred before its opening.

Table 2: Monolayer and multilayer coatings structures.

Coating	Number of layers		Total coating thickness (µm)
	Ti or Zr (thickness bond coat)	TiO_2 or ZrO_2 (thickness oxide layer)	
TiO_2	1 (≈100 nm)	1	5.60 ± 0.01
Ti/TiO_2	1 (200 nm)	1 (4.84 ± 0.04 µm)	5.04 ± 0.04
(Ti/TiO_2)x5	5 (200 nm)	5 (800 ± 20 nm)	5.04 ± 0.03

(Ti/TiO_2)x10	10 (200 nm)	10 (235 ± 10 nm)	4.35 ± 0.03
ZrO_2	1 (≈100 nm)	1	7.90 ± 0.08
Zr/ZrO_2	1 (200 nm)	1 (6.01 ± 0.02 µm)	6.21 ± 0.02
(Zr/ZrO_2)x5	5 (200 nm)	5 (1.11 ± 0.03 µm)	6.56 ± 0.06
(Zr/ZrO_2)x10	10 (200 nm)	10 (520 ± 20 nm)	7.17 ± 0.05

The deposition time of the various coatings is determined by measuring the deposition rates of the metal and oxide on control samples. Oxygen flow is regulated via a feedback loop by photoemission monitoring (PEM) of the intensity of an emission line of metal atoms. The PEM set point value was determined by test coatings on a glass slide and by XRD analysis after various tests to determine the good deposition parameters. All parameters configurations are summarized in Table 2. It should be pointed out that all coating parameters were not fully optimized, further experiments are needed. For example, higher peak current density, which can increase ionization of metal species in the HIPIMS plasma. This may be lead to denser coating as a result of an increase of adatom mobility due to ion bombardment. Hence, the coating performances could be hampered by their limited densities and/or poor adherence.

1.2 STRUCTURAL AND CHEMICAL PROPERTIES

1.2.1 Ti-based thin films

Figure 2 shows the SEM-BSE images of cross-sections of the various Ti-based oxide coatings (TiO_2, Ti/TiO_2, (Ti/TiO_2)×5 and (Ti/TiO_2)×10 multilayers) on 304L steel substrate. In addition, coating thicknesses are usually around 5 µm (Table 2), with a slight dispersion, from 5.6 µm for TiO_2 coating to 4.4 µm for (Ti/TiO_2)×10. TiO_2 and Ti/TiO_2 coatings show an open columnar microstructure that develops from a dense microstructure, which should promote correct substrate/coating adhesion to a porous one at their surface. In the case of (Ti/TiO_2)×5 coating, the columnar growth of TiO_2 does not seem to have been interrupted by the intercalation of the metallic Ti layers. However, the metallic layers appear to be dense, likely due to sufficient metal ion bombardment during film growth. The porous columnar microstructure is still observed at the extreme surface but a lower number of intercolumnar regions is noticed. A similar effect is noticed for the (Ti/TiO_2)×10 coating even if the first two oxide layers from the substrate seem denser than the others. As the number of intercolumnar regions decreases by increasing the number of layers, it can be assumed that the roughness will be lower for the multilayer coatings, as it will be discussed later. Here, the columnar width, measured at the extreme surface using SEM images, decreases from around 0.6 µm for TiO_2 to 0.25 µm for (Ti/TiO_2)×10 coating. Based on these observations, it can be concluded that TiO_2 layers exhibit typical zone T feature (see section 1.1.4 of “Literature review” chapter), which indicates that adatom mobility was

insufficient during the growth, probably due to low ion bombardment. This columnar microstructure tends to indicate that the ability of these multilayers to prevent the electrolyte from reaching the substrate may be reduced from what would be expected according to literature [1-3].

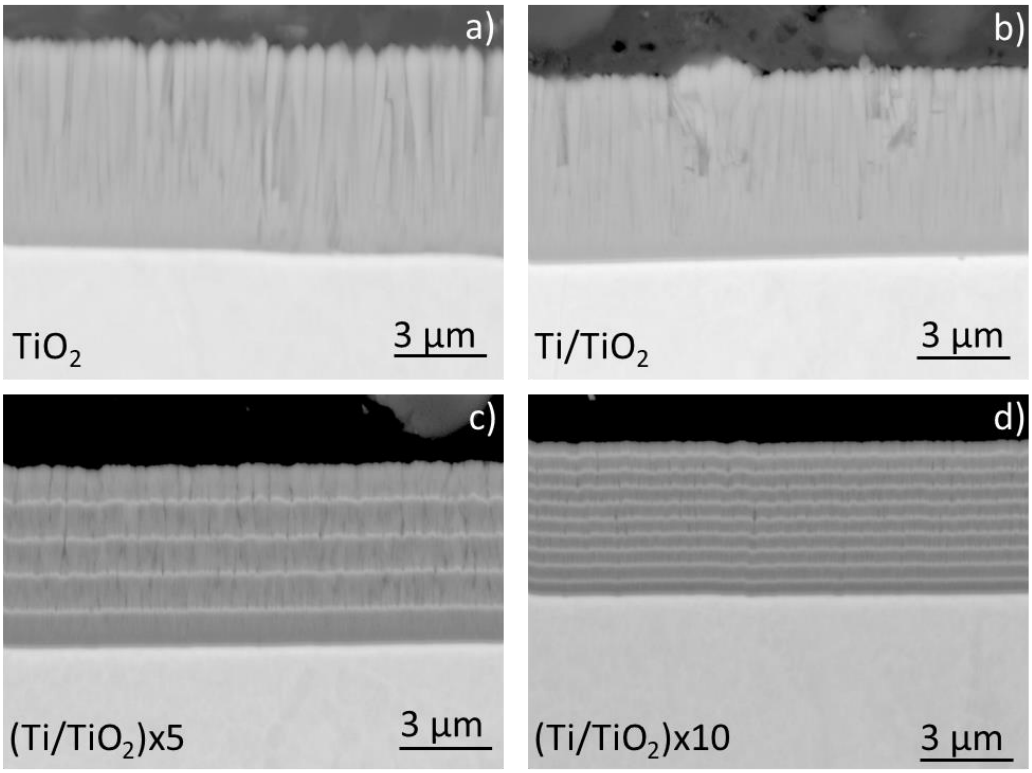

Figure 2: SEM-BSE images of cross-sections of a) monolayer TiO_2, b) bilayer Ti/TiO_2, c) $(Ti/TiO_2)x5$ and d) $(Ti/TiO_2)x10$ coatings.

EDX line scans of the cross-sections of Ti-based coatings are shown in Figure 3. Due to the lack of standard calibration sample, the absolute concentration of the individual elements is not measurable. Nevertheless, the intensity variations of each element are reliable. No obvious difference is observed between TiO_2 and Ti/TiO_2 coatings due to the deposition of a metallic thin layer in both cases, *i.e.* 100 and 200 nm respectively. In multilayer structure, periodic oscillations of Ti and O profiles are noticed, where the intensity of O and Ti distributions are opposite. This is particularly noticeable for the $(Ti/TiO_2)\times10$ coating. Moreover, an O enrichment of the coating at the extreme surface seem to be observed, which is probably due to Ti high affinity with O when removed from the deposition machine and exposed to air. A stable Ti-based oxide is formed in contact with air, as reported by the Ellingham diagrams [23].

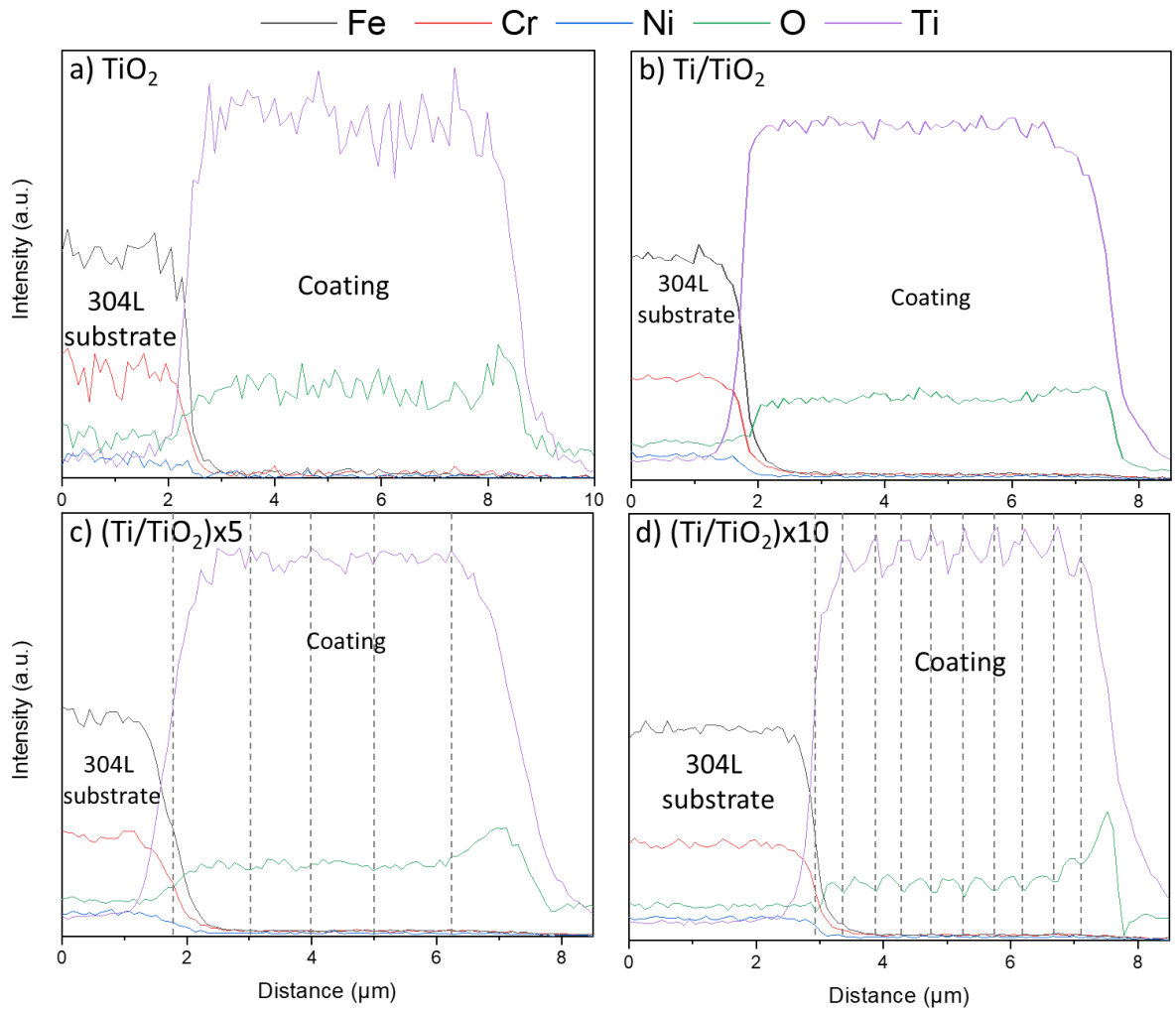

Figure 3: SEM-EDX line scans of cross-sections of a) monolayer TiO_2, b) bilayer Ti/TiO_2, c) $(Ti/TiO_2)x5$ and d) $(Ti/TiO_2)x10$ coatings.

The coating crystalline structure is investigated by XRD in a θ-2θ mode, resulting in the observation of signals from both coatings and substrate (Figure 4). Contributions from 304L steel, anatase (TiO_2), rutile (TiO_2) and titanium are detected (PDF 00-004-0477, PDF 00-001-1292 and PDF 00-044-1294 for anatase, rutile and titanium, respectively). Note that the contribution of the titanium appears to be low, probably hidden by all the other contributions due to its too small thickness (200 nm). Austenite (γ) contributions from the substrate are observed at 43.8 (111) and 50.9°2θ (200) for all coated samples. These same XRD peaks was observed for the Ti^+-etched and, Ti^+-etched and Ti-coated samples in the previous chapter. Additionally, contribution from ferrite (α) phase from the substrate is observed for multilayer coatings at 44.7°2θ (110). On the other hand, the intensity of XRD peaks associated to Ti-based coatings vary between monolayer/bilayer and multilayer coatings, indicating different anatase and rutile phase proportions. Nonetheless, the major contribution is anatase (tetragonal) in all cases. Figure 4 shows a preferred orientation along the anatase (220) axis for TiO_2 and Ti/TiO_2 coatings while multilayer coatings are preferentially oriented along (101) and (004) axes of anatase. In addition, the contribution of metallic titanium to the XRD patterns is observed for multilayer coatings, but not in TiO_2

monolayer or Ti/TiO_2 bilayer. Finally, some XRD peaks can be attributed to two different crystalline structures and are noted (/).

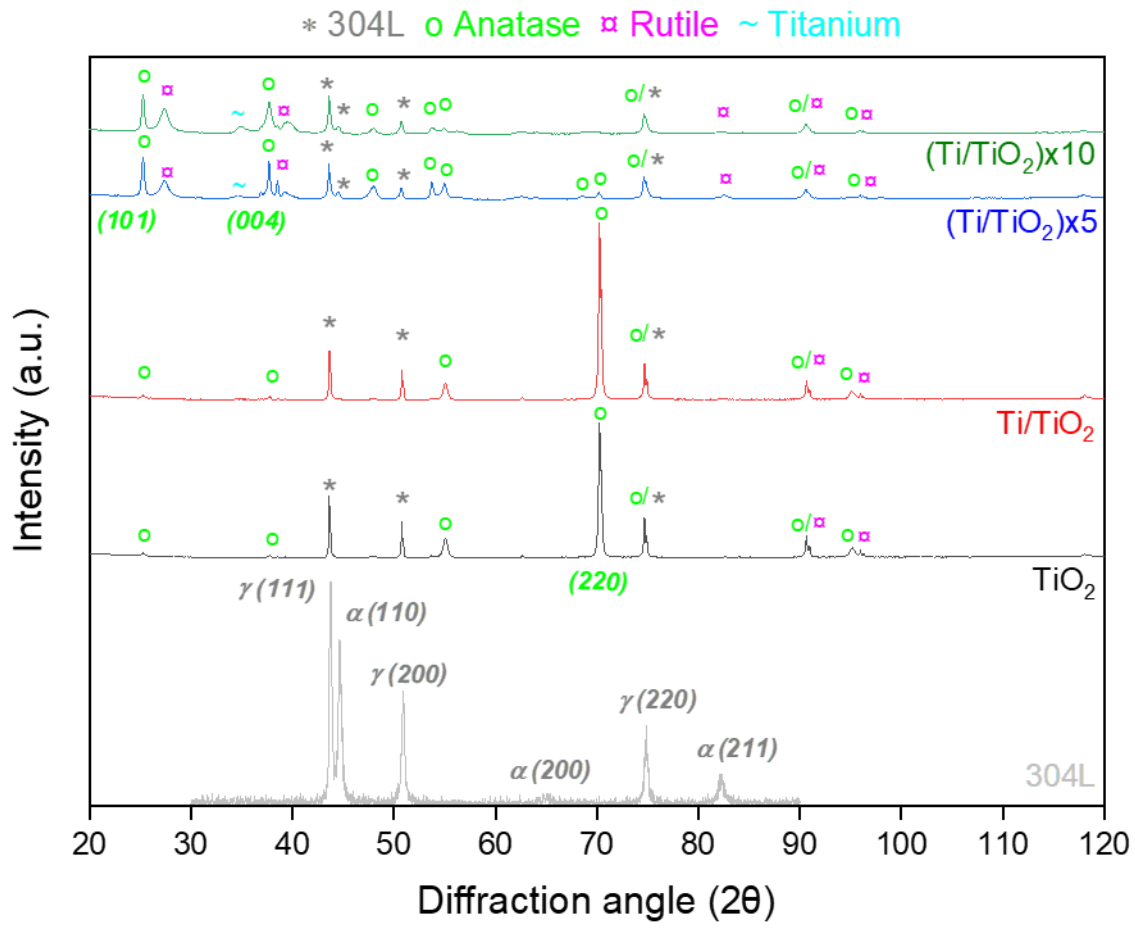

Figure 4: XRD patterns of Ti-based coatings synthesized by DEPHIS (θ-2θ mode).

The number of layers has an effect on the coating structure: when the number of layers increases, the number of XRD peaks also increases, as observed when comparing Ti/TiO_2 and (Ti/TiO_2)×10 coatings. This can be explained by a change of crystalline phases orientation of the multilayer coatings. Moreover, the major contributions of the (Ti/TiO_2)×10 coating are shifted to higher 2θ values such as the anatase (101), which is at 25.28°2θ for (Ti/TiO_2)×10 and 25.23°2θ for (Ti/TiO_2)×5 coatings. This can be due to the increase in compressive stresses produced during the deposition process that deforms the crystalline structure [2, 24]. Further characterization is needed to conclude on the effect of residual stresses. On the other hand, the detection of the low metallic Ti contribution in multilayer coatings XRD patterns is due to a higher total amount of metallic Ti in multilayer architectures.

1.2.2 Zr-based coatings

The SEM-BSE images of cross-sections from the various Zr-based oxide coatings (ZrO_2, Zr/ZrO_2, (Zr/ZrO_2)×5 and (Zr/ZrO_2)×10 multilayers) on 304L steel substrate are shown in Figure 5. The coatings show an open columnar microstructure less pronounced than the Ti-based coatings (Figure 2), suggesting that the Zr-based

coatings are denser. The Zr coating densities may be further enhanced by using optimized HiPIMS/DC pulsed process parameters. In contrast to the SEM observations of Ti-based coatings (Figure 2), the columnar growth of ZrO_2 appears to be limited by the deposition of Zr metal thin layers. The open columnar microstructure is observed only on the last oxide layer and has narrower intercolumnar regions than monolayer and bilayer coatings. Here, the columnar width, measured at the extreme surface, decreases from around 0.7 µm for ZrO_2 to 0.3 µm for $(Zr/ZrO_2)\times10$ coating. This can suggest that the ion bombardment was sufficient during the process, which induces an increase of adatom mobility. Hence, this can filling-up atomic-scale voids and probably allow changing the microstructure from zone T to zone 2 of the SZM (see section 1.1.4 of "Literature review" chapter). Moreover, coating thicknesses are slightly higher than those of the Ti-based coatings, around 7 µm with a dispersion from 6.6 µm for $(Zr/ZrO_2)\times5$ to 7.9-µm-thick for ZrO_2 monolayer (Table 2).

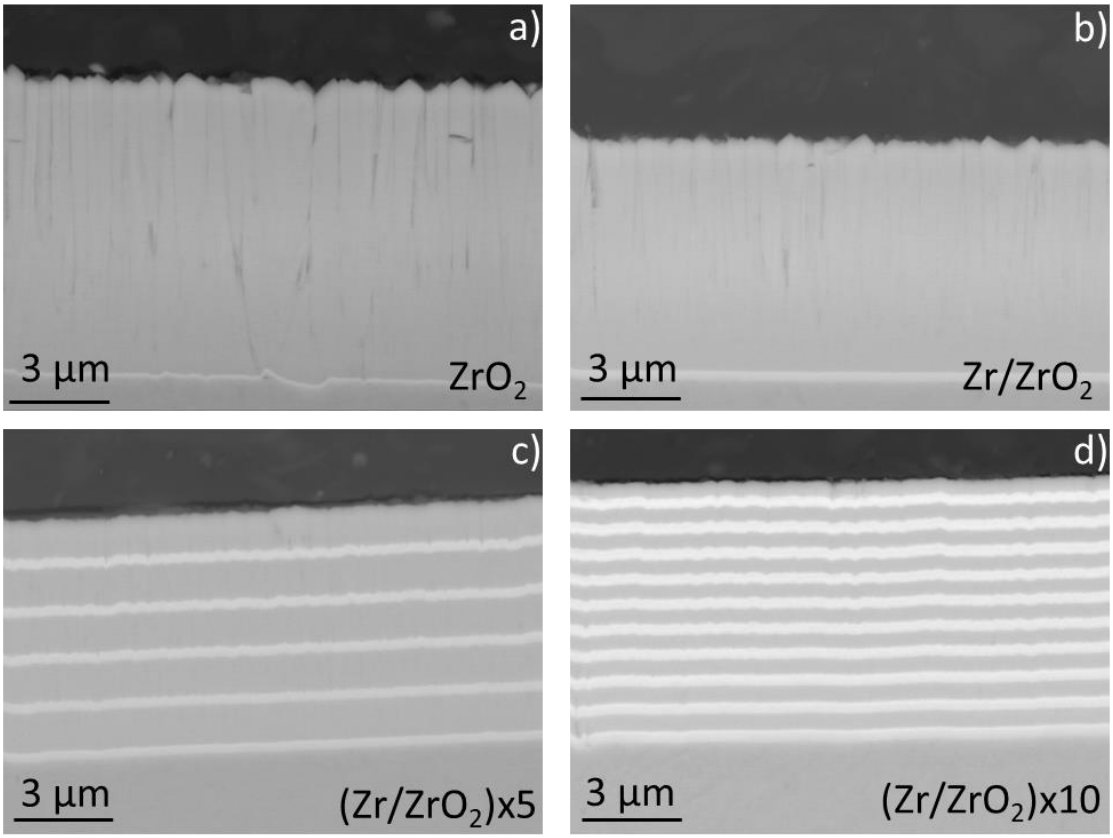

Figure 5: SEM-BSE images of cross-sections of a) monolayer ZrO_2, b) Zr/ZrO_2, c) $(Zr/ZrO_2)x5$ and d) $(Zr/ZrO_2)x10$ coatings.

Figure 6 shows EDX line scans of the cross-sections of Zr-based coatings. No obvious difference is observed between ZrO_2 and Zr/ZrO_2 coatings due to the deposition of a metallic thin layer in both cases (transition from metal etching to oxide coating deposition), as already observed for Ti-based coatings. Clear periodic oscillations of Zr and O profiles are noticed in multilayer structure, where the intensity of O and Zr distributions are opposite. Moreover, an O enrichment of the multilayer coatings at the extreme surface seem to be observed. This is related to the affinity of Zr with O when

the samples are removed from the vacuum chamber after deposition, resulting in the formation of a stable Zr-based oxide in air.

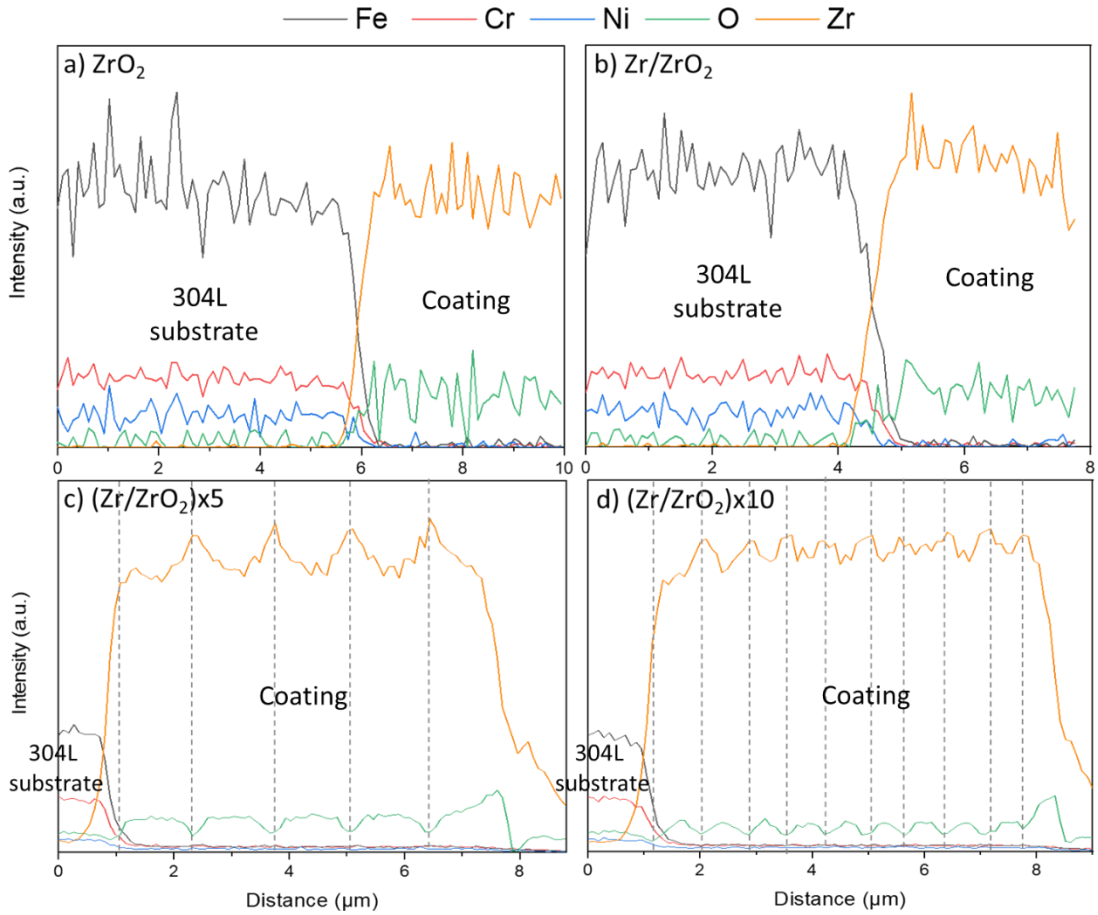

Figure 6: SEM-EDX profiles of cross-sections of a) monolayer ZrO_2, b) bilayer Zr/ZrO_2, c) $(Zr/ZrO_2)x5$ and d) $(Zr/ZrO_2)x10$ coatings.

The crystalline structure is investigated by XRD in θ-2θ mode (Figure 7). Contributions from the 304L substrate, baddeleyite (ZrO_2; PDF 00-001-0750) and zirconium (PDF 01-078-2921) are detected. For all coated samples, the only contribution observed from the substrate is the austenite (γ) phase at 43.8°2θ (111). This contribution being the most intense of our 304L ASS, it was already noticed for the Zr^+-etched and, Zr^+-etched and Zr-coated samples in the previous chapter. On the other hand, XRD peaks associated to the baddeleyite (ZrO_2) differ in intensity according to the coating considered and only one contribution from metallic Zr is only observed for $(Zr/ZrO_2)\times10$ coating. Figure 7 shows a preferred orientation along the baddeleyite (110) axis for ZrO_2 coating and along the (020) axis for Zr/ZrO_2 coating. In contrast, Zr/ZrO_2 multilayers are preferentially oriented along the (-111) axis, probably due to a texturing effect.

Compared to Ti-based coatings (Figure 4), the substrate is less visible on the XRD patterns, which is explained by a higher thickness of the Zr-based coatings and a probably denser structure (less pronounced columnar structure) of these coatings. Moreover, a shift of the diffraction peaks is noticed for Zr-based coatings towards

higher 2θ values. For instance, the contribution of baddeleyite (020) is observed at 33.95°2θ for ZrO_2, 33.98°2θ for Zr/ZrO_2, 34.30°2θ for $(Zr/ZrO_2)\times5$ and 34.36°2θ for $(Zr/ZrO_2)\times10$. This can be due to the increase in compressive stresses produced during the deposition process that deforms the crystalline structure [15, 24]. Residual stresses measurements can help to understand this phenomenon. On the other hand, the detection of metallic Zr contribution in the $(Zr/ZrO_2)\times10$ coating results from the higher amount of metallic Zr in this coating architecture compared to bilayer coatings.

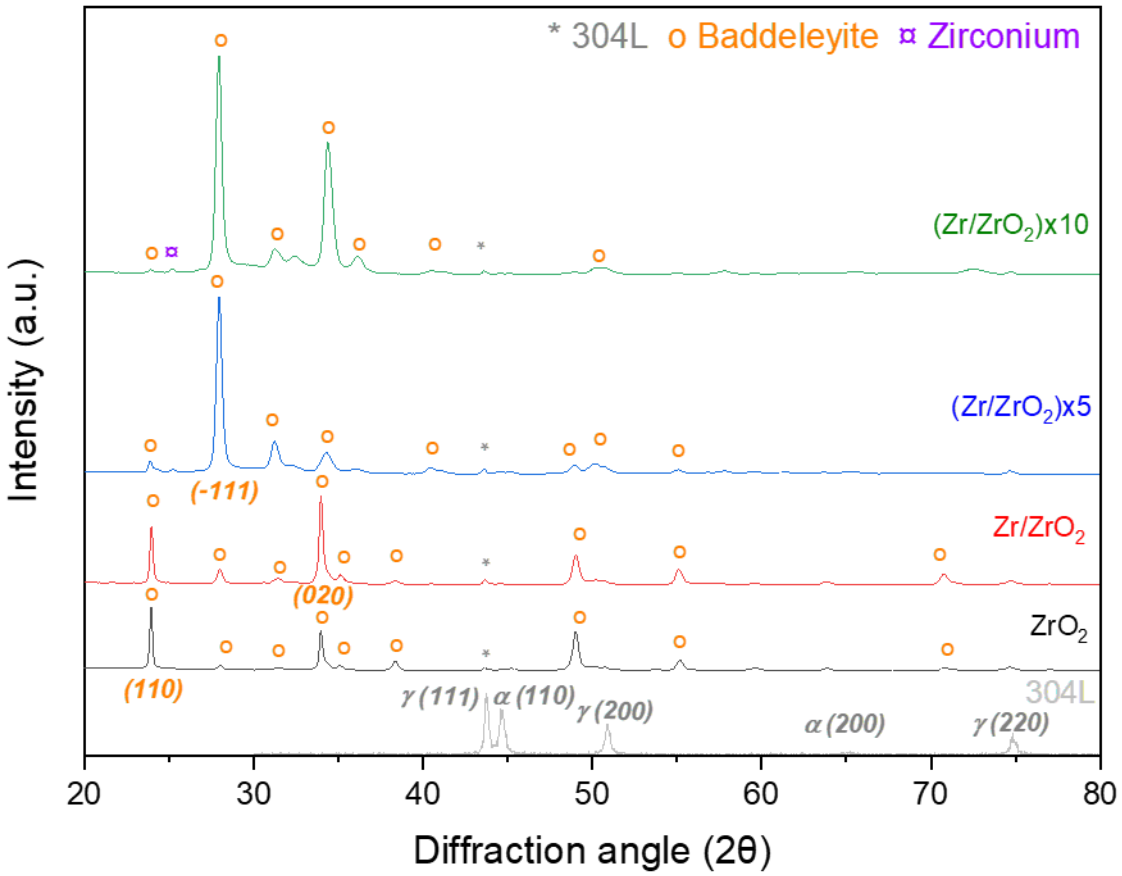

Figure 7: XRD patterns of Zr-based coatings synthesized by DEPHIS (θ-2θ mode).

In conclusion, both Ti-based and Zr-based coatings show not optimized open columnar microstructures, which will probably strongly affect the corrosion resistance properties by promoting accessibility of the corrosive medium through the coating. Characterizations performed show that Ti-based coatings are mainly composed of mixed anatase and rutile, and Zr-based coatings of baddeleyite. This phase mixture for Ti-based coatings could have an effect on the biocorrosion resistance of the coating systems as anatase is generally used for its antifouling properties [25]. Finally, the crystal orientation depends on the number of layers in the coating system, indicating a texturing effect for multilayer coatings. Optimization of the elaboration process will be necessary in the future to obtain denser microstructures in order to improve the corrosion resistance properties as well. The link with the first steps of

preparation of the coating as described in the previous chapter: etching and bond coat deposition will also have to be studied with these optimized coatings.

1.3 MECHANICAL PROPERTIES

The variation in the final surface roughness of the 304L steel, the single oxide layer and the different multilayer coatings measured by interferometric microscopy on polished samples is shown in Figure 8. The surface roughness of the 304L steel substrate is the lowest and equals 28 ± 1 nm. The increase in surface roughness between the monolayer oxide layer and the Zr/ZrO_2 coating (with a Zr bond coat) was not expected according to the literature, as increasing the number of layers decreases usually the surface roughness of the final coating [26]. It could also be related to measurement artifacts. Otherwise, the observations performed on the multilayer coatings are consistent with the literature by showing that an increase of the number of layers decreases the surface roughness. For example, the surface roughness for $(Zr/ZrO_2)\times10$ equals of 41 ± 2 nm compared to 95 ± 8 nm for the Zr/ZrO_2 coating. Since the roughness is related to the coating microstructure, this indicates that the coating overall density increases by increasing the number of layers, which is consistent with the SEM observations (Figure 5). To sum up, growth of columnar crystals and crack propagation are limited by adding layers within the coating, which leads to a lower surface roughness [27].

The very high surface roughness measured for TiO_2 and Ti/TiO_2 coatings is explained by poor re-polishing of these samples performed by DEPHIS company before deposition, which increase the shadowing effects at the substrate surface. Thus, it can affect the film growth due to the very limited adatom mobility (zone 1/zone T on the structure zone model shown in section 1.1.4 of the “Literature review” chapter), as all oxides coating exhibit columnar-like structure. As observed for the Zr-based samples, increasing the number of layers decreases the roughness of the final coating system, which is in line with the decrease in the number of intercolumnar regions observed for multilayer coatings (Figure 2). This high roughness modifies the surface of the samples and the real surface exposed to the corrosive medium will therefore be higher than the geometric surface. Therefore, current densities determined in electrochemical experiments will be overestimated and as well as weight losses. Moreover this high roughness could modify some surface phenomenon by creating cavities with localized accumulation of the corrosive medium. Results of electrochemical tests and immersion tests performs on these samples will have to be considered with care.

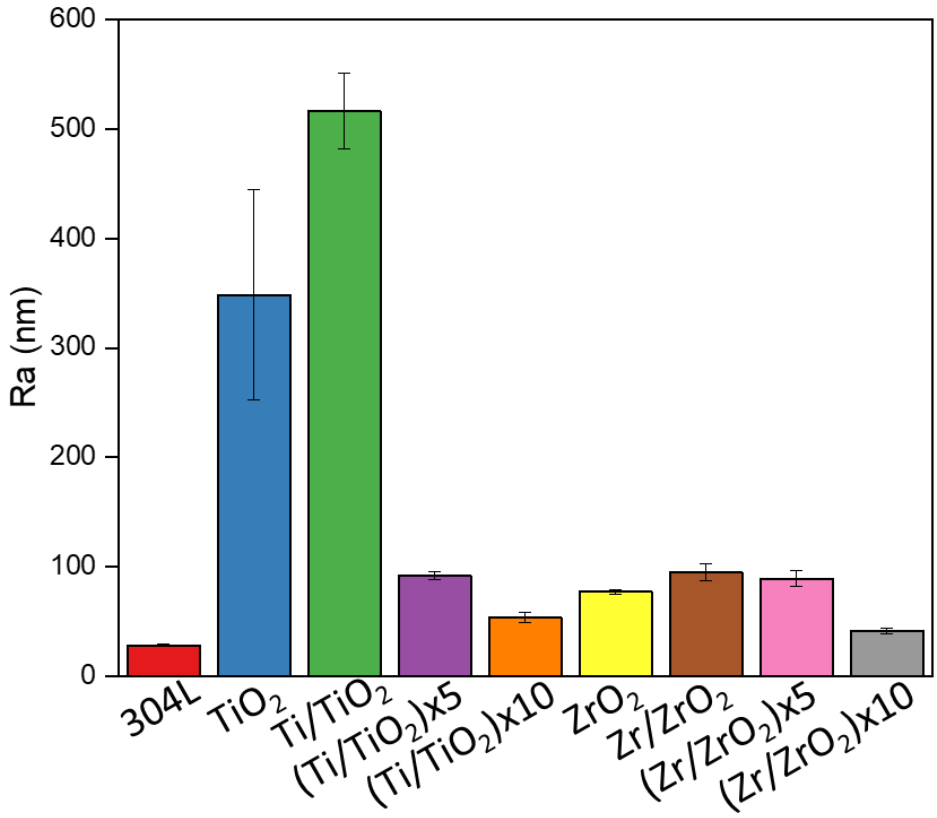

Figure 8: Surface roughness of the initial 304L substrate and all the oxide and multilayer-coated samples.

Scratch-test measurements from 0 to 50 N were performed on all the Ti- and Zr-based coatings pretreated by metal ion etching. Critical loads values (Lc), which correspond to total coating delamination, are given in Table 3. It is worth noticing that the critical load values depend on the metal used for the metal coating, which makes comparisons possible only for coatings of the same type *i.e.* Ti- or Zr-based. Furthermore, a direct comparison of the results obtained in previous chapter is not possible, as the coating thickness is different (200 nm *vs.* 5 µm here).

Table 3: Average value of the critical load determined for all the oxide and multilayer coatings.

	Lc (N)
TiO_2	18 ± 4
Ti/TiO_2	16 ± 1
$(Ti/TiO_2)x5$	19 ± 1
$(Ti/TiO_2)x10$	19 ± 1
ZrO_2	>50
Zr/ZrO_2	>50

$(Zr/ZrO_2)x5$	>50
$(Zr/ZrO_2)x10$	37 ± 1

In the case of Ti-based coatings, they all show delamination at close Lc values (16-19 N) as well as adhesive failures along the scratch grooves, indicating a poor adhesion of the Ti-based coatings, which can be due to lower-quality interfaces (metal bond coat/oxide coating or substrate/metal bond coat) or too high internal stresses. Figure 9 shows the SE micrographs of bilayer and 10 layers coatings surfaces after scratch test measurements. The Lc value (noted Lc on Figure 9) obtained by SE image analysis is similar to that obtained by the scratch test measurements tools (Table 3). All Ti-based coating exhibit a brighter area on the scratch groove (Figure 9c), indicating interfacial delamination occurred between the coating and the substrate at around 19 N. This is probably due to the low mechanical strength of the Ti bond coat, which dissipates most of the energy by shear deformation at the interface during the scratch test [28].

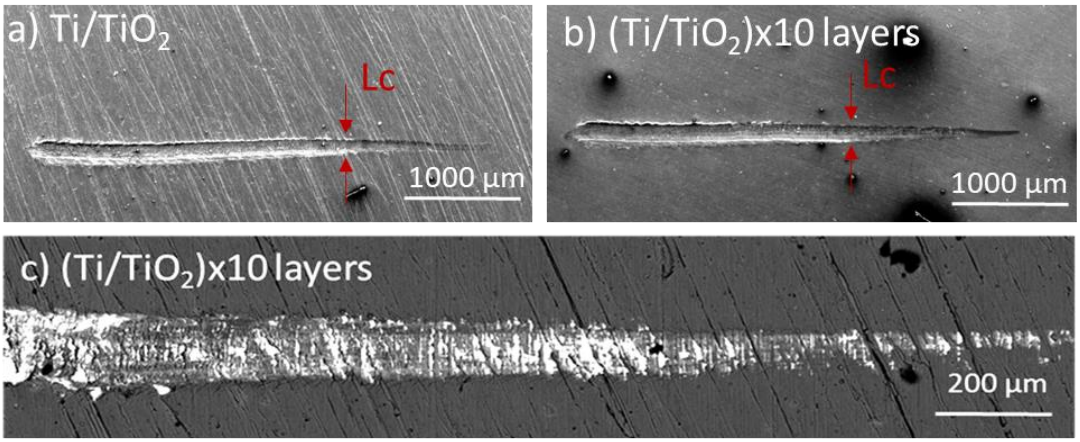

Figure 9: SEM-SE micrographs of Ti-based coating view after scratch test measurements. (a) Ti/TiO_2 and (b, c) $(Ti/TiO_2)x10$ coatings at various magnifications.

In contrast, Zr-based coating show a better adhesion to the substrate compared to Ti-based coatings (Figure 10), only $(Zr/ZrO_2)\times10$ delaminates at around 37 N (Figure 10c). However, these results differ from the literature as usually the adhesion is improved by increasing the number of layers. This is explained, e.g. for nitride multilayer coatings, by a better resistance to deformation due to an increase in the number of interfaces [24]. It should be pointed that the critical load values Lc are related both to the intrinsic parameters and to the coating/substrate combination properties (the extrinsic parameters), meaning that a direct comparison of the results obtained in different studies is complicated given a variety of critical values. Hence, this technique presents an engineering evaluation of the adhesion strength in the same test conditions. In our case, the limited adhesion of the $(Zr/ZrO_2)\times10$ coating can be due to the presence of high metal content in the final coating, which decreases the shear stress resistance compared to oxide (ceramic) layer. Hence, there is an optimum combination of alternate layers, *i.e.* number of metallic layers, which gives an optimal enhancement in coating scratch resistance. Finally, Zr/ZrO_2 and

$(Zr/ZrO_2)\times5$ coatings can be a good compromise as they allow the formation of a multilayer coating, which is expected to further enhance the protection against corrosion

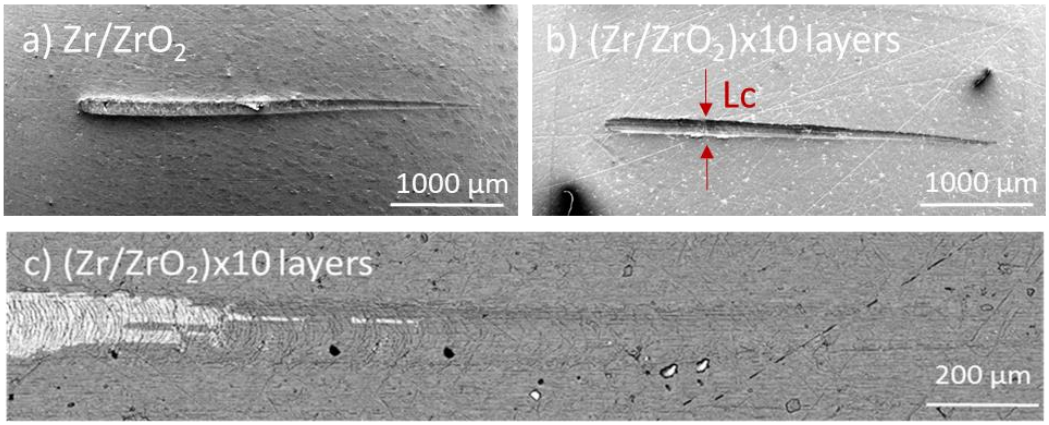

Figure 10: SEM-SE micrographs of Zr-based coating view after scratch test measurements. (a) Zr/ZrO_2 and (b, c) $(Zr/ZrO_2)x10$ coatings at various magnifications.

In conclusion, oxide and multilayer coatings have been deposited on a 304L steel substrate using a hybrid HiPIMS/DC pulsed technique. All these coatings show an open columnar structure (which is less visible for the Zr-based coatings), probably because of too weak ionic bombardment during deposition. The ZrO_2 oxide in the coatings is only monoclinic baddeleyite, whereas mixed anatase and rutile (both tetragonal TiO_2) are present for Ti-based coatings. These first characterizations also show that the number of layers has an influence on the orientation of the crystals and the surface roughness of the final coating system. Finally, the Ti-based coatings show poor adhesion properties, with delamination for all the samples, whereas the Zr-based coatings show a better adhesion on the 304L steel. The corrosion behaviour of these architectural coating systems, which are not optimized, will now be evaluated in nitric acid and sodium chloride solutions.

2. PERFORMANCE OF THE ARCHITECTURAL SUBSTRATE/COATING SYSTEM IN AGGRESSIVE ENVIRONMENTS

The non-optimized architectural coating systems presented in the previous section aim at increasing the lifespan of 304L steel in nitric acid and marine environments. Therefore, their performance in these two environments are studied using electrochemical measurements and immersion tests. The corrosion resistance properties of our systems are compared to those of their bulk forms where possible (bulk Ti for example) or to other materials that are currently being studied for corrosion protection (e.g. Ta in nitric acid). Note that we did not assess the performance of bulk Zr.

2.1 CORROSION IN NITRIC ACID SOLUTION

2.1.1 Electrochemical measurements

2.1.1.1 Potentiodynamic polarization curves

Figure 11 shows the potentiodynamic polarization curves of the initial 304L steel and Ti- and Zr-based coatings in a nitric acid solution at boiling temperature after 6 h and 2 d of immersion. Reference materials such as bulk Ti, bulk Ta, and 5-µm-thick Ta coating are also studied to compare with our architectural coating systems. The corrosion potential (E_{corr}) and corrosion current density (J_{corr}) are derived from a Tafel extrapolation of the measured anodic polarization experiment. Table 4 shows that the E_{corr} value for the 304L steel reaches 0.98 V/SHE after 6 h and 0.96 V/SHE after 2 d in nitric acid. In comparison, E_{corr} for the Ti- and Zr-based coatings are scattered around initial 304L value after 6 h of immersion, whereas E_{corr} for Ta-based samples are more positive than for 304L. The observed dispersion of E_{corr} could be explained by the non stabilization of the potential after 6 h due to kinetic limitations. After 2 d, a dispersion of Ti-based coatings is still noticed, whereas E_{corr} of Zr-based coatings and Ta-based samples are more positive than for 304L, as they have passivated. This shows also that no stationary state has been reached.

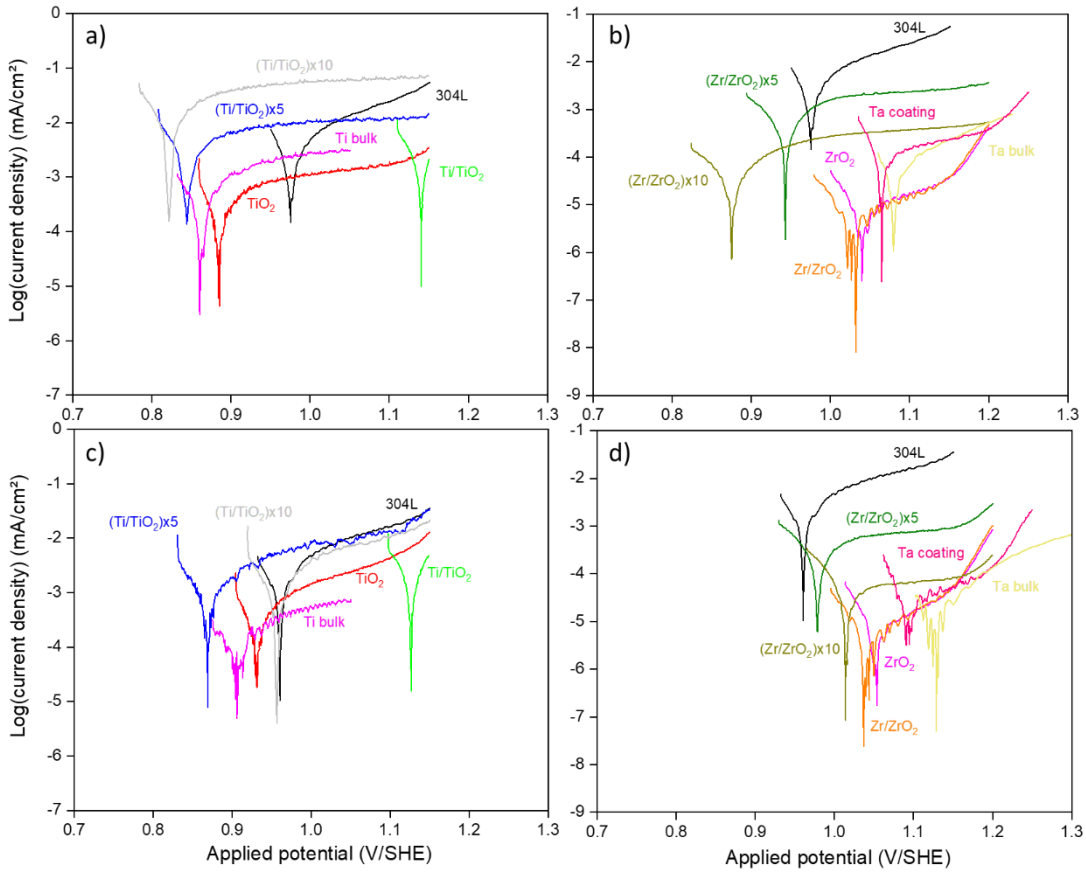

Figure 11: Potentiodynamic polarization curves of the 304L steel and coated substrates in a nitric acid (2.5 mol/L HNO_3, 2.5 mol/L $NaNO_3$ and 2 g/L $Fe(NO_3)_3$) solution at 110°C after 6 h for a) Ti-based, b) Zr-based coatings and 2 d of immersion for c) Ti-based, d) Zr-based coatings.

After 6 h of immersion, J_{corr} decreases by an order of magnitude for bulk Ti, TiO_2 and Ti/TiO_2 coated samples down to 10^{-4} mA/cm² compared to 1×10^{-3} mA/cm² for 304L steel (Figure 11a). However, for Ti-based multilayer coatings, J_{corr} is similar to the value of 304L steel (10^{-3} mA/cm²). On the other hand, J_{corr} decreases by an order of magnitude for $(Zr/ZrO_2)\times5$ coating (1×10^{-4} mA/cm²), by two for $(Zr/ZrO_2)\times10$ coating and Ta-based samples ($1\text{-}2\times10^{-5}$ mA/cm²) and by almost three orders of magnitude for ZrO_2 and Zr/ZrO_2 coatings (3×10^{-6} mA/cm²) compared to 304L steel (Figure 11b). It must be recalled that the high roughness obtained for some of the samples could modify the values of the current densities and could also influence the electrochemical response of the substrates.

After 2 d of immersion, J_{corr} for the initial 304L, bulk Ti, and Ti-based multilayer coatings slightly decreases to 6×10^{-4}, 4×10^{-5}, 4×10^{-4} and 9×10^{-4} mA/cm^2, respectively (Figure 11c). On the other hand, J_{corr} is almost invariant for the TiO_2 and Ti/TiO_2 coated samples (2×10^{-4} and 5×10^{-4} mA/cm^2). Therefore, all the Ti-based coatings show a J_{corr} value of the same order of magnitude as the 304L steel (Table). For the Zr-based coatings, J_{corr} is almost invariant for all of them, except $(Zr/ZrO_2)\times5$ coating that shows a decrease of J_{corr} down to 6×10^{-5} mA/cm² (Table 4). Similarly, J_{corr} is almost invariant for the Ta-based samples after 2 d of immersion (Figure 11d).

Assuming a uniform corrosion process, the Tafel slopes obtained from the extrapolation can be used to estimate the corrosion rate after 2 d (Table 4). The corrosion rate shows the highest value of 9 µm/year for $(Ti/TiO_2)\times10$ coating. Intermediate values of 6 µm/year for initial 304L, 5 µm/yeart for Ti/TiO_2 and 4 µm/year for $(Ti/TiO_2)\times5$ coating are noticed. The lowest values (< 0.5 µm/year) are obtained for Zr-based coatings *i.e.* ZrO_2, Zr/ZrO_2 and $(Zr/ZrO_2)\times10$ coatings. Comparing these corrosion rates with those of the etched samples (previous chapter), it is noted that all the Ti-based coatings show a higher corrosion rate than the Ti^+- and Zr^+-etched sample (around 1 µm/year). On the contrary, all the Zr-based coatings show a lower corrosion rate, confirming their higher corrosion resistance in this environment compared to the Ti-based coatings. Note that the corrosion rate values calculated from the electrochemical tests are qualitative and limited to a uniform corrosion process considering the stationary state has been reached. It is also necessary that Tafel extrapolation begins at least 50-100 mV away from E_{corr} and that the anodic or cathodic regions are observed over at least a decade of current.

Table 4: Corrosion potential (E_{corr}), current density (J_{corr}) and corrosion rate values after 6 h and 2 d of immersion in a nitric acid (2.5 mol/L HNO_3, 2.5 mol/L $NaNO_3$ and 2 g/L $Fe(NO_3)_3$) solution at 110°C.

	E_{corr} (V/SHE)		**J_{corr}** (mA/cm²)		**Corrosion rate** (µm/year)
	6 h	2 d	6 h	2 d	2 d
304L	0.98	0.96	1×10^{-3}	6×10^{-4}	6

TiO_2	0.88	0.93	1×10^{-4}	2×10^{-4}	2
Ti/TiO_2	1.14	1.13	6×10^{-4}	5×10^{-4}	5
$(Ti/TiO_2)x5$	0.84	0.87	1×10^{-3}	4×10^{-4}	4
$(Ti/TiO_2)x10$	0.82	0.96	7×10^{-3}	9×10^{-4}	9
ZrO_2	1.04	1.05	3×10^{-6}	2×10^{-6}	0.02
Zr/ZrO_2	1.03	1.04	3×10^{-6}	2×10^{-6}	0.02
$(Zr/ZrO_2)x5$	0.94	0.98	1×10^{-4}	6×10^{-5}	0.6
$(Zr/ZrO_2)x10$	0.88	1.01	2×10^{-5}	2×10^{-5}	0.2
Ti bulk	0.86	0.91	1×10^{-4}	4×10^{-5}	0.4
Ta bulk	1.08	1.13	1×10^{-5}	1×10^{-5}	0.1
Ta coating	1.06	1.09	2×10^{-5}	1×10^{-5}	0.1

After 2 d of immersion, all the Ti-based coatings have a similar (and even higher for the $(Ti/TiO_2)\times10$ coating) corrosion current density as the 304L substrate showing the bad quality of the coatings performed. Their columnar structure allows the electrolyte to penetrate the coating. No corrosion improvement is therefore observed. This differs from literature data showing that TiO_2 and Ti/TiO_2 coatings improve corrosion protection in 1 and 8 mol/L nitric acid solution at room temperature [6, 7]. This is confirmed by the good corrosion behavior obtained for the massive Ti. In addition, the poor adhesion of these coatings is also detrimental to corrosion resistance.

Zr-based coatings all show improved corrosion resistance by acting as a barrier against the electrolyte due to dense and stable ZrO_2 as it is observed in the literature [4, 11, 29]. For instance, ZrO_2 sol-gel coating act as a barrier and improve corrosion resistance of the 316L SS in 1 and 10 mol/L nitric acid at room temperature due to its inertness and high stability [4]. The corrosion protection offered by ZrO_2 and Zr/ZrO_2 coating is similar, which is explained by the very similar structure of these two thin films. In fact, during the entire deposition process, there is a time lag of a few seconds for the transition from Zr^+ etching step to oxide (ZrO_2) deposition step, which results in the formation of a thin (≈ 100 nm) layer of metallic Zr bond coat in all cases. Note that the bond coat is thicker, around 200 nm, for the Zr/ZrO_2 coating. This bond coat imparts a better resistance to corrosion to the final coating by decreasing the elastic deformation observed when an oxide is deposited on a metal. Since the ductility of ZrO_2 is lower than that of steel, fractures in the ZrO_2 coating can occur due to elastic

deformation [12], so its reduction is desired. Moreover, the bond coat can reduce the stresses by mitigating the surface oxidation during the deposition of an oxide on a metal [30]. On the other hand, using an almost uniform thickness for all layers of the $(Zr/ZrO_2)\times10$ coating (200-235 nm) is beneficial for reducing the large stress in the coating and consequently, results in a better corrosion resistance of this coating than $(Zr/ZrO_2)\times5$ coating [2]. However, multilayer coatings do not offer better corrosion resistance in our case, contrary to previous reports [1, 3, 31]. This is probably due to a higher defect density and/or the presence of higher stresses in these coatings. For instance, local droplet projectons related to electric arcs during the coating deposition and scratches from mechanical polishing of the 304L substrates can be present. Further analysis can be performed to determine the amount of these defects such as AFM.

2.1.1.2 Impedance spectroscopy measurements

Figure 12 displays the Nyquist diagrams of the initial 304L steel and Ti- and Zr-based coatings at open potential (E_{corr}) after 6 h and 2 d of immersion in a nitric acid solution at boiling temperature. The Nyquist diagrams show only one semicircle (capacitive loop) for all the samples, indicating a single time constant related to the charge transfer process [32, 33]. The increased loop radius for all the Zr-based coatings (Figure 12b) is explained by an increase in transfer resistance, i.e. an increase in corrosion resistance [33-35]. On the other hand, different behaviors are observed for Ti-based coatings. An increase in loop radius is noted for TiO_2 coating, whereas the Ti/TiO_2 and $(Ti/TiO_2)\times5$ coatings have loop radii similar to that of initial 304L steel, which confirms the low efficiency of these coatings to protect against corrosion. Finally, a decrease in the loop diameter compared to 304L steel substrate is observed for the $(Ti/TiO_2)\times10$ coating (Figure 12a). A maximum loop radius is reached for the Zr/ZrO_2 coating after 6 h in nitric acid (Figure 12b). The increase of the loop radius for some samples indicates a decrease of the corrosion rate, which can be related to a better passivation of these coatings compared to the initial 304L steel.

After 2 d of immersion, the diameter of the capacitive loops increases for the 304L steel substrate, $(Ti/TiO_2)\times10$ coating (Figure 12c) and $(Zr/ZrO_2)\times5$ coatings (Figure 12d), whereas the loop diameter of all other samples is almost invariant or slightly decreasing. However, when comparing to 304L steel, a higher loop radius is observed for all Zr-based and TiO_2 coatings, as was the case after 6 h of immersion. This indicates a better corrosion resistance of these samples, especially Zr-based coatings. This is due to the higher adhesion of these samples (Table 3) compared to the Ti-based ones. Moreover, another explanation could be the formation of a more stable passive ZrO_2 film in nitric acid than the Ti-based one, as is the case in air according to Ellingham diagrams [23].

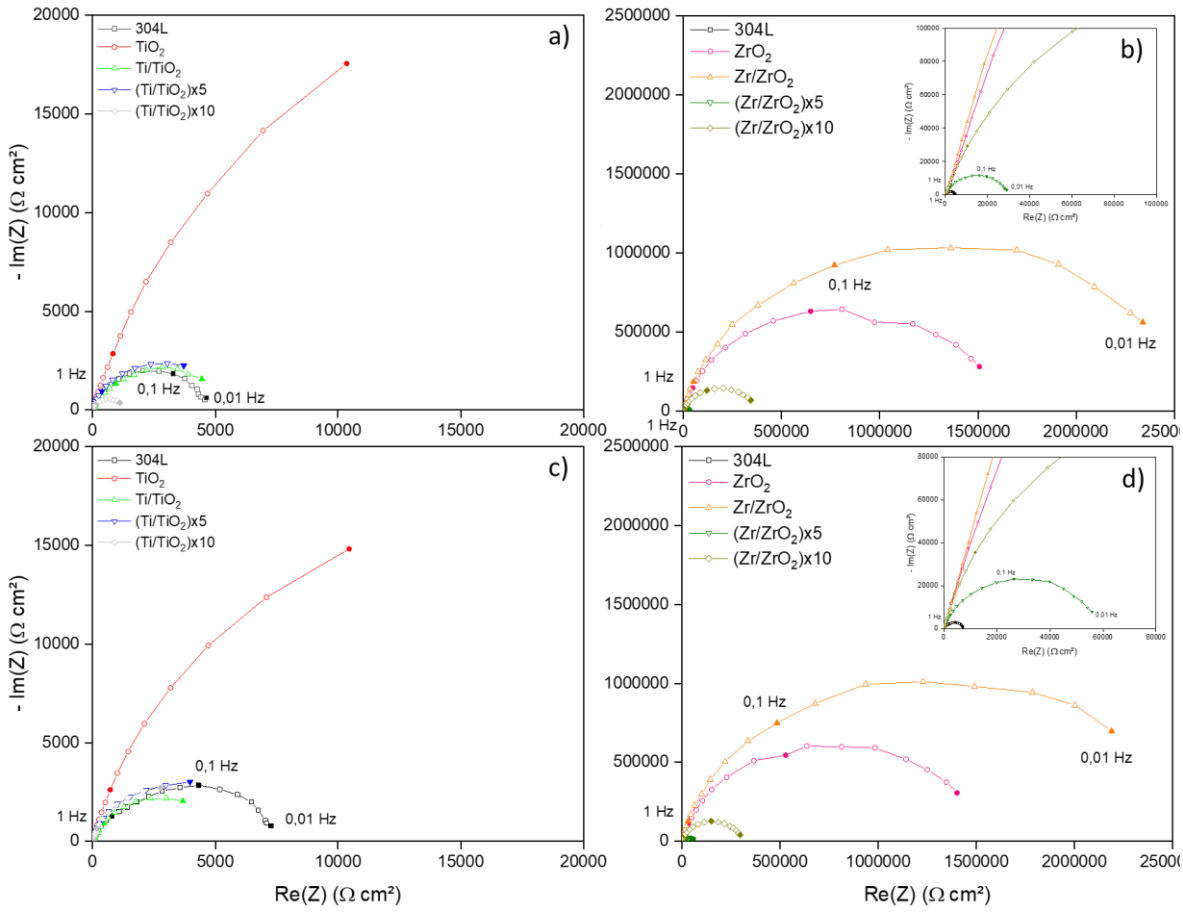

Figure 12: Nyquist diagram at open potential after 6 h for a) Ti-based, b) Zr-based coatings and after 2 d in a nitric acid (2.5 mol/L HNO_3, 2.5 mol/L $NaNO_3$ and 2 g/L $Fe(NO_3)_3$) solution at 110°C for c) Ti-based and d) Zr-based coatings.

As in the previous chapter, the EIS data can be fitted using an equivalent electrical circuit, which is shown in Figure 13. In this model, R_e is the resistance of the electrolyte, R_t is the charge transfer resistance and CPE indicates a constant phase element characterized by parameters α and Q.

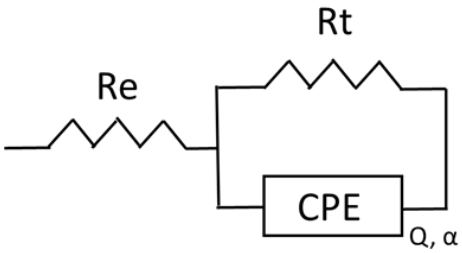

Figure 13: Equivalent electrical circuit of the initial and coated substrates in a nitric acid (2.5 mol/L HNO_3, 2.5 mol/L $NaNO_3$ and 2 g/L $Fe(NO_3)_3$) solution at 110°C.

The best-fit values obtained for the model parameters are listed in Table 5. The main differences between the initial 304L steel and the other samples lie in the values of the CPE parameters (α and Q) and the charge transfer resistance R_t, which is

associated with the capacitive loop of the Nyquist diagrams (Figure 12). Here, after 6 h in a nitric acid solution, all Zr-based and TiO_2 coatings show R_t values higher than for the 304L steel (Table 5). The high resistance values suggest an increase in corrosion resistance due to the formation of a more protective passive film [37]. This protective effect can be attributed to the modified composition of the passive layer, especially with the presence of oxidized Ti and Zr that increases the resistance in this environment. These improved properties, especially for Zr-based coatings, are explained by the high stability of the ZrO_2 film. In addition, $\alpha < 1$ for all samples, which indicates surface heterogeneities [38]. In our case, this seems rather related to surface heterogeneities because the surface of our samples is rough (Figure 8) due to the columnar structure. This is especially observed for TiO_2 and Ti/TiO_2 coatings that present the lowest α value. The CPE parameter Q_{eff} is determined using α and Im(Z) and shows the lowest values for the Zr-based coatings.

Table 5: Rt, α and Qeff values after 6 h and 2 d of immersion in a nitric acid (2.5 mol/L HNO_3, 2.5 mol/L $NaNO_3$ and 2 g/L $Fe(NO_3)_3$) solution at 110°C.

	R_t (kΩ cm²)		**α** (dimensionless)		**Q_{eff}** (s^{α}/Ω cm²)	
	6 h	2 d	6 h	2 d	6 h	2 d
304L	5	8	0.841 ± 0.015	0.822 ± 0.009	2.05×10^{-4} ± 8.77×10^{-6}	2.00×10^{-4} ± 5.52×10^{-6}
TiO_2	10	10	0.765 ± 0.012	x	7.87×10^{-4} ± 2.71×10^{-5}	x
Ti/TiO_2	4	4	0.743 ± 0.008	x	1.01×10^{-3} ± 2.47×10^{-5}	x
$(Ti/TiO_2)x5$	4	4	0.933 ± 0.008	0.858 ± 0.014	1.26×10^{-3} ± 1.05×10^{-3}	5.72×10^{-4} ± 4.41×10^{-5}
$(Ti/TiO_2)x10$	1	3	0.922 ± 0.005	0.844 ± 0.014	3.94×10^{-3} ± 2.29×10^{-3}	9.25×10^{-4} ± 3.79×10^{-5}
ZrO_2	1508	1402	0.829 ± 0.002	0.785 ± 0.004	1.15×10^{-6} ± 7.32×10^{-9}	2.27×10^{-6} ± 2.86×10^{-8}
Zr/ZrO_2	2340	2191	0.808 ± 0.004	0.765 ± 0.005	1.21×10^{-6} ± 1.27×10^{-8}	1.75×10^{-6} ± 4.71×10^{-8}

$(Zr/ZrO_2)x5$	29	56	x	x	x	x
$(Zr/ZrO_2)x10$	343	296	0.847 ± 0.002	0.824 ± 0.005	5.38×10^{-6} ± 3.73×10^{-8}	5.76×10^{-6} ± 1.53×10^{-7}

After 2 d of immersion in nitric acid at boiling temperature, similar R_t values are obtained for the initial 304L steel and TiO_2 coating, while other Ti-based coatings have lower R_t values. On the other hand, higher R_t values are obtained for all Zr-based coatings. A decrease in α with immersion time is observed for all the samples. This may be due to a change of structure of the passive film with applied potential related to chemical composition in the passive layer or to surface heterogeneity [39]. Lower Q_{eff} values (10^{-6} s^{α}/Ω cm^2) are obtained for the Zr-based coatings, especially for the Zr/ZrO_2 coated sample, compared to 304L steel. These results confirm the previous potentiodynamic polarization measurements, indicating the better corrosion resistance of the Zr-based coatings and especially Zr/ZrO_2 coating. Note that the values of the CPE parameters could not be determined for TiO_2 and Ti/TiO_2 coatings after 2 d of immersion and not at all for $(Zr/ZrO_2)\times5$ coating. This is due to the presence of a second time constant indicated by the non-linearity of the Im(Z) *vs.* frequency curve. This requires the implementation of another equivalent electrical circuit with a component associated with the presence of porosity (Appendix 3).

2.1.1.3 Characterization of the electrochemically investigated surfaces

Figure 14 shows SE micrographs and Raman spectra of the surface of the Ti-based coatings after 2 d in a nitric acid solution at boiling temperature. Blistering on the surface of all Ti-based coatings is observed after 2 days of immersion (Figure 14a). Moreover, peeling of all coatings except Ti/TiO_2 is noticed. Raman spectra obtained on different areas of the sample surfaces confirm this coating delamination by disclosing uncoated areas where the oxide signal has disappeared. The $(Ti/TiO_2)\times5$ and $(Ti/TiO_2)\times10$ coatings seem to be the most damaged after 2 d in nitric acid solution at boiling temperature, which is consistent with the previous electrochemical measurements results showing the bad corrosion resistance of the Ti-based coatings (Figure 11c).

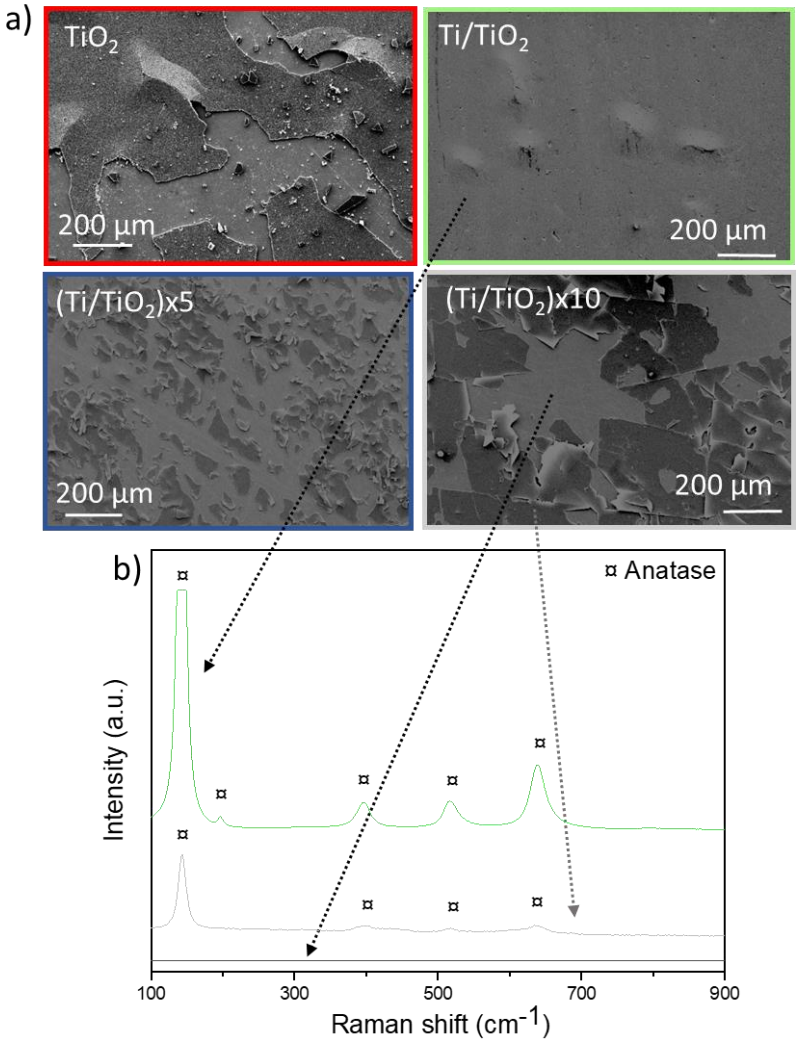

Figure 14: a) SEM-SE surface observation and b) Raman spectra of Ti-based coatings after 2 d in a nitric acid (2.5 mol/L HNO_3, 2.5 mol/L $NaNO_3$ and 2 g/L $Fe(NO_3)_3$) solution at 110°C.

In contrast to the surface observations of the Ti-based coatings, no surface changes are observed for the Zr-based coatings after 2 d of reactions and after the electrochemical measurements in nitric acid environment (Figure 15a). This is confirmed by the Raman spectra that show oxide signals everywhere after reaction (Figure 15b). These observations are consistent with the previous electrochemical measurements, indicating a better corrosion resistance of the Zr-based coatings compared to the Ti ones. Note that surface defects, such as droplets, are observed on all Zr-based coatings, which may corroborate the hypothesis of a higher defect density limiting the corrosion protection of multilayer coatings. Arcing during the deposition process, commonly encountered in reactive PVD process, may lead to the ejection of macro-particles from the sputtered target and could explain these defects. No further analysis was performed to determine the chemical composition of these droplets.

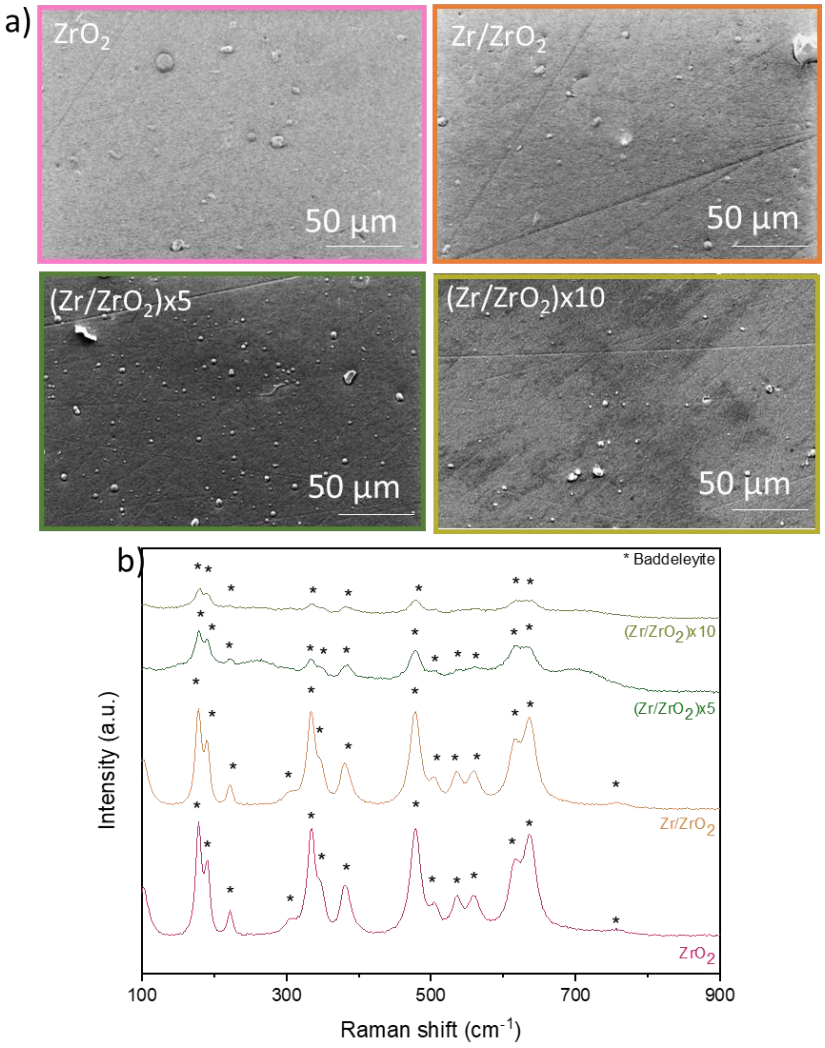

Figure 15: a) SEM-SE surface observation and b) Raman spectra of Zr-based coatings after 2 d in a nitric acid (2.5 mol/L HNO_3, 2.5 mol/L $NaNO_3$ and 2 g/L $Fe(NO_3)_3$) solution at 110°C.

BSE micrographs of the cross-section of the samples showing the best and worst corrosion resistance according to the previous electrochemical measurements are shown in Figure 16. Ti-based coatings are obviously more damaged than Zr-based ones. This confirms previous observations of the surface (Figure 14, 15), particularly the delamination of the Ti-based coatings. On the other hand, the Zr-based coatings seem intact after 2 days of immersion in nitric acid. The degradation of the Ti-based coatings is probably due to the very pronounced columnar structure that allows the electrolyte to easily penetrate the coating (Figure 16a) and/or to their poor adhesion to the substrate (Figure 16b). Another limiting effect could be the lower resistance of Ti in nitric acid environment compared to Zr.

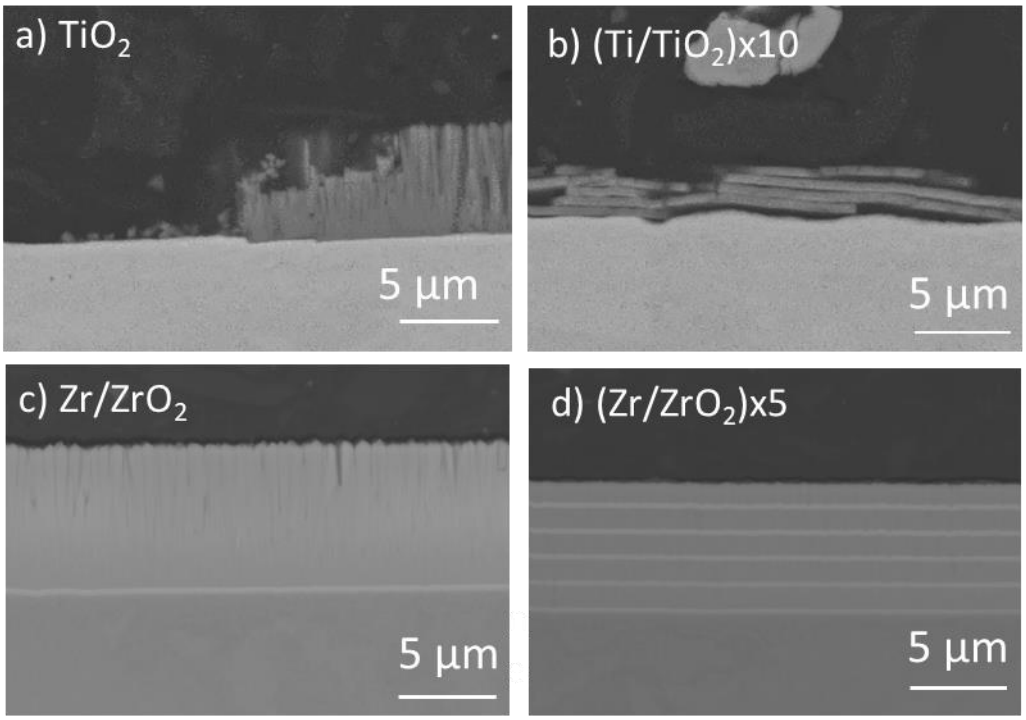

Figure 16: SEM-BSE micrographs of the cross-section of a) TiO_2, b) $(Ti/TiO_2)x10$, c) Zr/ZrO_2 and d) $(Zr/ZrO_2)x5$ after 2 d in a nitric acid (2.5 mol/L HNO_3, 2.5 mol/L $NaNO_3$ and 2 g/L $Fe(NO_3)_3$) solution at 110°C.

In conclusion, potentiodynamic measurements indicate that the Zr-based coatings show a better corrosion resistance in nitric acid compared to 304L steel and Ti-based coatings. In fact, all the Ti-based coatings show a J_{corr} value of the same order of magnitude as the 304L steel (10^{-4} mA/cm^2), whereas J_{corr} is quite lower for the Zr-based coatings (10^{-5}-10^{-6} mA/cm²) and similar to Ta materials (coating and bulk). These results are confirmed by EIS measurements, where the Zr/ZrO_2 coating shows the best corrosion resistance. The poor corrosion resistance of Ti-based coatings can be explained by their poor adhesion on the substrate and/or their columnar structure that do not prevent the electrolyte from reaching the substrate and can also cause galvanic coupling. On the contrary, Zr-based coatings have high adhesion properties and can act as a barrier against the electrolyte penetration due to a dense and stable ZrO_2 layer, which enhances corrosion resistance. This is especially observed for the Zr/ZrO_2 coating, while multilayer coatings do not offer a better corrosion resistance contrary to what might be expected. The characterization of the electrochemically investigated surfaces confirms these observations by showing undamaged Zr-based coatings compared to Ti-based ones. Blistering of all Ti-based coatings is observed, leading to delamination of the coatings except for Ti/TiO_2 coating. In the case of Zr-based coatings, only surface defects related to deposition process but no surface changes are observed. These electrochemical results showing the improved corrosion resistance of Zr-based coatings are encouraging considering that the coating systems are not optimized.

2.1.2 Immersion tests

2.1.2.1 Weight and thickness variations

Figure 17 shows the results of the immersion tests performed in a nitric acid solution at boiling temperature. The weight loss (Figure 17a) is calculated by weighing the samples before and after immersion. The solution used for the immersion tests (2.5 mol/L HNO_3, 2.5 mol/L $NaNO_3$ and 2 g/L $Fe(NO_3)_3$) was renewed at each period (every 24 h until 5 d and then every 48 h until 9 d) in order not to accumulated corrosion products and impact the behavior of the studied samples. Note that Ta coating were deposited using HiPIMS process by DEPHIS company. It is immersed as a comparison material because it is also studied for use in nitric acid to increase components lifespan. Considering a homogeneous dissolution of the material, a thickness loss can be estimated (Figure 17b). The exposed surface to the nitric acid solution during these immersion tests is 1 cm^2 and the density used is that of 304L (7.93 g/cm^3), Ta (16.69 g/cm^3) and ZrO_2 (5.68 g/cm^3). Then, the corrosion rate (µm/year), for a linear evolution of the weight loss, can be estimated from the thickness loss calculation (see section 3.2.1 of the previous chapter).

First, 5-d immersion tests were performed and then the sample showing a better corrosion resistance and the reference samples were immersed for an additional 4 d to reach a total duration of 9 d. The weight loss reached after 9 d of immersion is lower for the Zr/ZrO_2 coating (36 ± 4 mg/dm^2) than the Ta coating (71 ± 3 mg/dm^2) and the initial 304L steel (98 ± 3 mg/dm^2). The estimated thickness loss is lower for the Ta coating than for the Zr/ZrO_2 coating due to the higher density of Ta compared to that of ZrO_2. However, they are still very low compared to the 304L steel substrate. This suggests an improved corrosion resistance for these coatings that is consistent with the electrochemical results presented previously (Figure 11).

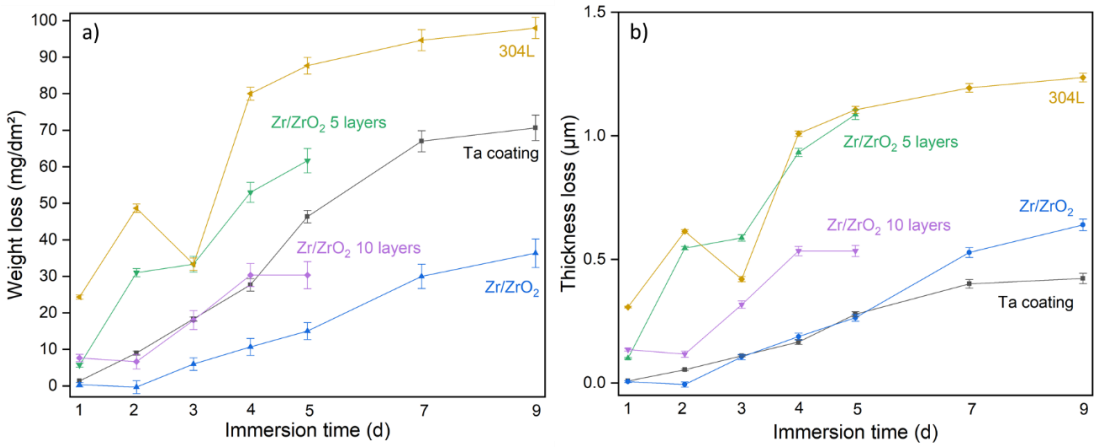

Figure 17: a) Weight loss measurements and b) thickness loss estimation after 5 and 9 d of immersion in a nitric acid (2.5 mol/L HNO_3, 2.5 mol/L $NaNO_3$ and 2 g/L $Fe(NO_3)_3$) solution at 110°C.

In this case, the evolution of the weight loss is not linear for the 304L ASS. In fact, 304L appears to show a parabolic curve rather than a linear one as observed in the previous chapter (see Figure 34). This shows that the corrosion rate decreases with time, which could be due to the formation of a more protective oxide layer on the 304L

surface. On the other hand, the evolution of the weight loss seems to be linear pour the Ta and Zr/ZrO_2 coatings. In addition, the SEM observations (Figure 18) show a homogeneous dissolution, therefore the corrosion rate can be estimated for the Ta and Zr/ZrO_2 coatings. The calculated corrosion rate indicates a value of 26 µm/year for Zr/ZrO_2 coating and 17 µm/year for Ta coating. Note that the corrosion rate values calculated are qualitative as they are limited to a uniform corrosion process and may be overestimated due to the surface roughness of our samples (Figure 8), which can increase the area exposed to the electrolyte and also create local cavities. Longer immersion tests would be necessary to confirm these tendencies for longer durations.

2.1.2.2 Characterization of the immersed samples

Figure 18 shows BSE micrographs of the surface of the immersed samples after 9 d of immersion in a nitric acid solution at boiling temperature. Only these three samples were observed in SEM to compare the effects on the surface after the same immersion time *i.e.* 9 d. The surface of the 304L steel shows grain boundaries that appear to be hollowed out (Figure 18a) compared to the other samples. Intergranular corrosion, *i.e.* preferential corrosion along the grain boundaries, is the form of localized corrosion observed for 304L ASS in nitric acid in sufficiently oxidizing conditions to allow the steel to reach its transpassive domain [40, 41]. This intergranular corrosion occurs uniformly on the surface of the material and is related to the oxidizing ability of the medium and to the preferential sensitivity of the grain boundaries which can be attributed to a specific chemical composition of the grain boundary or to a particular crystalline structure. The SEM analysis suggests the beginning of grooves formation after immersion in boiling nitric acid environment. The finer analysis of these grooves in terms of angle and depth could allow the determination of the specific corrosion rates of the grain boundary and of the grain surface. On the other hand, the coatings surfaces do not show grain boundaries but some particles and cracks are observed (Figure 18b, c), which could explain the significant corrosion rates measured (26 µm/year for Zr/ZrO_2 coating and 17 µm/year for Ta coating).

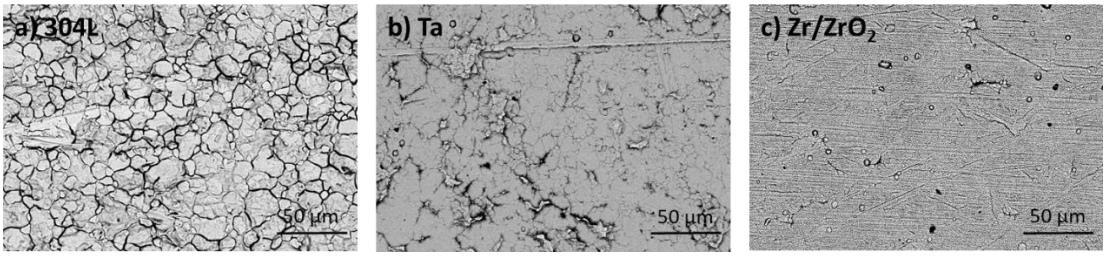

Figure 18: SEM-BSE observation of the surface of a) initial 304L steel, b) Ta and c) Zr/ZrO_2 coatings after 9 d in a nitric acid (2.5 mol/L HNO_3, 2.5 mol/L $NaNO_3$ and 2 g/L $Fe(NO_3)_3$) solution at 110°C.

Cross-sections of these three samples are performed to complete the surface analysis (Figure 19). The observation of the initial 304L steel shows intergranular attack grooves (Figure 19a). The Ta coating does not seem to be damaged but cavities are observed between the coating and the susbtrate, indicating that the electrolyte may have reached the substrate despite the Ta coating (Figure 19b). This can explain the previous measured corrosion rate (17 µm/year). On the other hand, the Zr/ZrO_2 coating shows defects and lack of material near the surface due to the electrolyte intrusion and dissolution of part of the coating (Figure 19c). However, the coating still

appears dense near the substrate and there are no apparent cavities as for the Ta coating. This could be due to the presence of the metallic bond coat, which allows better adhesion properties of this coating on the 304L ASS. These results show the ability of the Zr/ZrO_2 coating to improve corrosion resistance due to the inertness and stability of ZrO_2 in nitric acid [4]. Despite the beginning of damage after 9 d of immersion, it seems to keep its barrier property against the electrolyte penetration. The corrosion resistance properties of this coating could be improved by optimizing the parameters of the deposition process.

The thicknesses of the Ta and Zr/ZrO_2 coatings after 9 d of immersion in the boiling nitric acid solution are calculated from the weight loss and show values of 4.83 ± 0.24 µm and 5.85 ± 0.38 µm, respectively. Comparing these values with the initial thicknesses of the two coatings, thickness losses of 0.52 µm for Ta and 0.36 µm for Zr/ZrO_2 coatings are observed, which are in the same order to magnitude than the values estimated by the immersion tests i.e. 0.42 µm and 0.64 µm, respectively (Figure 14).

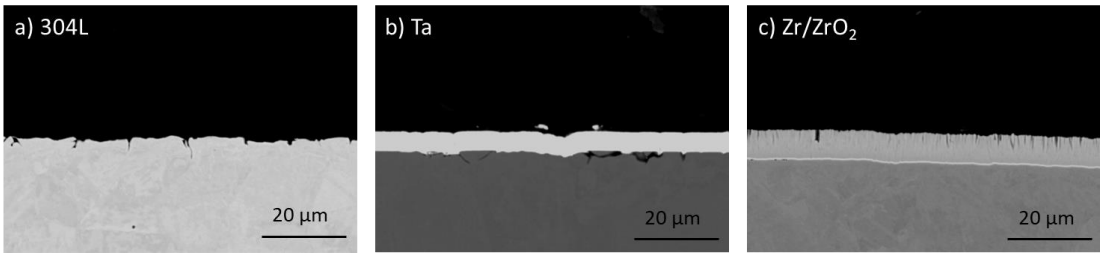

Figure 19: SEM-BSE micrographs of the cross-section of a) initial 304L steel, b) Ta and c) Zr/ZrO_2 coatings after 9 d in a nitric acid (2.5 mol/L HNO_3, 2.5 mol/L $NaNO_3$ and 2 g/L $Fe(NO_3)_3$) solution at 110°C.

The immersion tests confirm that the Zr/ZrO_2 coating could be a promising candidate for improving the corrosion resistance of 304L ASS. It shows a thickness loss lower than that of 304L and close to that of Ta, which is the solution currently studied to enhance corrosion protection in nitric acid. Moreover, the characterization of the immersed samples confirms these observations by showing an undamaged surface of the Zr/ZrO_2 coating compared to 304L where intergranular corrosion is observed. However, some particles and cracks are noticed at the coating surface, which can lead to a higher corrosion rate by increasing the surface area exposed to nitric acid solution. In addition, some defects and lack of material near the surface are observed, probably due to the electrolyte penetration and dissolution of part of the coating, Nonetheless, the Zr/ZrO_2 coating is dense and appears to continue to protect against corrosion after 9 d of immersion.

To sum up, corrosion investigations in nitric acid at boiling temperature show that Zr-based coatings are promising candidates for increasing the lifespan of 304L ASS, specifically the Zr/ZrO_2 coating that still protects effectively after 9 d of immersion. As these coatings are not optimized, it would be possible to further improve their corrosion resistance by studying the process parameters more precisely. In contrast, optimizations of Ti-based coatings are needed to improve their structure and adhesion in order to reconsider them as solutions to enhance initial 304L sustainability.

2.2 CORROSION IN SODIUM CHLORIDE (NACL) ENVIRONMENT

2.2.1 Electrochemical measurements

The potentiodynamic polarization curves of the 304L steel and Ti- and Zr-based coatings in 3.56 wt.% NaCl solution at ambient temperature after 6 h of immersion are shown in Figure 20. Bulk Ti has also been investigated to compare with our architectural coating systems. Table 6 shows that E_{corr} value for the 304L steel equals 0.14 V/SHE after 6 h in NaCl. As a comparison, E_{corr} of the Ti-based coatings is shifted toward positive values (Figure 20a), whereas a shift toward negative values is observed for E_{corr} of bulk Ti and Zr-based coatings (Figure 20b). The observed dispersion of E_{corr} could be explained by the non stabilization of the potential after 6 h due to kinetic limitations.

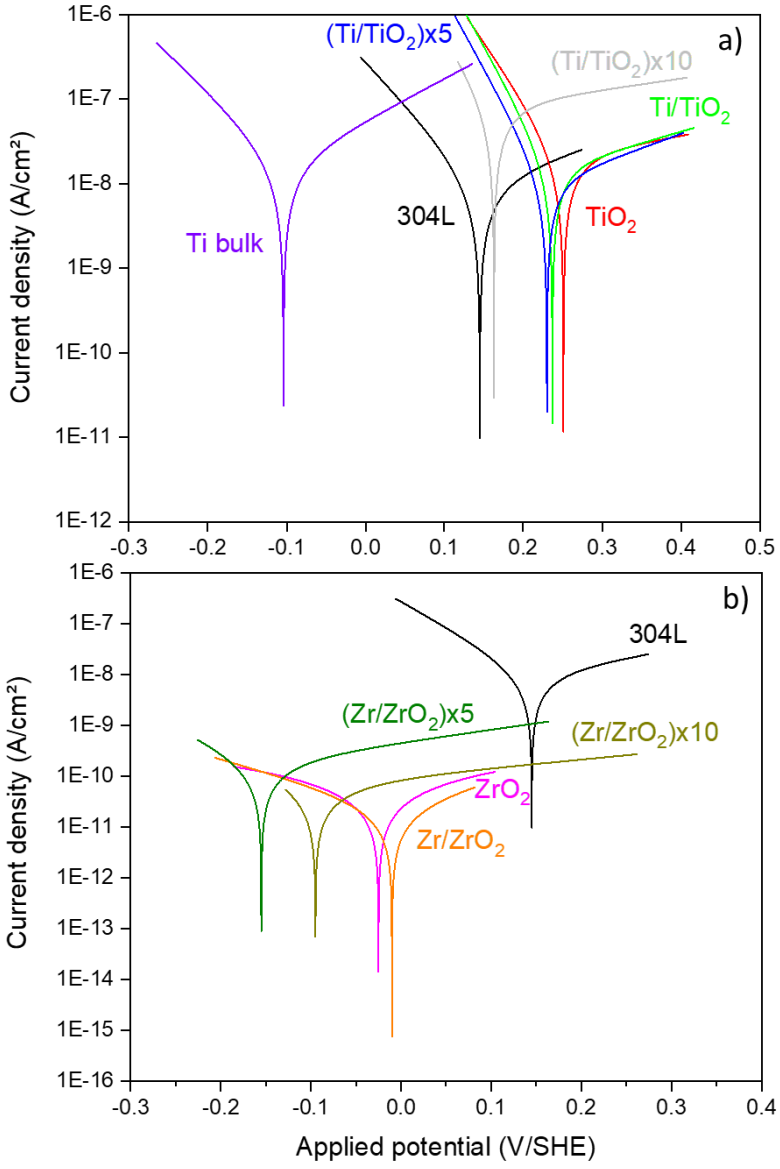

Figure 20: Potentiodynamic polarization curves of the initial 304L steel and coated samples in a 3.56 wt.% NaCl solution at ambient temperature after 6 h for a) Ti-based and b) Zr-based coatings.

The effect of coatings is observed on the corrosion currents. After 6 h of immersion, J_{corr} for the Zr-based coatings decreases by at least two orders of magnitude, down to 1-3×10^{-11} A/cm² ((Zr/ZrO_2)×5 and (Zr/ZrO_2)×10 coating) and 8-9×10^{-12} A/cm² for ZrO_2 and Zr/ZrO_2 coatings compared to 3×10^{-9} A/cm² for 304L steel (Figure 20b). However, J_{corr} for the Ti-based coatings is similar to the initial 304L steel (2-3×10^{-9} A/cm²) or even higher for (Ti/TiO_2)×10 coating (1×10^{-8} A/cm²). As a comparison, bulk Ti shows a J_{corr} value of 6×10^{-9} A/cm², which is in the same order of magnitude as the 304L steel (Table 6). These values are lower than the values observed for a carbon steel coated by TiO_2 in 3 %NaCl solution (8×10^{-6} A/cm²) [42] and those noticed for ZrO_2 coating on low carbon steel in 3.5 % NaCl solution (8.65×10^{-5} A/cm²) [43].

Table 6: Corrosion potential (E_{corr}) and current density (J_{corr}) values after 6 h of immersion in a 3.56 wt.% NaCl solution at ambient temperature.

	E_{corr} (V/SHE)	**J_{corr}** (A/cm²)
304L	0.14	3×10^{-9}
TiO_2	0.25	3×10^{-9}
Ti/TiO_2	0.24	2×10^{-9}
(Ti/TiO_2)x5	0.23	2×10^{-9}
(Ti/TiO_2)x10	0.16	1×10^{-8}
ZrO_2	-0.02	9×10^{-12}
Zr/ZrO_2	-0.01	8×10^{-12}
(Zr/ZrO_2)x5	-0.16	3×10^{-11}
(Zr/ZrO_2)x10	-0.09	1×10^{-11}
Ti bulk	-0.10	6×10^{-9}

The results indicate that the behavior of bulk Ti and Ti-based coatings in NaCl solution is close to that of the initial 304L steel. These results differ from the literature, where TiO_2 acts as a protective barrier on the steel surface in NaCl [44]. The limited corrosion resistance of our Ti-based coatings may be due to their pronounced columnar structure (Figure 2) and/or the presence of defects that do not prevent the electrolyte from reaching the 304L substrate. On the other hand, the Zr-based coatings show good corrosion resistance compared to initial 304L and Ti-based coatings. As in nitric acid, ZrO_2 and Zr/ZrO_2 offer a better protection against corrosion than multilayer coatings, probably due to smaller defect density and reduced stresses.

Figure 21 shows BSE micrographs of the cross-sections for the samples with the best and worst corrosion resistance according to the electrochemical measurements in 3.56 wt.% NaCl. All coatings appear undamaged compared to nitric acid environment (Figure 14, 15). This indicates that the better corrosion resistance of the Zr-based coatings is due to its structure and/or composition. As shown previously, these coatings are denser than the Ti-based ones, which limits the electrolyte penetration into the coating. Another explanation is a better stability of ZrO_2 in NaCl environment. The expected corrosion process in NaCl solution is pitting, but no pitting is observed on the sample surfaces compared to 304L steel and samples presented in the previous chapter.

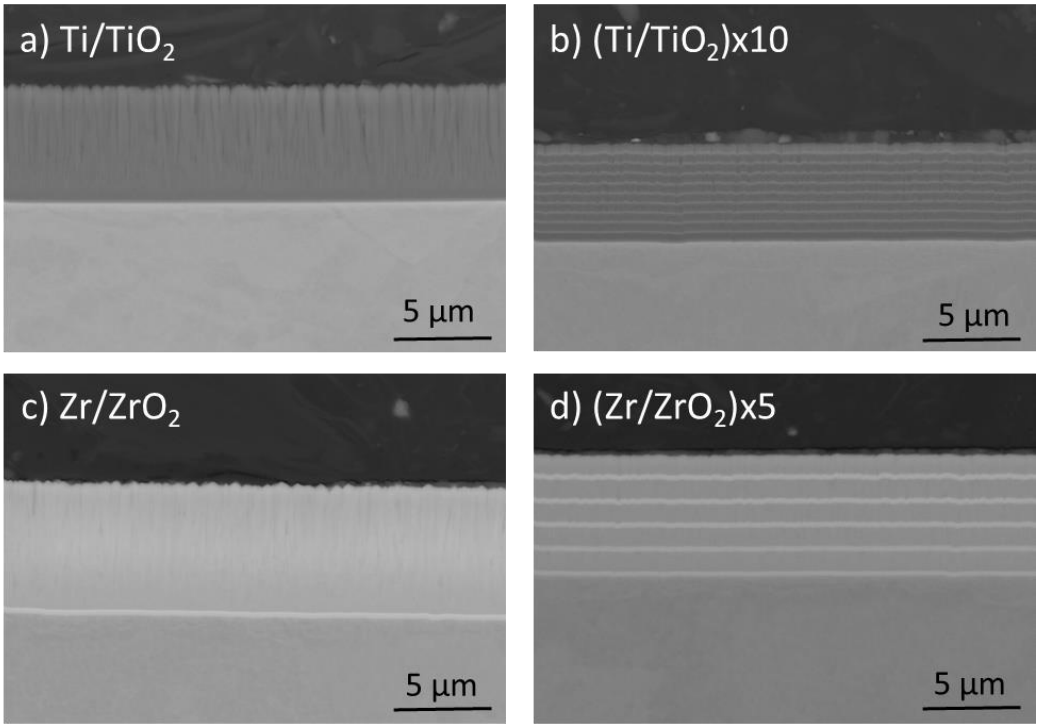

Figure 21: SEM-BSE micrographs of the cross-section of a) Ti/TiO_2, b) $(Ti/TiO_2)\times10$, c) Zr/ZrO_2 and d) $(Zr/ZrO_2)\times5$ coatings after electrochemical measurements in a 3.56 wt.% NaCl solution at ambient temperature.

EDX line scans of the cross-sections of the samples with the best and worst corrosion resistance according to the electrochemical measurements in 3.56 wt.% NaCl are shown in Figure 22. Due to the lack of standard calibration sample, the absolute concentration of the individual elements is not measurable. Nevertheless, the intensity variations of each element are reliable. No obvious difference is observed between the samples before (Figure 3, 6) and after immersion in 3.56 wt.% NaCl solution at ambient temperature, which indicated that the coatings are not damaged. The O enrichment of the coating at the extreme surface observed before immersion is due to the affinity of Ti and Zr with O when removed from the deposition machine and exposed to air, forming a stable oxide in contact with air (Figure 3, 6). This enrichment is still present or even amplified (higher intensity of O) after immersion in 3.56 wt.% NaCl solution, which can indicate the presence of a passive oxide film on the surface of the coatings.

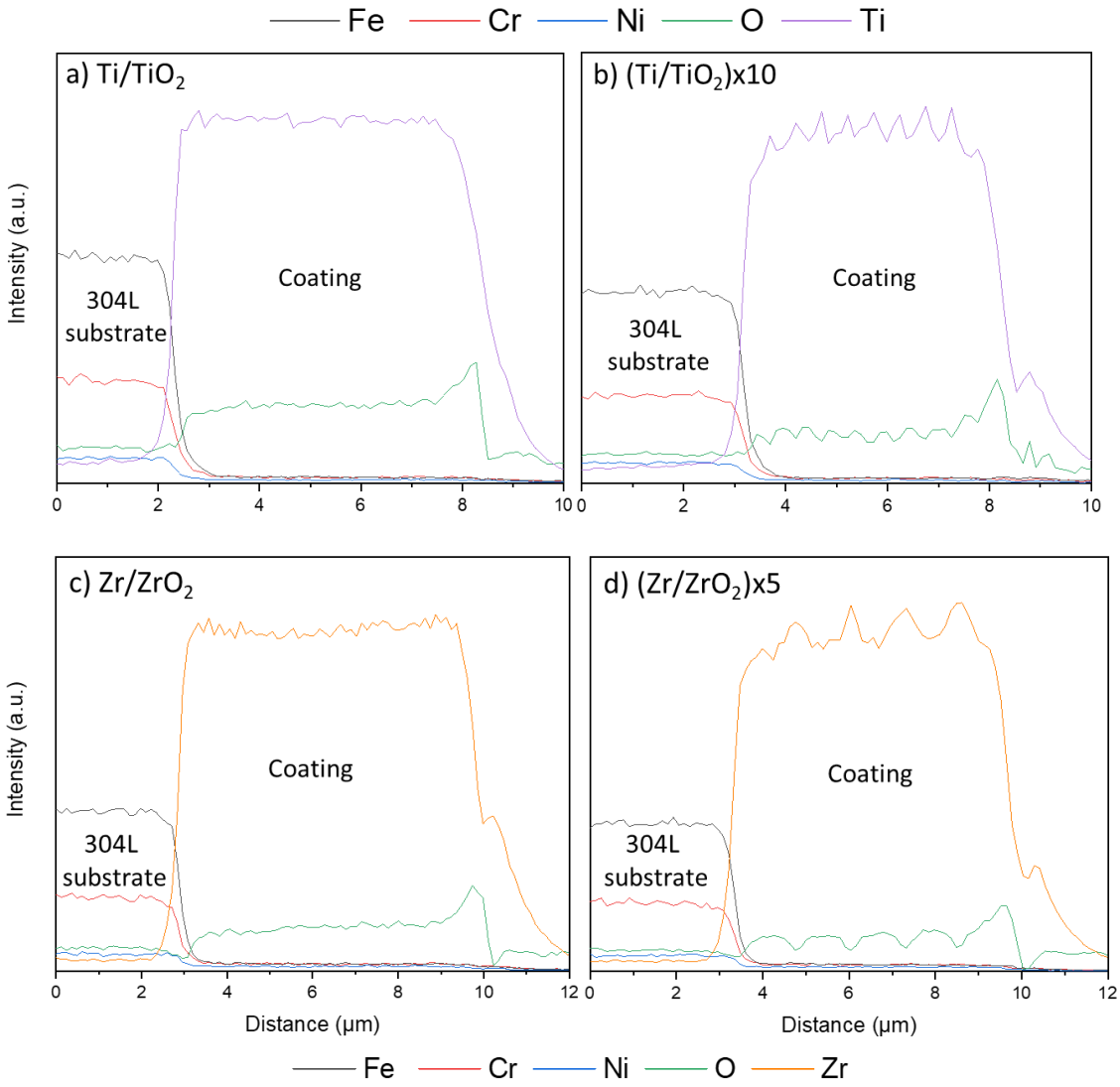

Figure 22: EDX line scans of cross-sections of a) Ti/TiO_2, b) $(Ti/TiO_2)x10$, c) Zr/ZrO_2 and d) $(Zr/ZrO_2)x5$ coatings after electrochemical measurements in a 3.56 wt.% NaCl solution at ambient temperature.

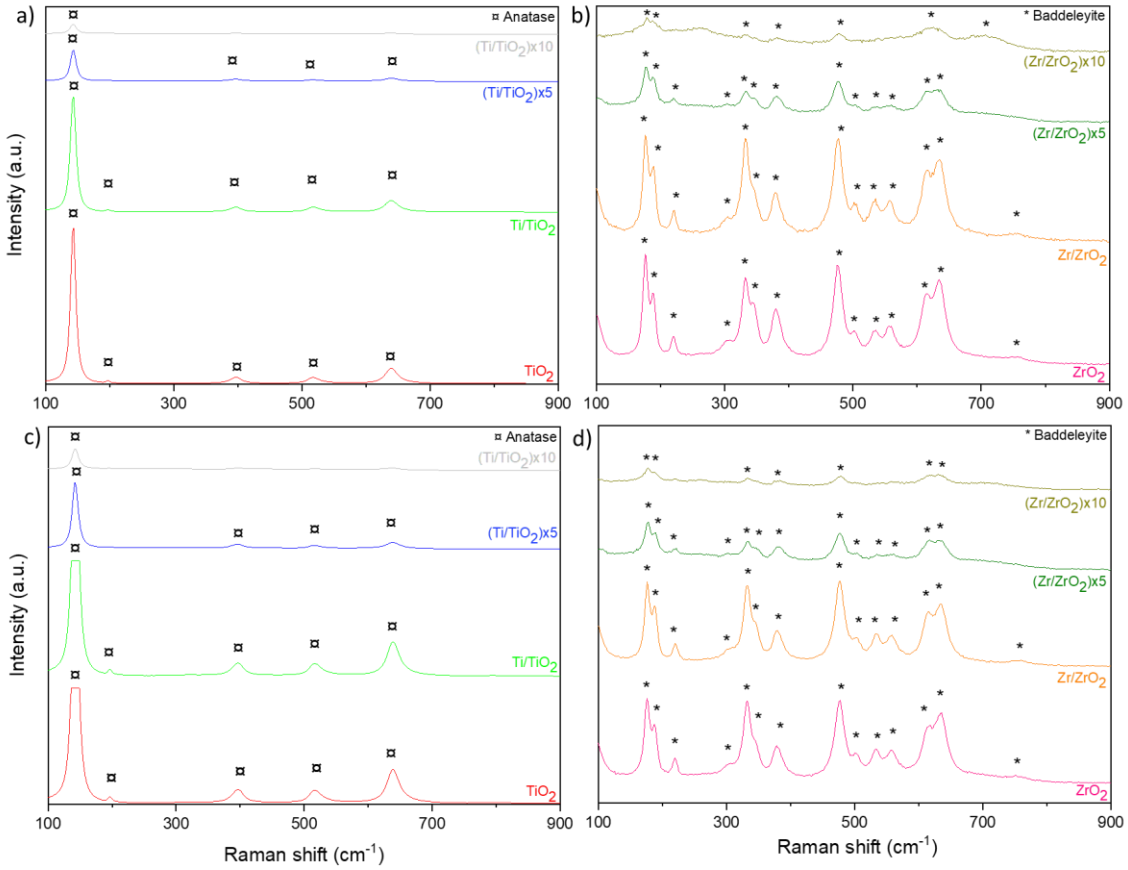

Figure 23: Comparison of Raman spectra before electrochemical measurements for a) Ti-based and b) Zr-based coatings and after electrochemical measurements in a 3.56 wt.% NaCl solution at ambient temperature for c) Ti-based and d) Zr-based coatings.

Raman spectra performed for the Ti-based and Zr-based coatings before and after electrochemical measurements in 3.56 wt.% NaCl solution at ambient temperature are shown in Figure 23. Contributions from anatase are detected before (Figure 23a) and after (Figure 23c) immersion in 3.56 wt.% NaCl solution for the Ti-based coatings. On the other hand, baddeleyite contributions are observed for the Zr-based coatings before (Figure 23b) and after (Figure 23d) electrochemical measurements in 3.56 wt.% NaCl. Thus, there are no difference observed between the spectra before and after electrochemical measurements for Ti- and Zr-based coatings. These results are consistent with the previous SEM observations, showing that all the coatings are undamaged.

In conclusion, as previously observed in nitric acid, Zr-based coatings improve the corrosion resistance properties of the 304L substrate in 3.56 wt.% NaCl solution at ambient temperature compared to Ti-based coatings. The Ti-based coatings show higher J_{corr} values (10^{-9} A/cm²) than those of the metal ion-etched samples (Ti^+ and Zr^+) and, the Ti^+-etched and Ti-coated sample (10^{-10} A/cm²), which confirms their limited corrosion resistance. On the contrary, the Zr-based coatings indicates lower J_{corr} values (10^{-11}-10^{-12} A/cm²) than all the etched and, etched and coated samples studied in the previous chapter. This shows that Zr-based coatings are promising candidates for enhancing the 304L steel lifespan. Moreover, no pitting corrosion was observed on our thick Ti- and Zr-based coatings (5-7 µm) compared to the etched

(few nm) and, etched and coated ones (200 nm). Noting that these Ti- and Zr-based coatings systems could be optimized by modifying process parameters to further increase their corrosion resistance.

2.2.2 Immersion tests

Immersion tests were performed in natural seawater to study the corrosion resistance of our architectural coating systems under conditions similar to service conditions. For this purpose, two seawaters were considered: Singapore natural seawater at an average temperature of 29-30 °C, and Cherbourg natural seawater at an average temperature of 12 °C.

2.2.2.1 Immersion in Singapore seawater

Figure 24a shows the evolution in thickness of the samples immersed for 60 d in Singapore natural seawater. This thickness measurement is performed with a caliper every 15 d when the samples were taken out of the water and inspected. The results indicate a lower initial thickness for TiO_2 and Ti/TiO_2 coatings due to re-polishing of the substrates before deposition, as explained in section 1.3. Therefore, the final thickness of these two samples is also smaller than for the others. As a general trend, the thickness of the samples increases with an increasing immersion time. The higher thickness variation is observed for the 304L steel (0.09 mm), while the lowest are noticed for ZrO_2, Zr/ZrO_2 and $(Zr/ZrO_2)\times10$ coatings (0.02 mm). This suggests the formation of a thicker compound on the surface of 304L than coated samples, which could be a biofilm or corrosion products (such as rust). Therefore, it can be assumed that the coatings decrease their formation on the surface.

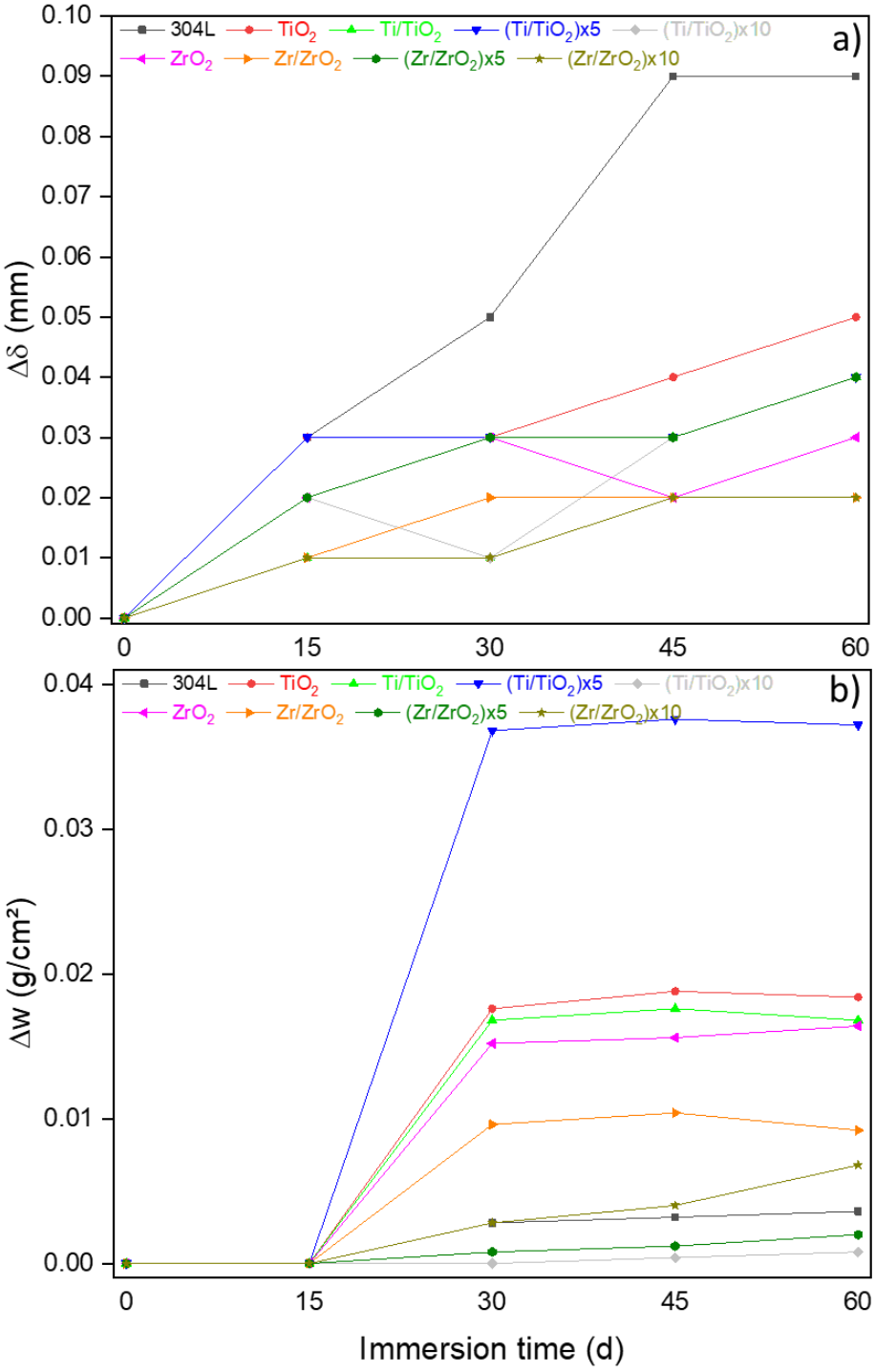

Figure 24: a) Thickness and b) weight variation of 304L steel and metal oxide-based coatings after 60 d of immersion in Singapore natural seawater.

The weight variation of the samples during the 60 d of immersion in Singapore seawater is shown in Figur 24b. As previously observed, the weight change between the initial and final immersion time. There is no net gain observed between 0 and 15 d for all samples. Weight gain increased mostly between 15 and 30 d of immersion and then, continued to increase at a lower rate or tends to stabilize over time depending on the sample studied. The higher weight variation is observed for

(Ti/TiO_2)×5 coating (0.0372 g/cm²), whereas the lowest are noticed for (Ti/TiO_2)×10 and (Zr/ZrO_2)×5 coatings (0.0008 and 0.0020 g/cm², respectively). These results differ from those obtained for thickness measurements, indicating that further observation of the samples is required to conclude on the improved corrosion resistance properties.

Figure 25 shows the visual inspections (macro images) of the samples, done every 15 d during the 60 d of immersion in Singapore seawater. After a short immersion time (15 d), the surface of initial 304L steel seems to be covered with dark deposits. The prolonged immersion time (60 d) leads to an increase of corrosion of the 304L steel, affecting the entire surface at the end. In the case of coated samples, corrosion seems to begin after longer immersion times, *i.e.* after 30 d for (Ti/TiO_2)×5 coating and 45 d for TiO_2, Ti/TiO_2, (Ti/TiO_2)×10 and (Zr/ZrO_2)×5 coatings. Moreover, corrosion seems to start near the edges of the sample or the suspension hole, which could be due to a lack of protection (varnish) in these areas. Nonetheless, there is no obvious deterioration indicating corrosion progress for the surface of ZrO_2, Zr/ZrO_2 and (Zr/ZrO_2) ×10 coatings after 60 d of immersion in Singapore seawater. This suggests that these three coatings improve corrosion resistance, probably by limiting the penetration of seawater into the substrate/coating system. These results are consistent with the thickness variation measurements mentioned above (Figure 24).

	Immersion time				
Samples	t = 0	t = 15 days	t = 30 days	t = 45 days	t = 60days
304L					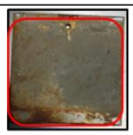
TiO_2					
Ti/TiO_2					
(Ti/TiO_2)x5		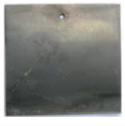			
(Ti/TiO_2)x10				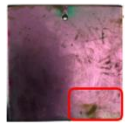	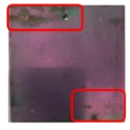

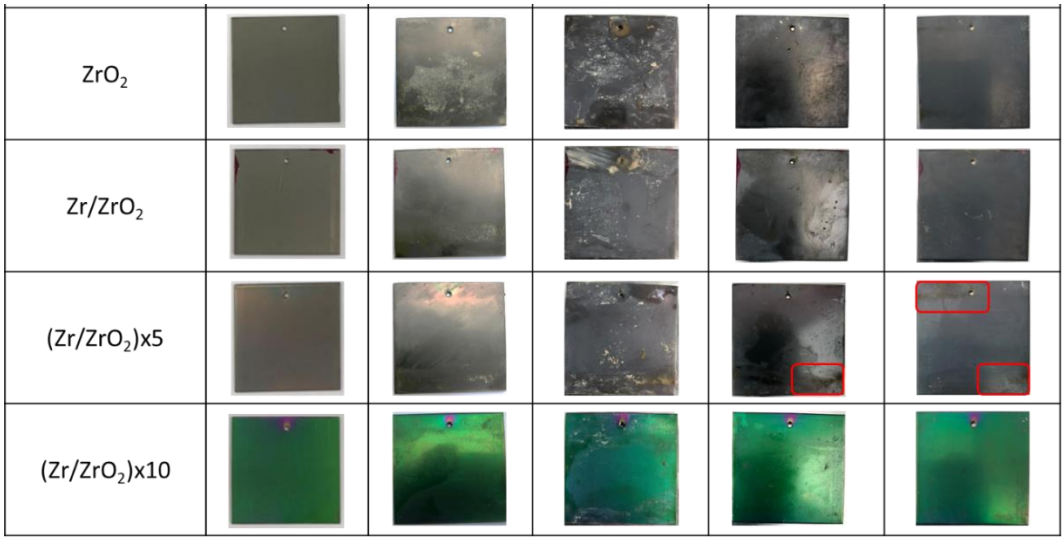

Figure 25: Visual inspection of 304L steel and metal oxide-based coatings each 15 d during the 60 d of immersion in Singapore natural seawater.

In conclusion, ZrO_2, Zr/ZrO_2 and $(Zr/ZrO_2)\times10$ coatings seem to provide a better corrosion protection after 60 d of immersion in Singapore seawater, according to thickness measurements and visual observations. This is consistent with the electrochemical measurements, indicating a better corrosion resistance of the Zr-based coatings. Nevertheless, additional studies are required and planned to understand the corrosion mechanism and characterize the deposited coatings in more detail when the samples return from Singapore.

2.2.2.2 Samples immersed in Cherbourg natural seawater

The immersion tests in Cherbourg natural seawater were performed only for Ti/TiO_2 coating as the electrochemical measurements show a lower current density for this sample compared to other Ti-based coatings (Figure 20). Moreover, for the Zr-based coatings, they were all immersed in this medium except ZrO_2, which presents similar properties (structure and corrosion resistance) to Zr/ZrO_2 coating. The monitoring of the evolution of the corrosion potential as a function of immersion time for 304L steel, Ti/TiO_2, Zr/ZrO_2, $(Zr/ZrO_2)\times5$ and $(Zr/ZrO_2)\times10$ coatings is shown in Figure 26. The curve obtained for the 304L steel shows an increase in potential from 0.141 V/SHE up to 0.409 V/SHE, which is consistent with the literature [45, 46]. Then, the potential drops to 0.041 V/SHE and increase slightly again, stabilizing at about 0.121 V/SHE after 56 d of immersion in natural seawater. A similar trend is observed for the metal ion-etched samples, with an increase in potential (up to 0.169 V/ECS for Zr^+-etched and 0.288 V/ECS for Ti^+-etched samples), then a decrease (down to -0.155 V/ECS for Zr^+-etched and -0.144 V/ECS for Ti^+-etched samples) and finally a stabilization around -0.120 V/ECS. Moreover, an increase in corrosion potential is visible (up to 0.273 V/ECS for Ti^+-etched and Ti-coated and 0.168 V/ECS for Zr^+-etched and Zr-coated samples) followed by a decrease tending towards a stabilization around -0.170 V/ECS for Ti^+-etched and Ti-coated and -0.099 V/ECS for Zr^+-etched and Zr-coated samples. To sum up, the etched and, etched and metallic bond coat-deposited samples show evolution in corrosion potential similar to that of initial 304L steel in Cherbourg natural seawater (previous chapter). However, a different trend is observed for Ti- and Zr-

based coatings, showing no potential drop (Figure 26). In fact, the immersed samples show either a slight increase followed by a faster increase (Ti/TiO_2, $(Zr/ZrO_2)\times5$ and $(Zr/ZrO_2)\times10$ coatings) or a stagnation of the potential (Zr/ZrO_2 coating) over the immersion time. Note that for the Zr/ZrO_2 and $(Zr/ZrO_2)\times5$ coatings a decrease is observed after 4 d of immersion before the increase or stagnation of the corrosion potential.

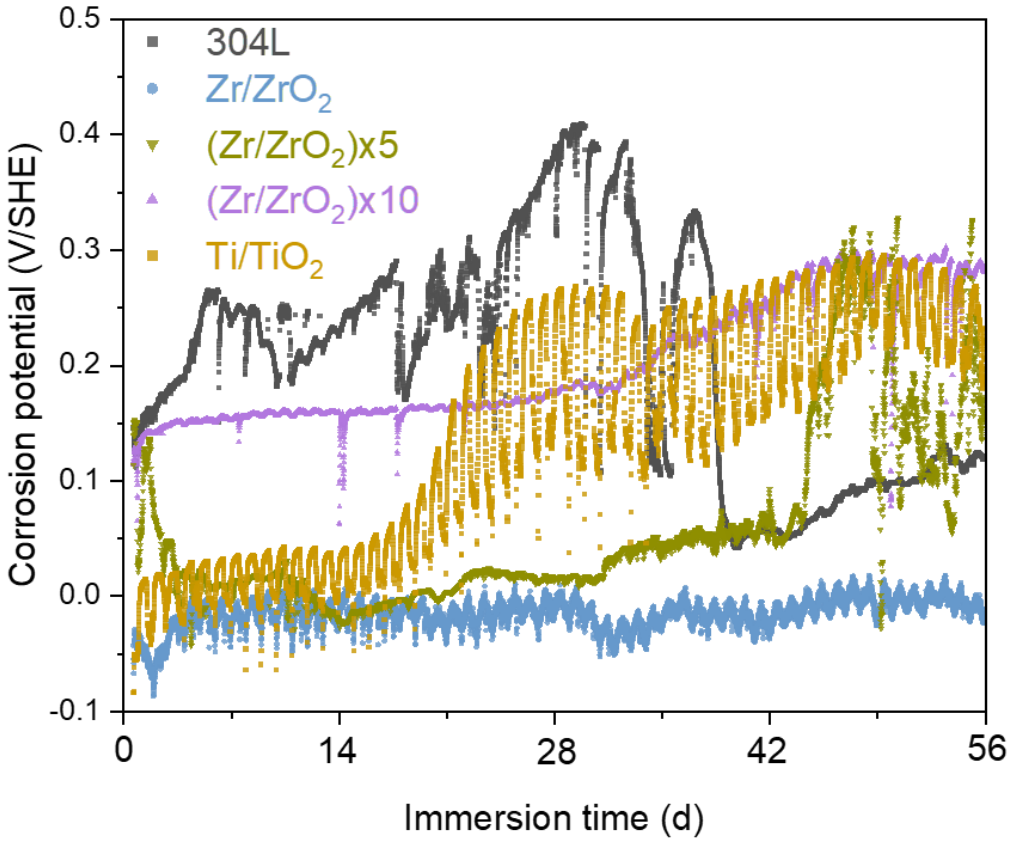

Figure 26: Monitoring of the corrosion potential vs. immersion time in natural seawater in Cherbourg for architectural systems.

The evolution of the corrosion potential shows oscillations with a period of 24 h, which is attributed to temperature fluctuation during the diurnal cycle (lower temperature during the night) [45]. The tendency for the corrosion potential to stabilize over time is attributed to the stability of the material in the tested environment, which may result in better corrosion resistance compared to 304L steel.

Microbiological analyses were performed on the biofilm collected from the surface of the samples to study their antifouling properties. The population density is relatively similar for all the samples in the order of 1×10^7 microorganisms/cm². Figure 27 shows the total microalgae biomass and total aerobic heterotrophic flora (viable and cultivable microbial communities) counted after 56 d of immersion in Cherbourg natural seawater. The total microalgae biomass (Figure 27a) is lower for all coatings compared to the 304L steel (1.1×10^5 microorganisms/cm²), especially for $(Zr/ZrO_2)\times5$ and $(Zr/ZrO_2)\times10$ coatings (6.5×10^3 and 1.3×10^4 microorganisms/cm², respectively). This differs from the results obtained for the etched samples where Ti^+-etched sample

showed a higher total microalgae biomass value than the initial 304L. On the other hand, the total aerobic heterotrophic flora (Figure 27b) is lower for all coatings compared to the 304L steel (5.7×10^4 UFC/cm²), especially for Ti/TiO_2 and $(Zr/ZrO_2)\times10$ coatings (3.3×10^3 UFC/cm² and 1.3×10^3 UFC/cm², respectively). Different results were observed previously with a higher value of total aerobic heterotrophic flora for Zr^+-etched and, Ti^+-etched and Ti-coated samples compared to initial 304L. The results of Ti- and Zr-based oxide coatings indicate a better antifouling behavior against microalgae and bacteria for these samples compared to initial 304L steel.

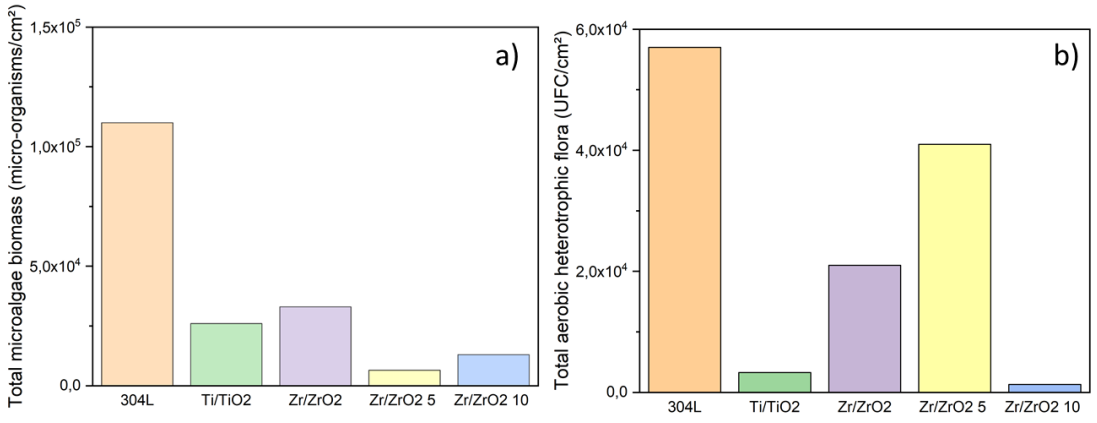

Figure 27: Results of microbiological analyses indicating the a) total microalgae biomass and b) total aerobic heterotrophic flora after 56 d of immersion in Cherbourg natural seawater for architectural systems.

The antifouling behavior of Ti/TiO_2 coating is consistent with the literature [47-51]. TiO_2 is known for its antibacterial effect due to its photocatalytic properties. Photocatalysis produces reactive oxygen species (ROS) that react with organic compounds present in cells and cause their decomposition [47-49]. This reaction protects the substrate from corrosion caused by biofilms by reducing the amount of microorganisms present on the surface. This bactericidal activity was observed on several species of microorganisms such as *Escherichia coli* [48], *Deinococcus geothermalis* [50], *Staphylococcus aureus* and *Pseudomonas putida* [51]. In contrast, the use of ZrO_2 to limit the growth of microorganisms is less known, although ZrO_2-Cu and ZrO_2-Ag doped coatings have already shown antibacterial properties against *Staphylococcus aureus* and *Actinobacillus actinomycetemcomitans* [52]. In conclusion, the results of these immersion tests show that Ti/TiO_2 and $(Zr/ZrO_2)\times10$ coatings offer some protection against biofouling in marine environment.

BSE micrographs of the surfaces of 304L steel, Ti/TiO_2 and $(Zr/ZrO_2)\times10$ coatings after 56 d of immersion in Cherbourg seawater are shown in Figure 28. These observations were performed after biofilm removal for microbiological analyses on the samples with better average antifouling properties. The grains and small residues of biofilm (diatoms) are visible on the 304L steel surface (Figure 28a) compared to the coated samples. These residues were also observed previously on the etched and etched and bond-coated samples. The surfaces of the coated samples show the presence of particles and scratches (Figure 28b, c), which were already present before immersion. The particles are probably due to local droplet projections related

to electric arcs during the coating deposition and the scratches are related to the 304L initial surface deposition.

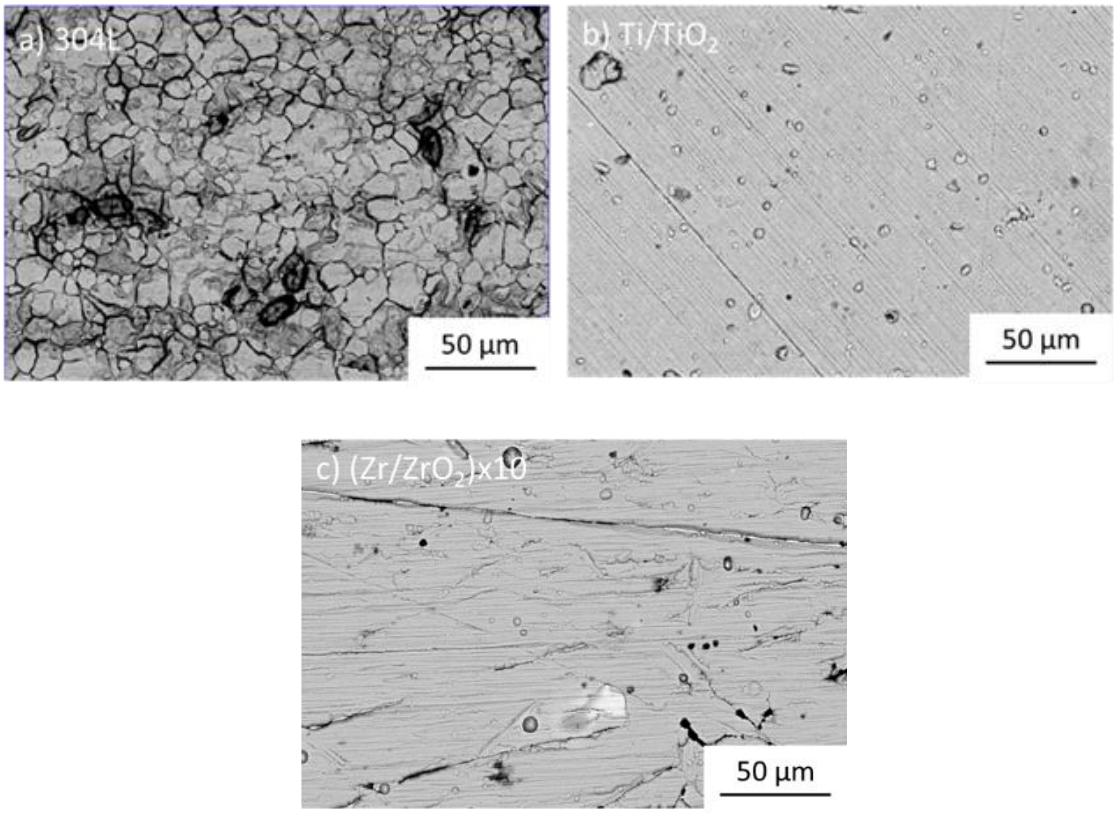

Figure 28: SEM-BSE micrographs of the surface of a) initial 304L substrate, b) Ti/TiO_2 and c) (Zr/ZrO_2)×10 coatings after 56 d of immersion in Cherbourg natural seawater.

Figure 29 shows SEM micrographs in BSE mode and EDX mapping of cross-sections of Ti/TiO_2 and (Zr/ZrO_2)×10 coatings after being immersed during 56 d in Cherbourg seawater. Both coatings appear undamaged and, contrary to the observations in nitric acid environment, there are no cavities near the substrate nor dissolution of material near the surface (Figure 19). This could be explained by the aggressiveness of nitric acid compared to NaCl. In addition, O enrichment is observed at the extreme surface of the coatings, as already noticed after electrochemical measurements in 3.56 wt.% NaCl solution at ambient temperature (Figure 22). This can indicate the presence of a passive oxide film on the surface of the coatings. On the other hand, no pitting is observed on the surface of the samples. This indicates good corrosion resistance in Cherbourg natural seawater for both coatings.

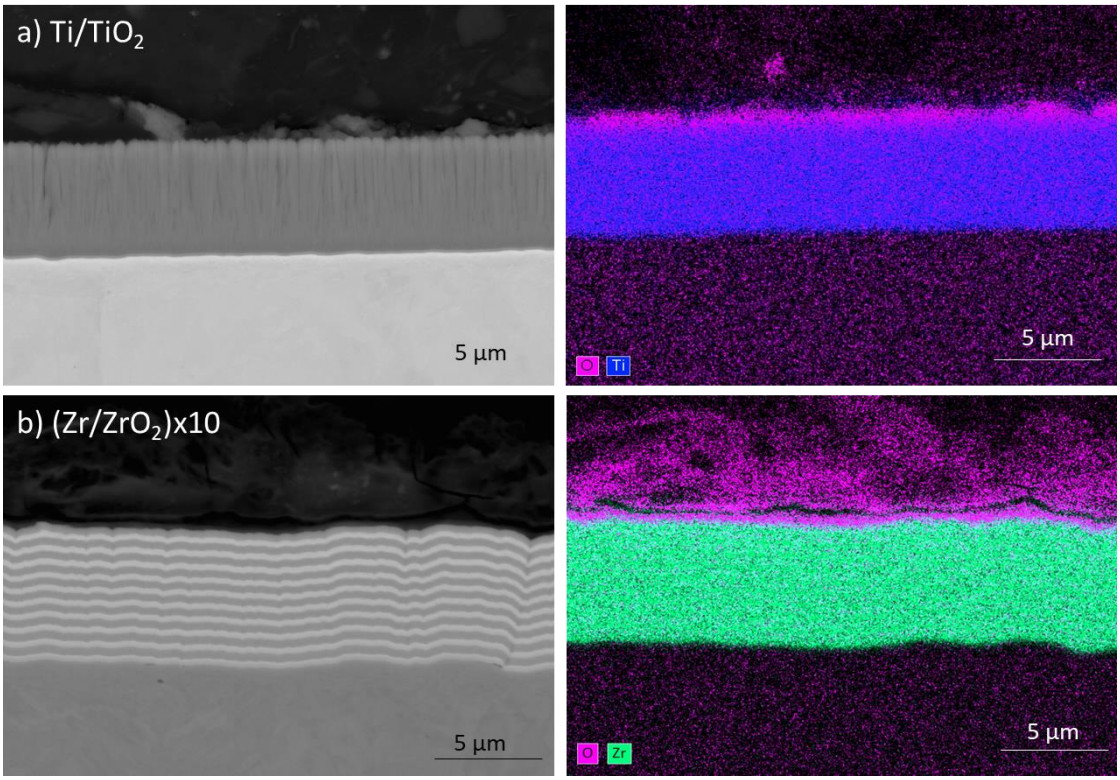

Figure 29: SEM-BSE micrographs and EDX mapping of the cross-section of a) Ti/TiO_2 and b) $(Zr/ZrO_2)\times10$ coatings after 56 d of immersion in Cherbourg natural seawater.

To sum up, the four coatings improve corrosion resistance of the 304L steel immersed in Cherbourg seawater. These results differ in part from those obtained in electrochemical measurements (Figure 20), and they suggest that the Ti/TiO_2 coating also offers some kind of protection in this environment. This confirms the interest of performing longer immersion tests to study the global behavior of the coated samples. Moreover, among these coatings, Ti/TiO_2 and $(Zr/ZrO_2)\times10$ coatings show better antifouling and antibacterial properties.

2.3 CONCLUSION

In conclusion, the corrosion resistance of non-optimized architectured coating systems is studied in nitric acid and saline environments using electrochemical measurements and immersion tests. Potentiodynamic polarization curves and EIS measurements show that the Zr-based coatings enhance corrosion resistance of initial 304L in nitric acid, particularly Zr/ZrO_2 coating. This is due to high adhesion properties of these coatings preventing them from delamination and their barrier effect against the electrolyte penetration thanks to a dense and stable oxide layer. The immersion tests confirm that the Zr/ZrO_2 coating is a promising candidate for improving the corrosion resistance of 304L ASS even if its microstructure is not optimized. The characterization of the electrochemically investigated and immersed samples indicates an undamaged surface and coating compared to 304L ASS that shows intergranular corrosion on its surface. However, some defects (particles, cracks, *etc.*) are observed at the coating surface. On the contrary, Ti-based coatings show a poor corrosion resistance probably due to their poor adhesion properties and columnar

structure that do not prevent the electrolyte from reaching the substrate and can cause galvanic corrosion. The more detailed observation of the Ti-based coatings after corrosion tests indicates delamination of the coatings, except for Ti/TiO_2 coating. It should be noted that as all these coatings are not optimized, it would be possible to further improve their adhesion and corrosion resistance by studying the process parameters more precisely. Moreover, as no comparative test with Ar^+ etching were performed due to time limitation, this would be interesting to perform this test to see if the tendency observed at the scale of the bond coat is still observed at larger scales.

As observed in nitric acid at boiling temperature, electrochemical measurements show that Zr-based coatings enhance the corrosion resistance of the initial 304L in 3.56 wt.% NaCl solution at ambient temperature while Ti-based ones show lower corrosion resistance than metal ion-etched and, Ti^+-etched and Ti-coated samples. This confirms the very limited protection against corrosion of these coatings. In addition, no pitting corrosion is noticed for all the oxide-based coatings compared to the etched and, etched and coated samples. The behaviour under service condition in natural seawater of our thick coating systems is studied using immersion tests. In Singapore seawater, ZrO_2, Zr/ZrO_2 and $(Zr/ZrO_2)\times10$ coatings seem to show a better corrosion protection after 60 d of immersion. However, additional studies are required to characterize the deposited coatings in more detail. On the other hand, Ti/TiO_2, Zr/ZrO_2, $(Zr/ZrO_2)\times5$ and $(Zr/ZrO_2)\times10$ coatings improve corrosion resistance of the initial 304L in Cherbourg seawater. These results are consistent with those of electrochemical measurements overall even if the Ti/TiO_2 coating seems to protect against corrosion in Cherbourg seawater. This confirms the interest of performing longer immersion tests to study the global behavior of the coated samples. In addition, Ti/TiO_2 and $(Zr/ZrO_2)\times10$ coatings indicate a good antifouling and antibacterial properties.

CONCLUSIONS

This chapter focuses on the properties of a non-optimized architectured substrate/coating system *i.e.* 304L steel substrate/metal bond coat/oxide coating.

First, the deposition of Ti-based and Zr-based oxide and multilayer coatings by a hybrid pulsed DCMS/HiPIMS process is performed. Four systems architectures are studied: substrate/oxide coating, substrate/metal/oxide coating, substrate/(metal/oxide)×5 layers coating and substrate/(metal/oxide)×10 layers coating. Note that even in the case of substrate/oxide coating a thin metal layer (≈ 100 nm) was deposited at the surface of the substrate due to the transition from metal to oxide deposition mode. The total thickness of these systems is about 5 µm for Ti-based and 7 µm for Zr-based ones. All these substrate/coating systems are not optimized and show an open columnar structure (which is less observed for the Zr-based coatings), probably due to too weak ionic bombardment during deposition. This type of structure can affect the corrosion resistance properties of the coating systems, probably by worsening them. Moreover, the Zr-based coatings are composed of monoclinic ZrO_2 and the Ti-based samples of mixed anatase and rutile (tetragonal TiO_2). The increase in the number of layers influences the crystal orientation due to a texturing effect and decreases the surface roughness. The study of the mechanical properties of the architectured coating systems shows a poor adhesion (delamination) of Ti-based coatings compared to Zr-based ones, which can be detrimental for corrosion resistance.

Next, the corrosion behavior of these architectured substrate/coating systems in nitric acid at boiling temperature is assessed using electrochemical measurements and immersion tests. Electrochemical investigations in this environment show a better corrosion resistance of the Zr-based coatings compared to 304L steel and Ti-based coatings. In fact, all the Ti-based coatings show a J_{corr} value of the same order of magnitude as the initial 304L, Ar^+/Ti^+-etched and Ti-coated samples and Ar^+-etched and Zr^+-coated sample after 6 h of immersion, confirming their limited corrosion resistance. The poor corrosion resistance of Ti-based coatings can be explained by their poor adhesion on the substrate and/or their columnar structure that do not prevent the electrolyte from reaching the substrate and can cause galvanic coupling. On the contrary, J_{corr} is quite lower for the Zr-based coatings and similar to Ta materials (coating and bulk) after 2 d of immersion. This is due to high adhesion properties of these coatings and the formation of a dense and stable ZrO_2 that acts as a barrier preventing the electrolyte from reaching the substrate. This is particularly observed for the Zr/ZrO_2 coating, while multilayer coatings do not offer a better corrosion resistance contrary to what might be expected. Moreover, the 9-d immersion tests performed to evaluate the global behavior of our coatings in nitric acid indicate similar results to electrochemical measurements i.e. Zr/ZrO_2 coating offer better anticorrosion properties. The Zr/ZrO_2 coating surface is undamaged after immersion in nitric acid compared to 304L ASS that shows intergranular corrosion. However, some particles and cracks are noticed at the coating surface, which can lead to a higher corrosion rate than expected by increasing the surface area exposed to nitric acid. Nevertheless, the Zr/ZrO_2 coating is dense and still protect effectively after 9 d of immersion.

The performance of architectured substrate/coating systems are also studied in marine environment. Electrochemical investigations in 3.56 wt.% NaCl solution at ambient temperature show a better corrosion resistance of the Zr-based coatings (especially Zr/ZrO_2) than 304L steel and Ti-based ones, as observed in nitric acid. The Ti-based coatings show higher J_{corr} values than those of the metal ion-etched samples (Ti^+ and Zr^+) and, the Ti^+-etched and Ti-coated sample, confirming their limited protection against corrosion. On the contrary, the Zr-based coatings indicates lower J_{corr} values than all the etched and, etched and coated samples studied in the previous chapter. This shows that Zr-based coatings are promising candidates for increasing the lifespan of 304L ASS. In addition, no pitting corrosion is observed on the Ti- and Zr-based coating systems (5-7 µm) compared to the etched (2-5 nm) and, etched and coated samples (200 nm). To study the corrosion resistance of our architectured coating systems under conditions similar to service conditions, 60-d immersion tests in two natural seawaters (Cherbourg and Singapore) are performed. The immersion results in Singapore seawater are consistent with the electrochemical measurements in NaCl solution, indicating a better corrosion resistance of Zr-based coatings and especially ZrO_2, Zr/ZrO_2 and $(Zr/ZrO_2)\times10$ coatings. Nonetheless, additional studies are required to understand the corrosion mechanism and to characterize more precisely the deposited coatings. Moreover, Ti/TiO_2, Zr/ZrO_2, $(Zr/ZrO_2)\times5$ and $(Zr/ZrO_2)\times10$ coatings improve corrosion resistance of the initial 304L in Cherbourg seawater. This differs slightly from the electrochemical measurements because the Ti/TiO_2 coating shows corrosion resistance, which confirms the need to perform several types of tests to characterize the anticorrosion performance of coatings. Finally, Ti/TiO_2 and $(Zr/ZrO_2)\times10$ coatings show good antifouling properties that would deserve to be studied in more detail.

The study of corrosion resistance of our architectured substrate/coating systems suggest that Zr-based coatings are promising anticorrosion solutions in both nitric acid and NaCl. In addition, they show interesting antifouling properties in marine environment. As these coatings are not fully optimized, it might be possible to further improve the protection properties (anticorrosion and antifouling) by studying the process parameters more precisely. Moreover, optimizations of Ti-based coatings are needed to improve their structure and adhesion in order to reconsider them as solutions to enhance initial 304L ASS sustainability.

REFERENCES

[1] Samim P. M., Fattah-alhosseini A., Elmkhah H. & Imantalab O. (2020) “Structure and corrosion behavior of ZrN/CrN nano-multilayer coating deposited on AISI 304 stainless steel by CAE-PVD technique.” Journal of Asian Ceramic Societies 8: 460-469.

[2] Lei Z., Zhang Q., Zhu X., Ma D., Ma F., Song Z. & Fu Y. Q. (2018) “Corrosion performance of ZrN/ZrO_2 multilayer coatings deposited on 304 stainless steel using multi-arc ion plating.” Applied Surface Science 431: 170-176.

[3] Wiklund U., Hedenqvist P., Hogmark S., Stridh B. & Arbell M. (1996) “Multilayer coatings as corrosion protection of Zircaloy.” Surface and Coatings Technology 86-87: 530-534.

[4] Kazazi M., Haghighi M., Yarali D. & Zaynolabedini M.H. (2018) “Improving Corrosion Resistance of 316L Austenitic Stainless Steel Using ZrO_2 Sol-Gel Coating in Nitric Acid Solution.” Journal of Materials Engineering and Performance 27: 1093-1102.

[5] Ningshen S., Kamachi Mudali U., Krishnan R. & Raj B. (2011) “Corrosion behavior of Zr-based metallic glass coating on type 304L stainless steel by pulsed laser deposition method.” Surface and Coatings Technology 205: 3961-3966.

[6] Padhy N., Kamal S., Chandra R., Mudali K. & Raj B. (2010) “Corrosion performance of TiO_2 coated type 304L stainless steel in nitric acid medium.” Surface and Coatings Technology 204: 2782-2788.

[7] Padhy N., Mudali K., Chawla V., Chandra R. & Raj B. (2011) “Corrosion behaviour of single (Ti) and duplex (Ti–TiO_2) coating on 304L stainless steel in nitric acid medium.” Materials Chemistry and Physics 130: 962-972.

[8] Li C., Chen W., Jiang Q., Wang L. & Luo D. (2014) “Corrosion resistance of Ti-based metallic glass coating in concentrated nitric acid.” Materials Chemistry and Physics 143: 900–903.

[9] Bensaha R. & Bensouyad H. (2012) “Synthesis, Characterization and Properties of Zirconium Oxide (ZrO_2)-Doped Titanium Oxide (TiO_2) Thin Films Obtained via Sol-Gel Process.” F. Czerwinski (Ed.) Heat Treatment - Conventional and Novel Applications, IntechOpen.

[10] Nouri E., Shahmiri M., Rezaie H. & Talayian F. (2011) “Investigation of structural evolution and electrochemical behaviour of zirconia thin films on the 316L stainless steel substrate formed via sol–gel process.” Surface and Coatings Technology 205: 5109-5115.

[11] Holgado J.P., Pérez-Sánchez M., Yubero F., Espinós J.P. & González-Elipe A.R. (2002) “Corrosion resistant ZrO_2 thin films prepared at room temperature by ion beam induced chemical vapour deposition.” Surface and Coatings Technology 151-152: 449-453.

[12] Cubillos G., Olaya J., Bethencourt M., Cifredo G. & Blanco G. (2013) “Resistance to Corrosion of Zirconia Coatings Deposited by Spray Pyrolysis in Nitrided Steel.” Journal of Thermal Spray Technology 22: 1242-1252.

[13] Kotoka R., Yarmolenko S., Pai D. & Sankar J. (2015) “Corrosion Behavior of Reactive Sputtered $Al2O_3$ and ZrO_2 Thin Films on Mg Disk Immersed in Saline Solution.” Journal of Materials Science & Technology 31: 873-880.

[14] Kaliaraj G.S., Vishwakarma V., Kirubaharan K., Dharini T., Ramachandran D. & Muthaiah B. (2018) “Corrosion and biocompatibility behaviour of zirconia coating by EBPVD for biomedical applications.” Surface and Coatings Technology 334: 336-343.

[15] Shajudheen V.P.M., Rani K.A., Kumar V.S., Maheswari A.U., Sivakumar M. & Kumar S.S. (2018) “Comparison of Anticorrosion Studies of Titanium Dioxide and Nickel Oxide Thin Films Fabricated by Spray Coating Technique.” Materials Today: Proceedings 5: 8889-8898.

[16] Kouznetsov V., Macák K., Schneider J.M., Helmersson U. & Petrov I. (1999) “A novel pulsed magnetron sputter technique utilizing very high target power densities.” Surface and Coatings Technology 122: 290-293.

[17] Horn E. M. & Kohl H. (1986) “Materials for the nitric acid industry.” Werkstoffe und Korrosion 37: 57-69.

[18] Wang T.-G., Dong Y., Gebrekidan B. A., Liu Y.-M., Fan Q.-X. & Kim K. H. (2017) “Microstructure and properties of the Cr-Si-N coatings deposited y combining high-power impulse magnetron sputtering (HiPIMS) and pulsed DC magnetron sputtering.” Acta Metallurgica Sinica 30: 688-696.

[19] Luo Q., Yang S. & Cooke K. E. (2013) “Hybrid HiPIMS and DC magnetron sputtering deposition of TiN coatings: deposition rate, structure and tribological properties.” Surface and Coatings Technology 235: 13-21.

[20] Arab Pour Yazdi M., Lomello F., Wang J., Sanchette F., Dong Z., White T., Wouters Y., Schuster F. & Billard A. (2014) “Properties of TiSiN coatings deposited by hybrid HiPIMS and pulsed-DC magnetron co-sputtering.” Vacuum 109: 43-51.

[21] Santiago J.A., Fernandez-Martinez I., Wennberg A., Molina-Aldareguia J.M., Castillo-Rodriguez M., Rojas T.C., Sanchez-Lopez J.C., Gonzalez M.U., Garcia-Martin J.M., Li H., Bellido-Gonzalez V., Monclus M.A. & Gonzalez-Arrabal R. (2018) “Adhesion enhancement of DLC hard coatings by HiPIMS metal ion etching.” Surface and Coatings Technology 349: 787-796.

[22] Bakoglidis K.D., Schmidt S., Greczynski G. & Hultman L. (2016) “Improved adhesion of carbon nitride coatings on steel substrates using metal HiPIMS pretreatments.” Surface and Coatings Technology 302: 454-462.

[23] Sahin E. O. (2016) “Development of rare earth-free negative electrode materials for NiMH batteries.” PhD thesis, Middle East Technical University, Turkey.

[24] Ortiz C. H., Colorado H. D., Aperador W. & Jurado A. (2019) “Influence of the number of bilayers on the mechanical and tribological properties in [TiN/TiCrN]n multilayer coatings deposited by magnetron sputtering.” Tribology in industry 41: 330-343.

[25] Nikkanen J.-P. (2016) “Synthesis of TiO_2 by various methods. Structural Characteristics, Photocatalytic Activity and Usability of Powders and Coatings.” Thesis, Tampere University of Technology.

[26] Vikram Kumar C. H. R., Kesavan Nair P. & Ramamoorthy B. (2008) “Characterization of multilayer pvd nanocoatings deposited on tungsten carbide cutting tools.” International Journal of Advanced Manufacturing Technology 38: 622-629.

[27] Li G., Lü W., Liu S., Li C., Zhou Y. & Wang Q. (2021) “Multilayer-growth of TiAlN/WS self-lubricating composite coatings with high adhesion and their cutting performance on titanium alloy.” Composites Part B 211, 108620.

[28] Ma K. J., Bloyce A. & Bell T. (1995) “Examination of mechanical properties and failure mechanisms of TiN and Ti-TiN multilayer coatings.” Surface and Coatings Technology 76-77: 297-302.

[29] Stambolova I. D., Boshkova N. D., Stoyanova D. D., Blaskov V. N., Simeonova S. S. & Boshkov N. St. (2020) “Corrosion behavior of low-carbon steel coated with different type of TiO_2/ZrO_2 layers.” Materials, Methods & Technologies 14: 300-307.

[30] Xin Y., Liu C., Zhang W., Huo K., Tang G., Tian X. & Chu P. K. (2008) “Corrosion resistance of ZrO_2-Zr-coated biodegradable surgical magnesium alloy.” Journal of Materials Research 23: 312-319.

[31] Marin E., Guzman L., Lanzutti A., Ensinger W. & Fedrizzi L. (2012) “Multilayer Al_2O_3/TiO_2 Atomic Layer Deposition coatings for the corrosion protection of stainless steel.” Thin Solid Films 522: 283-288.

[32] Jamesh M. I., Wu G., Zhao Y., McKenzie D. R., Bilek M. M. M. & Chu P. K. (2014) “Effects of zirconium and oxygen plasma ion implantation on the corrosion behavior of ZK60 Mg alloy in simulated body fluids.” Corrosion Science 82: 7-26.

[33] Zhu S., Huang N., Shu H., Wu Y. & Xu L. (2009) “Corrosion resistance and blood compatibility of lanthanum ion implanted pure iron by MEVVA.” Applied Surface Science 256: 99-104.

[34] Wu H., Xi K., Xiao S., Qasim A. M., Fu R. K. Y., Shi K., Ding K., Chen G., Wu G. & Chu P. K. (2020) “Formation of self-layered hydrothermal coating on magnesium aided by titanium ion implantation: Synergistic control of corrosion resistance and cytocompatibility.” Surface and Coatings Technology 401: 126251.

[35] Jamesh M., Wu G., Zhao Y. & Chu P. K. (2013) “Effects of silicon plasma ion implantation on electrochemical corrosion behavior of biodegradable Mg-Y-RE Alloy.” Corrosion Science 69: 158-163.

[36] Orazem M. E., Pébère N. & Tribollet B. (2006) “Enhanced graphical representation of electrochemical impedance data.” Journal of The Electrochemical Society 153: B129-B136.

[37] Arenas M. A., Garcia I. & de Damborenea J. (2004) “X-ray photoelectron spectroscopy study of the corrosion behaviour of galvanised steel implanted with rare earths.” Corrosion Science 46: 1033-1049.

[38] Alexander C. L., Tribollet B. & Orazem M. E. (2015) “Contribution of surface distributions to constant-phase-element (CPE) behavior: 1. Influence of roughness.” Electrochimica Acta 173: 416-424.

[39] Zhang Z., Ter-Ovanessian B., Marcelin S. & Normand B. (2020) “Investigation of the passive behavior of a Ni-Cr binary alloy using successive electrochemical impedance measurements.” Electrochimica Acta 353: 136531.

[40] Raj B. & Kamachi Mudali U. (2006) “Materials development and corrosion problems in nuclear fuel reprocessing plants.” Progress in Nuclear Energy 48: 283-313.

[41] Bhise S. & Kain V. (2012) “Methodology based on potential measurement for predicting corrosion behaviour of SS 304L in boiling nitric acid containing oxidizing ions.” Corrosion Engineering, Science and Technology 47: 61-69.

[42] Badet H. & Poineau F. (2020) “Corrosion studies of stainless steel 304L in nitric acid in the presence of uranyl nitrate: effect of temperature and nitric acid concentration.” SN Applied Sciences 2:459.

[43] Sathish S. & Geetha M. (2016) “Comparative study on corrosion behavior of plasma sprayed Al_2O_3, ZrO_2, Al_2O_3/ZrO_2 and ZrO_2/Al_2O_3 coatings.” Transactions of Nonferrous Metals Society of China 26: 1336-1344.

[44] Shan C. X., Hou X. & Choy K.-L. (2008) “Corrosion resistance of TiO_2 films grown on stainless steel by atomic layer deposition.” Surface and Coatings Technology 2020: 2399-2402.

[45] Marconnet C., Dagbert C., Roy M. & Feron D. (2008) “Stainless steel ennoblement in freshwater: From exposure tests to mechanisms.” Corrosion Science 50: 2342-2352.

[46] Landoulsi J., Kirat K. El, Richard C., Feron D. & Pulvin S. (2008) “Enzymatic approach in microbial-influenced corrosion: A review based on stainless steels in natural waters.” Environmental Science & Technology 42: 2233-2242.

[47] Soethe V. L., Delatorre R. G., Ramos E. M. & Parucker M. L. (2017) “TiO_2 thin films for biofouling applications.” Materials Research 20: 426-431.

[48] Lu Z.-X., Zhou L., Zhang Z.-L., Shi W.-L., Xie Z.-X., Xie H.-Y., Pang D.-W. & Shen P. (2003) “Cell damage induced by photocatalysis of TiO_2 thin films.” Langmuir 19: 8765-8768.

[49] Ohko Y., Saitoh S., Tatsuma T. & Fujishima A. (2001) “Photoelectrochemical anticorrosion and self-cleaning effects of a TiO_2 coating for type 304 stainless steel.” Journal of The Electrochemical Society 148: B24-B28.

[50] Raulio M., Pore V., Areva S., Ritala M., Leskelä M., Lindèn M., Rosenholm J. B., Lounatmaa K. & Salkinoja-Salonen M. (2006) “Destruction of *Deinococcus geothermalis* biofilm by photocatalytic ALD and sol-gel TiO_2 surfaces.” Journal of Industrial Microbiology and Biotechnology 33: 261-268.

[51] Jalvo B., Faraldos M., Bahamonde A. & Rosal R. (2017) “Antimicrobial and antibiofilm efficacy of self-cleaning surfaces functionalized by TiO_2 photocatalytic particles against *Staphylococcus aureus* and *Pseudomonas putida*.” Journal of Hazardous Materials 340: 160-170.

[52] Huang H.-L., Chang Y.-Y., Weng J.-C., Chen Y.-C., Lai C.-H. & Shieh T.-M. (2013) “Anti-bacterial performance of Zirconia coatings on Titanium implants.” Thin Solid Films 528: 151-156.

Conclusion and outlook

Sustainability issues are essential for component performance for carbon-free energies and marine infrastructures. For this purpose and in a Green Deal approach, the development of environmentally friendly, industrially and economically viable surface treatments is performed.

In this PhD work performed in the frame of a cotutelle agreement between Sorbonne University/CEA, France and Nanyang Technological University (NTU), Singapore, we selected coating systems developed by HiPIMS technique, which is a PVD process allowing the elaboration of dense and adherent coatings by the use of a highly ionized plasma. The impact of the different process steps on the substrate/coating system interfaces performed by HiPIMS was studied: substrate etching pre-treatment where a few nanometers of the substrate are modified, a 200 nm-thick bond coat deposition and coating architecture (coatings up to 5 µm-thick).

The objective was then, by the fine characterization and understanding of the building of these interfaces throughout the deposition process, to be able to master and potentially optimize these interfaces to improve the corrosion performances of the coating. For this objective, two aggressive environments were selected: hot and concentrated nitric acid for nuclear spent fuel reprocessing and marine environement. For these two case of applications, the substrate selected was 304L ASS, an austenitic stainless steel largely used in both environments. For the coatings, ceramic coatings were considered and more specifically, ZrO_2 and TiO_2 coatings due to their unique chemical, thermal and mechanical properties.

Both the literature review and our experimental work indicate that a clean, dense and defect-free substrate/coating interface is essential for good corrosion protection. This is because a clean interface leads to high adhesion of the coating to the substrate. Limiting electrolyte penetration to the substrate, e.g. by densifying the coating, is also an essential step in improving corrosion resistance of coatings. To this end, an ion etching pre-treatment was performed to first remove surface contaminants and then implant ions in the substrate surface to favor the growth of dense coating. In addition, a metallic bond coat could be deposited on the etched substrate to improve the final component behavior. Therefore, the influence of the HiPIMS ion etching on the substrate surface properties and the substrate/metallic bond coat interface was first studied. Finally, a thick oxide coating was deposited on the metallic bond coat. Different multilayer metal/oxide coatings were synthesized to evaluate the effect of adding interfaces on the final component properties.

In the first stage, the surface pre-treatment by HiPIMS ion etching and its influence on a substrate/metallic bond coat system are studied. To this end, three types of ion etching (Ar^+, Ti^+ and Zr^+) are performed and results in surface modification of the 304L substrate by implantation of the sputtered elements on the first nanometers. These etchings lead to partial amorphization of crystal phases and to reduction of the surface content in ferrite. The incorporation of etching species modify the composition of the substrate surface. In fact, we can assume that metal ions can be incorporated into the substrate structure by substituting lattice atoms (replacements), *i.e.* Ti could replace Cr while Zr could replace Fe in the FCC structure of 304L ASS, while Ar could be incorporated in interstitial sites. Results show that the amount of these incorporated species differs slightly from one etching to another: Ti (7 at.%) and Ar (5 at.%) after Ti^+ etching, Zr (6 at.%) and Ar (6 at.%) after Zr^+ etching and Ar (4 at.%) and Zr (7 at.%)

after Ar^+ etching. Unexpected Zr contribution was observed after Ar^+ etching, which was attributed to resputtering effects of the vacuum chamber walls and substrate-holder triggered by the high energetic bombardment of their surface. The presence of these implanted species leads to a modification of the chemical composition of the passive layer formed on the substrate surface, promoting the formation of TiO_2 and ZrO_2, which are more stable than Cr_2O_3 and Fe_2O_3. The estimated thickness of the surface oxide layer modified by metal ion implantation is around 3.5 nm for Zr and 4 nm for Ti calculated from SRIM software for ions at 0.9 keV. The evaluation of corrosion resistance of pre-treated substrates in nitric acid (2.5 mol/L HNO_3, 2.5 mol/L $NaNO_3$, 2 g/L $Fe(NO_3)_3$ at 110 °C) shows an increase in the corrosion potential and a decrease in the corrosion current density for all metal ion-etched samples. This is attributed to the modification of the surface crystalline structure by the substitution of 304L atoms by metal species that induces the formation of more protective passive layer, which hinders the charge transfer process. Immersion tests confirm these results by showing a reduced intergranular corrosion of the 304L ASS after Zr^+ etching. In comparison, no long-term improvement is observed when an inert gas ion (Ar) is used for etching, probably because these ions generate only minor changes in the crystalline structure in this case. In 3.56 wt.% NaCl solution, the beneficial effect of metal ion etching on corrosion resistance of the 304L ASS is also noticed. The explanation is the same as before *i.e.* the formation of stronger bonds at the substrate/bond coat interface due to structural modifications. These results differ from those of immersion tests that show only the positive effect of Ti^+ etching on the decrease of corrosion rate. Differences between electrochemical measurements and corrosion tests can be attributed to various factors. First, it can be observed that the stationary state was not reached at least for the electrochemical test performed after 6 hours of immersion. Moreover, uncertainties on the use of the Tafel method also remain showing also the complexity of the corrosion mechanisms as well which makes the use of electrochemisry as a frist evaluation test difficult.

In the second stage, Ti and Zr metallic bond coats of about 200 nm thickness are deposited on the etched substrates to study the substrate/metallic bond coat interface. The deposited metallic bond coats show a columnar structure and are fully crystallized, probably due to the high energetic bombardment of the surface with ionized inert gas and metal plasma species present in the HiPIMS discharge. Moreover, different crystalline orientations are observed depending on the type of etching performed. In fact, the Ti^+-etched and Ti-coated sample shows a preferential orientation along the (101) axis compared to the Ar^+-etched and Ti-coated sample. In addition, the Ar^+-etched and Zr-coated and, unetched and Zr-coated samples are preferentially oriented along the (100) axis, whereas there is no real preferential orientation observed for the Zr^+-etched and Zr-coated sample. This tends to indicate an effect of etching on the structure of the bond coat. Although further analysis is required to understand how the etching type can exactly influence on the bond coat microstructure. Nonetheless, a mechanism for the formation of the substrate/bond coat interface is proposed, suggesting that metal species can act as nucleation site for the growth of the bond coat and promote an epitaxial film, at least on the first layers. This could indicate the formation of a pseudodiffusion-type interface that is characterized by a gradient of composition between the substrate and the deposited bond coat. Moreover, this leads to a decrease of lattice mismatch and results in the

formation of strong bonds. On the contrary, since Ar incorporates into the interstitial sites, it cannot form bonds at the substrate/bond coat interface. This nanometer-thick (2-5 nm) interface is clean, free from external contamination and defects. However, questions remain about the possible presence of a mixing zone for both metal ion-etched and metal-coated samples after XPS, TEM and APT analyzes. This mixing zone could be related to a mixing of the elements due to the implantation of metallic ions during the etching step but it could also be attributed to analyses artifacts. Consequently, further investigations are required. Moreover, HiPIMS etching using metal ion results in stronger substrate/metallic bond coat adhesion compared to inert gas etching. The best adhesion is observed after HiPIMS metal ion etching due to the formation of stronger bonds at the interface, resulting from the substitution of lattice atoms by metal ions in the substrate structure. In comparison, diode (Ar) etching leads to poor adhesion of bond coats either because of contamination induced by the re-sputtering effect of substrate-holder and chamber walls or because of the incorporation of Ar as interstitials in the crystal lattice, which increases the stresses and weakens the interface. Taking together, these results confirm that the HiPIMS metal ion etching pre-treatment modifies the substrate/bond coat interface, which can be beneficial for the long-term performance of the coatings. After the deposition of the metallic bond coat, this beneficial effect is observed for both types of metal ion etchings in NaCl solution, which could be due to the epitaxial growth of the bond coat due to metal species that act as preferential nucleation sites. As a result, a denser film can be formed and improved corrosion resistance compared to the bond coat formed after Ar^+ etching that are probably more porous. However, this effect is noticed only for Zr^+ etching in nitric acid. This could be due to a better resistance of Zr in nitric acid solution inducing the formation of a more stable Zr-based passive oxide film. Immersion tests are also performed to evaluate the substrate/metallic bond coat system behavior over longer time than the electrochemical measurements. In nitric acid solution, similar results to those of electrochemistry are obtained while in NaCl, some results differs as the lower corrosion rate is observed for 304L ASS, Zr^+-etched and Zr-coated and, unetched and Zr-coated samples according to immersion tests. No major differences are obtained between these different samples regarding their corrosion rate. In contrast, immersion tests performed in the natural seawater at Cherbourg do not allow us to conclude on the improvement of the corrosion resistance after etching or etching and metallic bond coat deposition.

Having identified the HiPIMS ion etching offering better corrosion resistance properties of the substrate/metallic bond coat system, the study focuses in a second stage on a more complex but non-optimized substrate/coating system. Four architecture systems are deposited by a hybrid pulsed DCMS/HiPIMS process: substrate/oxide coating, substrate/bond coat/oxide coating, substrate coated with five (bond coat/oxide layer) successive sandwiches, and substrate coated with 10 (bond coat/oxide layer) successive sandwiches. Note that even in the case of substrate/oxide coating a thin metal layer (≈ 100 nm) was deposited at the substrate surface due to the transition from metal to oxide deposition mode. The total thickness of these systems is about 5 µm for Ti-based and 7 µm for Zr-based ones. An open columnar structure is observed for all substrate/coating systems, which is less visible for the Zr-based coatings, probably due to too weak ionic bombardment during deposition. This clearly indicates that the HiPIMS episodic stage cannot densify the

layer as much as is the case for direct HiPIMS deposition in the deposition configuration used in this work. Moreover, the increase in the number of layers influences the crystal orientation due to a texturing effect and decreases the surface roughness. Note that a high surface roughness can lead to a larger surface exposed to the electrolyte during corrosion tests. This can result in uncertainties about the corrosion current densities or the weight losses measured. Zr-based coatings show higher adhesion, suggesting better possible corrosion resistance, compared to Ti-based ones. Corrosion behavior investigations in nitric acid solution show better corrosion resistance of the Zr-based coatings (especially Zr/ZrO_2 sandwiches), compared to uncoated 304L substrate or Ti-based coatings. In fact, all the Ti-based coatings show a J_{corr} value of the same order of magnitude as the initial 304L, Ar^+/Ti^+-etched and Ti-coated samples and Ar^+-etched and Zr^+-coated sample after 6 h of immersion, confirming their limited corrosion resistance. The poor corrosion resistance of Ti-based coatings can be explained by their poor adhesion on the substrate and/or their columnar structure that do not prevent the electrolyte from reaching the substrate and can cause galvanic coupling. On the contrary, J_{corr} is quite lower for the Zr-based coatings and similar to Ta materials (coating and bulk) after 2 d of immersion. This could be due to high adhesion properties of these coatings and the formation of a dense and stable ZrO_2 that acts as a barrier preventing the electrolyte from reaching the substrate. Moreover, the 9-d immersion tests performed to evaluate the global behavior of our coatings in nitric acid indicate similar results to electrochemical measurements i.e. Zr/ZrO_2 coating offers better anticorrosion properties. The Zr/ZrO_2 coating surface is undamaged after immersion in nitric acid compared to 304L ASS that shows intergranular corrosion. However, some particles and cracks are noticed at the coating surface, which can lead to a higher corrosion rate than expected by increasing the surface area exposed to nitric acid. Electrochemical investigations in 3.56 wt.% NaCl solution at ambient temperature show a better corrosion resistance of the Zr-based coatings (especially Zr/ZrO_2) than 304L steel and Ti-based ones, as observed in nitric acid. The Ti-based coatings show higher J_{corr} values than those of the metal ion-etched samples (Ti^+ and Zr^+) and, the Ti^+-etched and Ti-coated sample, confirming their limited protection against corrosion. On the contrary, the Zr-based coatings indicates lower J_{corr} values than all the etched and, etched and coated samples. In addition, no pitting corrosion is observed on the Ti- and Zr-based coating systems (5-7 µm) compared to the etched (2-5 nm) and, etched and coated samples (200 nm). Therefore, the most promising candidates for improving the 304L ASS corrosion resistance are Zr-based coatings. Immersion tests are performed in Singapore and Cherbourg seawaters for 2 months to evaluate the corrosion resistance of the architectured coating systems under conditions similar to service conditions. In Singapore seawater, similar results to electrochemical measurements in NaCl solution are obtained, indicating better corrosion protection of Zr-based coatings while in Cherbourg seawater, the Ti/TiO_2 coating also show good corrosion resistance. Furthermore, good antifouling properties are noticed for Ti/TiO_2 and $(Zr/ZrO_2)x10$ layers coatings. Noting that antifouling properties of Zr-based coatings in marine environment had never really been studied before in the literature.

The first part of this work showed that HiPIMS metal ion etchings improved mechanical and corrosion resistance properties of the 304L ASS, particularly for Zr. The encouraging results obtained on the effect of etching on the substrate and

substrate/metallic bond coat interface call for further scrutiny. For instance, etching with ions of a different material than those used for the metallic bond coat and those of the substrate could help to understand ion implantation phenomenon in the substrate by performing TEM and APT analyses. In addition, a study of the variation of the bias of the substrate-holder could allow finding an optimum for deeper ions implantation into the substrate and modifying the thickness of substrate alteration. This could also help to understand the phenomena taking place at the interface *i.e.* elements' mixing zone or clear interface. In the same way, it could be interesting to perform an optimization of the etching duration, which may impact the substrate/coating adhesion. Another approach would be to study precisely the influence of the etching type on the formation and growth mechanism of the bond coat, maybe by performing finer characterizations. The second part of this work showed that Zr-based coating systems offered better corrosion protection, both with oxide and multilayer coatings compared to the 304L ASS. Because our architectured systems have not yet been optimized, higher protection properties (anticorrosion and antifouling) could certainly be obtained by an optimization procedure. For example, one way to optimize these systems could be to adjust the process parameters such as PEM set point or peak discharge current to minimize the coating columnar structure and obtain a denser coating. Another solution could be to superimpose the HiPIMS and pulsed DCMS signals on the same cathode to perform DC between the HiPIMS signals to densify the microstructure of the coatings. In the case of multilayer coating systems, a more detailed study of the thickness of the layers and their number could lead to a higher corrosion resistance of these coatings compared to single and bilayer coating. An optimal number of layers can probably be identified to obtain the best protection against corrosion. Moreover, the literature has shown that layers of similar thickness further improve the properties of multilayer coatings by reducing stresses in the coating. The immersion tests showed encouraging results for our systems, but longer tests have to be performed to determine the coating long-term behavior, especially in nitric acid. Finally, another way for improving our architectured coating systems could be to change the metallic bond coat for another component such as a nitride. In this case, an ion nitriding of the substrate is performed in order to obtain a hardness gradient and to deposit the nitride coating on it. For instance, ZrN shows good mechanical properties such as toughness, which can be combined with ZrO_2 properties to form promising protective multilayer coatings for 304L ASS.

APPENDIX 1: OPTIMIZATION OF IN SITU SUBSTRATE SURFACE PRE-TREATMENT

1. PRELIMINARY STUDY OF THE INFLUENCE OF ETCHING PARAMETERS ON SUBSTRATE/COATING INTERFACE

As mentioned above, three types of *in situ* plasma etching of the 304L substrate were studied in this project:

- argon ions using a glow (also called diode) discharge (Ar^+),
- titanium and argon ions produced by a HiPIMS discharge and a titanium target (Ti^+),
- and zirconium and argon ions using a HiPIMS discharge and a zirconium target (Zr^+).

A preliminary study was first conducted to evaluate the influence of three different etching parameters on substrate/coating interface:

- Etching duration (5 to 20 minutes),
- Energy of the incident ions on the substrates, depending partially on the plasma/substrate potential difference, controlled by the substrate bias potential imposed on the substrate-holder (from 500 to 900 V),
- Ion flux from each target source, depending partially on the sputtering yield and the plasma/cathode potential difference, tuned with the average electrical power applied on the target (1500 W or 2500 W).

1.1 PARAMETERS

All the parameters configurations are summarized in the Table 1 below.

Table 1: Etching parameters for the study of three different types of etching.

Etching type	Ar^+ etching				Ti^+ etching				Zr^+ etching			
	Etch Ar1	Etch Ar2	Etch Ar3	Etch Ar4	Etch Ti1	Etch Ti2	Etch Ti3	Etch Ti4	Etch Zr1	Etch Zr2	Etch Zr3	Etch Zr4
Pressure (Pa)	0,88	1,8	0,93	1,77	0,53	0,56	0,56	0,56	0,55	0,56	0,57	0,57
Argon flow (sccm)	100	100	100	100	100	100	100	100	100	100	100	100

Duration (min)	5	5	20	20	20	20	5	5	5	5	20	20
Target voltage (V)	X	X	X	X	900	900	900	900	900	900	900	900
Pulse width (µs)	X	X	X	X	20	20	20	20	20	20	20	20
Extinction time (µs)	X	X	X	X	1980	1980	1980	1980	1980	1980	1980	1980
Frequency (Hz)	X	X	X	X	250	250	250	250	250	250	250	250
Target power (W)	X	X	X	X	2500	1500	1500	2500	2500	1500	2500	1500
Substrate-holder voltage (V)	-900	-900	-900	-900	-700	-500	-700	-500	-700	-500	-500	-700

A negative DC substrate bias was applied to the substrate holder, which is rotating at 1 rpm. Two targets of the chosen material (Ti or Zr), operated in bipolar HiPIMS mode, are placed face to face into the vacuum chamber. Note that for Ar^+ etching, the shutters masking the Ti and Zr targets had to be removed because the magnetic field of the corresponding magnetrons are necessary to ignite the Ar discharge.

1.1.1 XPS analysis

The surface modification involved by the different etching types is analyzed using XPS for the chemical composition of the extreme surface and electrochemistry for the properties of the extreme surface. The XPS results are compared with the SRIM calculations simulating ion implantation in the substrate surface.

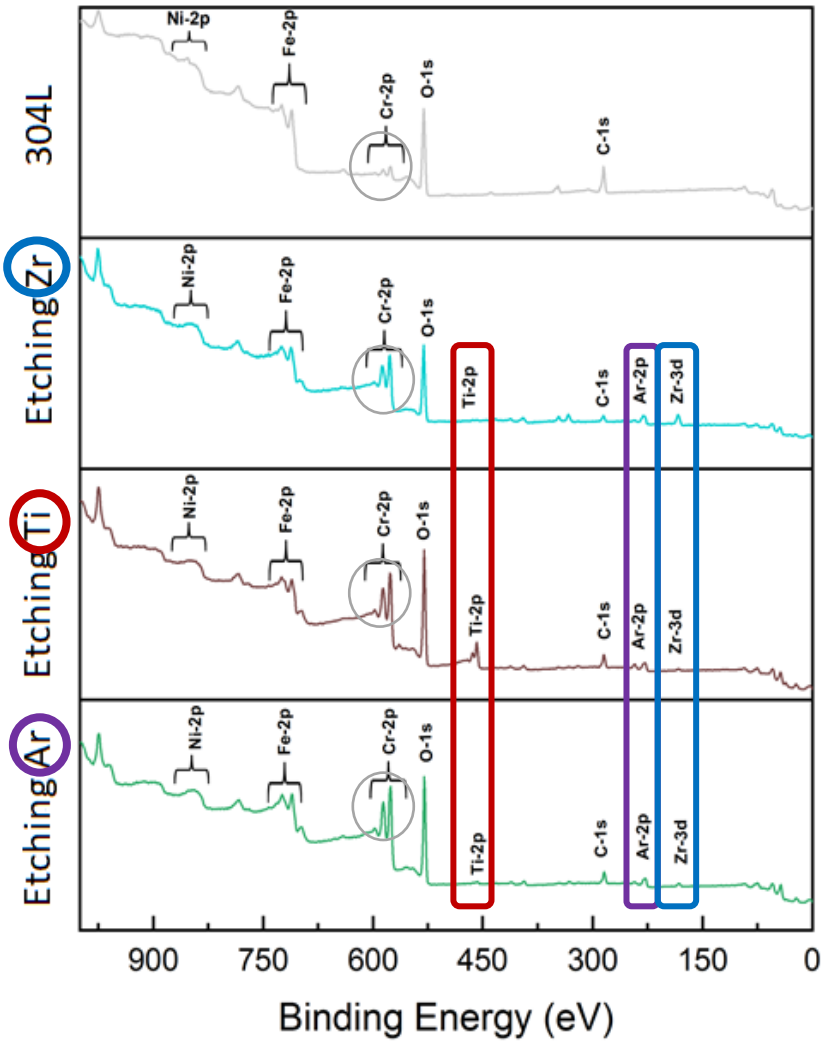

Figure 1: XPS wide-scan spectra of etched samples compared to the bare 304L substrate

Wide-scan XPS spectra of the three types of etched samples are shown in Figure 1 and compared to the bare substrate 304L. Peaks from substrate elements (Fe, Cr and Ni) and external contamination (C and O) are visible on all XPS spectra, which indicates that samples were etched and not coated. Ar, Ti and Zr peaks are observed on XPS spectra obtained for the Ar^+-etched samples. Since the plasmagenic gas used is argon, it makes sense to detect Ar in all spectra. Moreover, argon ions are accelerated on the substrate-holder to etch the sample, which means that some ions are implanted into the material. Ti and Zr targets are present inside the vacuum chamber and their shutters are open to obtain a sufficient magnetic field to ignite the argon plasma used for this etching, which may explain the presence of Ti and Zr peaks on the spectrum.

For Ti^+-etched samples, Ti and Ar peaks are conspicuous whereas Zr peaks are absent or weak. Ti peak is observed because Ti species are sputtered using two Ti targets in this type of etching. The Zr targets are masked during this etching and therefore Zr peaks are almost absent from the XPS spectrum; the presence of Zr could only be explained by some residual contamination from the vacuum chamber walls or the substrate-holder.

Finally, Cr peaks are much more intense for all the etched substrates than for bare substrate, which may indicate that etching has changed the surface chemistry of the substrate. This may be related either to the diffusion of Cr from the substrate to the extreme surface, to vacuum chamber contamination or resputtering of the 304L substrate-holder (mainly composed of Fe, Cr and Ni). Chromium enrichment has to be studied in detail to understand its origin. In addition, a quantification of the extreme surface elements is performed to complete the study of the XPS wide-scan spectra. A deconvolution of the peaks observed in the XPS spectra allows to identity their state (mainly metal or oxide) and to quantify them.

Table 2: Etching parameters and XPS quantification in (%) of atomic compositions on the Ar^+ etched sample surfaces.

		Etch Ar 1	Etch Ar 2	Etch Ar 3	Etch Ar 4	304L
Etching parameters	Pressure (Pa)	0.9	1.8	0.9	1.8	/
	Duration (min)	5	5	20	20	
	Bias voltage (V)	- 900				
XPS analysis	%at Cr (metal)	6	0	5	5	5
	%metal Cr (oxide)	35	27	49	53	17
	%at Fe (metal)	14	0	12	6	21
	%at Fe (oxide)	27	14	22	25	47
	%at Ni	1	3	1	1	10
	%at Ti	3	4	2	2	/
	%at Zr	9	42	3	3	/
	%at Ar	5	10	6	5	/

Chemical quantification of XPS spectra shows the presence of Ar, Ti and Zr on the surface of the Ar^+-etched samples (Table 2). In addition, the quantification attests the predominance of Cr in oxide state on the extreme surface of all etched samples consistent with the very high atomic percentages (up to 56 at.%). The quantification of the second Ar^+ etching (named etchAr2) shows very divergent results compared to the others, which can be due to the application of a very high power for a short time that may cause resputtering of Zr contaminants deposited on vacuum chamber wall from previous batches,

and redeposited on the substrate. Based on these results, for Ar^+-etched samples the average amount of Ar and Zr is higher than Ti.

In the case of metal ion etchings (Ti^+ and Zr^+), chemical quantification confirms the presence of Ti (Table 3) and Zr (Table 4) on the etched samples surface. After Ti^+ etching, a higher amount of Ti is observed at the extreme surface. The same behavior is shown for Zr^+ etching *i.e.* higher amount of Zr. In both cases, the amounts of Ti and Zr are higher than those obtained during Ar^+ etching, except for etchAr2 (as discussed earlier). Two etched samples appear to have a higher ion implantation in Ti (etchTi1) and Zr (etchZr3), which can be explained by a longer etching duration in both cases and higher power used for Ti and higher power applied on the targets in the case of Zr. Finally, based on the results obtained for Ti^+ etching, the average amount of Ti and Zr species is about 11 at.% and 2 at.%, respectively, while for Zr^+ etching, it is 8 at.% Zr and 2 at.% Ti.

Table 3: Etching parameters and XPS quantification in (%) of atomic compositions on the Ti^+ etched sample surfaces.

		Etch Ti 1	Etch Ti 2	Etch Ti 3	Etch Ti 4	304L
Etching parameters	Duration (min)	20	20	5	5	/
	Target power (W)	2500	1500	1500	2500	
	Bias voltage (V)	-700	-500	-700	-500	
XPS analysis	%at Cr (metal)	7	7	7	7	5
	%metal Cr (oxide)	47	49	44	36	17
	%at Fe (metal)	10	12	20	16	21
	%at Fe (oxide)	12	19	10	29	47
	%at Ni	1	1	2	1	10
	%at Ti	21	10	6	8	/
	%at Zr	2	2	2	2	/

Table 4: Etching parameters and XPS quantification in (%) of atomic compositions on the Zr^+ etched sample surfaces.

		Etch Zr 1	Etch Zr 2	Etch Zr 3	Etch Zr 4	304L
	Duration (min)	5	5	20	20	/

Etching parameters	Target power (W)	2500	1500	2500	1500	
	Bias voltage (V)	-700	-500	-700	-500	
XPS analysis	%at Cr (metal)	7	8	6	5	5
	%metal Cr (oxide)	44	38	50	56	17
	%at Fe (metal)	17	18	11	9	21
	%at Fe (oxide)	25	25	18	22	47
	%at Ni	2	1	1	1	10
	%at Ti	1	2	2	2	/
	%at Zr	5	8	13	5	/

In conclusion, the results show that the highest ion implantation is obtained for shorter etching duration and higher ion energy for Ar^+ etching. In the case of Ti^+ etching, the highest ion implantation is performed for longer etching time, higher ion energy and higher ion flux whereas for Zr^+ etching the highest ion implantation is observed for longer etching duration, lower ion energy and higher ion flow.

1.1.2 Interface characterizations

The substrate/coating interface is investigated by TEM, which allows observing materials at the nanometric scale, and nanoindentation to study its mechanical properties. For this purpose, a 200-nm-thick layer is deposited after etching, to prevent any external contamination. After the etching step, all generators are switched off. They are switched on again for the deposition step. Chemical mapping and profiles are performed to find out the chemical composition of the interface, and to better understand processes taking place at this interface. The results obtained for a sample etched with Ar^+ ions and then coated with a 200-nm-thick Zr layer are presented in Figure 2. The interface between the coating and the substrate was represented as a dashed line and added to all elemental maps.

The TEM mapping confirms that Cr is present at the substrate/coating interface (substrate side), indicating that chromium is present at the extreme surface of the substrate. This result corroborates the hypothesis of chromium contamination coming from the vacuum chamber or the substrate-holder. This is confirmed by the TEM profile showing a slight increase in the counts of chromium at the interface. In addition, mapping shows that a slight increase of Ar and depletion of Fe and Ni can be observed in the near-interface substrate. Finally, the profile also allows estimating the thickness of the substrate/coating interface (area from the increase of the deposited material to the decrease of susbtrate material (mainly Fe)) to approximately 23 nm.

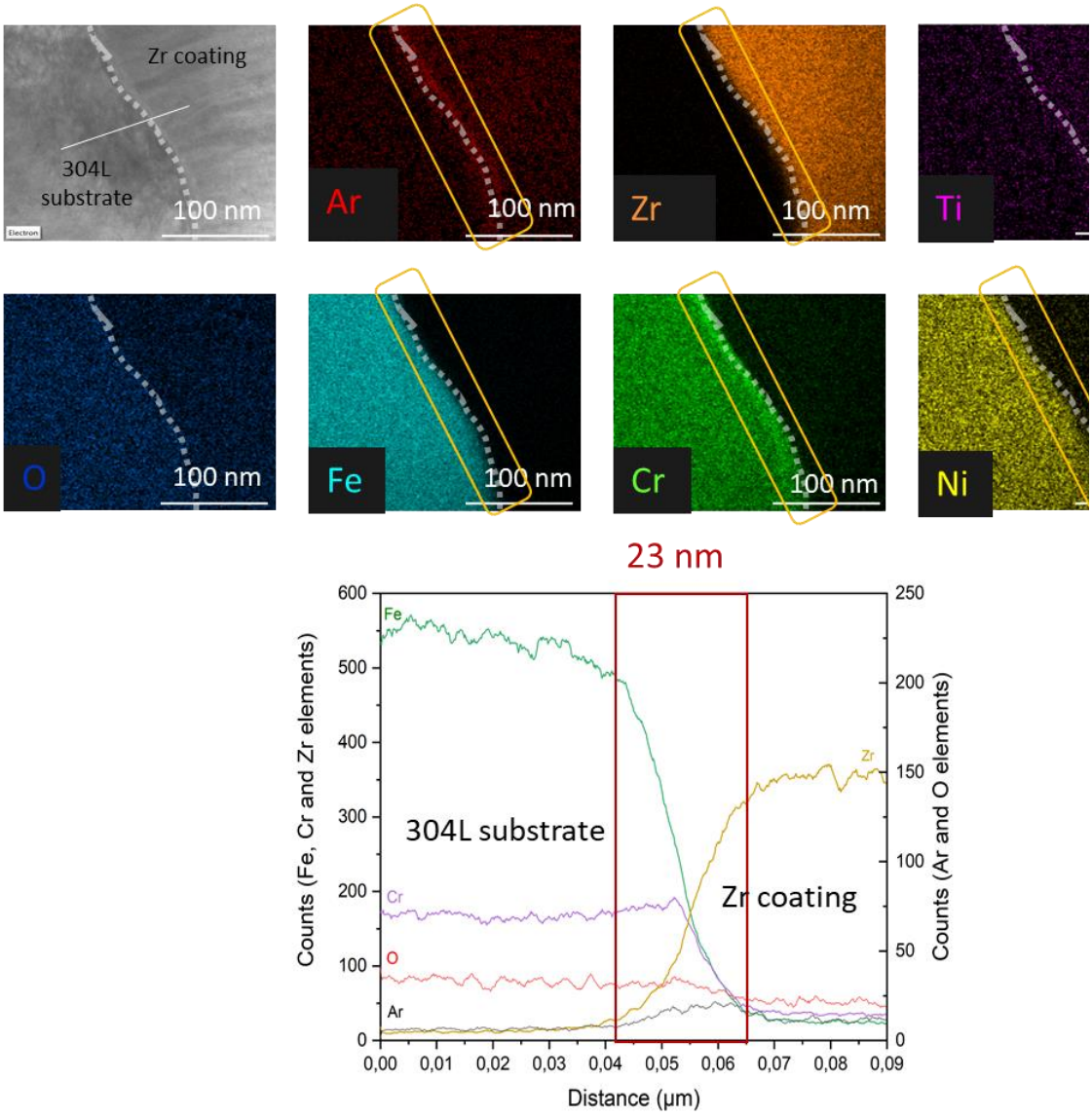

Figure 2: a) TEM mapping and b) TEM profile of an argon-etched and Zr-deposited sample and estimation of the interface thickness

The mechanical properties of etched samples are studied using the nanoindentation technique. The results are presented in Figure 3. They show that hardness of all etched samples is higher than that of substrate 304L, which is consistent with the literature indicating that an increase of hardness is expected after ion implantation process. However, hardness properties are statistically similar to one another for all types of etching. Etching allows ions to be implanted in small amounts and it seems that no significant differences in hardness measurements are observed for different etching parameters. Note however that the results are not only representative of the coating but also of the substrate (10% rule for indentation depth on coatings is not respected).

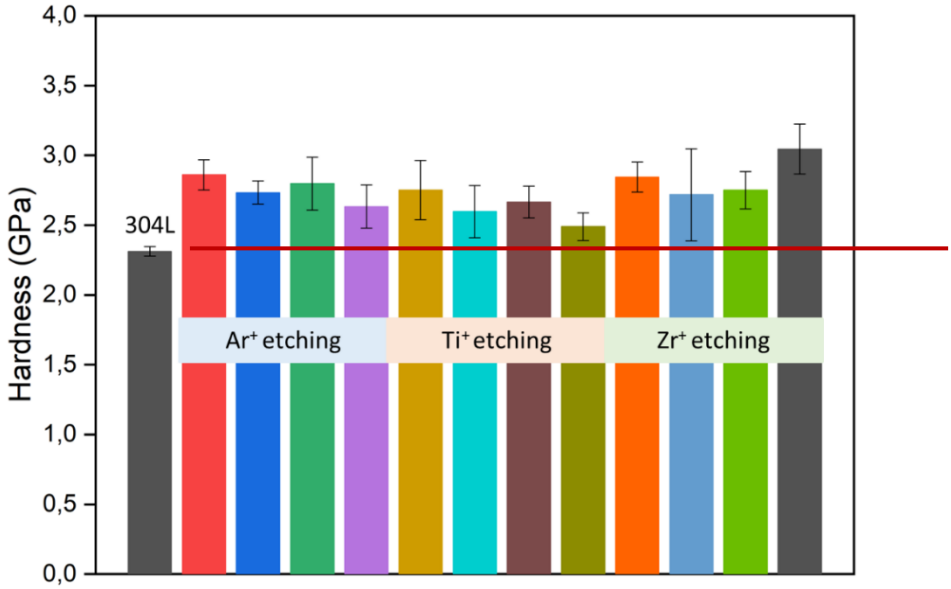

Figure 3: Hardness measurements of etched samples compared to 304L substrate obtained by nanoindentation technique

The TEM analysis confirmed the contamination observed previously and the measurement of hardness does not allow concluding on the influence of etching on the mechanical properties. This contamination may play a part in the hardness. The only way to validate the results obtained so far is to reduce or even eliminate this contamination.

1.1.3 Electrochemical measurements

In addition, anodic polarization measurements are performed in a 5 wt% NaCl solution to understand the etched samples properties against corrosion. The results are summarized in Figure 4 and showed that all etchings shift corrosion potential to more positive values (-0.11 to 0.05 V/NHE), which is consistent with a surface oxidation. Etched surfaces usually appear to decrease the corrosion current density (from 10^{-7} to 10^{-8} A/cm²) and become nobler than the bare 304L substrate. This can be explained by the densification of the interface due to an ion bombardment and to the chemical modification of the native oxide layer or to the formation of more reactive surface defects, which accelerates the formation of a passive layer. In addition, no relationship between the etching parameters and the polarization curves obtained seems to appear. In conclusion, the best corrosion protection can be obtained for these etchings: Zr^+ etching (etchZr4) > Ti^+ etching (etchTi1) > Ar^+ etching (etchAr1). Note that the improvement in corrosion resistance may be related to the etching itself, to contamination (especially Cr) or both.

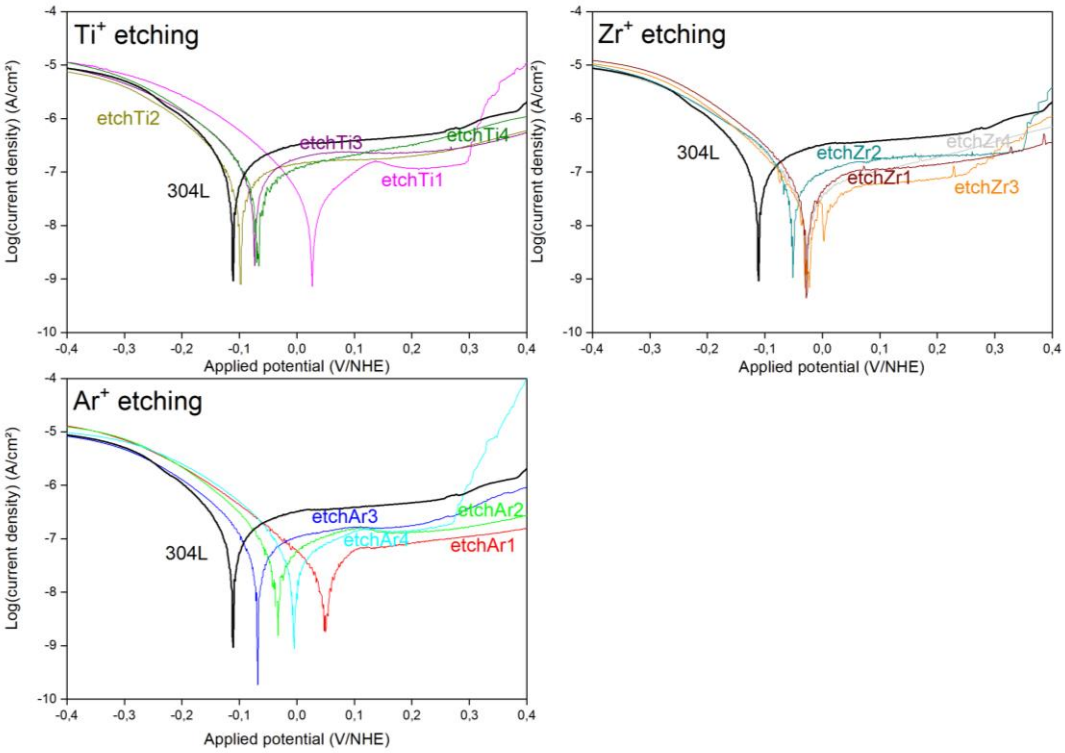

Figure 4: Comparison of anodic polarization curves for bare 304L and etched samples after 6 h in a 5 wt% NaCl solution

Cr, Fe and Ni are present on the extreme surface before and after etching. These species come mainly from the substrate used. However, a modification of their concentration after etching is observed compared to the concentration of the bare 304L stainless steel. This modification can be due to several factors: the surface treatment leading to ion implantation and/or contamination coming from the walls of the vacuum chamber and the substrate-holder. Consequently, it is necessary to try to reduce or even eliminate the contamination to be sure that the good performance observed is only due to etching.

2. OPTIMIZATION OF ETCHING PARAMETERS TO REDUCE CONTAMINATIONS

Different approaches have been tested in order to reduce the previously identified contamination (mainly Cr) and are summarized below. All these methods involve etching in a static position. In addition, a preliminary treatment of the deposition chamber is performed by preliminarily covering the substrate-holder and the walls of the deposition chamber with the material to be deposited. The aim is to limit contamination from resputtering of the substrate-holder and/or the chamber walls.

2.1 ALUMINUM PLATE TECHNIQUE

The first approach to reduce the contamination was to change the configuration of the substrates in the deposition chamber. For this purpose, aluminum plates were used as substrate support. They were attached to the substrate-holder and then the chamber was covered with the material to be deposited (named pre-treatment of chamber). Following this one-hour pre-treatment, the substrates were fixed with Kapton tape to the aluminum plates to replace the stainless-steel suspension wires previously used (Figure 5). The use

of these plates prevented the rotation of the substrate-holder. These plates were then placed in front of one target of the chosen material (Ti or Zr). The same three etchings types were studied. Their parameters are presented in Table 5.

Table 5: Etching parameters used with aluminum plates.

Parameters	Ti^+ etching	Ti^+ etching	Ar^+ etching (A)	Ar^+ etching (C)	Zr^+ etching	Zr^+ etching
Pressure (Pa)	0,57	0,57	0,97	0,97	0,57	0,57
Argon flow (sccm)	100	100	100	100	100	100
Duration (min)	20	20	5	20	20	20
Target voltage (V)	900	900	X	X	900	900
Pulse width (µs)	20	20	X	X	20	20
Extinction time (µs)	1980	1980	X	X	1980	1980
Frequency (Hz)	250	250	X	X	250	250
Substrate-holder voltage (V)	-700	-700	-900	-900	-700	-700

Figure 5: Substrates arrangement in the chamber for the aluminum plate technique

The various surfaces of the etched samples are analyzed using XPS technique (Figure 6) and, if necessary, their chemical composition at the extreme surface is quantified from the resulting XPS spectra. XPS wide-scan spectra of the three etched samples are shown below and compared to that of the bare substrate 304L. The results highlight that substrate peaks (Fe, Cr and Ni) are still visible on the XPS spectrum after the Ar^+ etching, indicating that an etching has been indeed performed. However, in the case of Ti^+ and Zr^+ etchings, only the Cr peak is observed. The intensity of the Ti and Zr peaks is very high, which suggests that a thin Ti or a Zr layer was deposited instead of the intended etching action. This shows that this aluminum plate technique works for Ar^+ etching but not for metal ion etching. It is therefore possible to quantify the results obtained for the Ar^+ etching as shown in Table 6.

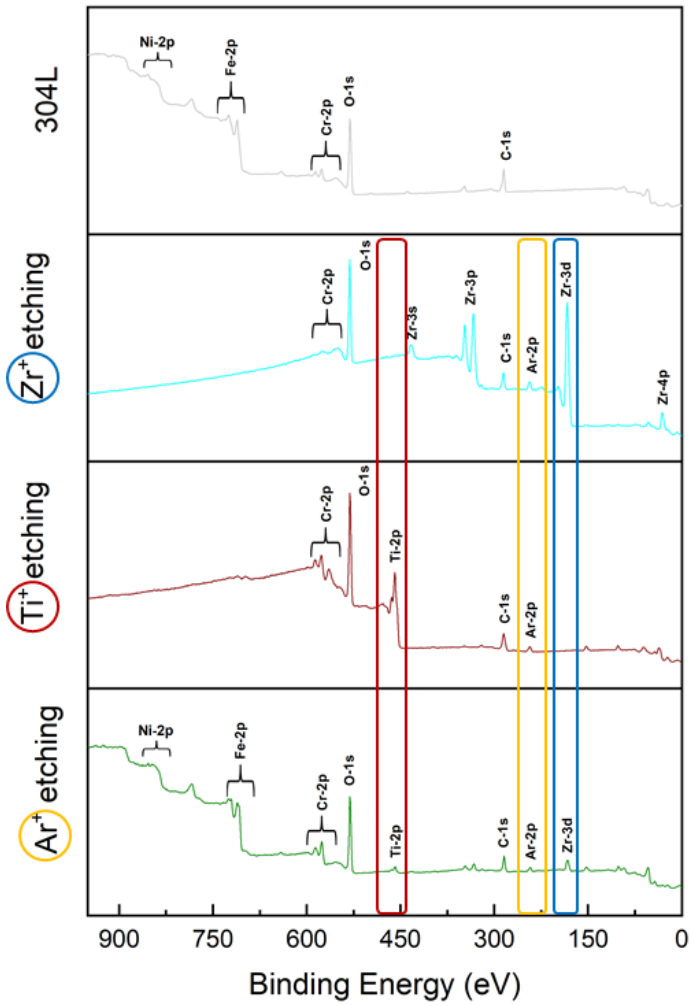

Figure 6: XPS wide-scan spectra of etched samples suing the aluminum plate technique compared to the bare 304L substrate

Chemical quantification from Ar^+ etching XPS spectra shows the presence of Ar (6 and 8 at.%), Ti (4 and 8 at.%) and Zr (9 and 11 at.%) on the samples surface. It is consistent to note the presence of Ar because Ar species are sputtered and the plasmagenic gas used is argon. In addition, Ti and Zr targets are present inside the vacuum chamber and their covers are open to obtain a sufficient magnetic field to ignite the argon plasma used for this etching, which may explain the presence of Ti and Zr. In addition, the amount of oxidized chromium is around 10-13 at.%, which is quite lower than the previous Ar^+ etchings.

This could indicate that the chromium contamination is reduced using this method. Finally, the amounts of chromium metal and iron metal are higher than previous Ar+ etchings, which could show that the etching is effective and that the metal substrate appears using XPS analysis. In addition, the absence of aluminum is to be noted and can be explained by the effectiveness of the pre-treatment of the vacuum chamber before etching (chamber elements coated with the material of interest).

Table 6: Etching parameters and XPS quantification in (%) of atomic compositions on the etched sample surfaces using aluminum plate technique

		Etch Ar A	Etch Ar C
Etching parameters	Pressure (Pa)	0.9	0.9
	Duration (min)	5	10
	Bias voltage (V)	- 900	
XPS analysis	%at Cr (metal)	6	13
	%metal Cr (oxide)	10	13
	%at Fe (metal)	25	25
	%at Fe (oxide)	32	17
	%at Ni	9	3
	%at Ti	4	8
	%at Zr	9	11
	%at Ar	6	8

Although this method seems effective with Ar^+ etching, an alternative approach that would reduce contamination for all etchings have to be investigated. This would be complicated if different contamination reduction methods were to be used for different etching processes. In addition, it would make it difficult to certify the reproducibility of the experiments.

2.2 NEW TECHNIQUE

The second approach was to change the etching parameters. For this purpose, suspension wires of stainless steel were used to suspend the substrates. A three-hour pre-treatment of the deposition chamber was performed to coat with the material of interest as many of the elements present in the chamber as possible, particularly the suspension wires. The etching parameters were selected after several etching tests and their effectiveness verified by XPS analysis. During these three etching processes, the bias voltage was the same whereas the power and voltage varied (Table 7).

Table 7: Parameters of etchings using the new technique.

Parameters	Ti^+ etching	Zr^+ etching	Ar^+ etching
Pressure (Pa)	0,57	0,57	0,97
Argon flow (sccm)	100	100	100
Duration (min)	20	20	20
Target voltage (V)	600	400	X
Pulse width (µs)	20	20	X
Extinction time (µs)	1980	1980	X
Frequency (Hz)	250	250	X
Substrate-holder voltage (V)	-900	-900	-900

The surface modification involved by the different etching processes is analyzed using XPS. Wide-scan spectra of the three etched samples are shown in Figure 7a and compared to the 304L substrate. In addition, chemical quantification from XPS spectra is performed to identify the amount of the extreme surface elements (Figure 7b). The results highlight that substrate peaks (Fe, Cr and Ni) and external contamination peaks (C and O) are visible on all XPS spectra. Ar peaks are observed on all XPS spectra because the plasmagenic gas used is argon. Therefore, Ar species are sputtered during all etchings and integrate the samples. In the case of Ti^+ etching, Ti and Ar peaks are visible. The same applies to Zr^+ etching.

a)

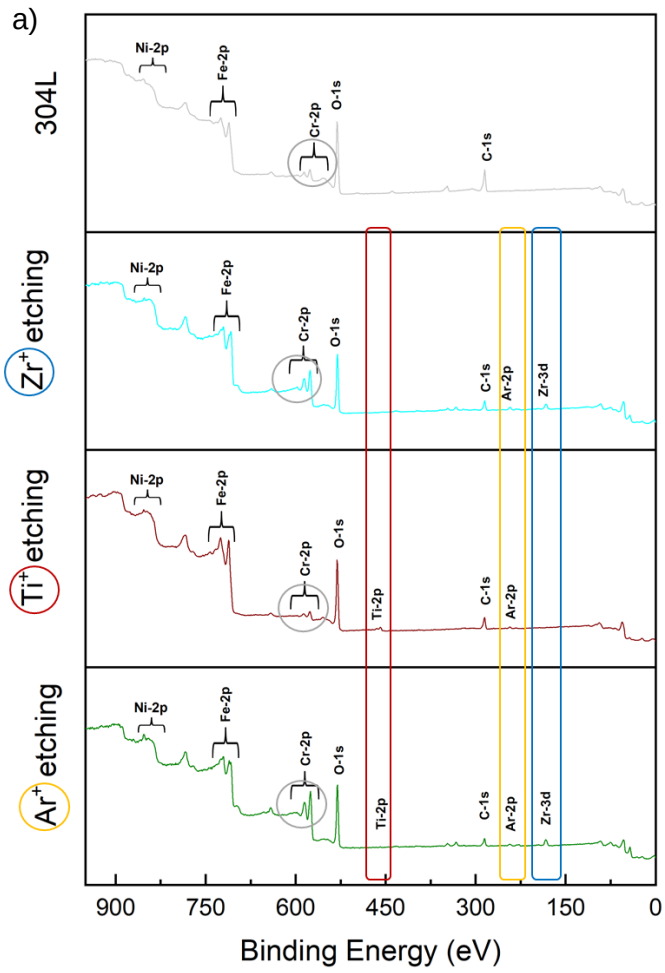

b)	Ti^+ etching	Zr^+ etching	Ar^+ etching
%at Cr (metal)	5	16	32
%metal Cr (oxide)	7	21	15
%at Fe (metal)	20	30	21
%at Ni	48	17	14
%at Ti	6	4	5
%at Zr	7	1	1
%at Zr	1	6	7
%at Ar	5	6	4

Figure 7: a) XPS wide-scan spectra of etched samples suing the new technique compared to the bare 304L substrate and b) XPS quantification in (%) of atomic compositions of the etched sample surfaces

Chemical quantification from XPS spectra confirms the presence of Ar (4 at.%) and Zr (7 at.%) on the surface of the Ar^+-etched samples but also a very small amount of Ti (1 at.%). The relatively high amount of Zr (7 at.%) compared to Ar could be explained by the chronology of the etchings because the Ar^+ etching tests were performed after the Zr^+ ones. Moreover, in the case of Ar^+ etching, the pre-treatment of the deposition chamber uses a mixture of Ti and Zr to coat the interior of the chamber. This may involve a higher amount of Zr inside the vacuum chamber and therefore a higher resputtering of this element. The amount of Ar is approximately constant for the three etchings. In the case of Ti^+ etching, chemical quantification confirms the presence of Ti (7 at.%) and small amount of Zr (1 at.%) on the etched samples surfaces and for Zr^+ etching, the presence of 6 at.% of Zr and Ti (1 at.%) is observed.

The effectiveness of the contamination reduction method is determined by comparing the results of the two etching test series (2019: with contamination and 2020: with the new technique). The results (Table 8) show that the amount of oxidized chromium has significantly decreased for the three etching tests compared to the previous ones, which seems to indicate that the native surface oxide layer is no longer chromium-based. It

appears that this layer is chromium and iron based or iron-based in the case of the Ti^+ etching (48 at.% Fe ox). In addition, the results show that globally the amount of iron, nickel and chromium metal has increased compared to previous etchings, indicating the metallic substrate observation and showing the efficiency of this new etching method.

Table 8: Comparison of XPS quantification in (%) of atomic compositions of the etched sample surfaces with contamination (2019) and with the new technique (2020)

Name		Ti^+ etching (2019)	Ti^+ etching (2020)	Zr^+ etching (2019)	Zr^+ etching (2020)	Ar^+ etching (2019)	Ar^+ etching (2020)	304L
At. % Cr metal		7	5	5	16	6	32	5
At. % Cr oxide		49	7	57	21	50	15	17
At. % Fe metal		12	20	9	30	13	21	21
At. % Fe oxide		20	48	22	17	23	14	47
At. % Ni		1	6	1	4	2	5	10
6 hours	*Ecorr (V/NHE)*	1.07	1.05	1.1	1.08	1.08	1.07	0.98
	Jcorr (mA/cm²)	5.10^{-4}	1.10^{-4}	5.10^{-4}	1.10^{-4}	3.10^{-4}	4.10^{-4}	1.10^{-3}

During previous etchings, the contaminating elements were mainly in their oxide state because they had been deposited on the extreme surface and therefore oxidized as soon as they were exposed to air. However, these new etchings show distinct results, especially such as the presence of elements in their metallic states.

In conclusion, the influence of etching on substrate/coating interface was investigated. The first results showed the presence of contamination at the interface, mainly chromium contamination according to the results obtained by XPS and TEM analyzes. Two different approaches to reduce contamination were then studied. It seems that a method relying on a three-hour pre-treatment of the vacuum chamber and modification of etching parameters allows the amount of oxidized chromium on the extreme surface to be reduced for all etching processes.

APPENDIX 2: CORROSION RESISTANCE OF THE METAL BOND COAT WITH INTERFACE CONTAMINATION

Immersion tests and electrochemical measurements are performed to investigate the effect of the interface contamination on the corrosion resistance of the metal bond coat. These tests are carried out in the laboratory, and in an outdoor environment for immersion tests in a marine environment on etched + coated samples. The results are presented as weight changes after immersion for immersion tests and polarization curves for electrochemical measurements.

1. ELECTROCHEMICAL MEASUREMENTS

1.1 IN SALINE ENVIRONMENT

Electrochemical measurements are performed in saline environment at ambient temperature (5 wt% NaCl 20°C) and the results are presented and explained below (Figure 1). The corrosion potential of the bare 304L stainless steel after 24 hours of OCP is around -0.11 V/NHE. In addition, Ti and Zr coatings induce a shift of the corrosion potential towards positive values. Ti^+ etching performed prior to Ti coating seems to further shift corrosion potential to positive values, which means that the material becomes nobler. Contrary to these results, only two Zr^+ etching appear to further shift corrosion potential to positive values.

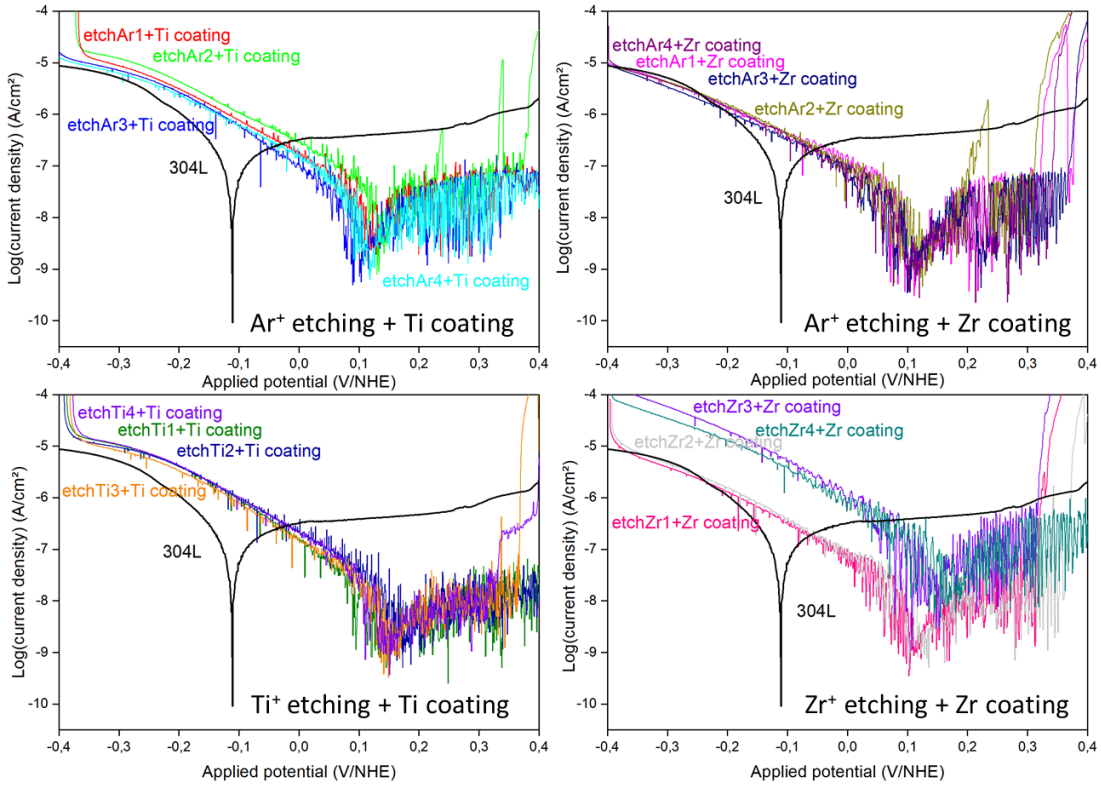

Figure 1: Comparison of anodic polarization curves for bare 304L and coated samples in a 5 wt% NaCl solution

In addition, Ti and Zr coatings lead to decrease of the corrosion current density compared to bare 304L stainless steel. Nevertheless, two Zr^+ etching (etchZr3 and etchZr4) reduce the corrosion current density less than the others. These results imply that Ti and Zr coatings provide good protection against corrosion, showing more positive corrosion potential and lower corrosion current density (Figure 1).

1.2 IN NUCLEAR FUEL REPROCESSING ENVIRONMENT

Electrochemical measurements are performed in a simplified nuclear fuel reprocessing solution (2.5 mol/L HNO_3, 2.5 mol/L $NaNO_3$, 2 g/L $Fe(NO_3)_3$ at 110°C) on etched + coated samples before and after etching optimization. Additional measurements are carried out to enable a more precise understanding of the phenomena occurring at the coating/environment interface. Etched-only and etched + coated samples are studied using electrochemical tests to understand the substrate/coating and coating/environment interfaces. The electrochemical results obtained for etched-only samples are summarized in Figure 2 (etchAr1, etchTi1 and etchZr4). The corrosion potential of the bare 304L stainless steel after 6 hours of OCP is around 0.98 V/NHE (Figure 2a)) and 0.96 V/NHE after 2 days (Figure 2b)). Etching only induces a shift of the corrosion potential towards positive values (up to 1.10 V/NHE), indicating a nobler sample surface. Moreover, it leads to a decrease of the corrosion current density compared to bare 304L stainless steel after 6 hours (10^{-3} for 304L to 10^{-4} mA/cm² for etchings). These results imply that etching improves corrosion protection at this moment, resulting in more positive corrosion potential and lower corrosion current density (Figure 2). However, after 2 days of experiment, it seems that Ar^+ etching decreases the corrosion current density more than other etchings. Indeed, comparison of corrosion current densities after 6 hours and 2 days of experiment show that the steepest decrease of these values is observed for Ar^+ etching only. However, these samples are contaminated mainly with Fe and Cr, which may affect the results. Post-test analyses were performed using optical microscopy and Raman spectroscopy. The results obtained in Raman spectroscopy show the presence of iron-oxide on the surface in the area that was in contact with the solution.

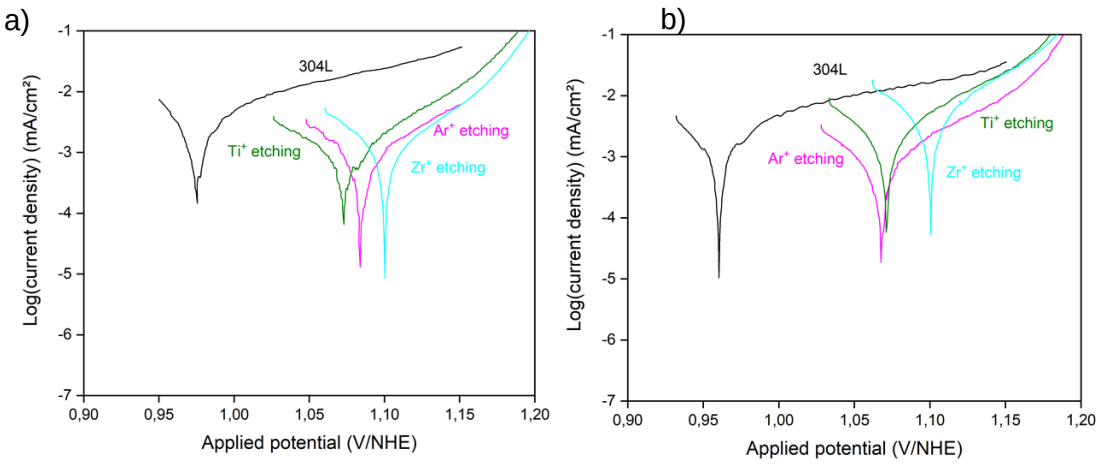

Figure 2: Anodic polarization curves of etched samples in a nitric acid solution at boiling temperature (2.5 mol/L HNO_3, 2.5 mol/L $NaNO_3$, 2 g/L $Fe(NO_3)_3$ at 110°C) after a) 6 h and b) 2 days compared to bare 304L before etching optimization

The etched + coated samples are studied using electrochemical tests and the results are compared to other materials such as bulk Ti, bulk Ta, bulk Zr and Ta coating (Figure 3). Tantalum is the currently studied material to be used as corrosion protection in the nuclear field for various applications. They indicate that corrosion potentials of bulk Ta and Ta coating after 6 hours of OCP are more positive, and their corrosion current density are lower, than bare 304L substrate (10^{-3} for 304L to 10^{-5} mA/cm² for Ta component). Similar results in corrosion potential and corrosion current density are obtained for Zr bulk. In addition, bulk Ti sample shows a more negative corrosion potential than 304L substrate, indicating a less noble sample surface and its corrosion current density (10^{-4} mA/cm²) is smaller than bare 304L (10^{-3} mA/cm²). Shifts of the corrosion potential towards negative and positive values are observed for the different samples (Figure 3). These shifts can be explained by an influence of surface roughness, coating microstructure and defects or experimental conditions (slight variation in temperature, concentration or volume of solution).

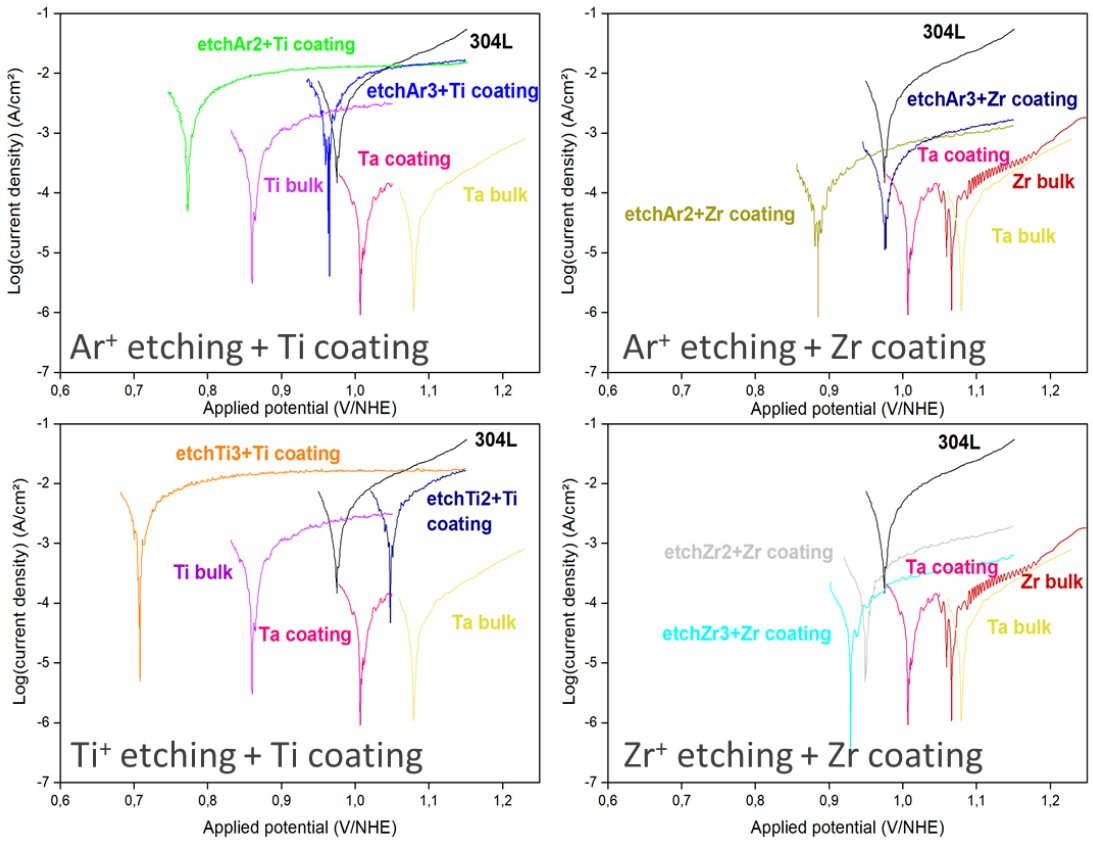

Figure 3: Anodic polarization curves of coated samples in a nitric acid solution at boiling temperature (2.5 mol/L HNO_3, 2.5 mol/L $NaNO_3$, 2 g/L $Fe(NO_3)_3$ at 110°C) after 6 hours compared to other materials before etching optimization

The corrosion current density of Ti coatings is of the same order of magnitude as that of bare 304L stainless steel (10^{-3} mA/cm²). In contrast, the results indicate a lower corrosion current density for Zr (10^{-5} mA/cm²) compared to bare 304L (10^{-3} mA/cm²). All these

electrochemical results show improvement of corrosion protection of bare 304L stainless steel by the deposition of thin Zr coatings.

2. IMMERSION TESTS

Immersion tests are performed in three environments:

- Singapore seawater at ambient temperature (29-30°C),
- 3.56 wt% NaCl solution at ambient temperature (20°C),
- and nitric acid solution at boiling temperature (110°C).

The results are presented and explained below.

2.1 SINGAPORE SEAWATER

Coated samples are immersed during 15 days in natural seawater at Sentosa, Singapore, at a depth of 2 meters. The weight of all samples has increased whether it is the bare 304L substrate or the coated samples as shown in Figure 4.

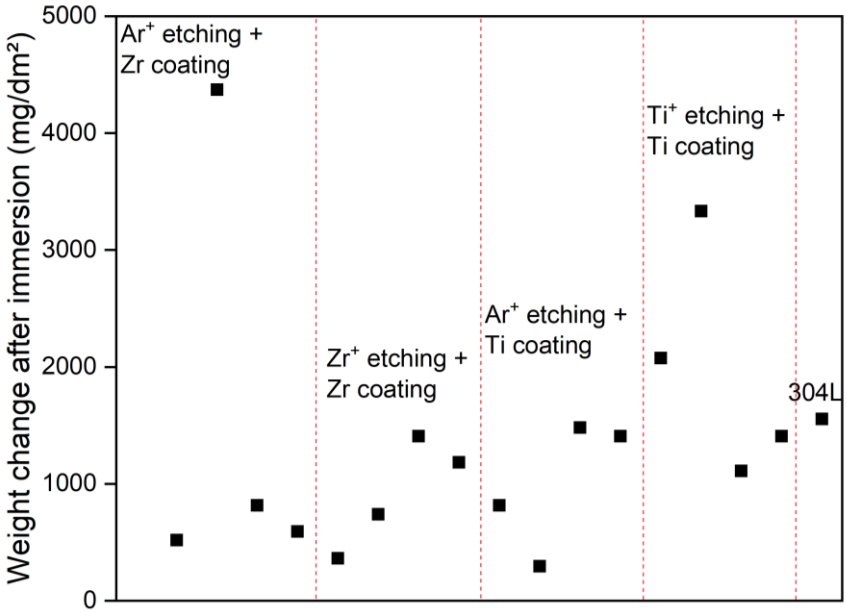

Figure 4: Weight change measurements after 15 days of immersion in natural seawater at Sentosa at ambient temperature (29-30°C)

However, these results showed that most of the coated samples had a smaller weight gain than bare 304L substrate, resulting in a better protection of the stainless steel in this environment. Moreover, it seems that this weight gain varies from one sample to another depending on the etching + coating system considered. Weight gain values are mostly between +300 and +1500 mg/dm², only three values are higher. This increase could be explained by the formation of fouling and/or oxides on the sample surface.

2.2 IN A 3.56 WT.% NACL SOLUTION

Coated samples are immersed during 24 hours in a 3.56 wt.% NaCl solution and this cycle is repeated five times to reach a total immersion time of 120 hours. No difference is observed after 120 hours of immersion in a 3.56 wt.% NaCl solution as shown in Figure 5.

Figure 5: Naked-eye observation of coated sample before and after 120 h of immersion in 3.56 wt.% NaCl solution

The results after 24 hours of immersion are summarized in Figure 6. The weight of all samples has decreased and this could be explained by the sample surface degradation caused by the environment. Moreover, the decrease appears to be smaller for Ti coatings (0 to - 0.1 mg/cm²) than for Zr coatings (- 0.1 to - 0.35 mg/dm²) indicating that Ti coatings could be more resistant in this aggressive environment compared to Zr coatings.

a)

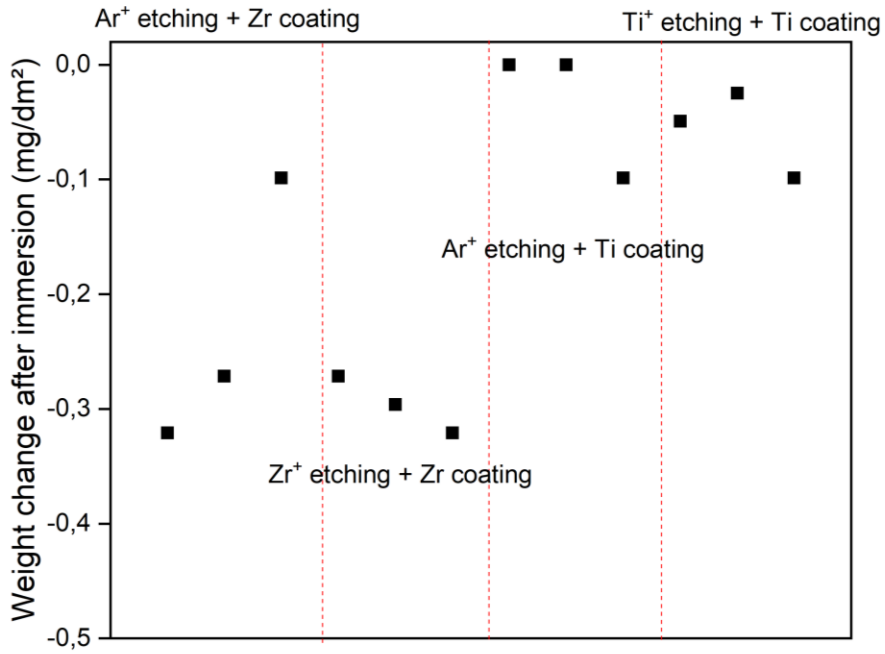

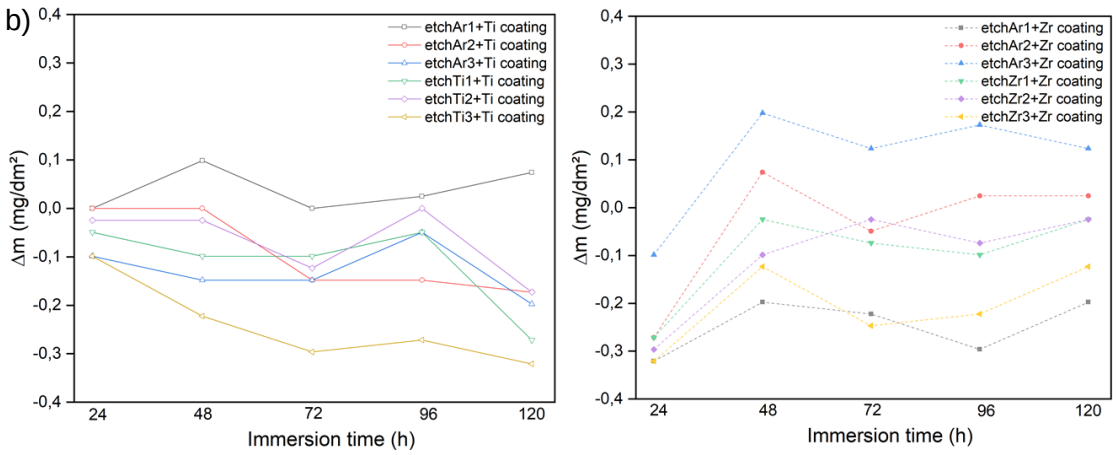

Figure 6: a) weight change measurements after 24 hours of immersion and b) kinetics of weight change during immersion in 3.56 wt.% NaCl solution at ambient temperature (20°C)

2.3 NITRIC ACID SOLUTION

Coated samples are immersed during 24 hours in a nitric acid solution (2.5 mol/L HNO_3, 2.5 mol/L $NaNO_3$, 2 g/L $Fe(NO_3)_3$ at 110°C) and this cycle is repeated five times to reach a total immersion time of 120 hours. The results after 24 hours of immersion are presented in Figure 7. The weight of all samples have decreased suggesting sample surface degradation caused by the aggressive environment. Moreover, the decrease appears to be smaller for Zr coatings (- 2 to - 6 mg/dm²) than for Ti coatings (- 7 to - 10 mg/dm²) compared to the previous results in 3.56 wt% NaCl solution. These results indicate that Zr coatings are probably more resistant in this aggressive environment compared to Ti coatings. The poor resistance of Ti coatings is unexpected, so further analyses of the sample surface after immersion are performed to understand the origin of this behavior. XPS is the most suitable technique to continue this analysis because it allows us to observe the extreme surface and to perform concentration profiles in depth to observe the evolution of our coatings after immersion.

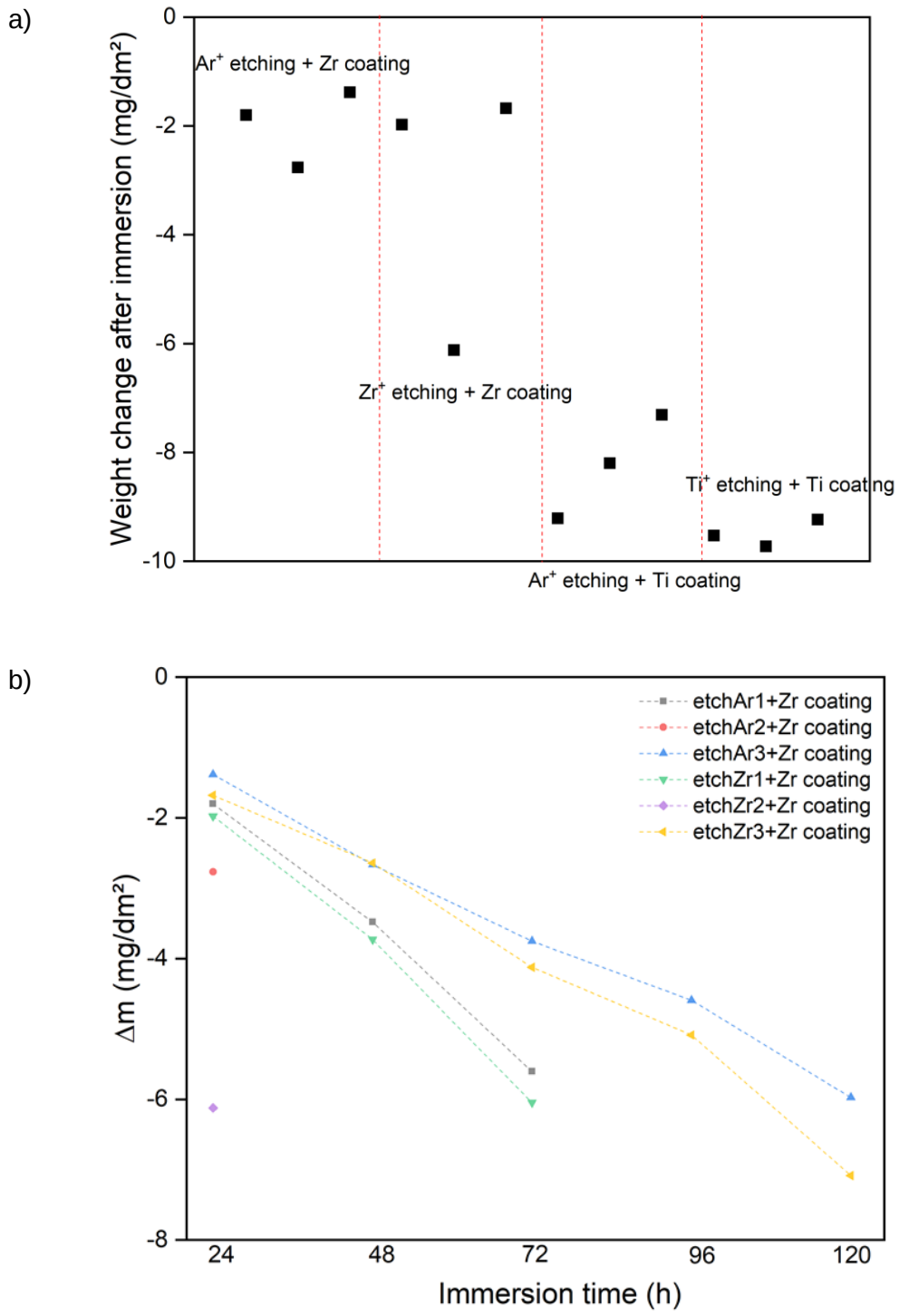

Figure 7: a) weight change after 24 hours of immersion and b) kinetics of weight change of Zr-coated samples during immersion in a nitric acid solution at boiling temperature (2.5 mol/L HNO_3, 2.5 mol/L $NaNO_3$, 2 g/L $Fe(NO_3)_3$ at 110°C)

The XPS analysis performed on two Ti coatings and two Zr coatings after 24 h of immersion in reprocessing nitric acid solution at boiling temperature are summarized in Figure 8. XPS wide-scan of two Ti coatings shows different behaviors: Ti is no longer present on the surface of the Ar^+-etched and Ti-coated sample whereas the Ti^+-etched and Ti-coated sample has a small amount of Ti on its surface (Figure 8a)). However, the substrate elements are conspicuous (Fe and Cr) indicating that this Ti amount is limited

and does not block the XPS signal of the substrate. Thus, Ti coating is dissolved during the immersion and therefore could not effectively protect against corrosion in this environment. These results are confirmed by SEM analysis. The formation of this oxide layer needs several steps before the protective TiO_2 is obtained: $TiO \rightarrow Ti_2O_3/TiO_2$ (mixed oxide) $\rightarrow Ti_5O_9$ or $Ti_6O_{11} \rightarrow Ti_3O_5 \rightarrow TiO_2$. The non-stoichiometric oxides formed during these steps (for example, Ti_2O_3 and Ti_3O_5) can dissolve rapidly in concentrated solutions. Consequently, the dissolution can be explained by the passive layer (TiO_2) on the surface of the Ti coating, which could not form quickly enough and stabilize properly. In contrast, XPS wide-scans of two Zr coatings showed that Zr coatings are always present on the surface unlike the previous Ti coatings (Figure 8b)). In addition, the presence of O can be attributed to surface contamination even though a layer of ZrO_2 is likely to form on the extreme surface. The detailed analysis of the Zr spectrum shows that Zr is in oxide state, which corroborates the hypothesis of the formation of a ZrO_2 layer. XPS depth profiles can help to validate this hypothesis and are presented below (Figure 9).

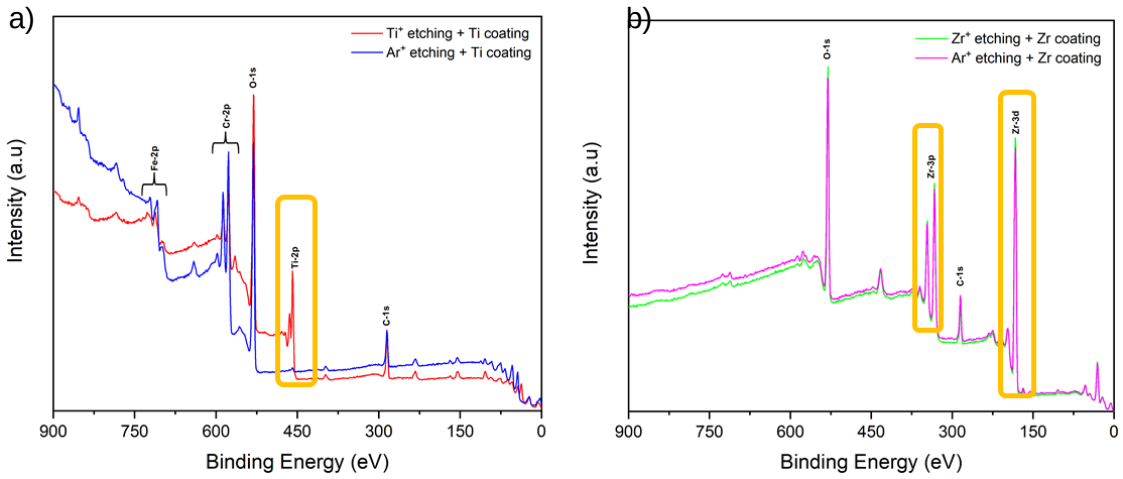

Figure 8: Comparison of XPS wide-scan after 24 hours of immersion in a nitric acid solution at boiling temperature (2.5 mol/L HNO_3, 2.5 mol/L $NaNO_3$, 2 g/L $Fe(NO_3)_3$ at 110°C) of a) Ti coating and b) Zr coating

Figure 9 shows XPS depth profiles on samples immersed in a reprocessing nitric acid solution at boiling temperature for two durations of (a) 24 h and b) 120 h). The results indicate that a zirconium oxide film is formed on the surface after 24 hours and that the thickness of this oxide layer increases with immersion time. The XPS quantification and Raman analysis performed after the immersions seem to show that the oxide film is a ZrO_2 layer. In addition, these profiles show a shift in the erosion time of the ZrO_2 layer/Zr coating interface and the Zr coating/304L substrate interface. Additional XPS depth profile are performed on the same sample at different durations (0, 48 and 72 h) to follow more precisely the formation and growth of this ZrO_2 layer (not shown here).

b)

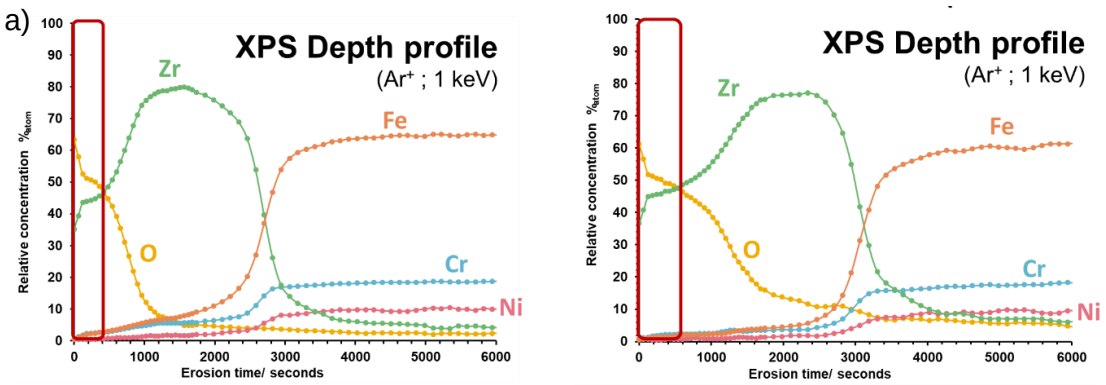

Figure 9: XPS profile showing the formation of a ZrO_2 thin layer at the extreme surface of Zr coating after a) 24 h and b) 120 h of immersion in a nitric acid solution at boiling temperature (2.5 mol/L HNO_3, 2.5 mol/L $NaNO_3$, 2 g/L $Fe(NO_3)_3$ at 110°C)

In conclusion, corrosion resistance properties are studied using immersion and electrochemical techniques. The results show that Ti and Zr coatings provide a good corrosion protection in saline environment. In contrast, in nitric acid environment (Table 1), all results seem to indicate that Ti coatings deposited over surfaces contaminated during etching offer no protection against corrosion (immersion tests and electrochemical measurements).

Table 1: Summary of all E_{corr} and J_{corr} values obtained in a nitric acid solution at boiling temperature (2.5 mol/L HNO_3, 2.5 mol/L $NaNO_3$, 2 g/L $Fe(NO_3)_3$ at 110°C) with and without interface contamination.

Sample	*6 hours*	
	Ecorr (V/NHE)	*Jcorr (mA/cm²)*
304L	*0.98*	*1.10^{-3}*
With interface contamination (2019)		
Etch Ar + Ti band coat	*0.8 à 1*	*1.10^{-3}*
Etch Ti + Ti band coat	*0.7 à 1*	*1.10^{-3}*
Etch Ar + Zr band coat	*0.9*	*4 à 8.10^{-5}*
Etch Zr + Zr band coat	*0.9*	*à à 6.10^{-5}*
Without interface contamination (2020)		
Etch Ar + Ti band coat	*0.92*	*1.10^{-4}*
Etch Ti + Ti band coat	*1.02*	*1.10^{-4}*

Etch Ar + Zr band coat	*0.86*	*1.10^{-4}*
Etch Zr + Zr band coat	*0.82*	*2.10^{5}*

However, after etching optimization, *i.e.* reduction of contamination, it is clear that the corrosion resistance properties of Ti coatings are improved. Zr coatings protect against corrosion in both cases (before and after etching optimization) even if there are significant differences. In particular, the protective effect of the Zr coating is lower with Ar^+ etching or without etching. Finally, after etching optimization, Ti and Zr coatings provide good protection against corrosion in the simplified nuclear fuel reprocessing environment. This study highlights the detrimental effect of residual contaminations, such as resputtering of previous materials deposited on the chamber walls, on the corrosion resistance of PVD coating.

APPENDIX 3: BODE DIAGRAMS OF TI- AND ZR-BASED OXIDE COATINGS SHOWING THE PRESENCE OF POROSITY

The EIS data of the Ti- and Zr-based coatings can be fitted using an equivalent electrical circuit, which is shown in Figure 1. In this model, R_e is the resistance of the electrolyte, R_t is the charge transfer resistance and CPE indicates a constant phase element characterized by parameters α and Q.

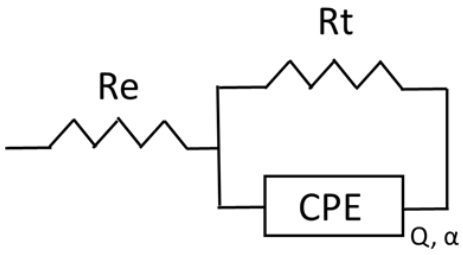

Figure 1: Equivalent electrical circuit of the coated substrates in a nitric acid (2.5 mol/L HNO_3, 2.5 mol/L $NaNO_3$ and 2 g/L $Fe(NO_3)_3$) solution at 110°C.

The imaginary part of the impedance (Im(Z)) is plotted as a function of the frequency (Figure 2) to determine the α parameter. If only one slope is observed (green circled on Figure 2) *i.e.* one time constant, its value is estimated at high frequency at – α. Then, the CPE coefficient (Q), which is defined from the imaginary part of the impedance by Equation 1 can be calculated.:

$$Q_{eff} = sin(\frac{\alpha\pi}{2}) \frac{-1}{Im(Z)(2\pi f)^{\alpha}} \qquad \textit{Equation 3}$$

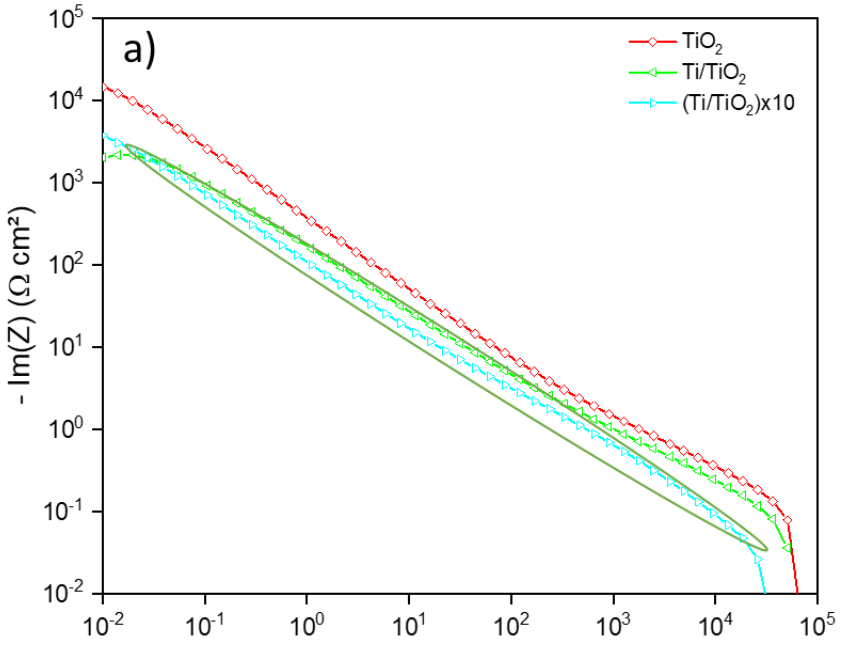

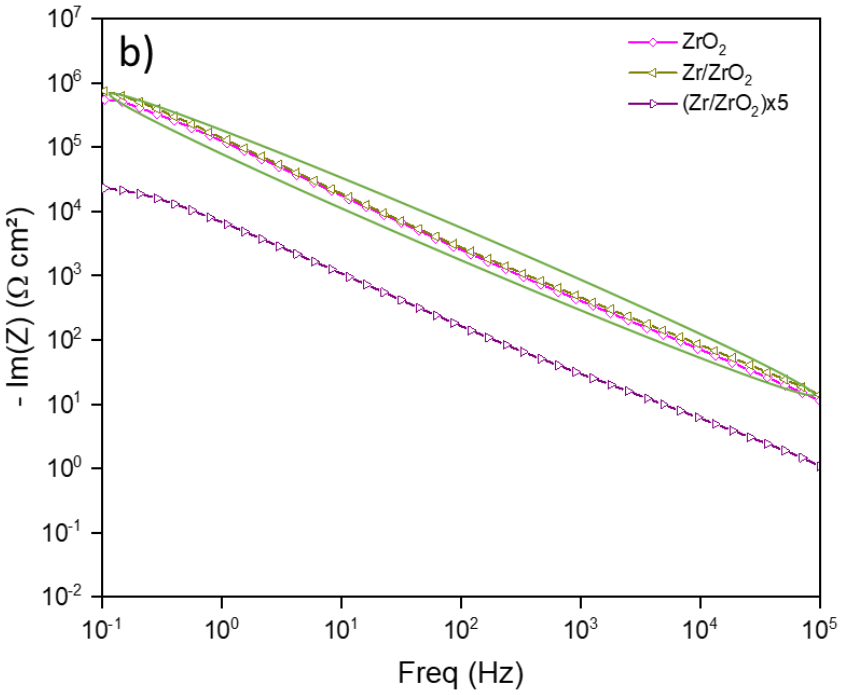

Figure 2: Imaginary part of the impedance as a function de frequency of a) Ti- and b) Zr-based coatings after immersion in a nitric acid (2.5 mol/L HNO_3, 2.5 mol/L $NaNO_3$ and 2 g/L $Fe(NO_3)_3$) solution at 110°C – focus on single slope curves.

However, in some cases, the values of the CPE parameters could not be determined as for TiO_2, Ti/TiO_2 and (Zr/ZrO_2)×5 coatings after 2 d of immersion. This is due to the non-linearity of the Im(Z) *vs.* frequency curve (Figure 3). In fact, two slopes can be observed on these curves indicating two time constants (circled on Figure 3) and thus, more complex phenomena than for the other samples. This is probably due to the presence of porosity and therefore, this requires the implementation of a new equivalent electrical circuit with a component associated with this porosity. An example of the electrical circuit equivalent that could be used is shown in Figure 4. However, more detailed calculations are needed to determine the validity of this equivalent circuit.

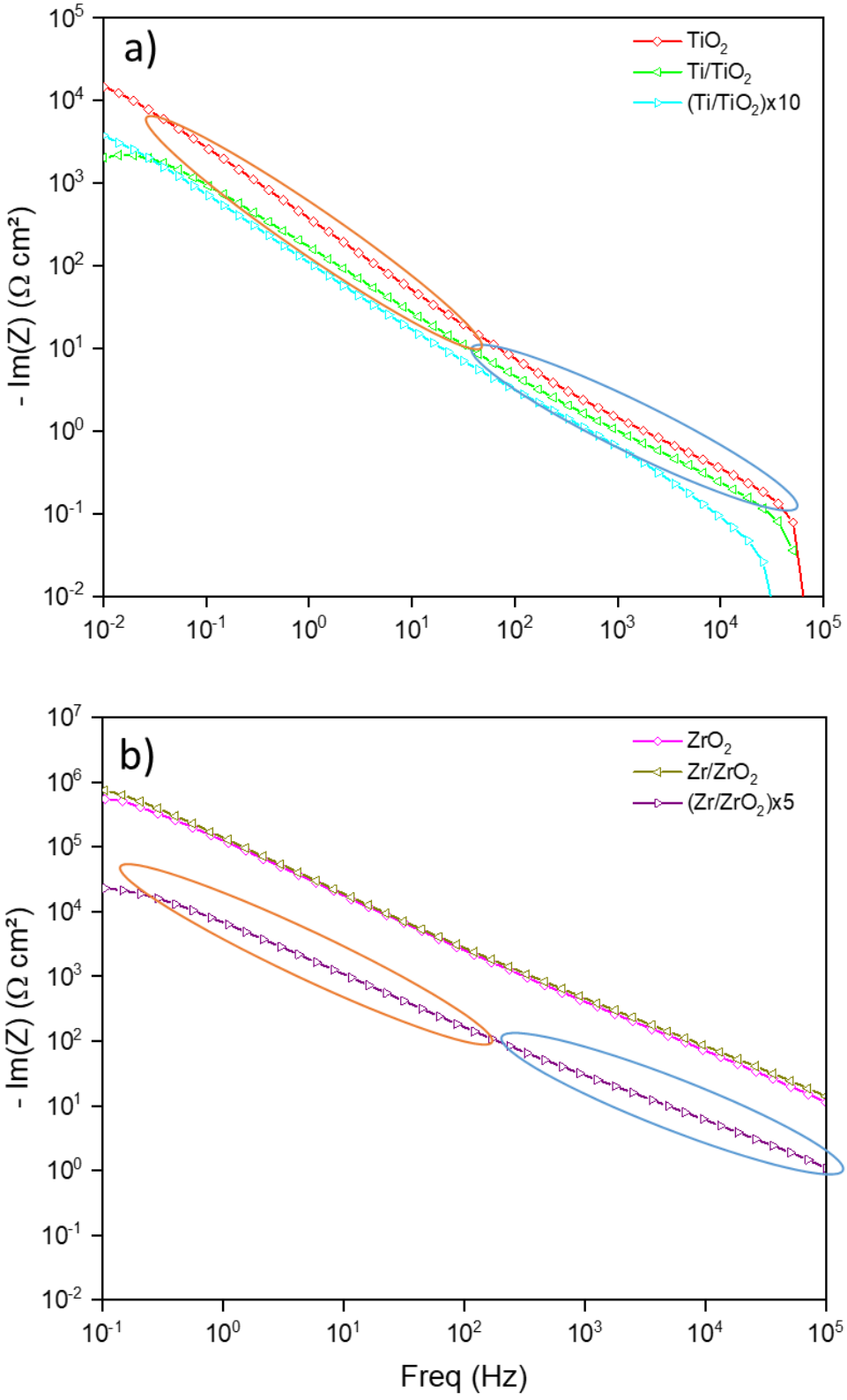

Figure 3: Imaginary part of the impedance as a function de frequency of a) Ti- and b) Zr-based coatings after immersion in a nitric acid (2.5 mol/L HNO_3, 2.5 mol/L $NaNO_3$ and 2 g/L $Fe(NO_3)_3$) solution at 110°C – focus on two slopes curves.

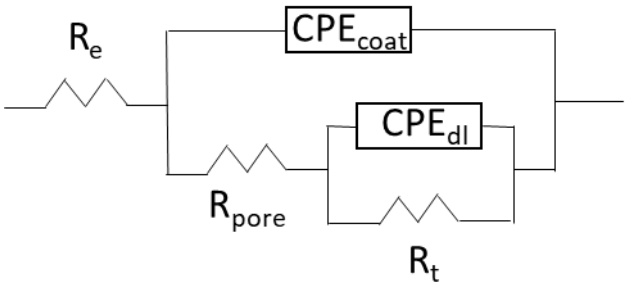

Figure 4: Equivalent electrical circuit of the TiO_2, Ti/TiO_2 and (Zr/ZrO_2)×5 coating systems in a nitric acid (2.5 mol/L HNO_3, 2.5 mol/L $NaNO_3$ and 2 g/L $Fe(NO_3)_3$) solution at 110°C.

R_e is the resistance of the electrolyte, R_t is the charge transfer resistance, R_{pore} is the pore resistance, CPE_{coat} is the constant phase element associated to the coating and CPE_{dl} is the constant phase element attributed to the double layer.